University of Alberta

K-alpha X-Ray and Hot Electron Emission from Microjoule Femtosecond Laser Produced Plasmas

by

Cristina Serbanescu ©

A thesis submitted to the Faculty of Graduate Studies and Research in partial fulfillment
of the requirements for the degree of **Doctor of Philosophy**.

Department of Electrical and Computer Engineering

Edmonton, Alberta
Fall 2007

Library and
Archives Canada

Published Heritage
Branch

395 Wellington Street
Ottawa ON K1A 0N4
Canada

Bibliothèque et
Archives Canada

Direction du
Patrimoine de l'édition

395, rue Wellington
Ottawa ON K1A 0N4
Canada

Your file Votre référence
ISBN: 978-0-494-33060-9
Our file Notre référence
ISBN: 978-0-494-33060-9

NOTICE:
The author has granted a non-exclusive license allowing Library and Archives Canada to reproduce, publish, archive, preserve, conserve, communicate to the public by telecommunication or on the Internet, loan, distribute and sell theses worldwide, for commercial or non-commercial purposes, in microform, paper, electronic and/or any other formats.

The author retains copyright ownership and moral rights in this thesis. Neither the thesis nor substantial extracts from it may be printed or otherwise reproduced without the author's permission.

AVIS:
L'auteur a accordé une licence non exclusive permettant à la Bibliothèque et Archives Canada de reproduire, publier, archiver, sauvegarder, conserver, transmettre au public par télécommunication ou par l'Internet, prêter, distribuer et vendre des thèses partout dans le monde, à des fins commerciales ou autres, sur support microforme, papier, électronique et/ou autres formats.

L'auteur conserve la propriété du droit d'auteur et des droits moraux qui protège cette thèse. Ni la thèse ni des extraits substantiels de celle-ci ne doivent être imprimés ou autrement reproduits sans son autorisation.

In compliance with the Canadian Privacy Act some supporting forms may have been removed from this thesis.

While these forms may be included in the document page count, their removal does not represent any loss of content from the thesis.

Conformément à la loi canadienne sur la protection de la vie privée, quelques formulaires secondaires ont été enlevés de cette thèse.

Bien que ces formulaires aient inclus dans la pagination, il n'y aura aucun contenu manquant.

Canada

To my parents

Abstract

The keV X-ray emission from laser-produced plasmas using a tabletop femtosecond laser system is studied in order to develop a compact and efficient K_α X-ray source to be operated at kilohertz repetition rate. These sources are of considerable interest for applications of time-resolved X-ray diffraction and X-ray microscopy. These studies were carried out using 120fs, 800nm, 0.75mJ Ti:Sapphire laser pulses focused on solid targets to intensities in the range of 10^{16} -10^{17} W/cm^2. The experiments were concentrated on the characterization and the comparison of the keV X-ray emission generated in both air and vacuum. Scaling of K_α X-ray conversion efficiency, dependence on pulse energy, prepulse contrast ratio and angle of incidence were investigated. Using the knife-edge technique, the size of the K_α X-ray emission was measured to be approximately 8 μm.

A K_α X-ray point source was constructed to be operated at 1 kHz repetition rate. Emission rates of 6.7×10^9 photons/s into 2π sr at 1 kHz repetition rate were demonstrated resulting in peak observed X-ray conversion efficiency into Cu K_α line emission of 3.2×10^{-5}. This is the highest K_α X-ray flux reported for kHz sources from microjoule femtosecond laser pulses.

Hot electron emission produced in the same intermediate intensity range was characterized as well. The experimental results show strong emission of hot electrons with energies from 80 keV to above 250 keV created with both *p*- and *s*-polarized 250 μJ laser pulses. Directional emission of accelerated electrons with energies above 250 keV was observed, which was dependant on the laser polarization and target geometry.

The electron jet is sufficiently intense that can be used for electron radiographic imaging experiments. Modeling of the interaction process for p-polarized laser pulses was carried out using a 2D particle-in-cell (PIC) code. Hot electrons with energies over 200 keV emitted between normal and specular direction were observed in simulations as well. The generation of a very energetic and directional beam of electrons is tentatively attributed to two-plasmon decay or stimulated Raman scattering. The generation mechanism for the bulk of the hot electron emission leading to K_α radiation is attributed to resonance absorption.

Acknowledgements

I would like to thank my supervisor Dr. Robert Fedosejevs for his support and advice during my PhD program. I would also like to acknowledge Dr. Y. Y. Tsui for providing his lab facility. Further thanks go to Dr. W. Rozmus and Dr. C. Capjack for helpful discussions on PIC simulations and short-pulse laser-plasma interactions.

I warmly thank Blair Harwood for his technical expertise and Rick Conrad for his help building a darkroom. I would also like to thank Herbert Dexel and people from ECE machine shop for their fine work over many years.

I am grateful to my friends and colleagues for interesting discussions. In particular, I wish to acknowledge specific help by late Dr. J. Santiago and Dr. J. A. Chakera. I warmly thank to Dr. D. Romanov for his support with PIC simulations and for helpful discussions with Neda Naseri and Dr. Paul-Edouard Masson-Laborde.

Finally, I am very grateful to my family, especially to my husband who has been extremely understanding and supportive of my studies.

Table of Contents

INTRODUCTION 1

1.1 Motivation 3

1.2 Contribution of this thesis 5

1.3 Thesis contents 6

THEORETICAL BACKGROUND 8

2.1. Laser plasma interaction 8

2.2 Hot electron temperature 23

2.3 Hard X-ray emission processes from femtosecond laser-produced plasmas 27

2.3.1 Bremsstrahlung radiation 27

2.3.2 Characteristic X-ray line radiation 29

2.4 K_α X-ray generation process from femtosecond laser-produced plasmas 31

2.5 Previously reported K_α X-ray sources from femtosecond laser-produced plasmas 39

EXPERIMENTAL SETUP 44

3.1 Laser and target systems 44

3.1.1 Description of the laser system 44

3.1.2 Laser spot size measurements 49

3.1.3 Description of the target system 58

3.1.4 Description of the vacuum system 63

3.2 Description of the experiments 64

3.3 X-ray diagnostics 67

3.4 Electron jet diagnostics 77

X-RAY EXPERIMENTAL RESULTS AND DISCUSSION 80

4.1. Study of K_α X-ray emission in single shot mode 80

4.2 K_α X-ray source operated at kilohertz repetition rate 97

HOT ELECTRONS AND ELECTRON JETS FROM SOLID TARGETS 107

5.1 Electron jets measurements and discussion 107

5.2 Angular dependence of the hot electrons 122

5.3 Electron radiography using hot electron jets 131

PIC SIMULATION 137

6.1 General description of the particle in cell (PIC) code 137

6.2 Simulation results 145

6.3 Simulations of angular hot electron distribution 166

6.4 Plasma density scale length effect on the hot electron emission 173

CONCLUSION 183

BIBLIOGRAPHY 189

Appendix A: ENERGY LEVEL DIAGRAM FOR COPPER 200

Appendix B: PIC FILES 202

List of Tables

Table 2.1. Measurements of T_{hot} using short pulse lasers................................24

Table 2.2. K_{α} X-ray generation with ultrashort laser pulses focused on solid targets unless otherwise specified. The laser pulses are less than 1 ps unless otherwise specified 42

Table 3.1. Theoretical values of the beam waists and the spot sizes (FWHM) of the laser beam obtained with the four different microscope objectives used to focus the laser pulses. These values have been calculated using Gaussian beam theory (equations 3.1 and 3.3). The measured value of the input beam waist (ω_{01} = 3.56 mm) was used to determine ω_{02} 50

Table 6.1 The peak of the outgoing electrons with energies over 80 keV obtained at three different times, at 301 fs, 339 fs and 377 fs when laser beam is incident on a 5.0 μm thick metal foil, at 45° angle of incidence. The peak laser pulse hits the 5 μm thick foil target at the time t = 285 fs. The initial foil density profile is exponential starting from 0.03 n_c to 5 n_c, corresponding to a density scale length of 1 μm. The angles are measured from the PIC code x-axis...169

Table 6.2 The peak of the outgoing electrons with energies over 80 keV obtained at three different times, at 301 fs, 339 fs and 377 fs. The peak laser pulse hits the 2.5 μm thick foil target at the time t = 285 fs. The initial foil density profile is exponential starting from 0.03 n_c to 5 n_c, corresponding to a density scale length of 0.5 μm. The angles are measured from the PIC code *x*-axis……………………………………….175

Table 6.3 The peak of the outgoing electrons with energies over 80 keV obtained at three different times, at 301 fs, 339 fs and 377 fs. The peak laser pulse hits the 5 μm thick foil target at the time *t* = 285 fs. The initial foil density profile is exponential starting from 0.03 n_c to 7.5 n_c, corresponding to a density scale length of 0.45 μm. The angles are measured from the PIC code *x*-axis……………………………………….176

Table 6.4 The peak of the outgoing electrons with energies over 80 keV obtained at three times at 301 fs, 339 fs and 377 fs. The peak laser pulse hits the 5 μm thick foil target at the time *t* = 285 fs. The initial foil density profile is exponential starting from 0.03 n_c to 7.5 n_c, corresponding to a density scale length of 0.45 μm. The ions are free to move and have a mass of 1840 m_e and charge of q = +1. The angles are measured from the PIC code *x*-axis…………………………………………………….180

List of Figures

Figure 2.1 Schematic diagram of the electron density structure of laser produced plasma [28]. Laser light is reflected at the critical surface. The laser light is absorbed at the critical density and in the region below the critical density............................10

Figure 2.2 An illustration of the laser plasma interaction, showing the laser pulse interaction with the hot plasma formed at the surface of the target material and the subsequent emission of high-energy electrons and X-ray photons. 13

Figure 2.3 Schematic diagram illustrating a light wave obliquely incident at an angle θ_{inc} onto a plasma density profile for p-polarized light (E-field in the plane of ∇n_e). The laser beam will propagate up to density $n_c \cos^2 \theta_{inc}$ before it is specularly reflected (Following [42]). 16

Figure 2.4 Angular absorption dependence for three density scale-lengths: $L/\lambda = 1$, $L/\lambda = 0.1$ and $L/\lambda = 0.01$ [43] for both p- and s-polarized laser pulses. The maximum absorption for p-polarized laser pulses occurs at larger angles of incidence as the plasma density gradient becomes steeper (Following [43]).. 19

Figure 2.5 Measurements of the hot electron temperature T_{hot} from laser produced plasma using sub-picosecond laser pulses (open squares). Four theoretical models for T_{hot} are superimposed on the experimental results: Forslund (equation 2.16 assuming

$T_{cold[keV]} = 0.5$ keV), Brunel (equation 2.17), Gibbon& Bell (equation 2.20) and Wilks (equation 2.21). (Following Gibbon [43])......26

Figure 2.6 Bremsstrahlung radiation occurs when an incident hot electron is accelerated as it passes a nucleus [28]........28

Figure 2.7 An incident hot electron of sufficiently high energy to overcome the binding energy knocks out a core electron from the K-shell leaving the atom with a core vacancy. K_α radiation is generated as the atom readjusts to the core vacancy through the emission of characteristic energy. 29

Figure 2.8 K-shell ionization cross section for copper as a function of parameter U, which is the ratio between the incident electron energy E and the ionization energy E_K of the target electrons in the K-shell ($U=E/E_K$). 1barn = 10^{-24} cm^2. For Cu target, E_K = 8.98 keV. The full curve represents the cross section determined by Homourger [67], which is compared with other works [Refs. 25, 29 and 33 within]........32

Figure 2.9 X-ray transmission through copper material of different thickness: 10 μm, 20 μm, 30 μm and 40 μm. The transmissions of Cu K_α photons ($E_{K\alpha}$=8.05 keV) are $T_{10\mu m}$=0.64, $T_{20\mu m}$=0.41, $T_{30\mu m}$=0.26, and $T_{40\mu m}$=0.17........34

Figure 2.10 The geometry of X-ray emission from a one-dimensional target........35

Figure 2.11 The average path length (CSDA range) traveled by an electron as it slows down to rest in copper target........36

Figure 2.12 (a) Simulated K_α X-ray yields from bulk targets for four metals: Titanium (Z=22), Copper (Z=29), Silver (Z=47) and Tantalum (Z=73). (b) Optimum laser intensity versus the target material, line is from analytical model-equation (2.25) and the points are from simulations [71]..38

Figure 3.1 A sample of the photodiode signal that is used to measured the main laser pulse (top) and the prepulse train (bottom) for the case of 5×10^{-4} contrast ratio... The signal from the main laser pulse is totally saturated causing clipping and also shifting the baseline after the pulse is finished (bottom)..46

Figure 3.2 A sample of the photodiode signal that provides an image of the main laser pulse and the prepulse train for the case of 10^{-1} contrast ratio. Multiple prepulses are observed in this case...48

Figure 3.3 The photodiode signal versus the knife-edge position 52

Figure 3.4 Laser beam profile: (a) Two dimensional profile display as measured by an infrared CCD camera (Ultrak K-500 1/2") with Spiricon Software (LBA-400PC), (b) the beam profile measured along *x*-direction and (c) the beam profile measured along *y*-direction. The beam profile on *x*- and *y*- direction was fitted with a Gaussian function using the method of least squares...56

Figure 3.5 The target system used with the plane targets made of 500 nm thick copper film sputtered onto a silicon wafer. The system consists of three-axis computer controlled translation mounts, two of them used to translate the target and one to move the focusing objective..60

Figure 3.6 Image of the first target a 500 nm thick copper film sputtered onto a silicon wafer: side view (top) and top view (bottom).. 61

Figure 3.7 Schematic diagram of the experimental setup. M is a mirror, λ/2 is a half-wave plate, POL is a polarizer, L is a lens (positive), PD is a photodiode, CdTe is a Cadmium Telluride detector, MCA is a multichannel analyzer............................ 65

Figure 3.8 The target geometry: (a) top view and (b) side view........................... 66

Figure 3.9 The theoretical response function for (a) PIN diode and (b) PIN diode with Al filters of three different thickness: 9 μm, 62.5 μm and 125 μm.........................69

Figure 3.10 The response function of the silicon PIN diode detector employed with: (a) two different foil filters:15 μm Ni + 9 μm Al (solid line) and 25 μm Fe (dashed line) and (b) the sensitivity of the Ross filter pair when taking the difference of the two detector signals...70

Figure 3.11 The intrinsic efficiency of CdTe detector... 72

Figure 3.12 The X-ray transmission of 100 μm thick Be window........................ 73

Figure 3.13 The X-ray transmission of 139 cm thickness of air.......................... 73

Figure 3.14 The transmission of 75 μm thick Mylar window.................................74

Figure 3.15 Schematic diagram of the experimental setup used for X-ray imaging.... 75

Figure 3.16 (a) Geometry for measurement of the electron jets, (b) details of the geometry in the case of *s*-polarized laser pulses.. 77

Figure 3.17 Side view of the experimental geometry employed to determine the angular distribution of the hot electrons...78

Figure 4.1 X-ray focal scans obtained in air for two different prepulse regimes when using the 4X microscope objective with p-polarized laser light at an energy of about 210 μJ incident on the target for similar angles of incidence: (a) with a prepulse contrast ratio of 10^{-1} and a angle of incidence of 24°; (b) with a prepulse contrast ratio of 5×10^{-4} and an angle of incidence of 22.5°. The x-axis scale is not related between the two plots.. 82

Figure 4.2 X-ray focal scans obtained when using the 10X microscope objective at an energy of about 160 μJ incident on the target with p-polarized laser light, a prepulse contrast ratio of 5×10^{-4} and a angle of incidence of 22° in air..................................83

Figure 4.3 X-ray focal scans obtained when using the 4X microscope objective at an energy of about 210 μJ incident on the target with p-polarized laser light in air, a prepulse contrast ratio of 10^{-1} and a angle of incidence of 42° 83

Figure 4.4 SEM images of the resultant craters of copper film coated onto a silicon wafer from laser pulses with energies of about 250 μJ in air.............................. 84

Figure 4.5 X-ray signals measured in air from copper film on silicon target. The X-ray signal rapidly increases with laser pulse energy and eventually saturates. (a) for a prepulse contrast ratio of 10^{-1} using the 4X microscope objectives. (b) for a prepulse contrast ratio of $5\text{x}10^{-4}$ using the 10X microscope objectives. The lines are drawn as a visual aid..85

Figure 4.6 Measured reduction in X-ray signal transmitted through aluminum foil filters (normalized to the signal through a 62.5 μm-thick aluminum foil) versus filter thickness. The circles represent the experimental data and the lines represent calculated ratios for different photon energy X-rays...86

Figure 4.7 The X-ray conversion efficiency as a function of background ambient gas pressure. The 8.0 keV Cu K_α X-ray signals where detected using X-ray PIN diodes filtered with a 15 μm Ni + 9 μm Al and 25 μm Fe filter Ross pair. The two different data points are from two different measurements. Data was taken with the 10X objective at θ_{inc}=22°.. 87

Figure 4.8 A schematic diagram of the knife-edge technique...............................90

Figure 4.9 The scan of the DEF film at the location of the penumbra. The DEF film is the X-ray detector employed to measure the K_α X-ray source size using the knife-edge technique. The knife-edge is a 25 μm Fe filter located 7 mm from the source. Due to its *K*-edge absorption edge at 7.11 keV, the filter completely blocks the Cu K_α 8.05 keV radiation. The DEF stripfilm is located 147 mm away from the knife-edge. The scanned region was a strip 300 μm wide on the film.. 92

Figure 4.10 Summary of the X-ray experimental results. The solid squares represent the results from 4X objective on copper film and the solid circles for the 10X objective on a bulk target for a contrast of 5x10^{-4} and p-polarized incidence. The solid triangles are for the case of the 4X objective on copper film for 10^{-1} contrast and p-polarized incidence. The measurements with the 4X objective were taken with a simple 62.5 μm aluminum filter while those for 10X objective were taken using the Ross filter pair. The solid line is a visual aid to connect the data points corresponding to 5x10^{-4} contrast taken at 1 atm pressure...95

Figure 4.11 (a) Raw Cu X-ray spectrum obtained with CdTe detector from 275 μJ femtosecond laser pulses at 1 kHz repetition rate. The spectrum was recorded in 63 seconds. (b) The signal from the high-energy tail has been fitted by a Maxwellian electron distribution and the hot electron temperature has been found to be T_h = 7.6±0.5

keV. Only the X-ray bremsstrahlung signals with energies in the range of 10.5 keV to 30 keV have been considered for the fit.. 97

Figure 4.12 (a) Raw Cu X-ray spectrum obtained with CdTe detector from 290 μJ femtosecond laser pulses at 1 kHz repetition rate. The spectrum was recorded in 58 seconds. (b) The signal from the high-energy tail has been fitted by a Maxwellian electron distribution and the hot electron temperature has been found to be $T_h = 7.7 \pm 0.4$ keV. Only the X-ray bremsstrahlung signals with energies in the range of 10.5 keV to 30 keV have been considered for the fit..98

Figure 4.13 Cu K_α X-rays conversion efficiency generated for different laser repetition rate. P-polarized laser pulses with energies of 200-300 μJ have been employed and focused with the 10X objective onto the rotating disk copper target at an angle of incidence of 30°..100

Figure 4.14 A simulated Cu K_α X-ray spectrum obtained after the raw Cu K_α X-ray spectrum from Figure 4.12 is filtered with 15 μm Ni foil. The ratio of the K_α line and the residual radiation 1-7.51 keV plus 8.48 keV-30 keV is 0.69 after filtering..............105

Figure 5.1 Electron jet images on the front and back sides of DEF film for >80 keV and >250 keV energies ranges respectively for p-polarized 30° incidence (top). The image from the electrons with energies higher than 250 keV, on the back side of the film, can be seen in the central line of the DEF film. The exposure resulted from 7 shots on target. Measured electron distribution of the outgoing hot electrons given by the optical density of both the front and rear sides of DEF film (bottom). The DEF film was placed at 5.5 mm from the target spot..110

Figure 5.2 Electron jet images on the front and back sides of DEF film for >80 keV and >250 keV energies ranges respectively for s-polarized 30° incidence (top). The image from the electrons with energies higher than 250 keV, on the back side of the film, can be seen in the central line of the DEF film. The exposure resulted from 7 shots on target. Measured electron distribution of the outgoing hot electrons given by the optical density of the both front and rear sides of DEF film (bottom). The DEF film was located at 16.5 mm from the target spot...111

Figure 5.3 The density response curves for X-rays, 80 keV electrons and 250 keV electrons. The exposures are calculated for 80 keV electrons on the first film emulsion surface and for 250 keV electrons on the second emulsion surface of the DEF film. The X-ray exposures are given for X-rays with energies of 4.51 keV and 4.93 keV, which are taken from Rockett at al. [91] from an experimental calibration data of Kodak DEF film..113

Figure 5.4 The angular distribution of the outgoing hot electrons for > 80 and > 250 keV energies ranges respectively, deduced from the DEF film measurements: (a) p-polarized at 30° incidence and (b) s-polarized at 30° incidence. The DEF films were covered with 33 μm Al filter in both cases. For p-polarization case: θ is measured with respect to the target normal, in the plane of incidence. For s-polarization case: φ is measured with respect to the electric field direction in the plane of laser electric field polarization..114

Figure 5.5 The schematic diagram of the setup used to scan the DEF films. M is a mirror, PD is a photodiode, RF is a reflective filter (different filters have been used), A is an aperture, L is a lens (positive). The DEF film was mounted on two-axis stages as to allow movement in both the horizontal and vertical directions. The optical densities are measured using matched influx-efflux optics of 0.1 N.A. The lenses used were L_1=6 cm f.l. and L_2=10 cm f.l...115

Figure 5.6 A hot electron focal scan performed to determine the location for maximum hot electron signal using PIN diode detector. Each point represents the average of a minimum of three laser shots. The error bars represents the standard deviation. The PIN diode was located at a distance of 4.9 cm at $\theta = 35°$ for p-polarized laser pulses incident at $\theta_{inc} = 30°$...122

Figure 5.7 A hot electron angular plot obtained by means of PIN diode detector filtered with 50 μm Al foil for p-polarized laser pulses with energies of E =260 μJ (± 5%) incident at θ_{inc}=30°. Each point represents the average of five laser shots. The error bars represents the standard error. The PIN diode was located at a distance of 4.9 cm. The angle interval from -26° to 26° was blocked by the 10X microscope objective. The emission angle is given with respect to the direction of the incidence of the laser. Normal and specular directions are represented by the angle θ=30° and 60°, respectively...123

Figure 5.8 A hot electron angular plot obtained by means of PIN diode detector filtered with 50 μm Al foil for p-polarized laser pulses with energies of E =275 μJ (± 5%) incident at θ_{inc}=30°. Each point represents the average of a minimum of three laser shots. The error bars represents the standard error. The PIN diode was located at a distance of 6.1 cm. The angle interval from -26° to 26° was blocked by the 10X microscope objective. The emission angle is given with respect to the direction of laser propagation. Normal and specular directions are represented by the angle θ=30° and 60°, respectively 124

Figure 5.9 A hot electron angular plot obtained by means of PIN diode detector filtered with 50 μm Al foil for p-polarized laser pulses with energies of *E* =235 μJ (± 5%) incident at θ_{inc}=30°. Each point represents the average of a minimum of three laser shots. The error bars represents the standard error. The PIN diode was located at a distance of 6.1 cm. The angle interval from -26° to 26° was blocked by the 10X microscope objective. The emission angle is given with respect to the direction of laser propagation. Normal and specular directions are represented by the angle θ=30° and 60°, respectively 125

Figure 5.10 Hot electron angular plot obtained by means of PIN diode detector filtered with 50 μm Al foil for p-polarized laser pulses with energies of *E* =200 μJ (full circles) and *E* =275 μJ (open circles) incident at θ_{inc}=36°. The PIN diode was located at a distance of 5.4 cm. The angle interval from -26° to 26° was blocked by the 10X microscope objective. The emission angle is given with respect to the direction of laser propagation. Normal and specular directions are represented by the angle θ=36° and 72°, respectively 126

Figure 5.11 A hot electron angular plot obtained by means of PIN diode detector filtered with 33 μm Al foil for p-polarized laser pulses with energies of *E* =250 μJ (± 5%) incident at θ_{inc} =42°. Each point represents the average of eleven laser shots. The error bars represents the standard error. The PIN diode was located at a distance of 5.5

cm. The angle interval from -26° to 26° was blocked by the 10X microscope objective. The emission angle is given with respect to the direction of laser propagation. Normal and specular directions are represented by the angle θ=42° and 84°, respectively..127

Figure 5.12 A hot electron angular plot obtained by means of PIN diode detector filtered with 33 μm Al foil for p-polarized laser pulses with energies of E =290 μJ (± 5%) incident at θ_{inc} =65°. Each point represents the average of seven laser shots. The error bars represents the standard error. The PIN diode was located at a distance of 5.6 cm. The angle interval from -26° to 26° was blocked by the 10X microscope objective. The emission angle is given with respect to the direction of laser propagation. Normal and specular directions are represented by the angle θ=65° and 130°, respectively..128

Figure 5.13 Angular dependence of laser angle of incidence obtained by means of PIN diode detector filtered with 50 μm Al foil for p-polarized laser pulses with energies with energies of E =200-300 μJ. The emission angle is given with respect to the direction of laser propagation..129

Figure 5.14 Geometric layout for obtaining the radiographic images for two test objects, a metal grid and a bee. The images were obtained using hot electrons with energies higher than 250 keV generated by *s*-polarized laser pulses: (a) a metal grid was located between two film strips at a distance of 17.1 mm from the focal point. (b) A bee was positioned at a distance of 14.7 mm from the focal point. Both objects were located against the DEF film covered in 33 μm aluminum, which is shown as black bands in the pictures......132

Figure 5.15 Radiographic images obtained with the hot electrons with energies higher than 250 keV when the laser pulses were s-polarized. (a) The test object was a nickel grid placed between two DEF filmstrips. The exposure was taken using 17 laser shots on target. (b) The test object was the leg of a bee placed in front of a DEF filmstrip, which was initially covered in aluminum foil of 33 μm. The exposure was taken using 23 laser shots on target......133

Figure 5.16 Lineout of the test pattern shown in Figure 5.15 (a). The experimental data indicates a 10% to 90% resolution of 103 μm......133

Figure 6.1 The basic cycle of a particle in cell simulation cycle. (Following Kruer [29])......138

Figure 6.2 Schematic diagram of the PIC run setting. The laser beam propagates along the *x* direction. The laser beam is incident on a metal foil at 45°. $\overrightarrow{N}_1$ is the direction of the front side foil normal ($\varphi_z = 135°$). $\overrightarrow{N}_2$ is the direction of the back side foil normal ($\varphi_z = -45°$). $\overrightarrow{S}$ is the specular direction ($\varphi_z = 90°$)......142

Figure 6.3 Schematic diagram of the PIC run setting. The laser beam is propagating along the *x* direction. The laser beam is incident on a metal foil at 45°. The initial electron density profile of the foil is set to be exponential from 0.03 n_c to 5 n_c......143

Figure 6.4 The laser electric field squared $\left|\overrightarrow{E}_L\right|^2$ at $t = 80$ fs. (a) The laser electric field squared $\left|\overrightarrow{E}_L\right|^2$ ($\left|\overrightarrow{E}_L\right|^2 \propto I_L$) propagating in the domain, and (b) $\left|\overrightarrow{E}_L\right|^2$ extracted along the foil normal direction as a function of *x*-coordinate. The beam enters the simulation domain from left and propagates along the *x* direction into the vacuum until it interacts with a 5-μm thick metal foil located in the central part of the domain at an angle of 45° with respect to the laser propagation direction..146

Figure 6.5. The electron charge density (n_e) at t = 80 fs. (a) The magnified central part of the electron density (n_e) profile, and (b) n_e extracted along the foil normal direction as a function of *x*-coordinate. The beam enters the simulation domain from left and propagates along the *x* direction into the vacuum until it interacts with a 5-μm thick metal foil located in the central part of the domain at an angle of 45° with respect to the laser propagation direction...147

Figure 6.6 The laser electric field squared $\left|\vec{E}_L\right|^2$ at t = 140 fs. (a) The laser electric field squared $\left|\vec{E}_L\right|^2$ ($\left|\vec{E}_L\right|^2 \propto I_L$) propagating in the domain for y=25 μm, and (b) $\left|\vec{E}_L\right|^2$ extracted along the foil normal direction as a function of *x*-coordinate. The beam enters the simulation domain from left and propagates along the *x* direction into the vacuum until it interacts with a 5-μm thick metal foil located in the central part of the domain at an angle of 45° with respect to the laser propagation direction.................149

Figure 6.7 Electron density at t = 140 fs. (a) The magnified central part of the electron density (n_e) profile, and (b) n_e extracted along the foil normal direction from (x=31μm, y=21 μm) to (x=21μm, y=31 μm). The beam enters the simulation domain from left and propagates along the *x* direction into the vacuum until it interacts with a 5-μm thick metal foil located in the central part of the domain at an angle of 45° with respect to the laser propagation direction..150

Figure 6.8 The laser electric field squared, $\left|\vec{E}_L\right|^2$ ($\left|\vec{E}_L\right|^2 \propto I_L$) at the peak of the laser pulse (t = 244 fs): (a) in the whole domain and (b) a magnified image of the interaction area. The laser beam is reflected by 5-μm thick metal foil located in the central part of the domain at an angle of 45° with respect to the initial laser propagation direction. The laser pulse has a peak intensity of 5.7×10^{16} W/cm^2, pulse duration (FWHM) of 130 fs and a beam diameter (FWHM) of 5 μm. The initial electron density profile of the foil is set to be exponential from 0.03 n_c to 5 n_c..152

Figure 6.9 The electron density (n_e) at time t=244 fs when the peak of the laser pulse interacts with the 5-μm thick foil positioned at 45° with respect to the initial laser propagation direction: (a) in the whole domain and (b) a magnified image of the interaction area. The laser pulse has a peak intensity of 5.7×10^{16} W/cm^2, pulse duration (FWHM) of 130 fs and a beam diameter (FWHM) of 5 μm. The initial electron density profile of the foil is set to be exponential from 0.03 n_c to 5 n_c. Accelerated electrons are leaving the foil from both front and rear sides. Waves in plasma can be observed at different electron densities.. 153

Figure 6.10 Profiles of (a) the laser electric field squared $\left|\vec{E}_L\right|^2$ at y=25 μm and (b) the electron density n_e extracted along the foil normal direction at t=244 fs. The normal direction used to extract n_e is defined by the two points, A(x= 21 μm, y=31 μm) and B (x= 31 μm, y=21 μm)..154

Figure 6.11 Profiles of the electron density n_e extracted along the foil normal direction at t=244 fs. (a) The foil normal direction is defined by the two points A(x=21 μm, y =29μm) and B(x=29 μm, y = 21μm) (b) The foil normal direction is defined by the two points A(x=21μm, y = 30μm) and B(x=30 μm, y = 21μm)....................................156

Figure 6.12 Electron density n_e extracted parallel to the foil surface close to the original critical density contour at t=244 fs. It can be observed that the electron wave has a period of 1 μm when plotted as a function of x-coordinate as done here, which is, as expected, the same as the laser period...157

Figure 6.13 Electron density n_e extracted along the x-direction at y = 25 μm t=244 fs. Besides the electron density perturbation observed at critical density, another electron density perturbation can be seen in the underdense plasma close to the quarter critical density (¼ n_c)..157

Figure 6.14 Profiles of the electron density n_e extracted along x-direction (a) at y = 25.6 μm and (b) at y = 26.4 μm at t=244 fs. These indicate that the laser light is also causing perturbations at several times the critical density..158

Figure 6.15 Electron energy distribution versus angle φ_z at the peak of laser pulse (t=244 fs). Two electron jets with energies over 200 keV are observed. The electron jet emitted from the front side is found to be between the specular and normal directions (angle φ_z = 120°). The jet from rear side of the thin foil is also observed in the simulations (angle φ_z=-35°), which is not measured in the experiments since a solid target was employed. The metal foil has 5-μm thickness and an initial exponential density profile from 0.05 n_c to 5 n_c. The laser pulse has a peak intensity of 5.7×10^{16}

W/cm^2, pulse duration (FWHM) of 130 fs and a beam diameter (FWHM) of 5 μm. The normal direction of the front side, $\overrightarrow{N_1}$ is described by the angle $\varphi_z = 135°$. The normal direction of the rear side, $\overrightarrow{N_2}$ is represented by the angle $\varphi_z = -45°$, and the specular direction, $\vec{S}$ is describe by the angle $\varphi_z = 90°$... 160

Figure 6.16 The electron distribution function of all electrons in the simulation box is fitted with three electron Maxwellian distributions using the least-square fit. T_{cold}=2.6 keV describes the temperature of the bulk of the electrons. The hot electron component is described by two electron temperatures: T_{1hot}=15 keV and T_{2hot}=41 keV............ 163

Figure 6.17 The hot electron component is described by two electron temperatures: T'_{1hot}=15 keV and T'_{2hot}=41 keV. Only the outgoing electrons have been considered in this case, which are located in the box described by the coordinates, x = [21, 27] and y=[25.5 33.6] at *t*=244 fs... 164

Figure 6.18 Angular distributions of the plasma electrons for two different times. The laser beam is incident on a 5.0 μm thick metal foil, at 30° angle of incidence in a p-polarized beam. The foil initial density profile was exponential starting from 0.03 n_c to 5.0 n_c corresponding to a density scale length L_n = 1 μm...............................167

Figure 6.19 Angular distributions of the plasma electrons for three different times. The p-polarized laser beam is incident on a 5.0 μm thick metal foil, at 45° angle of incidence. The foil initial density profile was exponential starting from 0.03 n_c to 5.0 n_c corresponding to a density scale length L_n = 1 μm.......................................168

Figure 6.20 Angular distributions of the plasma electrons for three different times. The laser beam is incident on a 5.0 μm thick metal foil, at 60° angle of incidence. The foil initial density profile was exponential starting from 0.03 n_c to 5.0 n_c corresponding to a density scale length $L_n = 1$ μm……170

Figure 6.21 The angular distribution of the hot electrons with energy higher than 80 keV. The filled diamond points represent the experimental data while the open circles represent the simulation results. The angles obtained from the simulations are considered for the latest time for each simulation run, but before the particles reach the walls of the simulation box as they bounce back in the domain and alter the results. For θ_{inc}=30° this occurred before the peak of the laser pulse……171

Figure 6.22 Angular distributions of the hot electrons with energies over 80 keV for three different times. The laser beam is incident on a 2.5 μm thick metal foil, at 45° angle of incidence. The foil initial density profile was exponential starting from 0.03 n_c to 5.0 n_c corresponding to a density scale length $L_n = 0.5$ μm……175

Figure 6.23 Angular distributions of the hot electrons with energies over 80 keV for three different times. The laser beam is incident on a 2.5 μm thick metal foil, at 45° angle of incidence. The foil initial density profile was exponential starting from 0.03 n_c to 7.5 n_c corresponding to a density scale length $L_n = 0.45$ μm……176

Figure 6.24 Angular distributions of the hot electrons with energies over 80 keV for three different times. The laser beam is incident on a 5.0 μm thick electron foil. The initial density profile was set to be exponential starting from 4.9 n_c to 5.0 n_c corresponding to a density scale length $L_n = 0$ μm……178

Figure 6.25 Angular distributions of the hot electrons with energies over 80 keV for three different times. The laser beam is incident on a 5.0 μm thick electron foil accompanied by a 5.0 μm thick ion foil at 45° angle of incidence. The initial density profile for both foils was set to be exponential starting from 0.03 n_c to 5.0 n_c corresponding to a density scale length L_n = 1 μm. The ions have charge q=+1 and mass m=1840 m_e (where m_e is the electron mass)..........179

List of Symbols, Abbreviations and Acronyms

Symbols

$\vec{B}$	magnetic field
c	speed of light in vacuum
d_{FWHM}	beam diameter at full width at half maximum; the diameter at which the beam intensity drops to (½) of its peak
e	electronic charge
$\vec{E}$	electric field
f	focal length
h	Planck's constant
I	intensity
$\vec{J}$	current density
$\vec{k}$	wave vector
L_n	plasma density scale length
m	mass
n_e	plasma electron density
n_c	critical electron density
P	power
q	charge
t_L	laser pulse duration

T	transmission function
T_e	electron temperature
T_{hot}	hot electron temperature
T_{cold}	cold electron temperature
v_e	thermal velocity
v_{os}	oscillation velocity
z_R	Rayleigh range
ϵ	dielectric function
ε_0	permittivity of vacuum
η	conversion efficiency
λ	wavelength
μ_0	permeability of vacuum
μ/ρ	mass attenuation coefficients
Φ_p	ponderomotive potential
ν	frequency
ρ	density
φ, θ	angle
ω_0	laser beam waist
ω	frequency

Abbreviations and Acronyms

f.l.	focal length
kHz	kilohertz
keV	kilo-electron-volt
CSDA	continuous-slowing-down approximation
DEF	Direct Exposure Film
FWHM	Full Width at Half Maximum
ICF	Inertial Confinement Fusion
NA	numerical aperture
NIST	National Institute of Standards and Technology
PIC	Particle-in-cell

Chapter 1

INTRODUCTION

X-ray generation from laser-produced plasmas has been employed for a long time as a valuable diagnostic to characterize high-density plasma generated in laser-matter interactions. Much of the understanding of the X-ray emission from laser-produced plasmas has been obtained in the context of inertial confinement fusion (ICF). For instance, K_α X-rays have been used to measure the electron energy distribution function and target preheating [1-3]. With the development of ultrafast laser technology, significant research efforts have concentrated on understanding and optimizing the generation of short X-ray pulses from laser-produced plasmas [4-9]. Laser produced plasmas can generate ultrashort pulses of both soft X-rays (<1keV) and hard X-rays (>1keV) by focusing an intense sub-picosecond laser beam onto a solid target. Unlike the soft X-rays, the hard X-rays are produced by the hot electrons generated near the laser focal spot due to high-intensity collective effects in laser-plasma interactions. These hot electrons can penetrate in the cold region of the material behind the plasma where they can create bremsstrahlung or line radiation by knocking out bound electrons from the *K*-shell. Since the hot electrons are only generated during the duration of the high intensity laser pulse, the K_α emission will have a duration similar to that of the laser pulse duration. Therefore, these plasmas are unique sources of hot electrons and multi keV X-rays with exceptional characteristics such as very short duration, and very small size. As a result, they have become very attractive for X-ray probing of the ultrafast dynamics such as innershell electronic processes in atomic systems, chemical reactions and phase transitions in materials [10, 11]. Moreover, these laser-produced plasma sources have the potential to be very small X-ray sources such that high resolution can be achieved in various medical imaging techniques [12].

The generation of hot electrons from the interaction of high-intensity laser pulses with solid targets has received considerable attention in the past as well. This is not only because they are responsible for the generation of ultrashort hard X-ray radiation that can be utilized in time-resolved studies but also because ultrashort electron pulses from femtosecond laser plasmas can be employed for advanced structural investigation as well [13]. Nevertheless, the most extensive investigations of hot electrons from laser-produced plasmas have been related to ICF studies because the hot electrons are undesirable for ICF targets used in the conventional central spot ignition scheme due to premature heating of the fuel material. On the other hand, the newly proposed fusion scheme, i.e. the fast ignitor scheme, depends on achieving the highest possible conversion efficiency of laser energy into hot electrons at a specific energy that also has led to extensive studies of the generation of hot electrons from laser-produced plasmas.

1.1 Motivation

The objective of this thesis is to investigate the hard X-ray emission from laser produced plasmas by using a tabletop femtosecond laser system in order to develop a compact and efficient K_α X-ray source to be operated at kilohertz repetition rate. The development of such a source leads to applications of time-resolved X-ray diffraction and X-ray microscopy.

Until now, the most efficient laser-produced K_α X-ray sources have been reported using laser pulse energies between several to hundreds of mJ with the laser repetition rate in the range of a few tens of Hz [6, 14-16]. The laser pulses have been focused on solid targets and the X-ray conversion into K_α radiation using such lasers is reported to be in the range of 10^{-5} to 10^{-4}. To be widely used in applications, these sources must become compact, require low maintenance, exhibit high average power, and satisfy the application requirements with short exposure times. As laser systems decrease in energy but operate higher in repetition rate, it is possible to provide the required laser pulses with smaller footprint systems, with lower capital cost and low maintenance operation. Moreover, they have become commercially available as user friendly systems. The remaining question is whether the quantity and the quality of the X-rays from lower energy pulses are similar to those generated by high energy laser pulses. Recently, research efforts have been concentrated to develop compact K_α X-ray sources with kilohertz repetition rates [17-22] using various kinds of targets and laser pulse energies from sub-mJ to several mJ. However, a decrease in the energy conversion efficiency into the K_α line from these kHz sources by a factor between 10 and 100 times has been observed. Moreover, a very low K_α X-ray conversion of 10^{-9}-10^{-8} has been reported for solid targets using laser pulses of sub-mJ energies [18] and higher (~ 6×10^{-6}) conversion efficiency have been reported from tape targets [19]. No results with high conversion efficiency into K_α X-ray line emission, similar to that obtained from laser systems with high-energy pulses and low repetition rates, have been reported using sub-millijoule laser pulses operated at kilohertz repetition rates.

Since K_α X-ray radiation is generated by the hot electrons, understanding the generation mechanisms and characteristics of hot electrons in the intermediate intensity range from 10^{15} to 10^{17} W/cm^2 is very important for the applications of such fast electrons and keV X-rays from laser produced plasmas using femtosecond laser pulses. Therefore, the second main objective of this thesis is to better characterize the generation and outward propagation of the hot electrons from the small focal spot region. Both particle-in-cell (PIC) simulations and experimental measurements have been undertaken to investigate the hot electrons emitted from laser-produced plasmas using femtosecond laser pulses.

1.2 Contribution of this thesis

The main goal of this thesis is to design, develop and optimize an efficient Cu K_α X-ray source operating at 1 kHz using sub-mJ energies from small-scale femtosecond laser system. In order to develop the X-ray source, the generation of K_α X-rays from copper targets has been investigated for different working conditions. In particular, we study the scaling of conversion efficiency, dependence on pulse energy and prepulse contrast ratio, background pressure, and angle of incidence. The size of the resultant emission spot and brightness of the source is also characterized in preparation for assessing the suitability of the source for future time resolved phase transition and microscopy studies. Specifically, we demonstrate that an efficient K_α X-ray source can be obtained using sub-millijoule femtosecond laser pulses operated at kHz repetition rate. With modest input laser pulses of 290 μJ, X-ray K_α fluxes of 6.7×10^9 photons/s into 2π sr at 1 kHz repetition rate have been produced, resulting in a peak observed conversion efficiency of $\eta_{K\alpha} = 3.2\times10^{-5}$. The results demonstrate for the first time that the efficient X-ray emission reported for high-pulse-energy-systems can be maintained for sub-millijoule laser pulse energies operated at kilohertz repetition rate. The resultant X-ray emission spot have been measured to be several microns in size, demonstrating suitability of the source for future X-ray microscopy studies.

In the second part of this thesis, we have examined the generation of hot electrons and electron jets from solid metal target using sub-millijoule laser pulses. Using the same experimental setup as that for X-ray detection, we have observed for the first time that hot electron jets of energies over 250 keV are emitted from microjoule laser produced plasmas. In preparation for future applications, an initial electron radiography imaging experiment is demonstrated using these hot electron jets.

1.3 Thesis contents

The road map of this thesis is as follows. Chapter 2 is dedicated to the background theory related to the generation of X-rays and hot electrons from laser produced plasma. Some of the laser absorption mechanisms that couple the laser energy to plasma and generate hot electrons combined with the experimental observations will be described as well. The laser and target systems will be presented in Chapter 3. Furthermore, the X-ray and hot electron diagnostics will be examined. In the fourth chapter the experimental X-ray results will be presented. These materials have been published in SPIE [23] and submitted to Review of Scientific Instruments [24]. The results consist of a parametric study of the X-ray emission in preparation for the development of a K_α X-ray source. The tabletop K_α X-ray source obtained with sub-millijoule femtosecond laser pulses operated at 1 kHz repetition rate is described in this chapter as well. In chapter 5, the experimental results describing the emission of hot electron and electron jets from femtosecond laser produced plasmas will be presented. The hot electron jets have been also used for radiographic imaging. Parts of this chapter have been published in Proceedings of the IFSA conference [25] and Applied Physics B [26]. In chapter 6, 2D PIC simulation results are presented and compared to the experimental results. Various mechanisms contributing to the generation of hot electrons and electron jets and their propagation outwards from the small focal point region will be discussed as well. Finally, several possibilities are presented to extend this work in the future and the conclusions will be presented with an emphasis on this thesis's original contributions.

Chapter 2

THEORETICAL BACKGROUND

2.1. Laser plasma interaction

By focusing an intense short laser beam onto a solid target, high density and high temperature plasmas are created. For 100 fs laser pulses, laser ablation requires intensity in the range of ~ 10^{13} W/cm^2. Therefore, for 100 fs laser pulses with peak intensities in the range of 10^{16} W/cm^2 (the case of the experiments discussed in this thesis), ionization of practically any target material takes place early in the laser pulse. Thus, most of the pulse interacts with a very steep density plasma instead of an ionized solid. In the absence of prepulse, the resultant plasma has a very steep density profile, as there is little time to form and expand a significant region of coronal plasmas during the laser pulse. The surface plasma layer formed has a density many times the critical density n_c. The critical density is the electron density where the laser frequency ω becomes equal to the local electron plasma frequency, ω_p. The dispersion relation that governs the light waves in a plasma is given by equation 2.1:

$$\omega^2 = \omega_p^2 + k^2c^2 \tag{2. 1}$$

where k is the wavenumber of the laser light and c is the speed of light. The plasma frequency ω_p is the minimum frequency for propagation of light wave in plasma since k becomes imaginary for $\omega < \omega_p$. The electron density n_e determines the electron plasma frequency, ω_p, which is given by:

$$\omega_p^2 = \frac{e^2 n_e}{\varepsilon_0 m} \tag{2. 2}$$

where e and m are the charge and mass of the electron respectively, ε_0 is the permittivity of free space. Consequently, the condition $\omega = \omega_p$ determines the maximum electron density to which a light wave can penetrate into the plasma [27]. At the density where $\omega = \omega_p$, the plasma becomes opaque, an electromagnetic wave with frequency ω no longer propagates, but it is reflected. The critical density is defined by the relation:

$$n_c = \frac{\varepsilon_0 m \omega^2}{e^2} \tag{2. 3}$$

Practically, this density can be expressed in terms of the wavelength (in microns):

$$n_c = \frac{1.1 \times 10^{21}}{\lambda^2 (\mu m)} \ [\mathrm{cm}^{-3}] \tag{2. 4}$$

where λ is the wavelength of the laser in vacuum in microns. Thus, for Ti: Sapphire laser of wavelength of 800 nm the critical density is $n_c = 1.73 \times 10^{21}$ cm^{-3}.

This is true assuming that the prepulse level of the laser system is sufficiently low that the metal target surface remains pristine until the laser main pulse arrives. However, this is not always the case as many short-pulse laser systems emit the main pulse preceded by one or few lower energy short prepulses or a long pedestal on the nanosecond timescale or both. If the prepulse intensity is above the target ablation threshold, then the main laser pulse will interact with the preformed plasma formed by the prepulse instead of the fresh target surface. Because the laser plasma interaction is very sensitive to the plasma density profile, the prepulse can influence significantly the outcome of the interaction. The general physical structure of the laser-produced plasma is depicted in Figure 2.1 [28].

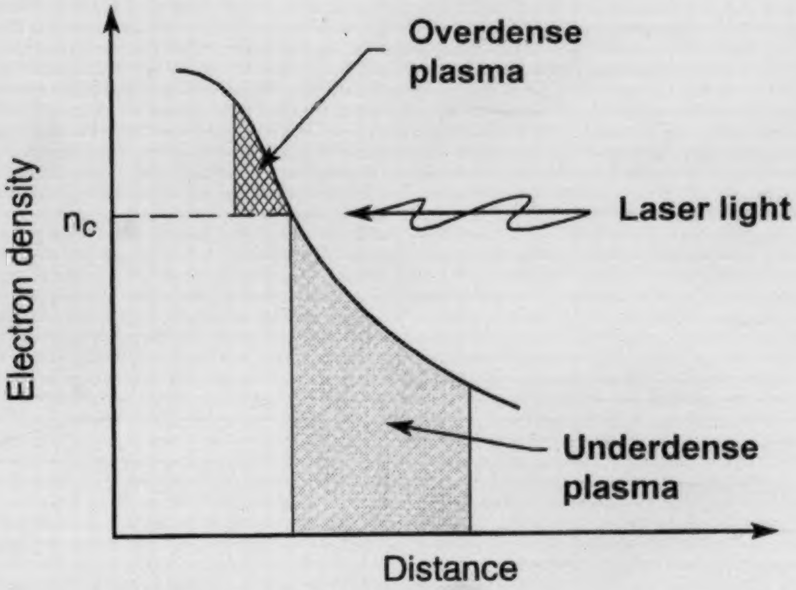

Figure 2.1. Schematic diagram of the electron density structure of laser produced plasma [28]. Laser light is reflected at the critical surface. The laser light is absorbed at the critical density and in the region below the critical density.

The coupling of the laser energy to the free electrons is due to a diverse number of absorption processes that occur in plasma and the importance of any of these processes depends greatly on the laser and plasma parameters. For laser intensities above 10^{16} W/cm^2, these processes are determined by the laser irradiance parameter $I\lambda^2$, i.e. the threshold intensity of a process can vary depending on the laser wavelength squared. This is because at high laser intensity the oscillatory component of the velocity, v_{os} (quiver velocity) becomes comparable to the electron's random thermal velocity, v_e that can be taken as:

$$v_e = \sqrt{\frac{kT_e}{m}} \tag{2. 5}$$

The oscillation velocity v_{os} is given by:

$$v_{os} = \frac{eE}{m\omega} \tag{2. 6}$$

Hence, the ratio of electron energy in coherent oscillations to that in random motions is given by:

$$\left|\frac{v_{os}}{v_e}\right|^2 = \frac{e^2E^2}{m\omega^2 kT_e} = \frac{I/c}{n_c kT_e} \tag{2. 7}$$

If v_{os} is greater than the thermal velocity v_e, then a number of nonlinear processes are stimulated with little damping. Equation 2.7 can be rewritten in terms of $I\lambda^2$ as [28]:

$$\left|\frac{v_{os}}{v_e}\right|^2 = \frac{0.021 \times I_{14}[W/cm^2] \times \lambda^2[\mu m]}{kT_e[keV]} \tag{2. 8}$$

where I_{14} is the laser intensity in units of 10^{14} W/cm^2 and λ is the laser wavelength in microns and kT_e is in keV. Thus, for a plasma produced by a Ti:Sapphire laser of wavelength of 0.8 μm with a focused laser intensity of 10^{16} W/cm^2 and assuming a electron temperature of 300 eV (typically, in the literature the temperature range is from 100 to 500 eV in this intensity range), the ratio of coherent to thermal electron energies is 4.48. This results in excitation of non-thermal processes in a laser-produced plasma. We observe that an 800 nm laser with $I = 10^{16}$ W/cm^2 gives a peak electron oscillation energy of $U_{os} = 1.34$ keV.

Theoretical and experimental studies have investigated the coupling of high-intensity laser light to plasmas, and several absorption processes and generation mechanisms of the hot electrons have been proposed. The properties of the hot electrons change from sub-relativistic to relativistic case for which the electron velocity approaches the speed of light. This regime is described by the parameter a_0, which is the classical normalized momentum of electrons quivering in the laser electric field E relative to mc and is given by:

$$a_0 = \frac{eE}{m\omega c} \tag{2. 9}$$

For a sub-relativistic ($a_0 < 1$) laser intensity of $I\lambda^2 < 1.37\times10^{18}$ W μm^2/cm^2, the absorption of intense laser pulses changes from resonance absorption [29-37] to vacuum heating as the intensity increases above $I\lambda^2 \sim 4\times10^{16}$ W μm^2/cm^2 [38]. Some of these processes will accelerate electrons in the target normal direction. Other processes such as Raman heating at the quarter critical density surface can also become important for larger density scale length plasma profiles. Part of the laser energy is transferred into hot electrons during the interaction of the short laser pulse with the sharp density gradient plasma. When these high-energy electrons penetrate into the cold region of the solid target material it results in X-ray generation via the process of K-shell ionization and emission, and by bremsstrahlung. This is schematically shown in Figure 2.2.

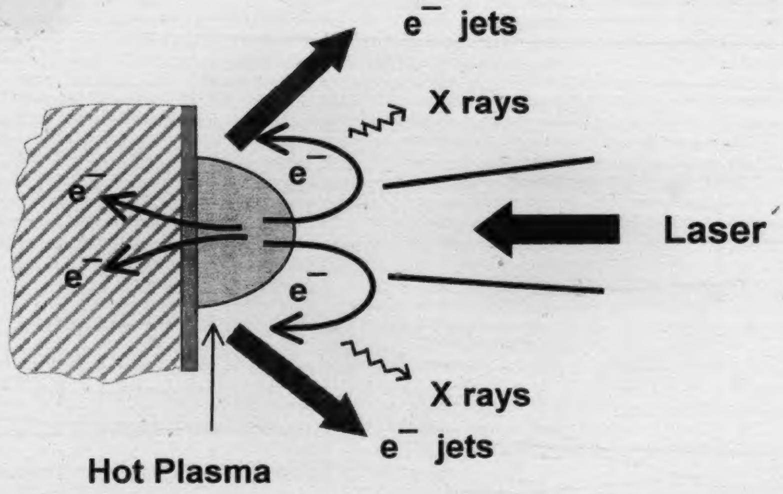

Figure 2.2. An illustration of the laser plasma interaction, showing the laser pulse interaction with the hot plasma formed at the surface of the target material and the subsequent emission of high-energy electrons and X-ray photons.

The characteristics of the X-ray emission depend on the hot electron distribution, which in turn is determined by the absorption mechanism. For relativistic laser intensities of $I\lambda^2 > 1.37\times10^{18}$ W μm^2/cm^2 ($a_0 > 1$), ponderomotive acceleration, $\vec{J}\times\vec{B}$ heating, and wake field interactions dominate. These processes will generally accelerate electrons along the direction of laser propagation.

As mentioned above, the hot electrons are generated by different nonlinear processes when intense femtosecond laser pulses interact with plasmas. Although, the energy distribution of the hot electrons is anisotropic and non-Maxwellian, these hot electrons are usually described by either one or more Maxwellian distributions [39,40]. Generally, the hot electron distribution can be characterized by a hot electron temperature, T_{hot} which depends on the laser pulse parameters, i.e. intensity, duration, wavelength and contrast ratio, and plasma properties, i.e. electron scale length, maximum electron density, etc. In some of the previously reported experiments, T_{hot} is on the orders of tens of keV, while in other cases only a moderately hot electron temperature can be observed on the order of few keV.

The main absorption processes for laser intensities in the range of 10^{15}-10^{17} W/cm^2, the range for the experiments discussed in this thesis, are described below.

Inverse bremsstrahlung

Inverse bremsstrahlung refers to the process in which an electron quivering in the laser field absorbs energy from the laser when passing through the electric field of an ion, resulting in an increase of the energy and temperature of the electron particle. Subsequently, it loses its energy in collisions with ions, heating up the ions in the process. In the non-relativistic case, the inverse bremsstrahlung absorption coefficient is given by equation 2.10 [41]:

$$\kappa_{ib} = \frac{7.8\times10^{-9}\, Zn_e^{\;2} \ln\Lambda(v)}{v^2 (k_B T)^{3/2}} \frac{1}{(1-v_p^2/v^2)^{1/2}} \quad [\mathrm{cm}^{-1}] \qquad \textbf{(2. 10)}$$

where $k_B T$ is in eV, $\Lambda(v)$ =minimum of ($\mathrm{v}_e/\omega_p p_{min}$, $\mathrm{v}_e/\omega p_{min}$), v_e is the thermal velocity of the electrons, p_{min} is the minimum impact parameter for electron-ion collisions [$p_{min} \cong$ maximum of $Ze^2/k_B T$ or $\hbar/(m_e k_B T)^{1/2}$], $v = \dfrac{\omega}{2\pi}$ is the wave frequency and $v_p = \dfrac{\omega_p}{2\pi}$ is the plasma frequency, Z is the charge of the ions, n_e is the electron density and T_e is the electron temperature.

From the equation above, we observe that the absorption through inverse bremsstrahlung is large for low temperature, high densities and high Z plasmas. Thus, for the laser intensities above ~ 10^{15} W/cm^2, collisions become ineffective during the interaction since the plasma temperature increases very quickly. Different absorption mechanisms take over to account for the high absorptions seen in past experiments at these higher laser intensities. There are several collisionless absorption processes, which can couple the laser energy to the plasma. The main candidate is resonance absorption.

Resonance Absorption

Resonance absorption was studied extensively in order to understand the generation of hot electrons from nanosecond laser-plasma interactions in the context of laser fusion [30-33]. However, the process was originally investigated to describe radio wave absorption in the ionosphere. In the standard picture, the resonance absorption process involves p-polarized laser light at an angle of incidence relative to target normal such that the laser electric field vector $\vec{E}$ has a component in the direction of the density gradient $\vec{\nabla} n_e$. This component of the field directly excites an electron plasma wave through the resonance $\omega = \omega_p$ at the critical density. If p-polarized laser radiation is incident on an expanding plasma at an angle θ_{inc} from the surface normal as seen in Figure 2.3 [42], the laser beam will propagate up to density $n_c \cos^2 \theta_{inc}$ before it is specularly reflected. However, part of the laser electric field will tunnel into the critical density $n_e = n_c$ and will strongly drive plasma oscillations at $\omega = \omega_p$.

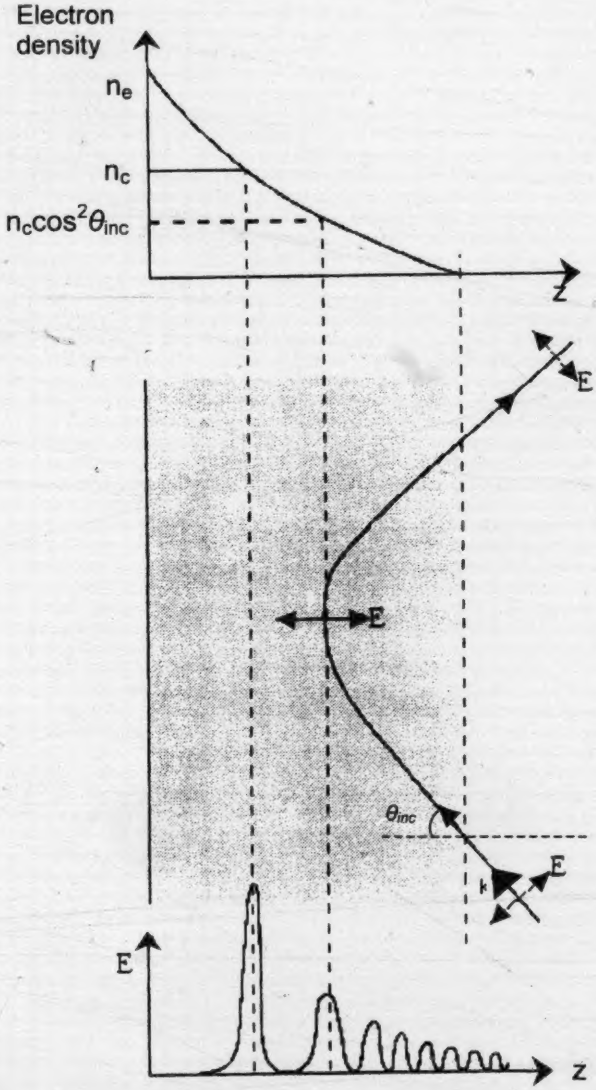
Electron density
n_e
n_c
$n_c\cos^2\theta_{inc}$
z
E
E
θ_{inc}
k
E
E
z

Figure 2.3. Schematic diagram illustrating a light wave obliquely incident at an angle θ_{inc} onto a plasma density profile for p-polarized light (E-field in the plane of ∇n_e). The laser beam will propagate up to density $n_c \cos^2 \theta_{inc}$ before it is specularly reflected (Following [42]).

By considering the following Maxwell equation in the dielectric plasma medium, it can be shown that the electric field of the p-polarized light has a singularity, i.e. a resonance at the critical surface:

$$\nabla \cdot (\varepsilon \vec{E}) = 0 \tag{2. 11}$$

where $\varepsilon(z) = 1 - \frac{\omega_p^2(z)}{\omega^2}$ is the dielectric function of the plasma and the electric vector is taken to be in the plane of incidence, i.e. $\vec{E} = E_y \hat{y} + E_z \hat{z}$.

Because $\nabla \cdot (\varepsilon \vec{E}) = \varepsilon \nabla \cdot \vec{E} + \nabla \varepsilon \cdot \vec{E}$, using equation (2.11) one has:

$$\nabla \cdot \vec{E} = -\frac{1}{\varepsilon}\frac{\partial \varepsilon}{\partial z} E_z \tag{2. 12}$$

The resonant response can be observed at $\omega = \omega_p$ where the dielectric function $\varepsilon(z)$ is zero, but the electric field in the z-direction E_z does not vanish. When the p-polarized laser radiation is reflected, the electric field has a component parallel to the density gradient (E_d) causing charge density fluctuations as the electrons oscillate along the gradient.

The important physical feature of the resonance absorption can be inferred by evaluating the field driving the resonance, E_d [29] assuming a linear density profile ($n_e = n_c z / L$). This is given by:

$$E_d = \frac{E_{FS}}{\sqrt{2\pi\omega L / c}} \Phi(\tau) \tag{2. 13}$$

where $\Phi(\tau) \approx 2.3\tau \exp(-2\tau^3/2)$ and τ is a new variable defined as $\tau = (\omega L / c)^{1/3} \sin\theta$. E_{FS} is the value of the electric field of the laser radiation in free space. $\Phi(\tau)$ is the characteristic resonance function, which describes the excitation strength as a function of plasma density scale length and the angle of incidence. When $\tau \to 0$ ($\sin\theta \to 0$) the field E_d vanishes because it is a function of $\sin\theta$. Similarly, the field E_d becomes very small for large τ as the incident laser light has to tunnel through a too large distance to reach the critical density surface. There is an optimum angle of incidence between these two limits, which is given by:

$$(\omega L/c)^{1/3} \sin\theta \cong 0.8 \qquad \textbf{(2.14a)}$$

$$\Rightarrow \theta_{\max} \cong \sin^{-1}[0.8(c/\omega L)^{1/3}] \qquad \textbf{(2.14b)}$$

The fractional absorption of the incident light is calculated to be [29]:

$$\eta_a \cong \Phi^2(\tau)/2 \qquad \textbf{(2.15)}$$

The effect of this feature can be observed in Figure 2.4, which shows the absorption fraction η_a for three different scale lengths [43]. The optimum absorption for *p*-polarized light occurs at an angle of incidence, which increases as the density gradient becomes steeper.

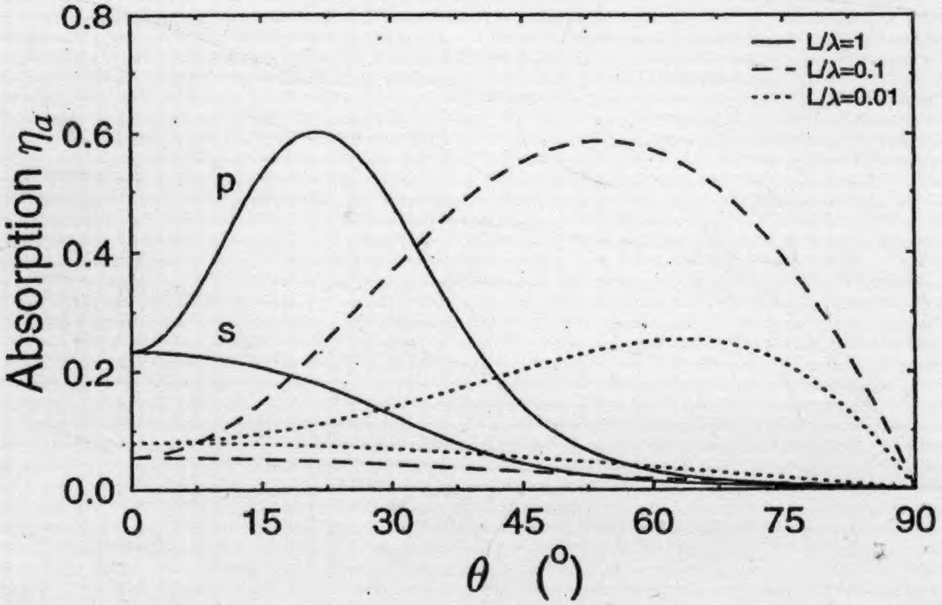

Figure 2.4. Angular absorption dependence for three density scale-lengths: $L/\lambda = 1$, $L/\lambda = 0.1$ and $L/\lambda = 0.01$ [43] for both p- and s-polarized laser pulses. The maximum absorption for p-polarized laser pulses occurs at larger angles of incidence as the plasma density gradient becomes steeper (Following [43]).

This energy is transferred to the hot electrons, which are accelerated from the overdense to underdense regions of plasma when the plasma wave breaks. The expected dependence on the angle of incidence and polarization of the laser was shown in Refs. [44] and [45].

The temperature of hot electrons due to resonance absorption from series of PIC simulation runs is observed to scale as [31]:

$$T_{hot[keV]} \approx 14(I_{16}\lambda_{\mu m}^{2})^{1/3} T_{cold[keV]}^{1/3} \tag{2. 16}$$

where I_{16} is the laser intensity in units of 10^{16} W/cm^2, λ is the laser wavelength in micrometers and T_{cold} is the background plasma temperature in keV, where T_{hot} is also in keV.

The standard analysis of inverse Bremsstrahlung and Resonance Absorption break down once one approaches single cycle pulses or at intensities where the electron oscillation distance exceeds the local density scale length. This generally occurs for pulse lengths below 10 fs or intensities above 10^{17} W/cm^2. There is generally good agreement for various measurements done with sub-picosecond laser pulses and intensities up to 10^{17} W/cm^2 [46-48].

"Not-so-resonant" resonance absorption

Brunel first discussed this absorption mechanism in 1987 and it is also known as Brunel effect or vacuum heating [38]. In this process, the laser electric field drives the plasma electrons across the density as in the case of "classical" resonance absorption but the laser energy is coupled into an electrostatic plasma wave non-resonantly. If the density scale length is very small and the amplitude of a p-polarized component of the laser field is sufficiently large, the electrons are dragged away from the target surface into vacuum, turned around and accelerated back into the solid target with a random phase. The hot electron temperature according to Brunel's model is proportional to the electron quiver velocity squared and is given by:

$$T_{hot[keV]} \cong 3.7 I_{16} \lambda^2 \qquad \textbf{(2. 17)}$$

where I_{16} is the laser intensity in units of 10^{16} W/cm^2 and λ is the wavelength in microns. The equation 2.16 predicts a strong hot temperature scaling with $I_{16}\lambda$ and, thus, for high laser intensities the electrons sent back into the target can acquire high energies. For instance, for 800 nm laser pulses with intensity of 10^{17} W/cm^2, the hot electron temperature is 23 keV according to equation 2.16, while for 10^{18} W/cm^2, the hot electron temperature is 230 keV. The mechanism saturates for relativistic laser intensities due to deflection of the electron orbits by the $\vec{v}\times\vec{B}$ force [43].

Two-plasmon ($2\omega_{pe}$) decay instability

The two-plasmon ($2\omega_{pe}$) decay instability is an important mechanism for laser energy deposition in underdense plasma. This instability can be most simply described as the resonant decay of an incident photon into two electron plasma waves. The equations for energy and momentum conservation for this process are:

$$\begin{aligned} \omega_0 &= \omega_{ek1} + \omega_{ek2} \\ \overrightarrow{k_0} &= \overrightarrow{k_1} + \overrightarrow{k_2} \end{aligned} \qquad \textbf{(2. 18)}$$

where ω_0 and $\overrightarrow{k_0}$ are the laser light frequency and wave number. ($\omega_{ek1}, \overrightarrow{k_1}$) and ($\omega_{ek2}, \overrightarrow{k_2}$) are the frequencies and the wave numbers of the electron plasma waves. Because ω_{ek1} and ω_{ek2} are approximately ω_p (electron plasma frequency), this instability takes place at an electron density $n_e=(1/4)n_c$.

The growth rate for this instability as derived by Kruer [29] is given by :

$$\gamma = \frac{\vec{k}\cdot\vec{v}_{os}}{4}\left|\frac{\left(\vec{k}-\vec{k}_0\right)^2 - k^2}{k\left|\vec{k}-\vec{k}_0\right|}\right| \qquad \textbf{(2.19)}$$

where k and $k - k_0$ represent the wave numbers of the electron plasma waves.

For $k \gg k_0$, the growth rate maximizes at $\gamma \approx \frac{k_0 v_{os}}{4}$ for plasma waves propagating at 45° to both $\vec{k}_0$ and $\vec{v}_{os}$.

Important features associated with the $2\omega_{pe}$ decay instability are hot electron generation and 3/2 harmonics emission. Like other parametric instabilities, $2\omega_{pe}$ decay was also studied extensively in the context of ICF because it was a preheat concern. Figueroa et al. [49] observed high-energy electrons from plasmas with densities below n_c with more intense emission at $n_c/4$. The plasma was formed by a 1.05 μm prepulse with an intensity of 5×10^{11} W/cm^2 that preceded the 0.35 μm main pulse by 1 ns. The main pulse intensity was approximately 10^{15} W/cm^2. A T_{hot} of 30-40 keV was inferred from the electron spectra when measured in the plane of the laser electric field (p-pol) and T_{hot} of 15-20 keV when measured out of the plane of the laser electric field (s-pol). The polarization dependence was more pronounced at -45° with respect to the laser (in the direction of density gradient). The angular and the polarization dependence points to $2\omega_{pe}$ decay as the probable generation mechanism for the high-energy electrons near the $n_c/4$. Similarly, Ebrahim et al. [50] observed intense hot electron emission from a plasma with maximum electron density of $n_c/4$. The emission was localized in the plane of polarization of the incident laser beam and had a maximum about the 45° directions with respect to the k-vector of the laser beam. The electron spectra at 45° and 135° had a T_{hot} of 60 keV, while at other angles (18°, 90°, 170°) the flux was lower with a T_{hot} of

15 keV. Their measurements suggest that the hot electrons are generated by the two-plasmon decay instability at quarter-critical density.

2.2 Hot electron temperature

As stated before, the final hot electron energy spectrum may be influenced by several competing absorption processes, which may vary depending on different factors, such as laser intensity, pulse duration, angle of incidence, prepulse contrast ratio and so on. Because it is difficult to isolate an absorption mechanism experimentally or even in simulation, experimental measurements of the hot electron temperature have been performed in the last decade or so, hoping it will provide some information on the predominant mechanism, for a specific laser intensity range. Some results are summarized in table 2-1 and Figure 2.5.

Table 2.1. Measurements of T_{hot} using short pulse lasers.

Reference	I [W/cm^2]	T_{hot} [keV]	Prepulse Contrast Ratio	θ_{inc}	Target	t_L [fs]	λ [nm]
H. Chen [7]	3×10^{15}	3	10^{-5}	60p	Al/Si	1300	1050
Rousse [6]	2×10^{16}	8.5	Optimum ASE (0.7 J/cm^2)	7p	Al/Si	100	620
Bastiani [51]	4×10^{16}	19	10^{-5}	45p	Si	120	800
Eder [14]	$\sim10^{17}$	40	10^{-4}	45p	Cu	200	790
Schnuerer [52]	5×10^{17}	66	10^{-6}	45p	Ta	700	1056
Yu [53]	5×10^{17}	25		45p		400	530
Teubner [54]	1×10^{18}	8	10^{-7}	45p	Al/Si	400	248
L. M. Chen [15]	2.4×10^{18}	25	10^{-4} ps 10^{-5} ns	56p	Ag	70	800
L. M. Chen [15]	4×10^{18}	40	10^{-4} ps 10^{-5} ns	56p	Ag	70	800
Pretzler [39]	2×10^{18}	200		45p	Cu/Si	130	800
Kmetec [9]	3×10^{18}	300	10^{-6}	30p	Ta	120	807
Schnuerer [55]	3×10^{18}	250	10^{-5}	45p	Ta	80	800

The open squares in Figure 2.5 represent the experimental results presented in Table 2.1. Each number inside the square denotes the reference number. All data points are for laser pulses shorter than 1 ps with one exception for reference [7], for which the duration of the laser pulse is 1.3 ps, still short enough to be distinguished from the long (nanosecond) laser pulses. Four theoretical scaling laws for hot electron temperature are plotted versus the experimental findings for comparison. Two of these models have described in the previous section. One is the scaling law argued by Forslund et al. [31]

described by the equation (2.16) and is denoted as T_{hot}^{F} for an assumed value of $T_{cold[keV]} = 0.5$ keV. The second model is that described by Brunel [38] given by equation (2.17), which is denoted as T_{hot}^{B}. The third model is an approximate scaling law determined by Gibbon and Bell [56] from PIC simulations with fixed ions for short pulses obliquely incident on steep but finite density gradients, $L/\lambda \leq 0.1$, denoted as T_{hot}^{GB}:

$$T_{hot[keV]}^{GB} \cong 7\left(I_{16}\lambda^{2}\right)^{1/3} \tag{2. 20}$$

The fourth scaling law of the hot electron generation was predicted by Wilks et al. [57], who assumed that at 'relativistic' laser intensities, the energy associated with the electrons is given by the potential they feel during the interaction. Thus, the temperature of the hot electrons, which absorb laser light via the potential and are accelerated due to it is $T_{hot} \propto e\Phi_p$, where Φ_p is the ponderomotive potential:

$$T_{hot[keV]}^{W} \approx 511\left(\sqrt{1+\frac{I\lambda_{\mu}^{2}}{1.37\times10^{18}}}-1\right) \tag{2. 21}$$

where I is now in units of W/cm^2 and λ_{μ} is in units of microns.

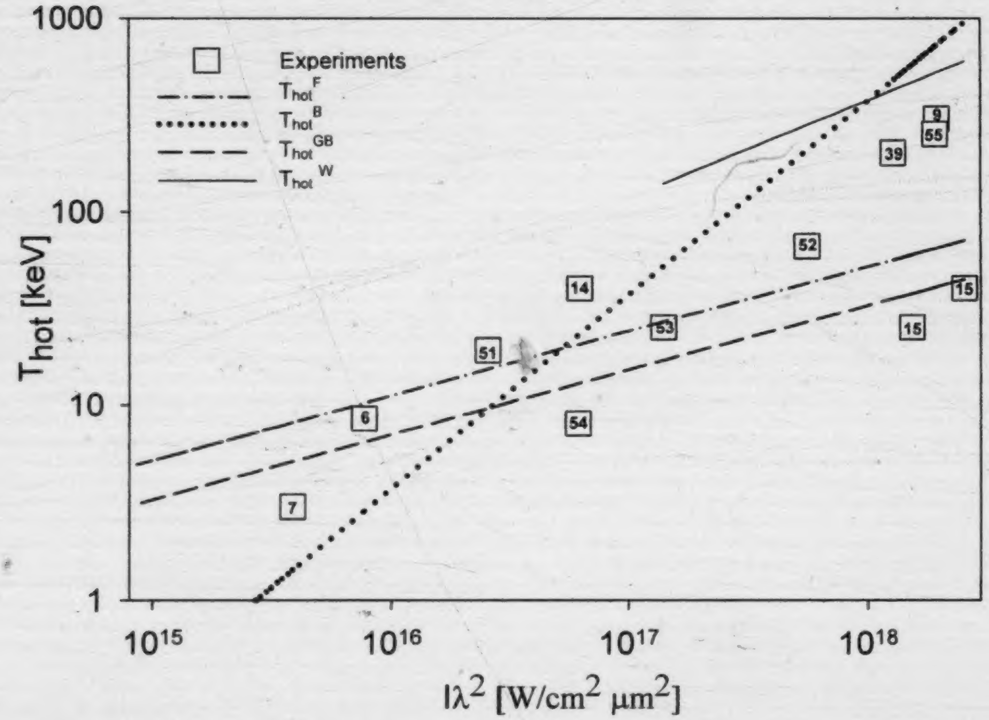

Figure 2.5. Measurements of the hot electron temperature T_{hot} from laser produced plasma using sub-picosecond laser pulses (open squares). Four theoretical models for T_{hot} are superimposed on the experimental results: Forslund (equation 2.16 assuming $T_{cold[keV]} = 0.5$ keV), Brunel (equation 2.17), Gibbon& Bell (equation 2.20) and Wilks (equation 2.21). (Following Gibbon [43]).

Notice that for $I\lambda^2 = 10^{15} - 10^{17} W/cm^2 \mu m^2$ the hot electron temperature should make a transition from the scaling law for resonance absorption to that given by vacuum heating. At $I\lambda^2 = 10^{18} W/cm^2 \mu m^2$, it should make another transition to the relativistic scaling law of Wilks.

The emission direction of these hot electrons plays an important role in many applications, such as laser acceleration of particles and the fast ignition scheme.

Therefore, there has been much interest in the generation of jets of hot electrons [58-65]. Recently, there have been reports of hot electron jets formed at these intermediate intensities in the target normal, specular and the E-field directions depending on the polarization and prepulse levels [60, 64, 65].

2.3 Hard X-ray emission processes from femtosecond laser-produced plasmas

Due to their long mean-free-path, the hot electrons can penetrate into the material target and generate bremsstrahlung X-ray and characteristic line radiation. Consequently, the X-ray emission spectrum from a solid target bombarded by high-energy electrons consists of both characteristic line emission and bremsstrahlung continuum emission. The X-ray spectrum from laser-produced plasmas resembles very well the one from a standard anode X-ray tube since both emissions are based on the same principle, accelerated electrons colliding with a metal target. In the subsequent two sub-sections both the bremsstrahlung and line radiation will be briefly discussed.

2.3.1 Bremsstrahlung radiation

Bremsstrahlung X-rays are produced when the electrons experience accelerations upon collisions with the atoms in the metal target. These X-rays are commonly called bremsstrahlung from the German word "braking radiation". Figure 2.6 [28] provides a simple diagram of the process. The hot electrons of a given velocity $\vec{v}$ (or kinetic energy *E*) experience a wide range of accelerations (depending on the impact parameter *b*) as they come close to a nucleus. These in turn lead to synchrotron-like radiation along the curved path of the electron. With a variety of impact parameters and a large number of hot electrons, the emitted spectrum is a broad continuum one.

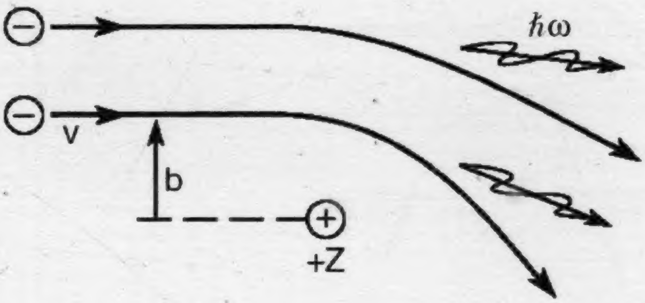

Figure 2.6. Bremsstrahlung radiation occurs when an incident hot electron is accelerated as it passes a nucleus [28].

The bremsstrahlung radiation from laser produced plasmas ranges anywhere from 0.1 keV to MeV depending on the laser intensity and plasma parameters. If the laser pulses are focused onto a solid target with a high-Z material, it is possible to generate a hot plasma, which generates mainly bremsstrahlung radiation [9] under certain illumination conditions. This type of radiation has become attractive for X-ray absorption spectroscopy [66], which requires a broad spectrum that overlaps the X-ray absorption edges of atoms under investigation.

Bremsstrahlung radiation is a valuable hot electron diagnostic because of its simple exponential spectral dependence, i.e. $e^{-h\nu/T_{hot}}$ for $h\nu \gg T_{hot}$, which allows a measurement of the hot electron temperature T_{hot} from hard X-rays.

2.3.2 Characteristic X-ray line radiation

If the hot electrons have sufficient energy, they can knock an electron out of an inner shell of the target metal atoms. Subsequently electrons from higher states drop down to fill the vacancy, emitting X-ray photons with precise energies determined by the electron energy levels. This emitted X-ray radiation is called characteristic X-ray emission for the given material. The process is displayed schematically in Figure 2.7:

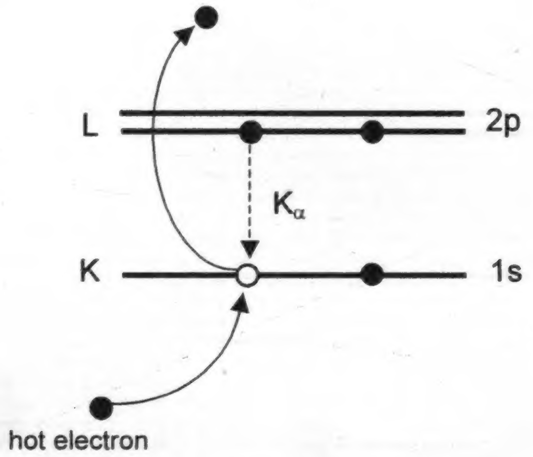

Figure 2.7. An incident hot electron of sufficiently high energy to overcome the binding energy knocks out a core electron from the K-shell leaving the atom with a core vacancy. K_α radiation is generated as the atom readjusts to the core vacancy through the emission of characteristic energy.

In addition, the thermally excited ions in the hot plasma emit line radiation corresponding to the energy transitions of the ion state. Overall, the X-ray line emission from laser produced plasmas can be in the 1-100 keV range depending on the atomic number of the target material. Because of its narrow bandwidth, short pulse duration, and small spot size, the X-ray line radiation, in particular K_a radiation is interesting for pump-probe structural investigation and for X-ray biomedical imaging. These applications have been the motivating factors for the development of K_α X-ray sources from femtosecond laser pulses.

2.4 K_α X-ray generation process from femtosecond laser-produced plasmas

Energetic electrons created by collective absorption mechanisms in laser-produced plasmas produce the characteristic K_α radiation. Analytically, the K_α yield can be expressed as:

$$N_{K\alpha} = \iint N_{hot} f_{hot}(E) Q_K(Z,E) n_A(Z) \eta_K(Z) f_K(Z,E_K,t) dE dt \qquad \textbf{(2.22)}$$

where $N_{K\alpha}$ is the number of emitted K_α photons in 4π sr assuming isotropic emission, N_{hot} is the total number of hot electrons, $f_{hot}(E)$ is their energy distribution, Q_K is the cross-section for *K*-shell ionization, n_A is the atomic number density, η_K is the K_α fluorescence yield, and f_K is the fraction of the K_α photons that escape the solid target.

The energy spectrum of the hot electrons is usually fitted by a one-dimensional Maxwellian energy distribution, $f_{hot}(E) = A\exp(-E/T_{hot})$ where A is a normalization constant.

The *K*-shell ionization by electron impact, Q_K can be taken from Ref. [67] as a function of the ratio U between the incident electron energy E and the ionization energy E_K of the target electrons in the *K*-shell: $U = \dfrac{E}{E_K}$. For a Cu target, E_K = 8.98 keV. Hombourger [67] established an empirical expression to describe the cross sections for *K*-shell ionization of atoms from ionization threshold to very high energies. The proposed empirical cross section is given by:

$$Q_K = n_K \pi a_0^2 G_r \left(\frac{Ry}{E_K} \right)^{C_U} D_U \quad [10^{-24}\ \mathrm{cm}^2] \qquad \textbf{(2. 23)}$$

where n_K is the number of electrons present in the *K*-shell, a_0 is the first Bohr radius, *Ry* is the Rydberg constant, E_K is the threshold energy, D_U is the reduced cross section, which is a function of *U*, C_U is an exponent which depends on *U*, and G_r is the relativistic factor of Grysinski, which is also a function of *U*. The *K*-shell ionization cross section $Q_K(U)$ for copper as determined by Hombourger [67] is shown in Figure 2.8. It appears that the cross section maximizes for electrons with energies about three times the ionization energy E_K.

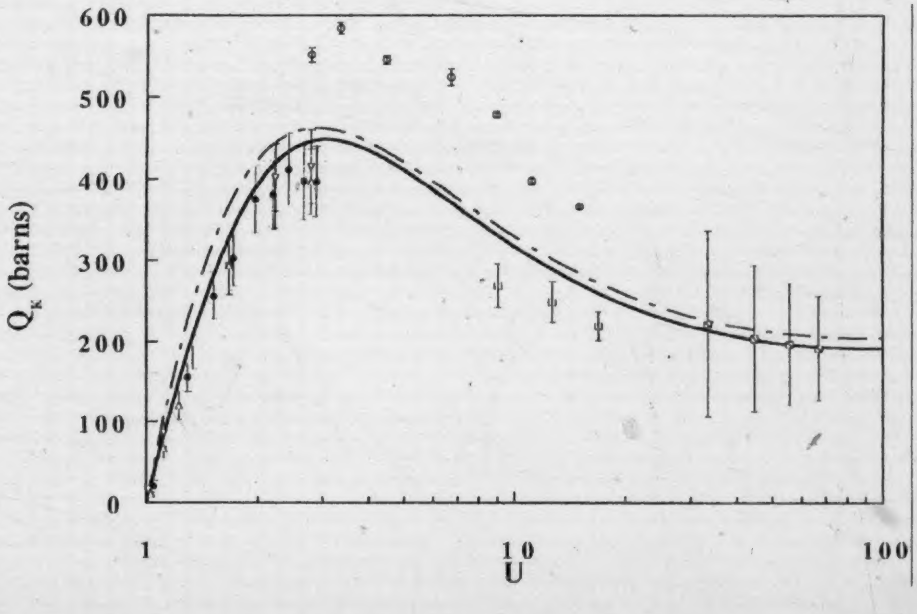

Figure 2.8. *K*-shell ionization cross section for copper as a function of parameter *U*, which is the ratio between the incident electron energy *E* and the ionization energy E_K of the target electrons in the *K*-shell ($U=E/E_K$). 1barn = 10^{-24} cm^2. For Cu target, E_K = 8.98 keV. The full curve represents the cross section determined by Homourger [67], which is compared with other works [Refs. 25, 29 and 33 within].

The fluorescence yield for K shell $\omega_K = \omega_K(Z)$ can be found in Ref. [68]. For instance, η_K=0.440 for Cu (Z=29).

The fraction f_K of the K_α photons that escape the solid target is a function of the K_α X-ray photon energy, target material and the distance traveled by the X-ray photon backward, toward the target surface. In a simple approximation, f_K is the transmission of the X-ray photons T_K through a slab of thickness t and can be calculated using the X-ray mass attenuation coefficients μ / ρ:

$$f_K = T_K = \exp[-(\mu / \rho)x] \qquad \textbf{(2. 24a)}$$

where x is the mass thickness and is obtained by multiplying the thickness t by the density ρ, $x = \rho t$. Values of X-ray mass attenuation coefficients μ / ρ (cm^2/g) as a function of photon energy for elemental media can be found in NIST [69], which are based on a compilation of the available experimental measurements and theoretical calculations. For instance, for a copper target, the X-ray transmission as a function of X-ray photon energy for four different thicknesses is shown in Figure 2.9. The transmissions of K_α photons ($E_{K\alpha}$ = 8.05 keV) through 10 µm, 20 µm, 30 µm and 40 µm thick copper material are 64%, 41%, 26% and 17% respectively.

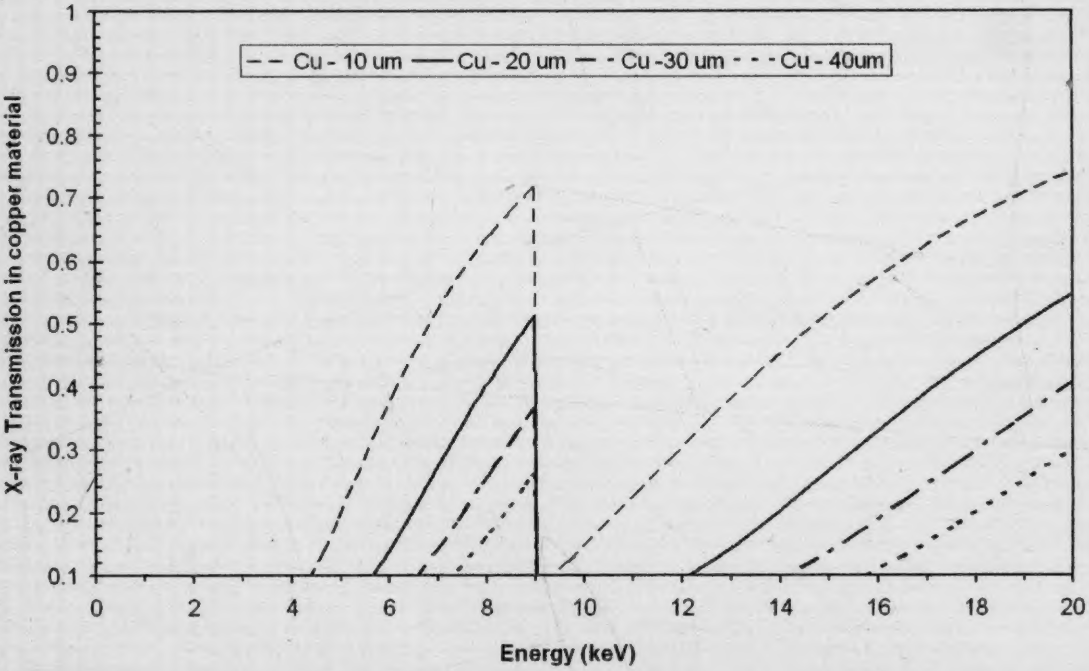

Figure 2.9. X-ray transmission through copper material of different thickness: 10 μm, 20 μm, 30 μm and 40 μm. The transmissions of Cu K_α photons $(E_{K\alpha}$=8.05 keV$)$ are $T_{10\mu m}$=0.64, $T_{20\mu m}$=0.41, $T_{30\mu m}$=0.26, and $T_{40\mu m}$=0.17.

However, the expression (2.24a) assumes that the X-ray photons travel in a straight line, while in the experiments the X-ray photons are emitted in any direction as shown in Figure 2.10. Therefore, it is necessary to incorporate a more complicated description such as an angle-dependant path in the analytical expression (2.24a):

$$f_K = T_K = \exp\left[-(\mu/\rho)\frac{x}{\cos\theta}\right] \qquad \textbf{(2. 24b)}$$

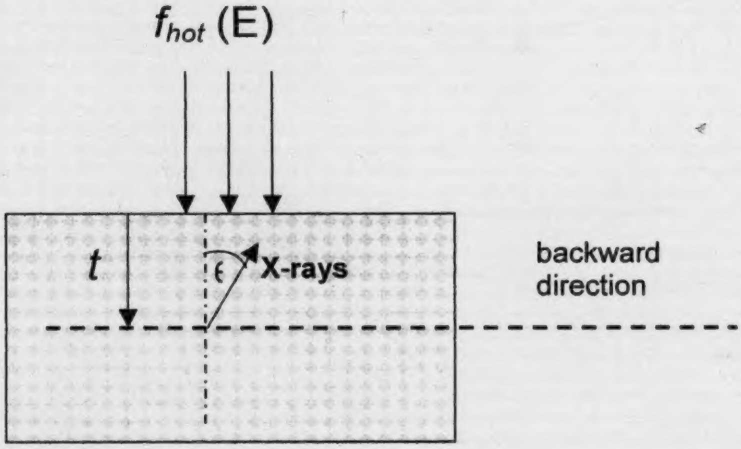

Figure 2.10. The geometry of X-ray emission from a one-dimensional target.

From previous measurements of hot electron temperature for laser intensities in the range of 10^{16}-10^{17} W/cm^2 (the case of the experiments discussed in this thesis), T_{hot} had values from few keV to tens of keV. For instance, Eder et al. [14] measured a T_{hot} of 40 keV from laser intensity of ~10^{17} W/cm^2 focused on solid copper target. Using the ESTAR program from NIST databases [70], the stopping power and the range for electrons in various materials can be calculated in continuous-slowing-down approximation (CSDA). Thus, the average path length (CSDA range) travelled by 40 keV electrons as they slow down to rest in copper material is 5 μm. In this approximation, the rate of energy loss at every point along the track is assumed to be equal to the mean rate of energy loss. The average path length travelled by an electron as it slows down in copper material as a function of kinetic electron energy is shown in Figure 2.11.

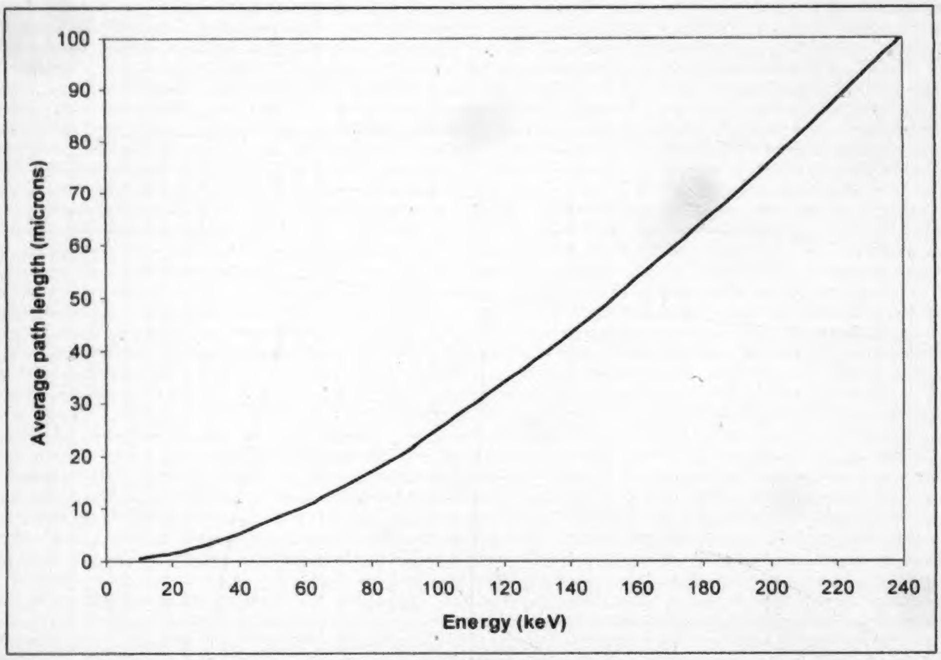

Figure 2.11. The average path length (CSDA range) traveled by an electron as it slows down to rest in copper target.

Calculations of the range of electrons are difficult due to the random path of the electrons. The interpretation of the range is also difficult because the electrons suffer single and multiple scattering in traversing the target material producing statistical fluctuations of the path length of the electrons in the stopping material. Therefore, the calculated electron energy loss and path length are average values. For each particle, the actual value fluctuates around the average value. There are two consequences: for a given path length, the energy loss fluctuates and for a given energy loss, the path length fluctuates. The latter phenomenon, which is called "straggling", makes the actual experimental length somewhat greater than the CSDA range. To account the electron scattering processes, Monte Carlo simulations are necessary. Knowing the exact path of hot electrons in the target material will allow precise determination of the X-ray photon absorption as it travels towards the target surface.

For experimental purposes, it is useful to know how many K_α photons can be obtained for a given target material under optimum working conditions (laser and target parameters). Reich et al. [71] utilized a slightly modified formula to that of their Ref [15] to determine N_{gen} (E, Z), the number of K_α photons generated by an electron of incidence energy E: $N_{gen}(E,Z) = 4 \times 10^{-3} Z^{-1.67} E^{3/2}$. The numerical coefficients have been determined from the fits to the results of Monte Carlo simulations using monoenergetic electron beams. They also simplify the calculations of the fraction f_K of the K_α photons that escape the solid target by introducing an "emission factor" f_{em} where only electrons with energies less than 20 times the K-shell ionization energy of the target are considered to produce X-ray photons not too deep in the target as to still be detected. Thus, they used $f_{em} = \begin{cases} 1 : U \leq 20, \\ 0 : U \geq 20. \end{cases}$. Their outcome shows that there is a universal optimum hot electron temperature $T_{hot} = 6.4E_K$ for the highest K_α yield, which is independent of Z. Setting $\partial N / \partial I = 0$, they described the dependence of the optimum laser intensity on the target material through the following equation:

$$I_{opt} = 7 \times 10^9 Z^{4.4} \text{ [W/cm}^2\text{]} \qquad \textbf{(2. 25)}$$

An exponential plasma density profile with a scale length L=0.3λ and $n_e(\max)=10n_c$ (n_c being the electron critical density) has been used for this prediction. To check the above analytical result, they have used combined PIC-Monte Carlo (PIC-MC) simulations to derive K_α fluxes and the numbers agree within a factor of three. Their X-ray yields determined from PIC-MC calculations are shown in Figure 2.12:

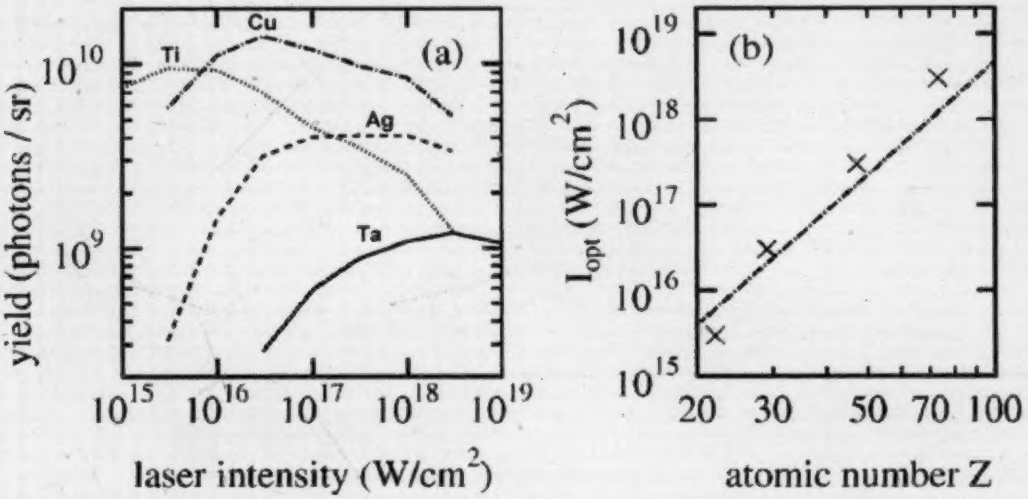

Figure 2.12. (a) Simulated K_α X-ray yields from bulk targets for four metals: Titanium (Z=22), Copper (Z=29), Silver (Z=47) and Tantalum (Z=73). (b) Optimum laser intensity versus the target material, line is from analytical model-equation (2.25) and the points are from simulations [71].

From the data provided in Figure 2.12, we can estimate the maximum theoretical conversion efficiency that can be expected for copper material, which is $\eta_{K\alpha} \cong 10^{-3}$ in 2π sr.

2.5 Previously reported K_α X-ray sources from femtosecond laser-produced plasmas

Because X-ray pulses from femtosecond laser plasmas have the potential to probe fast processes in matter [72], a great deal of research effort has been dedicated in the last decade or so to develop and optimize hard X-ray sources from femtosecond laser-produced plasmas by various means [6, 15, 16, 18-22]. X-ray diffraction experiments using K_α radiation from these plasmas have been investigated as well [73-75]. The first studies on the hard X-ray emission from these plasmas have been done using low-repetition-rate lasers systems with pulse energies in the range of hundreds of millijoules to joules per pulse that can emit a large number of X-ray photons per pulse. This choice of laser systems was considered best suited for X-ray generation because the X-ray flux increases proportional to laser intensity. However, very high laser intensity will produce a large hot electron temperature and the electrons will penetrate deep in the target material resulting in an increase in the size and duration of the X-ray emission. This suggests that to generate sub-picosecond K_α X-rays using femtosecond laser pulses one has to select a moderate intensity in spite of a lower X-ray flux per pulse. To maintain the large average X-ray flux it seems potentially better to use high laser repetition rates and moderate laser intensities than low repetition rates and large pulse intensities. Moreover, as mentioned in the previous section, Reich et al. [71] reported a study showing that the highest intensity achievable with a given laser system would not necessarily provide the largest K_α X-ray yields. They argue that higher laser intensities produce more hot electrons with energies well above K-shell ionization energy of the material, which have small cross sections for K-shell ionization. In addition, if the hot electrons generate K_α photons very deep in the material, some of them will be reabsorbed on their way to the surface of the target material. Therefore, a reduced number of emitted characteristic photons is expected. Also, they found that there is an optimum laser intensity depending on the atomic number Z of the target material described by equation (2.25), which can be found in the previous section. For low to medium Z target materials, the optimal K_α X-ray fluxes are obtained for laser intensities lower than 10^{17} W/cm^2, while for high Z material the optimum range of intensities is 10^{18}-10^{19} W/cm^2 as shown in Figure 2.12 in the previous section.

From a practical standpoint, the use of moderate laser intensities is also preferred for measurements of molecular or atomic structures because they are carried out with X-ray energies below 10 keV. The use of higher laser intensities will generate harder X-ray radiation, which will increase the background signal in the X-ray detector. There are also other practical consideration when to decide on the choice of the laser system for time-resolved structural measurements. First, to become practical for chemical and physical research, hard X-ray sources from femtosecond laser-produced plasmas must be reliable and easy to operate by a large group of scientists who are primarily not laser specialists or users. Currently, laser systems with kilohertz repetition rate operating at low energies satisfy this requirement since they are available as turn-key systems which are easy to operate and require low maintenance.

Many groups have recently embarked on optimizing hard X-ray sources by using different laser-target configuration, i.e. laser intensity, target material, and target thickness. Table 2.2 shows an overview of the recent measurements of K_α X-rays from laser-produced plasmas using femtosecond laser pulses.

Table 2.2. K_α X-ray generation with ultrashort laser pulses focused on solid targets unless otherwise specified. The laser pulses are less than 1 ps unless otherwise specified.

Reference	Target (Z)	X-ray energy [keV]	I_{peak} [W/cm^2]	Prepulse Contrast Ratio	Energy per pulse [mJ]	Laser rep. rate [Hz]	Conv. Eff. $\eta_{K\alpha}(2\pi)$
Hagedorn [18]	Cu (29) Ti (22) Cu (29)	8.05 4.51 8.05	2×10^{14} 2×10^{14} 3.6×10^{15}	10^{-3}	0.1 0.1 0.9	1000	3.9×10^{-9} 5.7×10^{-9} 3.0×10^{-8}
Jiang [20]	Cu (29)	8.05	$\sim10^{17}$	10^{-7}	4.25	2000	1×10^{-8}
Thogersen [17]	Cu (29)	8.05	3×10^{15}		0.28	1000	4.6×10^{-7}
Korn [21]	Ga (31) liquid	9.25	3×10^{16}	10^{-4}	1.8	1000	6×10^{-7}
Kutzner [19]	Fe (26) Cr (24) tape	6.40 5.41	4×10^{15} 2.8×10^{15}	10^{-3}-10^{-4} 10^{-1}	0.7 0.45	1000 1000	3.0×10^{-7} 6.3×10^{-6}
Bonvalet [76]	Cu (29)	8.05	3×10^{16}	2×10^{-7} ns 2×10^{-5} ps	12	1000	3.2×10^{-6}
Zhavoronkov [22]	Ga (31) liquid	9.25	1.2×10^{17}	10^{-7} ASE 10^{-5} ps	6.2	1000	9.0×10^{-6}
Rousse [6]	Al (13) Ca (20) Fe (26)	1.49 3.69 6.40	3×10^{16}	optimum ASE (0.7 J/cm^2)	1.5	10	1.6×10^{-5} 5.0×10^{-5} 3.4×10^{-5}
Chen [15]	Ag (47)	22.2	10^{18}	10^{-6}	460/260	10	2×10^{-5}
Park [16]	Ag (47)	22.2	1.9×10^{17}		192 J (70ps)		1×10^{-4}
Eder [14]	Cu (29)	8.05	$\sim10^{17}$	10^{-4}	200	10	4×10^{-4}

The most efficient K_α generation with ultrashort laser pulses is reported from laser systems with low repetition rate (≤ 10 Hz). The high-energy conversion efficiencies into K_α line radiation from these laser systems are in the range of 10^{-5}-10^{-4}. For instance, Eder et al. [14] reported a very high conversion efficiency of 4×10^{-4} Cu K_α using large energy laser pulses of 200 mJ and an intensity of nearly 10^{17} W/cm^2. Park et al. [16] also measured efficient K_α emission using pulse petawatt lasers with pulse energies of 192 J and 70 ps time duration. Using much higher laser intensities of 1×10^{18} W/cm^2, they measured the K_α X-ray conversion efficiency of $\sim1\times10^{-4}$ from Ag targets at 22 keV.

The previously reported conversion efficiency is an order of magnitude lower for higher repetition rate systems for solid targets. When a large prepulse was employed, Kutzner et al. increased the conversion efficiency by more than one order of magnitude [19] from 3.0×10^{-7} to 6.3×10^{-6}. Zhavoronkov et al. [22] reported a conversion efficiency of $\sim10^{-5}$ from a jet of liquid Ga using femtosecond laser pulses using a 1-kHz repetition rate laser system at 6 mJ pulse energy. A general trend of decreasing conversion efficiency with decreasing laser pulse energy is observed, especially, for Cu solid targets. However, for the sub-millijoule laser pulses from a laser system with 1 kHz repetition rate used in this thesis, conversion efficiencies of above 10^{-5} are obtained, similar to the ones reported from high-energy laser pulses with low repetition rates.

Chapter 3

EXPERIMENTAL SETUP

3.1 Laser and target systems

3.1.1 Description of the laser system

The experiments have been performed using femtosecond pulses from a regeneratively amplified Ti: Sapphire laser system (Spectra Physics Model Hurricane). It is a commercial system based on the regenerative chirped-pulse amplification technique. The laser system delivers pulses of 120 fs (Gaussian FWHM) operating at 800 nm with a pulse energy up to 0.75 mJ, and a repetition rate of up to 1 kHz. The laser pulse has a near diffraction limited TEM_{00} spatial profile as per manufacturer data. In addition, beam profile measurements confirm that the beam shape closely approximates the TEM_{00} mode as will be shown later on.

The laser system emits a series of very low energy prepulses in advance of the main pulse. These prepulses are generated by the laser system itself in the regenerative

Ti: Sapphire amplifier as leakage through the Pockels cell before the final pulse is switched out. As mentioned in the previous section, this is important when solid targets are used because it may lead to pre-plasma formation on front of the target material if the prepulse is sufficiently intense. The time separation between two consecutive pulses is one round trip, i.e. 8.5 ns and, thus, the prepulse comes out 8.5 ns prior to the main pulse. The prepulse is characterized by the contrast ratio, which is the ratio of the energy of the prepulse to the energy of the main pulse. The prepulse immediately preceding the main pulse is the largest prepulse and is characterized by a contrast ratio of about 5×10^{-4}, varying slightly from day to day depending on the laser operating parameters. The prepulse train is measured using a fast photodiode (FND-100) whose electronic circuit contains a fast capacitor that limits the stored charge. In this way, the main signal, which has a much higher amplitude is cut off, while the prepulse train signal is completely detected. To detect the main pulse signal the photodiode is used in conjunction with a couple of calibrated neutral density filters (Schott NG 4 and Schott NG 9 filters). The ratio of the signals multiplied by the attenuation factor of the filters gives the prepulse level in terms of the main pulse energy. A typical result is: main pulse 100 mV, prepulse 16 mV, attenuation factor 2.95×10^{-3}, yielding a contrast ratio of 4.72×10^{-4}. An example of the main pulse and the prepulse train signals measured by the photodiode is given in the Figure 3.1. The photodiode has been cross-calibrated against a Spectra Physics power meter (Model 407A) to allow monitoring the laser energy for each laser shot.

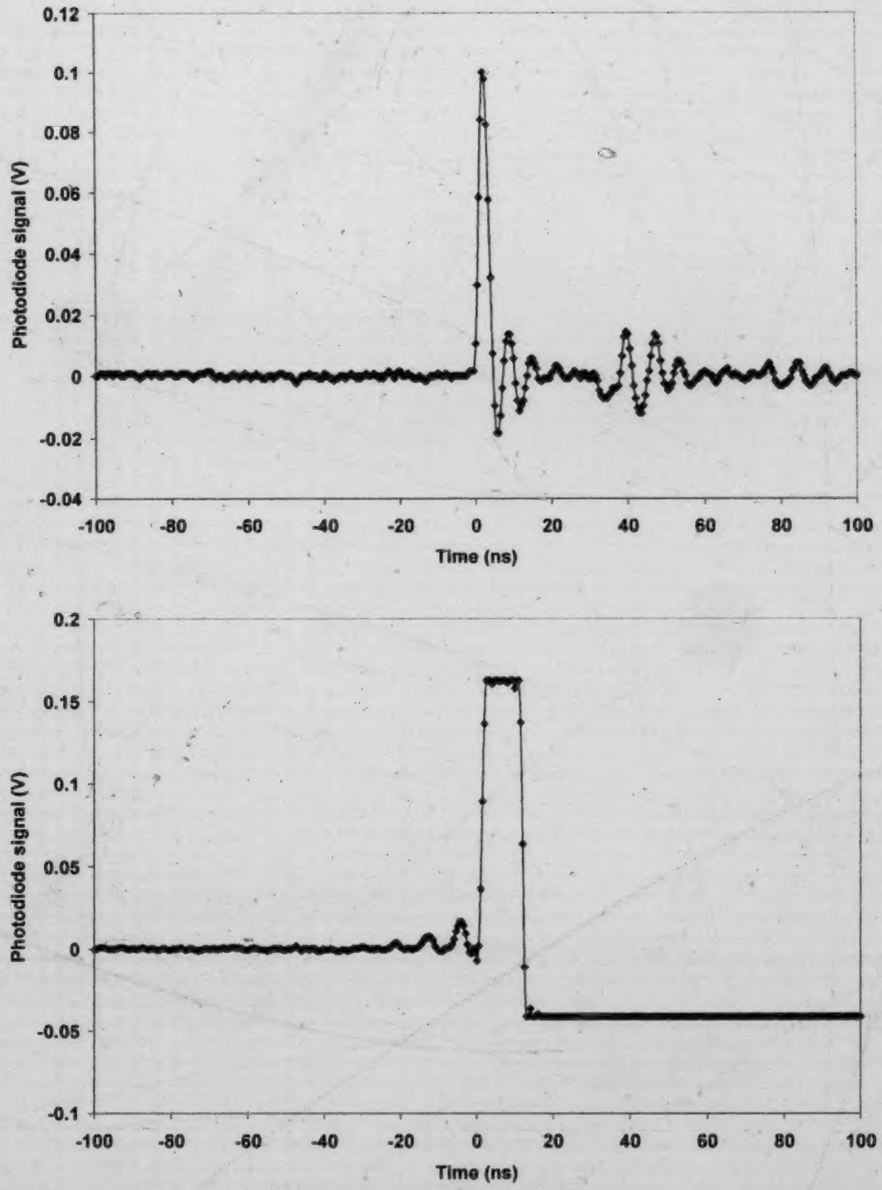

Figure 3.1. A sample of the photodiode signal that is used to measured the main laser pulse (top) and the prepulse train (bottom) for the case of 5×10^{-4} contrast ratio. The signal from the main laser pulse is totally saturated causing clipping and also shifting the baseline after the pulse is finished (bottom).

Because the prepulse is a femtosecond pulse as well and is focused under the same focusing conditions as the main pulse, the intensity contrast ratio is the same as the energy contrast ratio. The main pulse is focused to intensities on the order of 10^{16} W/cm^2 using either a 10X or a 4X microscope objective. For instance, the peak laser intensity is 3.4×10^{16} W/cm^2 for 250 μJ pulses of 130 fs duration and for a laser spot diameter of 2.24 μm at full width at half maximum (this number is based on the measured laser spot for the Mitutoyo 10X microscope objective). Thus, the prepulse is focused to an intensity of 1.7×10^{13} W/cm^2 for the same parameters. Laser ablation for metals requires intensity in the range of about 10^{12} - 10^{14} W/cm^2 for ultrashort pulse laser-matter interaction mode [77-79]. The ablation threshold for copper is measured to be 1.06 J/cm^2 for single shot for highly reflective copper [78] and ~0.49 J/cm^2 for multiple shots on the same spot due to incubation of damage [79], which is equivalent to intensities of 3.8–8.2×10^{12} W/cm^2 for 130 fs laser pulses. Therefore, the prepulse intensity is above the threshold for ablation in the femtosecond regime, leading to formation of a small amount of pre-plasma on the solid target.

Some measurements have been performed in two different prepulse regimes with prepulse contrast ratios of 10^{-1} and 5×10^{-4}. Both types of prepulses have similar origins as described above; the difference is only in the energy contrast ratio. A sample of the main pulse and the prepulse train signals measured by the photodiode in the case of a prepulse contrast ratio of 10^{-1} regime is given in the Figure 3.2.

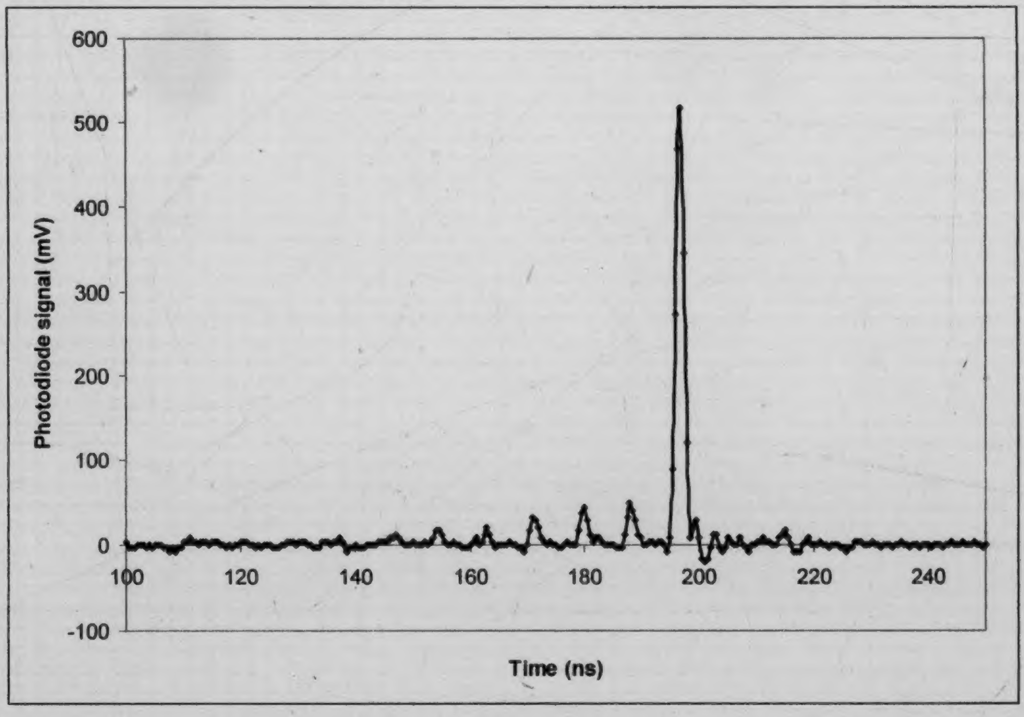

Figure 3.2. A sample of the photodiode signal that provides an image of the main laser pulse and the prepulse train for the case of 10^{-1} contrast ratio. Multiple prepulses are observed in this case.

3.1.2 Laser spot size measurements

For the experiments presented in this thesis, the laser beam was focused onto the target by two types of objectives: a 10X microscope objective and a 4X microscope objective. The 4X microscope objective (Edmund Optics, 4X DIN) has a focal length of 3.25 cm, a working distance of 17 mm and a numerical aperture of 0.10. Three types of 10X microscope objectives have been used: Cooke (model A3584), Mitutoyo (model M Plan Apo) and Newport (model M-10X). The 10X microscope objectives Cooke (model A3584) and Newport (model M-10X) have similar parameters: a working distance of 5.5 mm, focal length of 16.5 and 17 mm, respectively and a numerical aperture of 0.25. The 10X microscope objectives Mitutoyo (model M Plan Apo) has a working distance of 33.5 mm, a focal length of 20 mm and a numerical aperture of 0.28. The spot size measurements of the input beam show that the laser beam resembles closely a TEM_{00} mode, for which the beam waist is $\omega_{01} = 3.56\,\text{mm}$ and thus, its spot size at full width at half maximum (FWHM) is 4.20 mm. These measurements of the spot size of the input beam (the beam in front of the microscope objective) are presented in the next section. When a lens focuses a Gaussian laser beam, then the new laser beam waist in the lens focal plane can be calculated using the ABCD matrix associated with the lens element [80]. If the ω_{01} is the beam waist of the incident beam on the lens and ω_{02} is the new beam waist of the laser beam after the lens in its focal plane, then ω_{02} can be calculated using the equation (3. 1):

$$w_{02} = \frac{\lambda}{\pi} \cdot \frac{f}{\omega_{01}} \cdot \frac{1}{\sqrt{1+\left(\frac{f}{z_{R1}}\right)^2}} \tag{3.1}$$

where λ is the laser wavelength, f is the focal length of the focusing lens, and z_{R1} is the Rayleigh range of the incident beam, which is defined by:

$$z_{R1} = \frac{\pi \cdot \omega_{01}^{\ 2}}{\lambda} \tag{3.2}$$

Using $\omega_{01} = 3.56\,\mathrm{mm}$, z_{R1} becomes 49.7 m.

The beam diameter (FWHM) is given by:

$$d_{FWHM} = \sqrt{2\ln(2)} \cdot \omega_o \tag{3.3}$$

The calculated values of the beam waist and the spot size (FWHM) for each microscope objective using the measured value of the input beam waist $\omega_{01} = 3.56\,\mathrm{mm}$ are given in the Table 3.1.

Table 3.1. Theoretical values of the beam waists and the spot sizes (FWHM) of the laser beam obtained with the four different microscope objectives used to focus the laser pulses. These values have been calculated using Gaussian beam theory (equations 3.1 and 3.3). The measured value of the input beam waist ($\omega_{01} = 3.56\,\mathrm{mm}$) was used to determine ω_{02}.

	Theoretical beam waist ω_{02} (μm) (diffraction limited)	Theoretical Spot size at FWHM d_{FWHM} (μm) (diffraction limited)
4X (Edmund)	2.32	2.73
10X (Mitutoyo)	1.43	1.68
10X (Cooke)	1.22	1.44
10X (Newport)	1.18	1.39

The laser spot size (FWHM) is measured to be 2.24±0.15 μm for 10X objective (Mitutoyo), being 1.33 times diffraction limited. Thus, for laser pulse energies of 250 μJ and 130 fs duration, the laser peak intensity obtained with this objective is actually $(3.4\pm0.5)\times10^{16}$ W/cm^2 using the measured spot size $d_{FWHM} = 2.24$ μm (instead of 6.04×10^{16} W/cm^2 using the theoretical $d_{FWHM} = 1.68$ μm).

However, not all of the spot sizes have been verified directly, which might be affected by residual aberrations in the objectives and the small variation in shot to shot positioning of the target relative to the best focus. This leads to uncertainties in the quoted intensities compared with the values given here. In the results reported in this thesis the energy lost due to truncations of the wings of the beam at the entrance to the objective and the transmission of the objectives at 800 nm have been taken into account. Energies given refer to the energies incident on target.

The spot size obtained with the 10X microscope objectives Mitutoyo (model M Plan Apo) has been verified experimentally and the results are provided below. The setup is located inside of a vacuum chamber about 6m away from the laser output. The profile of the laser beam incident on the 10X focusing objective was analyzed using a knife-edge system. Both a photodiode and a sharp, straight edge (knife-edge) were placed in the laser beam path inside the vacuum chamber. The knife-edge was positioned in front of the photodiode, and it was mounted on a stage with micrometer resolution. As the knife-edge traversed the laser beam along the horizontal direction, the photodiode measured the intensity of the beam unblocked by the knife-edge. The photodiode signal was then correlated with the position of the knife-edge and displayed in Figure 3.3. For the reconstruction of the beam, it was assumed that the spatial profile of the incident laser beam closely resembles a TEM$_{00}$ mode.

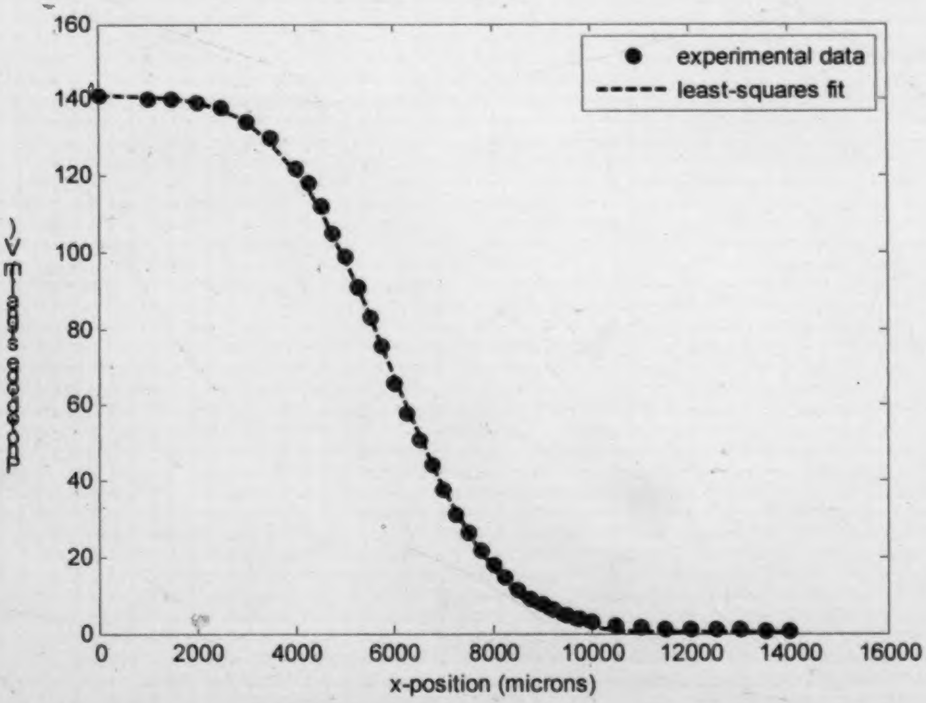

Figure 3.3. The photodiode signal versus the knife-edge position.

According to Gaussian beam theory [80], the intensity for a Gaussian beam is given by the following equation:

$$I(x,y) = \frac{2P_0}{\pi \cdot \omega_0^{\ 2}} \cdot \exp\left[-\frac{2(x^2+y^2)}{\omega_0^{\ 2}} \right] \qquad \textbf{(3. 4)}$$

where P_0 is the total input power and ω_0 is the beam waist. ω_0 is defined as the radius at which the beam intensity drops to $1/e^2$ of its peak value or radius at which the electric field amplitude drops to $1/e$ of its peak value.

Because the beam is cut by the edge in the *x* direction, while it is not cut in the *y* direction, the power blocked by the edge is given by the following equation:

$$P(x) = \frac{2P_0}{\pi \cdot \omega_0^2} \int_{-\infty}^{x} \int_{-\infty}^{\infty} \exp\left[-\frac{2(x^2 + y^2)}{\omega_0^2} \right] dydx \qquad (3.\ 5)$$

Each integral can be computed separately yielding a final result given by the equation (3. 6):

$$P(x) = \frac{P_0}{2}\left[1 + erf\left(\frac{\sqrt{2}}{\omega_0} \cdot x \right) \right] \qquad (3.\ 6)$$

Therefore, the signal measured by the photodiode is then proportional with beam power received by the detector and is given by equation (3. 7):

$$P_m(x) = \frac{P_0}{2}\left[1 - erf\left(\frac{\sqrt{2}}{\omega_0} \cdot x \right) \right] \qquad (3.\ 7)$$

The beam waist ω_0 is determined from the least squares fit of the experimental values with the theoretical model given by equation (3.7) and found to be 3.56±0.05 mm. The least-square fit is plotted in Figure 3.3. ω_0=3.56 mm is the laser beam waist before entering the objective.

This beam is strongly focused by a 10X microscope objective, which can be considered, in a zero-order approximation, as a lens of focal length *f*, which value is provided by the manufacturer. As mentioned above, the 10X microscope objective (M Plan Apo 10X Mitutoyo), which was used in part of the experiments, can be described by a single lens with a focal length of 20 mm, a working distance of 33.5 mm and a numerical aperture of 0.28 as per manufacture data sheet. The beam waist ω_{02} of the laser beam after the objective in its focal plane is calculated to be 1.43 μm using equation (3.1), which represents the diffraction-limited spot size. This assumes an ideal thin lens and high quality microscope objectives are designed to be close to diffraction limit. The actual spot size of the laser beam focused by the 10X microscope objective (M Plan Apo 10X Mitutoyo) was measured and the results are presented and compared to the above theoretical ones in the following.

Figure 3.4 shows the laser beam profile from a 10X microscope objective (M Plan Apo 10X Mitutoyo). The laser spot size was imaged onto an infrared CCD camera (Ultrak K-500 ½") with the Spiricon Software (LBA-400PC). Because the resolution of CCD camera is limited by its pixel size, which is approximately 10 μm, the focused laser spot was re-imaged with a 60X microscope objective (Olympus, A60, NA=0.8) along with a 7 cm beam tube connecting the objective to the camera resulting in a resolution of 0.26 μm. Before measuring the intensity beam profile, the laser beam was attenuated to avoid damaging the 60X objective and the CCD camera. A set of in-line attenuation filters were placed in front of the 10X microscope objective, to significantly reduce the power to the level acceptable by the camera. Because the in-line attenuation filters consisted of absorbing neutral density filters (Schott NG), the reflections from the filter surfaces were very small. However, the filters were positioned slightly angled to ensure that interference would not occur in the region of interest. The Spiricon computer software provides the two- and three-dimensional plots of profiles as shown in the Figure 3.4. The cross section profiles both in the *x*- and *y*- directions are drawn through the peak of the beam and displayed in Figure 3.4 (c) and (d). The laser beam widths are determined from the beam profiles in the *x*- and *y*- directions, which are fitted with a Gaussian function given below:

$$I = B + I_0 \cdot \exp[-(\chi - \chi_0)^2 / 2 \cdot b^2] \qquad \textbf{(3. 8)}$$

where: I is the intensity at the point χ, I_o is the intensity at the Gaussian center χ_0, B is the background, χ is the location of the pixel on x- or y- axis, and χ_0 is the location of the Gaussian center on x- or y- axis.

The laser spot diameter at full width half maximum intensity d_{FWHM}, was determined at 1/2 of I_o and the electric field beam waist ω_0 was calculated using the equation (3.3).

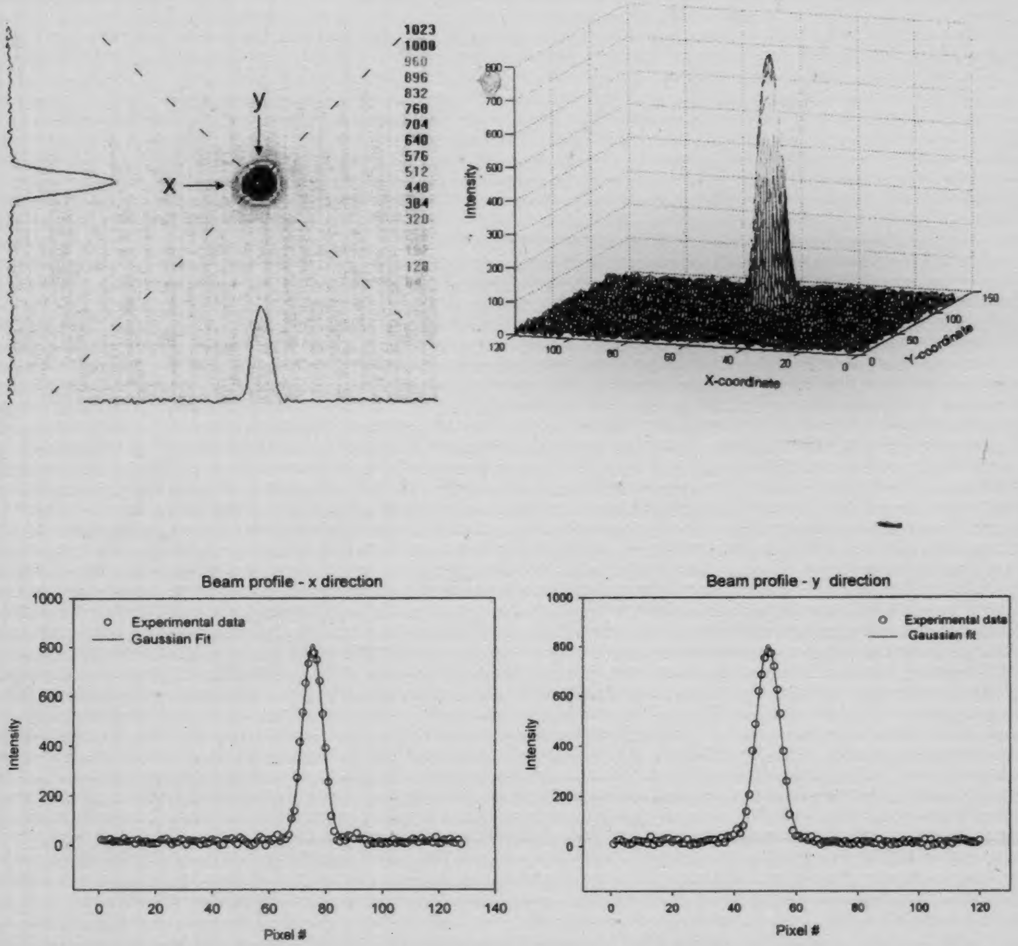

Figure 3.4. Laser beam profile: (a) Two dimensional profile display as measured by an infrared CCD camera (Ultrak K-500 1/2") with Spiricon Software (LBA-400PC), (b) the beam profile measured along *x*-direction and (c) the beam profile measured along *y*-direction. The beam profile on *x*- and *y*- direction was fitted with a Gaussian function using the method of least squares.

The laser focal spot appeared to be slightly asymmetric as the beam waist ω_0 along the *x*-axis was measured to be 1.85±0.13 μm while along the *y*-axis was 1.94±0.13 μm resulting in a beam waist of 1.90±0.13 μm averaged over the *x*- and *y*- coordinates. The beam diameter at full width at half maximum is then calculated to be 2.24±0.15 μm averaged over the *x*- and *y*- coordinates. As shown before, numerically, the beam diameter at full width at half maximum is calculated to be 1.68 μm for a laser beam waist of 3.56 mm incident on the Mitutoyo 10X objective. Consequently, the measured spot size is 1.33 diffraction limited. The Rayleigh range z_{R2} can be determined using equation (3. 2) and is calculated to be 14.2 μm for the measured spot size ω_0 =1.9 μm. This means that the laser beam waist will increase by a factor of $\sqrt{2}$ in a distance equal to the Rayleigh range, according to the equation (3. 9):

$$\omega(z = z_R) = \omega_0 \sqrt{2} \qquad \textbf{(3. 9)}$$

However, the Rayleigh range of the aberrated spot will be larger than the one for the ideal spot, which is only 8 μm, making the focal conditions demanding. The target should be kept in focus to less than ± 8 μm from the best focus to avoid variations of the laser intensities on the target that are larger than a factor of two. This range changes depending on the objective employed in the experiments. For instance, when using 10X objective from Newport or Cooke the target should be kept in focus to less than ± 5.5 μm from the best focus.

In practice, the laser beam should fill the aperture of the focusing objective without severe loss of power due to finite aperture of the lens. A focusing objective with an aperture with a diameter $d = \pi\,\omega_0$ will pass about 99% of the Gaussian beam power.

The 10X microscope objective (M Plan Apo 10X Mitutoyo) has an entrance aperture of 12 mm, which fulfills the above requirement. Both the 10X microscope objectives Cooke and Newport have a clear aperture of 8 mm.

Besides the geometrical factors, absorption in the objective glass can affect the transmitted laser power of each objective. Therefore, the transmission of each objective was measured separately to account for all the factors that may affect the transmitted laser power of the incident beam. The transmission factors are then considered in the calculations of the laser energy incident on the target, which in turn is used to calculate the X-ray conversion efficiency.

There may be additional distortion of the laser beam due to B-integral in the lens glass of the objectives.

3.1.3 Description of the target system

There are two major design considerations when selecting the target system from the practical point of view of an X-ray source operated at high repetition rate. First, it is necessary to use a stable and predictable mounting and positioning system, and a motorized target to present fresh surface to each laser pulse. An automatic correction of the position during the motion of target would help to keep the target in the same location. The latter feature is required, in particular, when a powerful lens is employed to focus the laser beam because its depth of focus is very small and an accurate position of the target is necessary to ensure that the laser spot size and, thus the laser intensity will not change significantly from one shot to another. The second consideration is the quality of the target surface. Given the small laser spot size, the target surface must be very smooth with no scratches or defects to ensure a clean laser-matter interaction and a well defined polarization of the laser pulses on the target.

The first target consisted of a 500nm copper film sputtered onto a silicon wafer. A compact, stable target/lens positioning system was built using three-axis computer-controlled translation mounts, achieving low vibration and lens to target position stability[1]. Two computer-controlled mounts were used to move the target vertically and horizontally to provide a fresh area of target for each laser shot. The microscope objective was mounted on a stage connected to a motorized linear actuator (Zaber Technology, Model # T-LA60). The rest of the system components necessary to complete the target system[2] were fabricated in the machine shop in the Electrical and Computer Engineering Department. This system was mostly used in the initial part of the experiments in single shot mode and is presented in Figure 3.5.

Figure 3.6 displays an image of the copper film sputtered onto a silicon wafer taken by the JEOL 6301F Field Emission Scanning Electron Microscope in the Department of Earth and Atmospheric Sciences at University of Alberta. The overall film thickness is slightly varying around 500 nm.

---

[1] The design of the target system was performed in collaboration with J. Santiago

[2] The engineering drawing of the target system was prepared by J. Santiago.

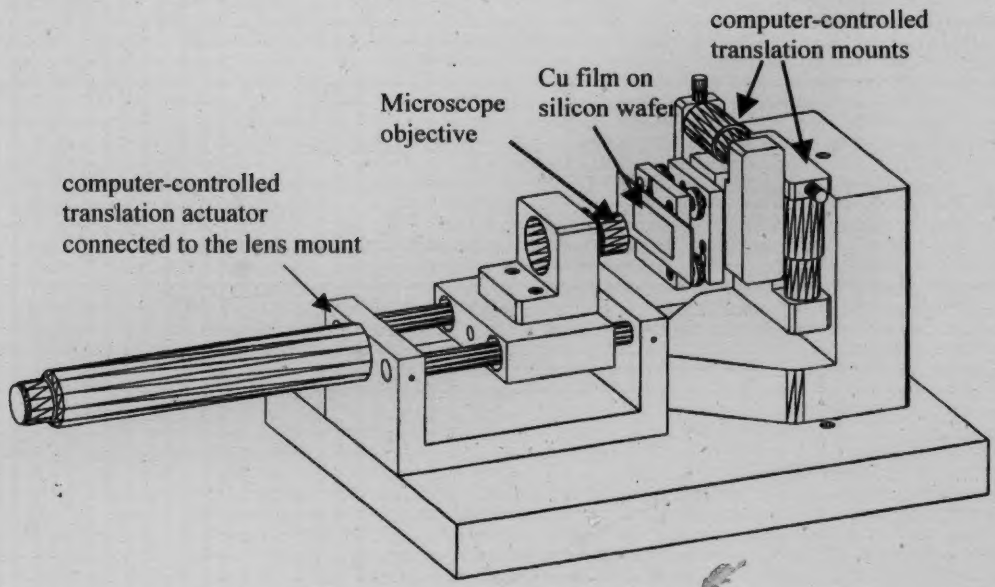
computer-controlled
translation mounts
Cu film on
silicon wafer
Microscope
objective
computer-controlled
translation actuator
connected to the lens mount

Figure 3.5. The target system used with the plane targets made of 500 nm thick copper film sputtered onto a silicon wafer. The system consists of three-axis computer controlled translation mounts, two of them used to translate the target and one to move the focusing objective.

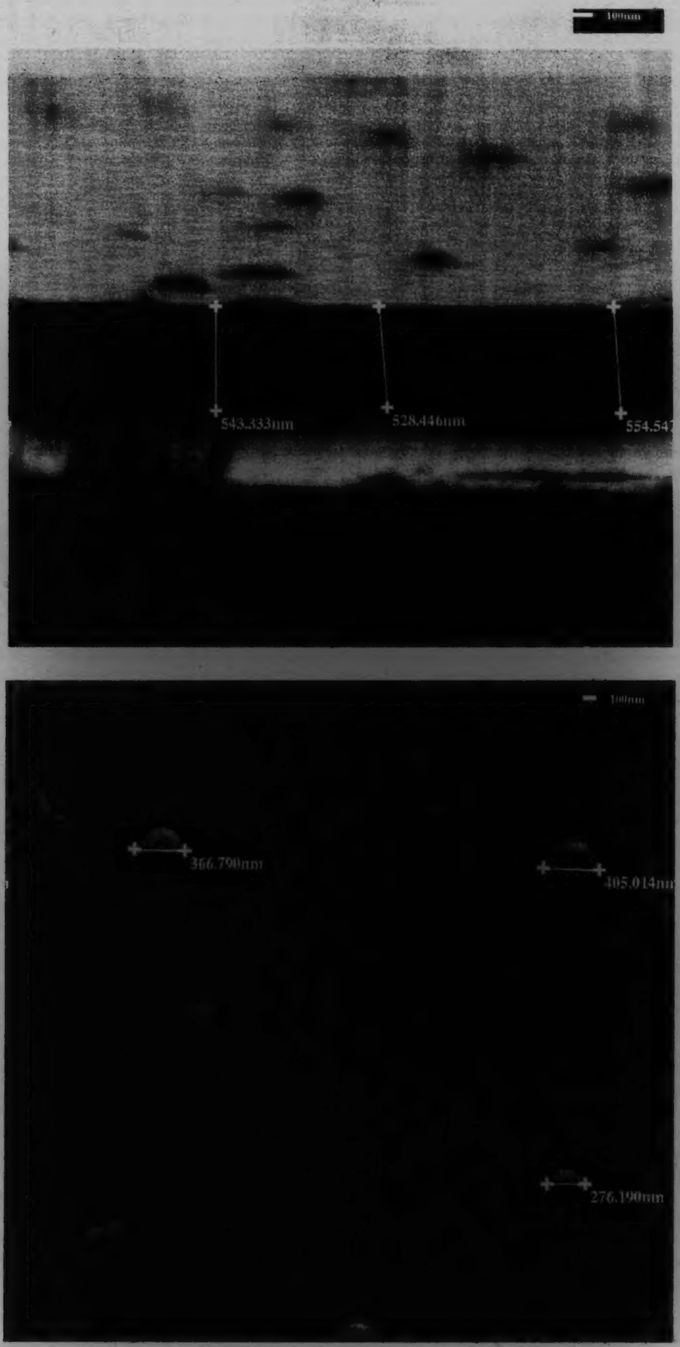
100nm
543.333nm
528.446nm
554.54
100nm
366.790nm
405.014nm
276.190nm

Figure 3.6. Image of the first target a 500 nm thick copper film sputtered onto a silicon wafer: side view (top) and top view (bottom).

The second target system that was used in both single shot and continuous shot modes is a copper disk with a diameter of 76 mm and thickness of 22 mm. The copper disk is polished with a diamond tool before use until it has the appearance of a mirror. The radius of the disk is kept constant in order to avoid longitudinal displacements since these will results in a considerable change in the focal spot size on the target, which in turn will induce variation of the laser intensity. However, the rotating disk wobbles slightly due to the mechanical imperfections. Using a DC motor, the disk is rotated slightly after each laser shot in order to ensure that the pulse interacts with a fresh target surface on each shot. After completing one rotation, the target is translated sideways in order to position the laser focus on a new circle. The target lasts for about 24 min with laser operating at 1 kHz, after which it must be repolished.

For most of the experiments, the target is kept in focus within ± 6 μm over one rotation. To control the deviation from the focus that occurs when the disk is rotated after each shot, a position-sensitive dial-gauge (Mμ-Checker, Mitutoyo) is pressed against the target surface on the back of the target disk as can be seen in Figure 3.7. It produces a signal, which is proportional to the target displacement and is displayed on a scale outside of the vacuum chamber. In this way, the distance between the target and the focusing objective can be maintained almost constant throughout the experiment when working in single shot mode. The optical viewing system built in the setup reveals a very flat surface with scratches, which are ~ 2-3 μm thick separated by distances of approximately 30-60 μm. In some cases, there are also damaged spots of different sizes scattered on the target surface due to the polishing process. By means of the viewing system, special care is taken to position the target surface to ensure that the laser pulses are interacting with a clean and flat target surface for the single shot experiments.

3.1.4 Description of the vacuum system

A new vacuum target chamber system has been constructed in order to carry out the measurements of K_α X-ray conversion efficiency and hot electron emission presented in this thesis. The system consists of a roughing pump and the diffusion pump coupled to a custom vacuum chamber (Kurt J. Lesker). The system is capable of reaching a base pressure of better than 10^{-6} torr measured with an Edwards Active Pirani Gauge (model APG-L-NW16). The ports of the vacuum chamber are equipped with electrical feedthroughs to control and maneuver the target positioning system from outside the vacuum chamber. The target disk can be rotated remotely from outside the vacuum chamber and the rotation speed can be adjusted to correspond to the laser frequency used.

Initially, the experiments were carried out at pressures of 10^{-5} torr. Some measurements were also performed at different background pressures. It was observed that the keV X-ray signal was constant for a large range of pressures, from 10^{-5} torr to approximately 50 torr. Therefore, for the bulk of the experiments the target chamber was evacuated by using only the roughing pump, which was able to reach a base pressure of 100 mtorr. In order to prevent the vibration from the roughing pump affecting the target position, flexible bellows were used to connect the rouging pump to the chamber.

3.2 Description of the experiments

The typical experimental setup employed for the measurements of X-ray and hot electron emission is shown in Figure 3.7. Various optical components were used to guide the laser beam from the laser area to the vacuum chamber. These include dielectric mirrors, polarizer, periscope, and half wave plates. The mirrors were designed for use at 45° angle of incidence with a high reflectivity coating at 800 nm. Near the output of the laser, the beam passes through a combination of a quartz half wave plate (CVI Laser Optics) and a broadband Glan-Taylor calcite polarizer (Coherent Inc.), combination that acts as a variable attenuator. A periscope was used to change the laser beam height and to redirect it towards the vacuum chamber. Additional mirrors were utilized to build an optical viewing system employed to monitor the target surface. A second half wave plate is utilized to control the laser polarization. Figure 3.8 displays the top and side views of the laser-target geometry for both *p*- and *s*-polarized laser pulses. When the laser electric field polarization is vertical, the beam is *p*-polarized on the copper target disk, and when the laser electric field polarization is horizontal, the beam is *s*-polarized on the copper target disk. For most of the experiments, both *p*- and *s*- polarized laser pulses with energies between 200 μJ to 300 μJ were used. A 30 μm thick transparent plastic foil shielded the focusing objective against the debris. The shield was continuously changed remotely from outside the vacuum chamber.

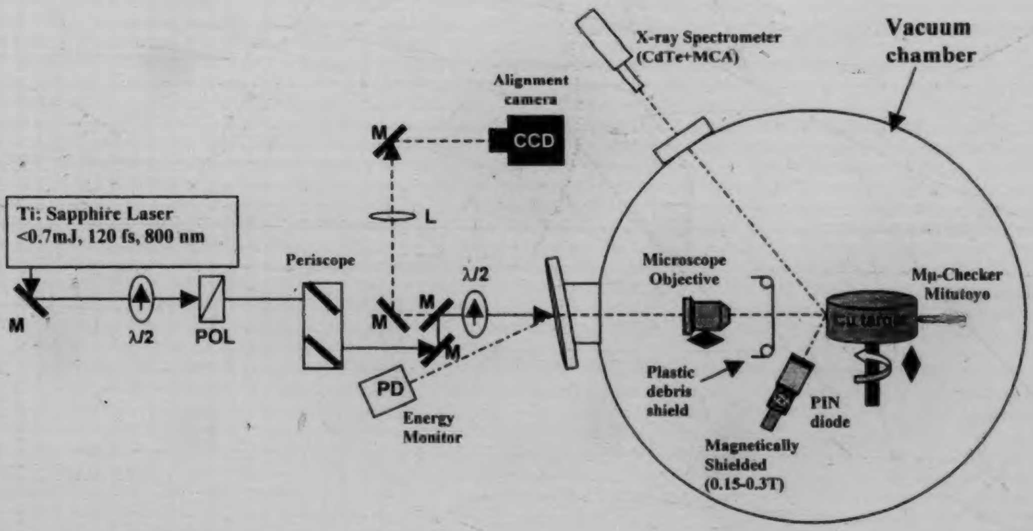
X-ray Spectrometer
(CdTe+MCA)
Vacuum
chamber
Alignment
camera
CCD
M
L
Ti: Sapphire Laser
<0.7mJ, 120 fs, 800 nm
Periscope
λ/2
M
λ/2
POL
M
M
M
PD
Energy
Monitor
Microscope
Objective
Mμ-Checker
Mitutoyo
Plastic
debris
shield
PIN
diode
Magnetically
Shielded
(0.15-0.3T)

Figure 3.7. Schematic diagram of the experimental setup. M is a mirror, λ/2 is a half-wave plate, POL is a polarizer, L is a lens (positive), PD is a photodiode, CdTe is a Cadmium Telluride detector, MCA is a multichannel analyzer.

The X-ray and electron measurements were made at different angles of incidence. The detection of the X-ray emission was carried out at angles of incidence of 22.5° and 42.5° using the flat copper target. The X-ray measurements from copper rotating disk were carried out at 30° angle of incidence. Measurements of the hot electrons and the electron jets were performed primarily at 30°angles of incidence, but also at a few other angles to study the angular scaling of the electron generation process.

(a)

Top view

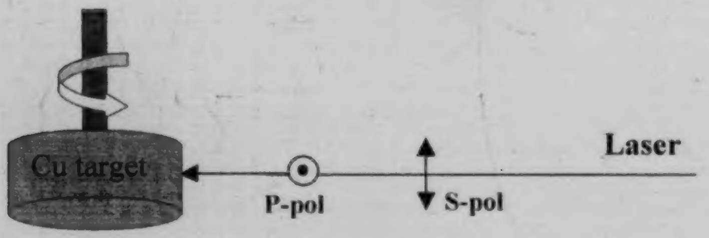
Cu target
Laser
P-pol
S-pol

(b)

Side view

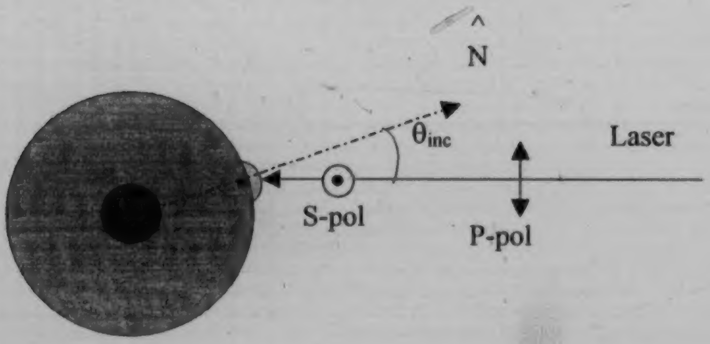
$\hat{N}$
θ_{inc}
Laser
S-pol
P-pol

Figure 3.8. The target geometry: (a) top view and (b) side view.

3.3 X-ray diagnostics

The X-ray emission was measured with silicon PIN diode X-ray detectors and an X-ray pulse height spectrometer using a CdTe detector and a multichannel analyzer. The PIN diode detectors were usually placed approximately 50 mm away from the target at angles between 60^0 and 75^0 with respect to the laser direction. The X-ray PIN diode detectors have $25mm^2$ active area with a 250 μm thick active layer and a 0.3 μm thick silicon entrance window. The sensitivity of the diode detector for X-ray photons detected is 0.276 C/J as per the manufacturer data sheet. The theoretical response function of the PIN diode was calculated based on silicon absorption data from the National Institute of Standards and Technology (NIST) [69] and CRC databases [81] and plotted in Figure 3.9 (a). Different filters were used to restrict the X-ray energies being measured and also to provide a light tight barrier. Figure 3.9 (b) shows the sensitivity of the PIN diode detector filtered with aluminum foils of three different thicknesses: 9 μm, 62.5 μm and 125 μm. The detector sensitivity S(E) filtered with a filter of transmission T(E) is given by:

$$S(E)= s(E)\cdot T(E) \qquad \textbf{(3. 10)}$$

where $s(E)$ is the basic sensitivity of the PIN diode detector in C/J that is shown in Figure 3.9 (a). The transmissions of the filters were calculated using the mass attenuation coefficients μ / ρ from the X-ray database at the National Institute of Standards and Technology (NIST) [69] and CRC database [81].

The filter transmissions are calculated using the exponential attenuation law [82]:

$$T = \frac{P}{P_0} \cdot \exp\left[-\left(\mu / \rho \right) \cdot x \right] \qquad \textbf{(3. 11)}$$

where P_0, is the power of the X-ray photons incident on a layer of material with mass thickness x and density ρ, and P is the power of the emerging X-ray photons. The mass thickness is defined as the mass per unit area, and is obtained by multiplying the thickness t by the density, i.e., $x = \rho \cdot t$.

In some experiments, a pair of filters consisting of 15 μm Ni + 9 μm Al and 25μm Fe is used as a Ross filter pair on the PIN diode detectors in order to measure the X-ray signal from a narrow energy range from 7.11 keV to 8.33 keV around the Cu K_α (8.05 keV) line. Figure 3.10 shows the PIN diode response function combined with the transmission of the Ross filters pair.

Two identical permanent magnets creating magnetic fields of 0.15-0.3 T were used in front of the PIN diode detectors to deflect the hot electrons and thus preventing them hitting the detectors.

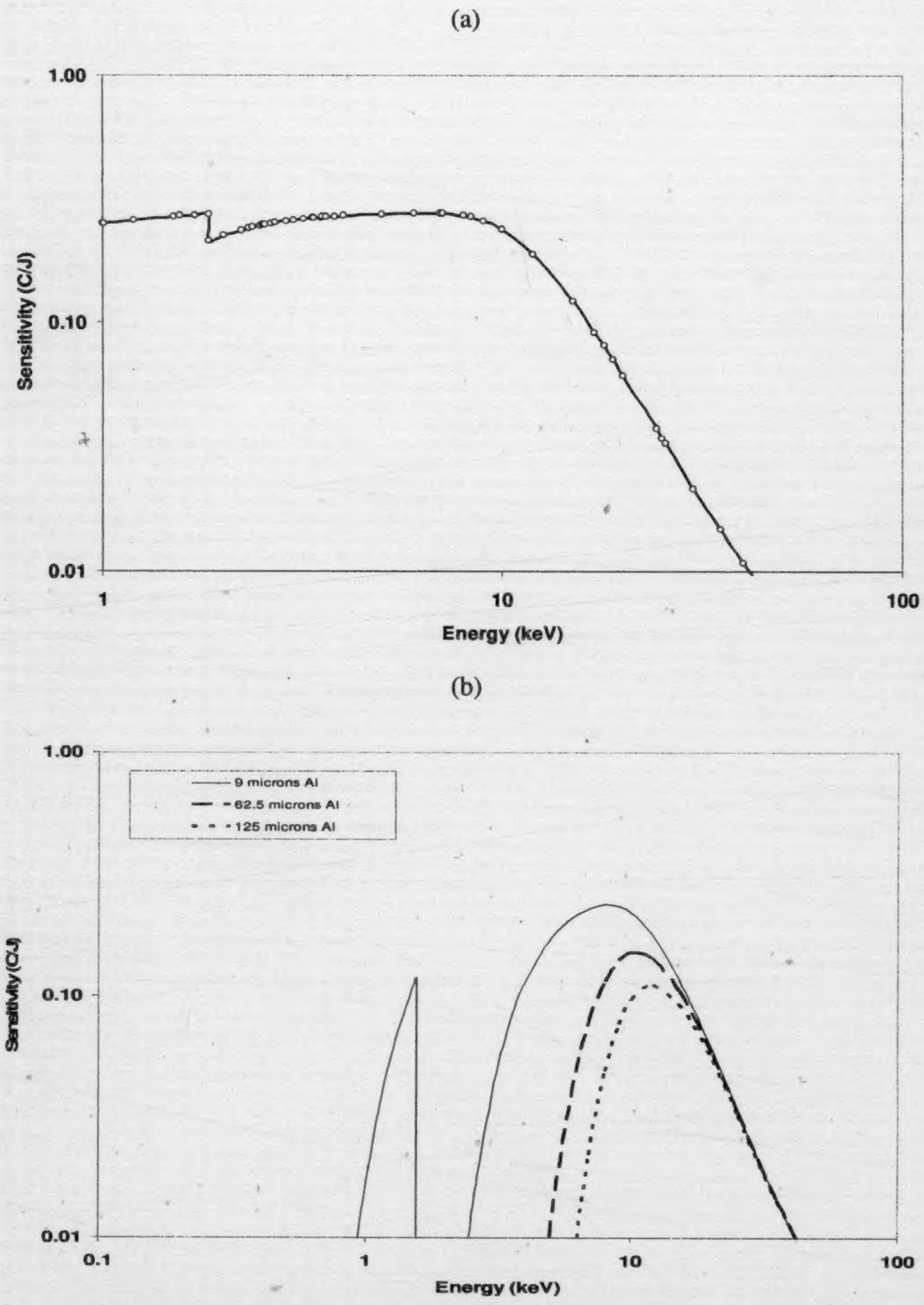

Figure 3.9. The theoretical response function for (a) PIN diode and (b) PIN diode with Al filters of three different thickness: 9 μm, 62.5 μm and 125 μm.

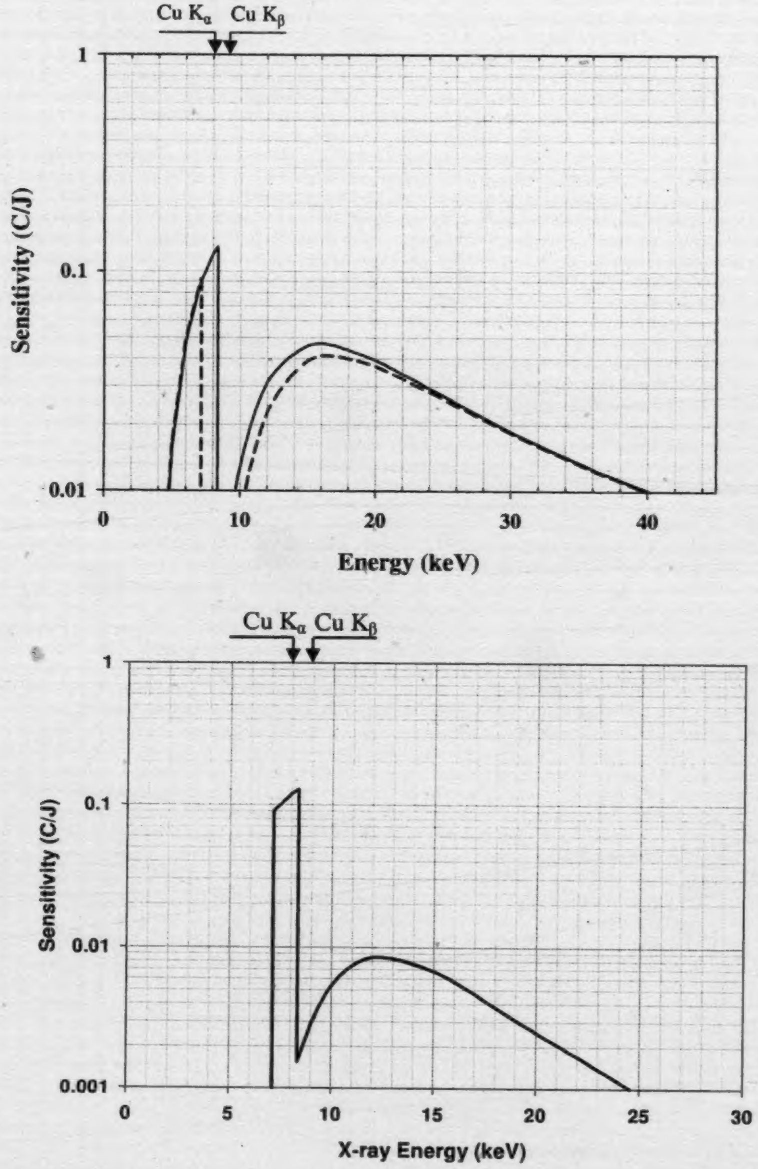

Figure 3.10. The response function of the silicon PIN diode detector employed with: (a) two different foil filters: 15 μm Ni + 9 μm Al (solid line) and 25 μm Fe (dashed line) and (b) the sensitivity of the Ross filter pair when taking the difference of the two detector signals.

For all of the experiments employing the flat copper targets and some of the measurements using the copper rotating disks, the measurements of the X-ray emission have been carried out using the PIN diode detectors with the Ross filter pair and other aluminum foils. A pulse height X-ray spectrometer has also been used to measure the X-ray spectra from copper disks. Firstly, focal scan measurements of the K_α X-ray signal have been carried out with the PIN diode detectors with the Ross pair filters. Once the location for maximum X-ray signal has been determined, the X-ray spectra have been measured with a thermoelectrically cooled CdTe detector (Amptek, XR-100T-CdTe). The detector efficiency is given in Figure 3.11. It has a 4 mil (~100 μm) thick Be light tight vacuum window. The X-ray transmission of the 100 μm Be window is plotted in Figure 3.12. The signal from the CdTe detector is amplified in a pre-amplifier (Amptek, PX2T). It is then fed in to a multichannel analyzer (Amptek, MCA 8000). In order to improve its energy resolution, the system is equipped with a Rise Time Discrimination (RTD) circuit and thus, only pulses corresponding to "full charge collection" events are allowed to be sent to the multichannel analyzer (MCA) for analysis. However, the energy resolution is of the order of few hundreds eV (e.g. 390 eV at 13.95 keV) and it is not possible to distinguish between the closely spaced emission lines Cu $K_{\alpha 1}$ (8.048 keV) and Cu $K_{\alpha 2}$ (8.028 keV). The response function of the CdTe detector with the 100 μm beryllium window remains constant (98-100%) in the energy range of 6-60 keV and it rolls off to 65% for 100 keV and 10% for 300 keV. The detector has been placed at a large distance of 170 cm (31 cm in vacuum and 139 cm in air) from the plasma source outside the vacuum chamber in order to operate it in single photon counting mode. Figure 3.13 shows the X-ray transmission of 139 cm in air. Further, a small aperture of ~ 550μm diameter of lead (thickness 2 mm) was placed at the detector head to reduce the X-ray flux. The CdTe detector was kept in the direction of ~ 50°-55° from the target normal and it is separated from the plasma chamber by a 75 μm thick Mylar window. The X-ray transmission of 75 μm thick Mylar window is plotted in Figure 3.14. The intrinsic efficiency of the CdTe detector and the X-ray transmissions of 139 cm in air, 100 μm Be detector window, and 75 μm Mylar window at the vacuum-air interface were calculated with the use of NIST databases [69]. The transmission of the 100 μm thick beryllium window, 75 μm thick Mylar window that separates vacuum from air and the distance in air traveled by the X-ray photons from the vacuum chamber window to the detector have been taken into account to compute the X-ray energy conversion efficiency. This is calculated in 2π sr solid angle assuming an isotropic X-ray emission into 2π sr [76].

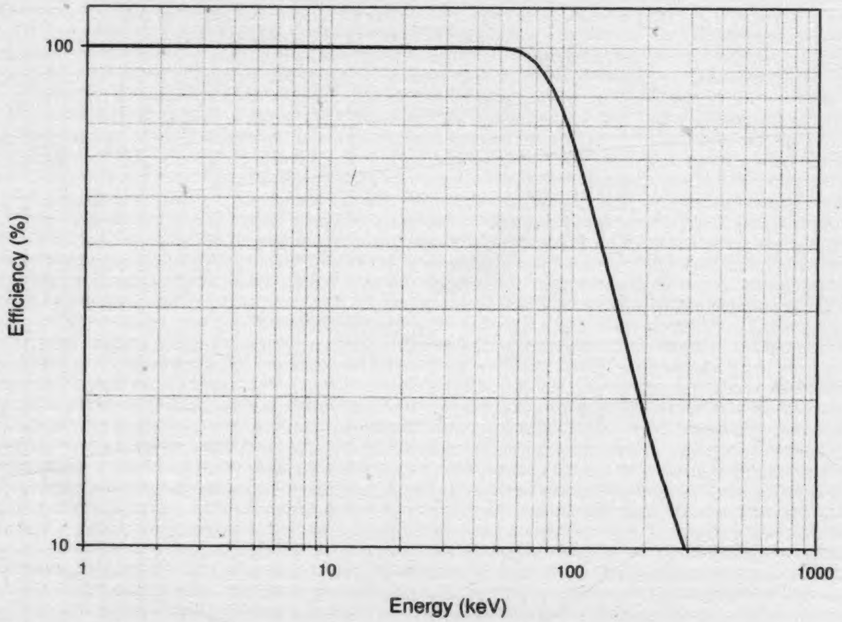

Figure 3.11. The intrinsic efficiency of CdTe detector.

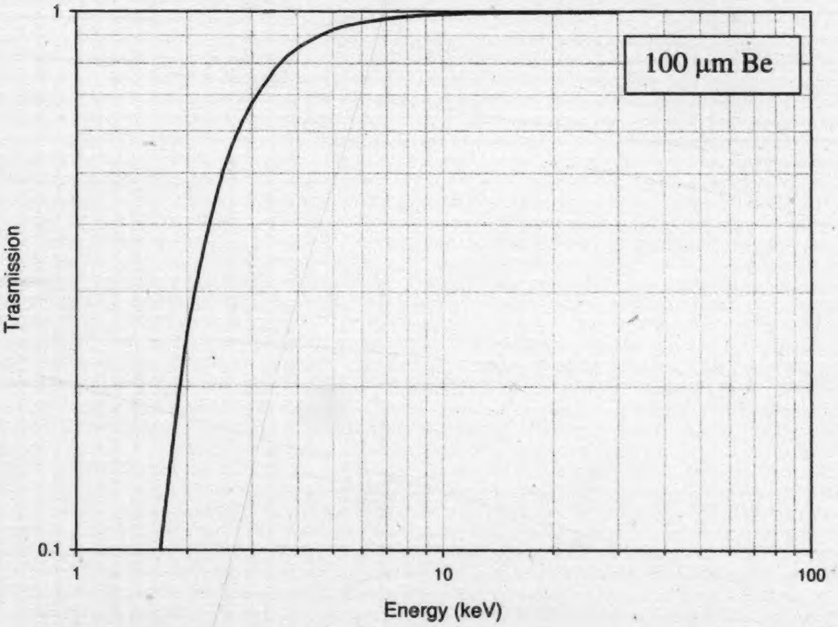

Figure 3.12. The X-ray transmission of 100 μm thick Be window.

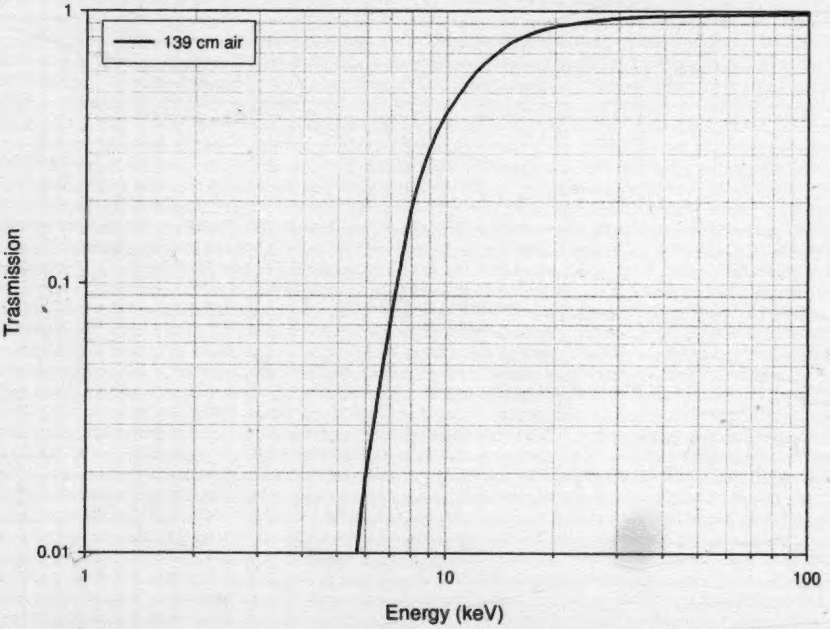

Figure 3.13. The X-ray transmission of 139 cm thickness of air.

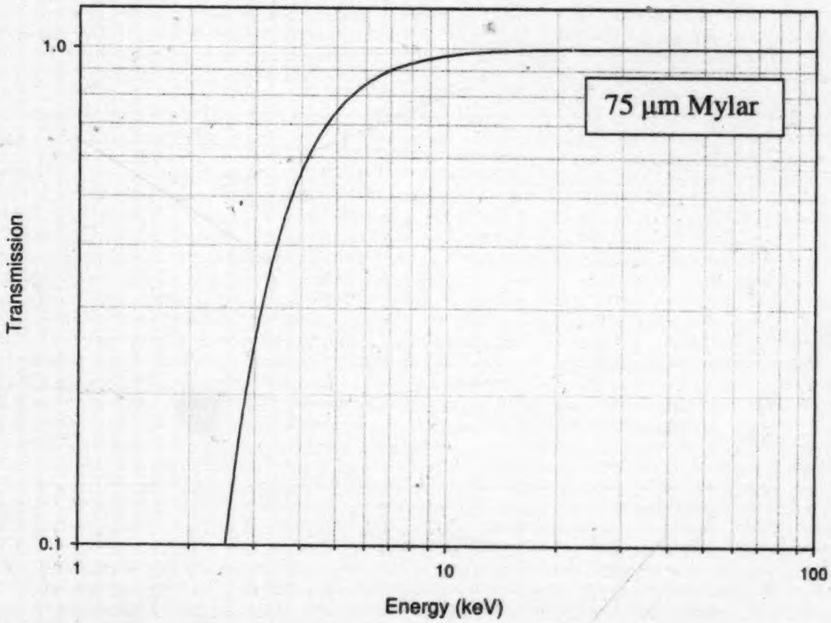

Figure 3.14. The transmission of 75 μm thick Mylar window

The K_α X-ray source size is measured by the knife-edge technique. The knife-edge was a 25 μm Fe foil located 7 mm from the source. Due to its *K*-edge absorption edge at 7.11 keV, the foil completely blocks the Cu K_α 8.05 keV radiation. The X-ray detector was an X-ray Kodak Direct Exposure (DEF-392) stripfilm located 147 mm away from the knife-edge. A schematic diagram of the experimental arrangement employed for the X-ray knife-edge diagnostic is shown in Figure 3.15.

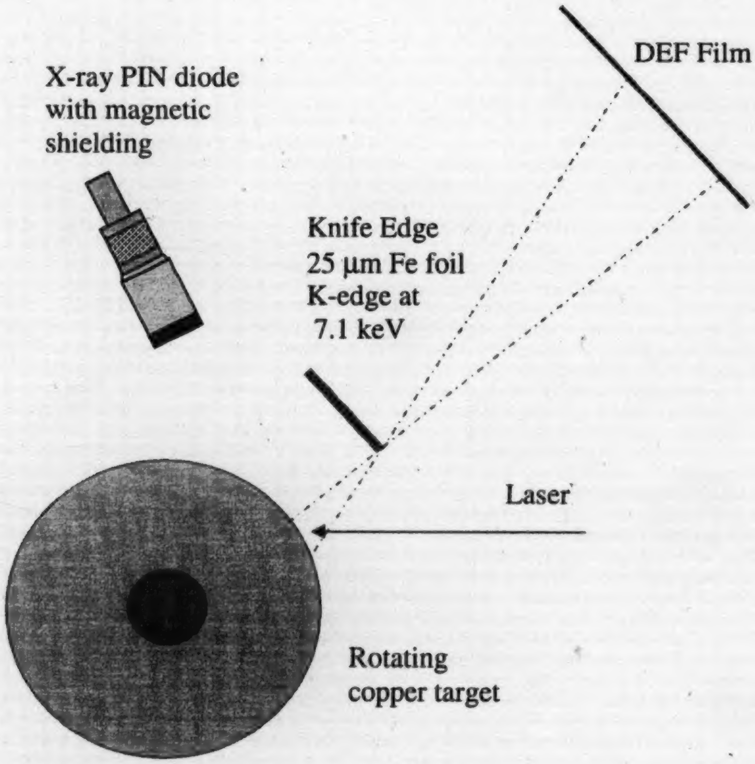
DEF Film
X-ray PIN diode
with magnetic
shielding
Knife Edge
25 µm Fe foil
K-edge at
7.1 keV
Laser
Rotating
copper target

Figure 3.15. Schematic diagram of the experimental setup used for X-ray imaging.

3.4 Electron jet diagnostics

The hot electrons ejected outwards from the plasma were measured using both silicon PIN diodes and the Kodak Direct Exposure film (DEF) placed around the laser focal point. Initially, PIN diodes are employed for focal scan measurements in order to determine the location for the maximum hot electron signal. The focal scan measurements were performed by translating the focusing objective along the incident laser direction to different positions, in front and behind the best focus position. The best focus position was defined as the location for the maximum hot electron signal. The same experimental setup shown in Figure 3.7 is employed to measure the hot electrons with one more PIN diode located on the direction of the X-ray spectrometer. The PIN diodes were filtered with a thin metal foil to prevent the exposure from stray light and low-energy electrons. Once the location of the best focus was determined, DEF filmstrips are used to measure the hot electron angular distribution. This film has an emulsion on both sides of a plastic substrate. The properties of the film are determined in Ref. [84]. The geometry used to measure the hot electrons emitted outwards from the plasma is depicted in Figure 3.16. DEF filmstrips were placed around the focal spot region and covered in 33 μm thick aluminum foil to prevent exposure from stray light and low-energy electrons. For both *p*- and *s*- polarized laser pulses, the film strips were placed both above the objective and in the lateral positions as shown in the Figure 3.16. To allow for better viewing, the lateral DEF film strips appear transparent in the figure.

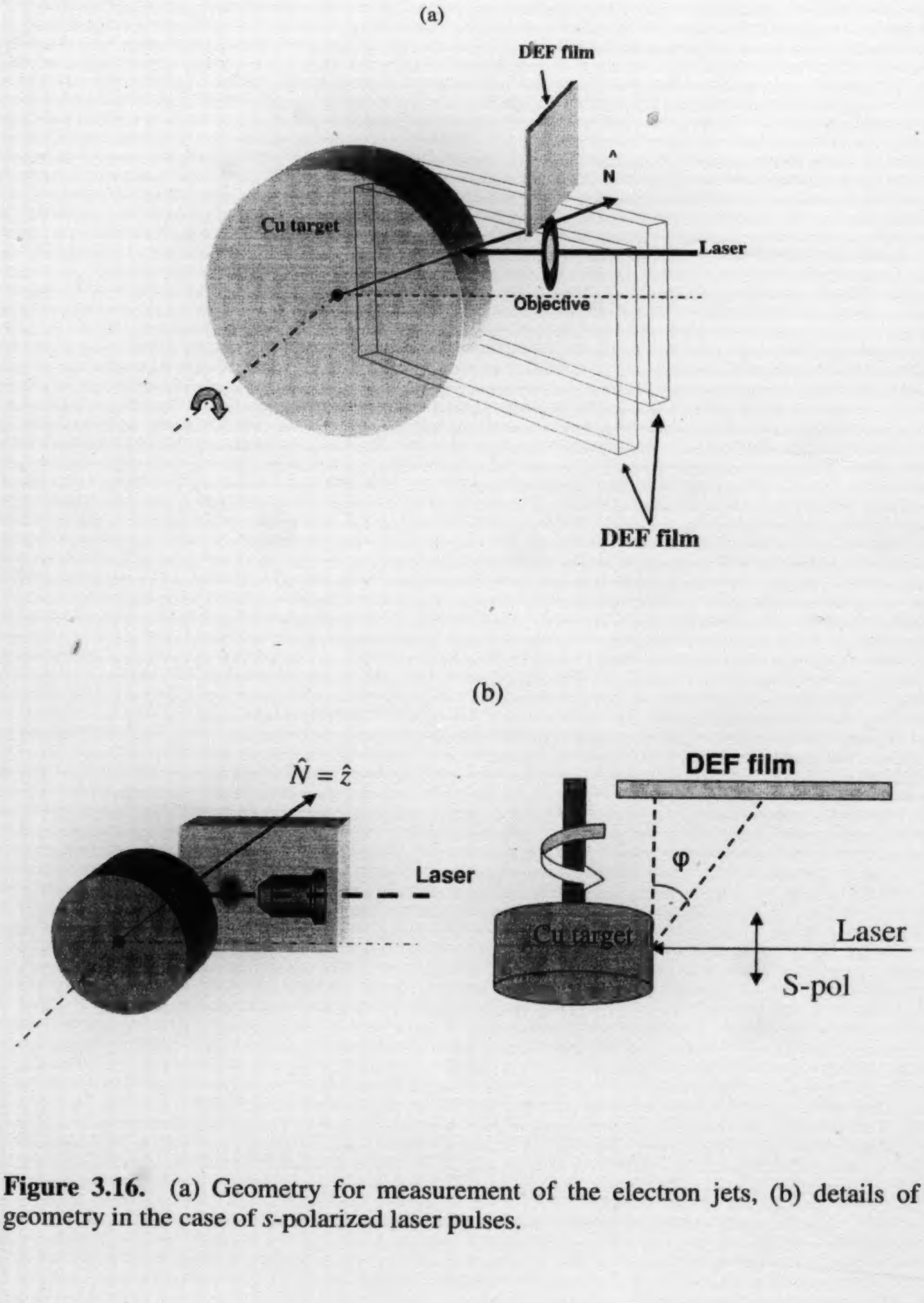
(a)
DEF film
N
Cu target
Laser
Objective
DEF film
(b)
$\hat{N} = \hat{z}$
Laser
DEF film
φ
Cu target
Laser
S-pol

Figure 3.16. (a) Geometry for measurement of the electron jets, (b) details of the geometry in the case of *s*-polarized laser pulses.

For *p*-polarized laser pulses, additional measurements of the emission direction of hot electrons with energies over 80 keV emitted outward from plasmas are performed for four different angles of incidence, i.e. 30°, 36°, 42° and 65°. A filtered PIN diode is used to measure the hot electron emission for different angles in the plane of incidence. In this way, the angular distribution of >80 keV electrons is studied under different angle of incidence conditions. A schematic of the experimental geometry is displayed in Figure 3.17.

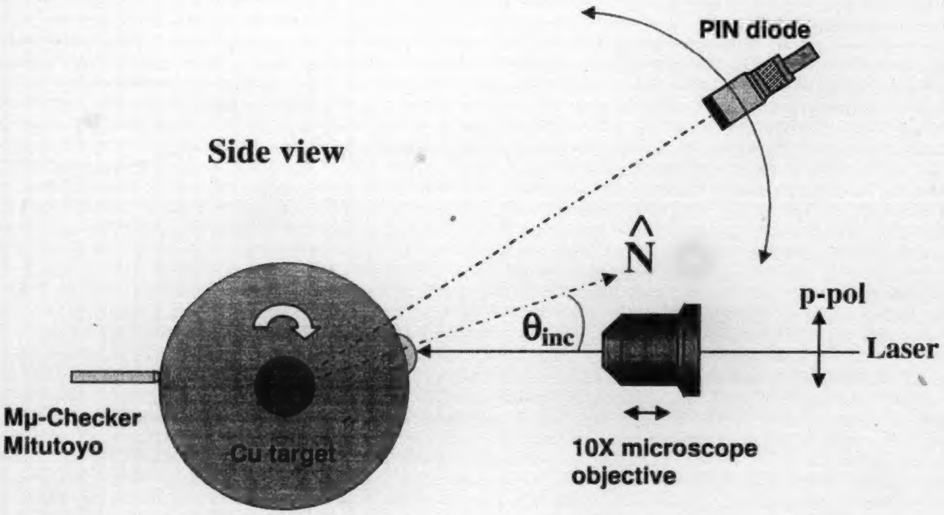
PIN diode
Side view
$\hat{N}$
θ_{inc}
p-pol
Laser
Mμ-Checker
Mitutoyo
Cu target
10X microscope
objective

Figure 3.17. Side view of the experimental geometry employed to determine the angular distribution of the hot electrons.

Chapter 4

X-RAY EXPERIMENTAL RESULTS AND DISCUSSION

4.1. Study of K_α X-ray emission in single shot mode

For the development of the K_α X-ray source, quantitative assessment of the X-ray conversion efficiency is needed for various working conditions. Several parameters have to be analyzed in order to obtain the optimum regime giving large absorption of the laser pulse into the solid target, and efficient generation of fast electrons, which in turn produces the K_α X-rays. The X-ray conversion efficiency has been analyzed for various parameters such as laser intensity, prepulse, angle of incidence, and background pressure. These studies have been carried out in single shot mode. Both the flat target consisting of a 500 nm copper film sputtered onto a silicon wafer and the Cu rotating disk have been used throughout this study. Results obtained for different laser repetition rates will be presented in the next section.

First, for each set of experiments, the K_α X-ray signal is measured as a function of the target position in order to determine the location for maximum X-ray signal. The focal-scan measurements are performed by translating the focusing objective along the incident laser direction to different positions in front of and behind the best focus position. The best focus position is defined by the location for maximum X-ray signal. The X-ray emission measurements have been done in two different prepulse regimes of 10^{-1} and 5×10^{-4}. Two angles of incidence have been used, smaller angles of 22°-24° and larger of 42°-45°. The variation of laser intensity has been obtained from the two different microscope objectives of 4X and 10X. The measurements have been carried out both in vacuum and in air.

X-ray focal scans are shown in Figure 4.1, Figure 4.2 and Figure 4.3 for different laser parameters. The X-ray focal scans are obtained with 10^{-1} and 5×10^{-4} prepulse contrast ratios for similar angles of incidence. Silicon PIN diode X-ray detectors filtered with various filters have been employed for these X-ray measurements. In some of the measurements, two permanent magnets with magnetic fields of 0.15-0.3 T were used to check whether fast electrons contributed to the measured signals by preventing them from hitting the detectors. Tests conducted with and without magnetic shielding indicated the contribution of hot electrons to the signal from unshielded detectors is small (<20%) for the geometries used here. Different foils (aluminum, nickel and iron) of various thicknesses are used as filters to measure the X-ray emission in different regions of the spectrum. The different PIN diode response functions combined with the transmission of filters used in these experiments are shown in Figure 3.9 and 3.10 (p. 69-70).

The focal scans exhibit an asymmetric behavior with respect to the best focus position for smaller angle of incidence (22°-24°) as seen in Figure 4.1 and Figure 4.2 regardless of the difference in the experimental conditions such as different laser intensity, vacuum versus air or different prepulse contrast ratios. The extended tails of emission when the focal point lies outside of the target might be explained by the interaction of the main pulse with the plasma formed by the prepulse. The extended tail is shorter in length for larger angles of incidence as can be seen in Figure 4.3, which is to be expected since the plasma expansion occurs preferentially normal to the target surface.

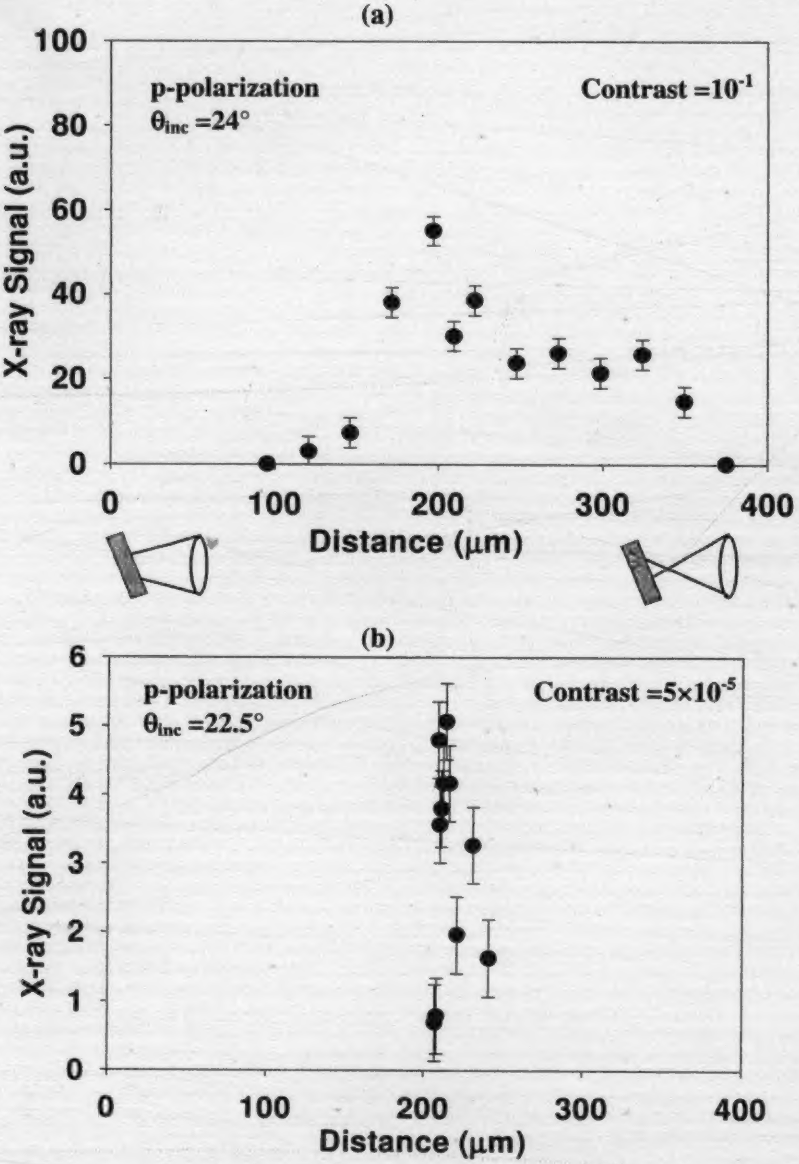

Figure 4.1. X-ray focal scans obtained in air for two different prepulse regimes when using the 4X microscope objective with p-polarized laser light at an energy of about 210 μJ incident on the target for similar angles of incidence: (a) with a prepulse contrast ratio of 10^{-1} and a angle of incidence of 24°; (b) with a prepulse contrast ratio of 5×10^{-4} and a angle of incidence of 22.5°. The x-axis scale is not related between the two plots.

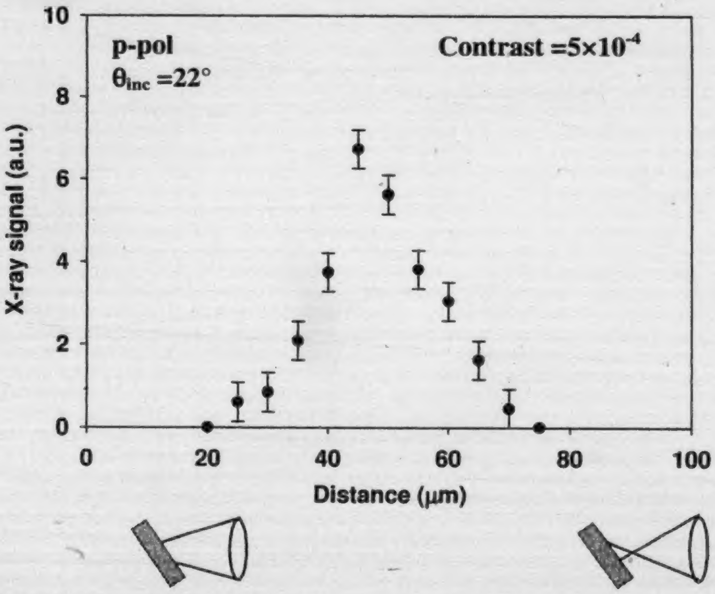

Figure 4.2. X-ray focal scans obtained when using the 10X microscope objective at an energy of about 160 μJ incident on the target with p-polarized laser light, a prepulse contrast ratio of 5×10^{-4} and a angle of incidence of 22° in air.

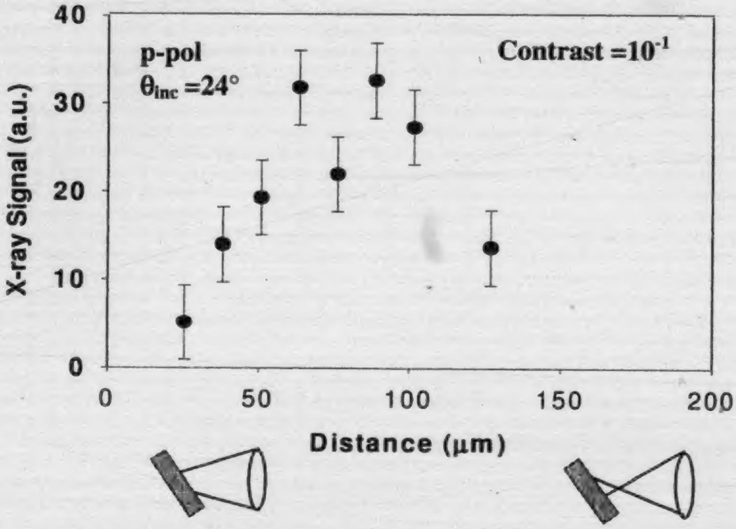

Figure 4.3. X-ray focal scans obtained when using the 4X microscope objective at an energy of about 210 μJ incident on the target with p-polarized laser light in air, a prepulse contrast ratio of 10^{-1} and a angle of incidence of 42°.

In Figure 4.4 we can see the SEM images of the resultant craters in the copper film coated onto a silicon wafer from laser pulses with energies of about 250 μJ.

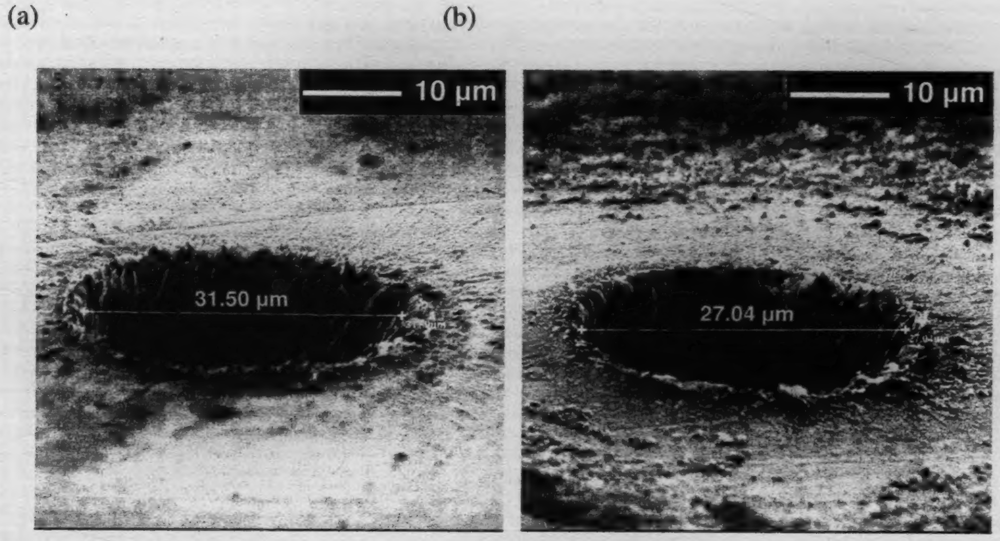

Figure 4.4. SEM images of the resultant craters of copper film coated onto a silicon wafer from laser pulses with energies of about 250 μJ in air.

When working in air with *p*-polarized light incident on the target at 24° angle of incidence and using the 4X microscope objective, the threshold energy for obtaining a detectable X-ray signal is around 180 μJ for a prepulse contrast ratio of 10^{-1}. The X-ray signal increases rapidly with energy and then saturates as shown in Figure 4.5 (a). The saturation might be explained by either a too large a prepulse or air breakdown with subsequent plasma shielding. Similar experiments are carried out using the 10X microscope objective on copper film with a prepulse contrast ratio of 5×10^{-4}. A threshold energy of around 20 μJ is observed in this case as shown in Figure 4.5 (b).

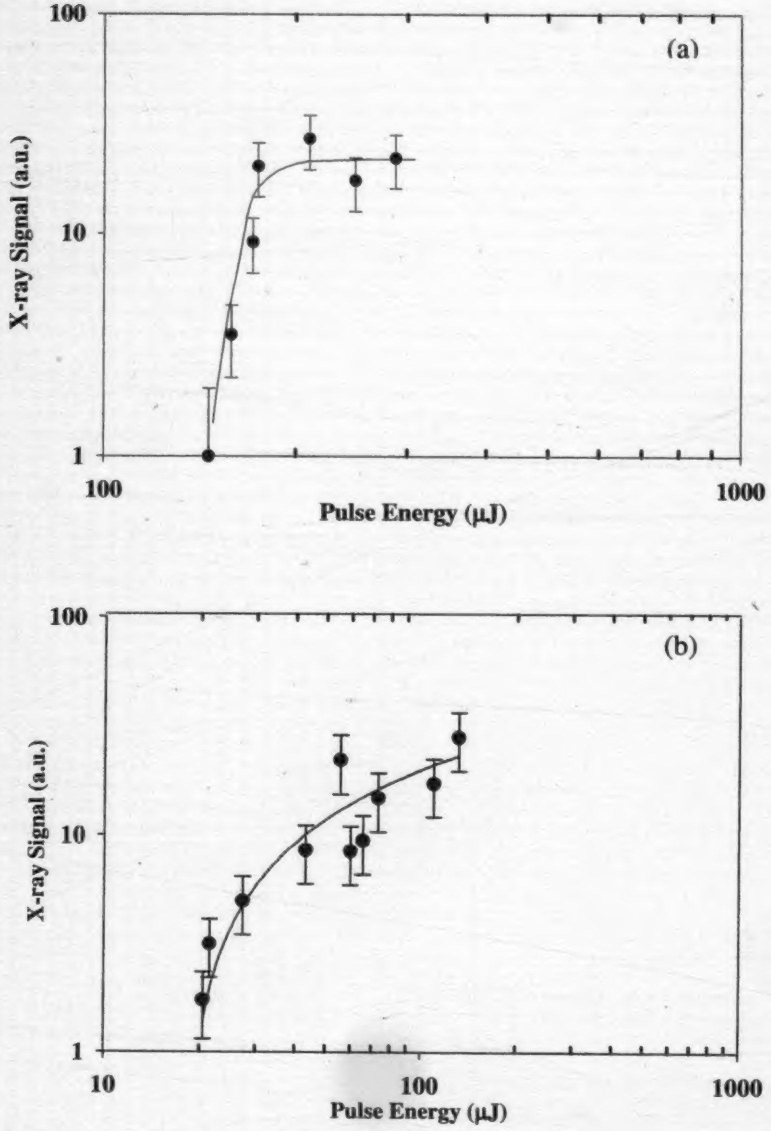

Figure 4.5. X-ray signals measured in air from copper film on silicon target. The X-ray signal rapidly increases with laser pulse energy and eventually saturates. (a) for a prepulse contrast ratio of 10^{-1} using the 4X microscope objectives. (b) for a prepulse contrast ratio of $5x10^{-4}$ using the 10X microscope objectives. The lines are drawn as a visual aid.

The ratio of transmission through various foil thicknesses has been measured in order to establish the photon energy of the X-rays observed in these experiments. The reduction in X-ray signals transmitted through aluminum foils of different thicknesses: 62.5 μm, 95 μm, and 125 μm in air have been measured. For comparison, the ratios of X-ray signals as a function of aluminum filter thicknesses, normalized to the 62.5-μm-thick foil, for various X-ray radiation energies have been computed. The results are plotted in Figure 4.6. The error bars represent the shot-to-shot variations in the data. Comparing the calculated curves with the measured data one can conclude that the results are consistent with the expected 8 keV K_α radiation from copper.

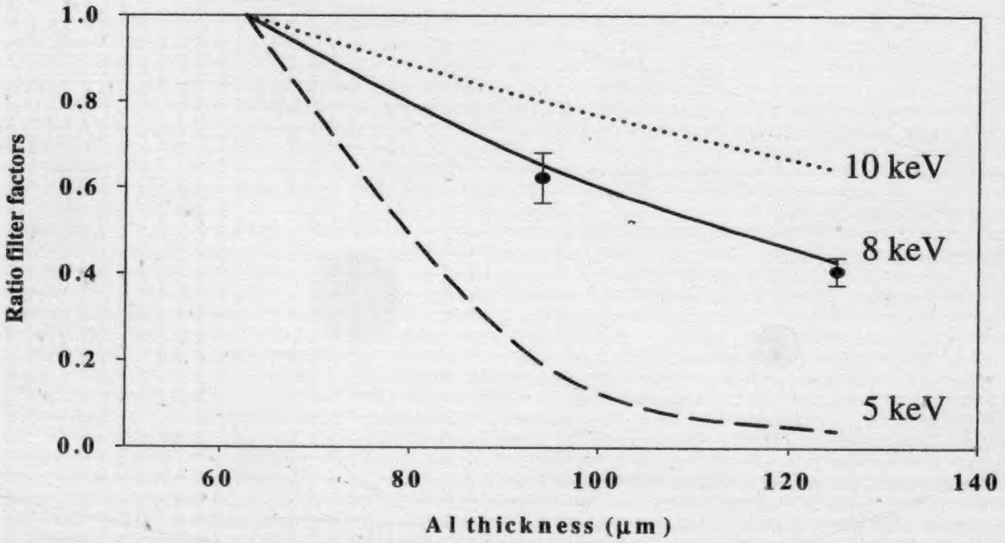

Figure 4.6. Measured reduction in X-ray signal transmitted through aluminium foil filters (normalized to the signal through a 62.5 μm-thick aluminum foil) versus filter thickness. The circles represent the experimental data and the lines represent calculated ratios for different photon energy X-rays.

Next, the influence of background pressure was investigated. In Figure 4.7 one can see the results from a series of experiments on the scaling of X-ray conversion efficiency into Cu K_α versus nitrogen pressure. The X-ray conversion efficiency into Cu K_α radiation, i.e. the efficiency of conversion of laser energy into Cu K_α X-ray energy, is calculated in 2π sr solid angle, on the assumption of isotropic emission into 2π sr. The measurements are based on the PIN diode signals with 15 μm Ni + 9 μm Al. The X-ray conversion efficiency into Cu K_α has an average value of about 1.3×10^{-5} for a large range of pressure values, from vacuum to approximately 50 torr, but it drops by approximately one order of magnitude when the background pressure increases to atmospheric pressure.

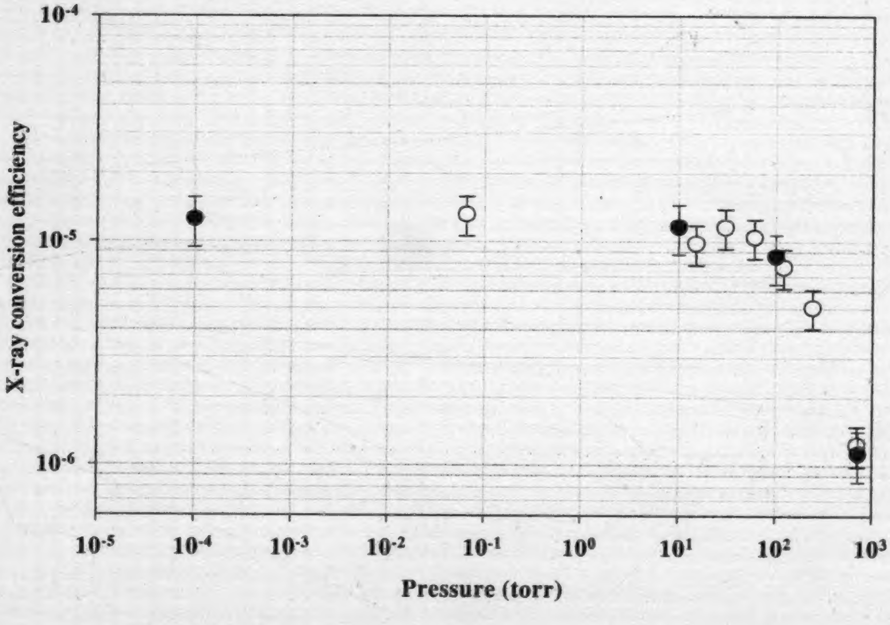

Figure 4.7. The X-ray conversion efficiency as a function of background ambient gas pressure. The 8.0 keV Cu K_α X-ray signals were detected using X-ray PIN diodes filtered with a 15 μm Ni + 9 μm Al and 25 μm Fe filter Ross pair. The two different data points are from two different measurements. Data was taken with the 10X objective at $\theta_{inc}=22°$.

At atmospheric pressure, the air breakdown is observed. This is expected as the threshold intensity is observed experimentally for laser intensities on the order of few times 10^{13} W/cm^2 [85]. Because of the plasma (air breakdown) formed in front of the copper target it is expected that the incident laser intensity would be smaller on the target due to absorption losses in the plasma. Also, refractive index gradients due to ionization of the air will cause defocusing of the beam leading to larger focal spots. Using a calibrated power meter (SpectraPhysics, model 407A) the absorption due to the air breakdown at a range of energies from 140 μJ to 300 μJ was measured to be about 5±1.6% when using a 10X objective. The power meter was placed after the air breakdown before the laser beam spread too much, so that the transmitted beam was totally captured by the power meter aperture and no significant clipping occurred. The loss of energy due to the air breakdown is too little to explain the decrease in the X-ray signal. However, the decrease in the X-ray conversion efficiency might be explained by the decrease in the laser intensity incident on the copper target, which might be due to refraction. A few research groups have reported defocusing of a laser pulse in underdense plasmas created with different gases [85, 86] due to refraction. This would deflect the incoming light from its initial path and thus, the peak intensity will be considerably less than the peak laser intensity achieved in vacuum for the same laser pulse energies. Li et al. [85] have shown that the incident laser light will be considerably deflected by the refractive index gradients set up by the electron density leading to lower peak laser intensity. The X-ray signal varies strongly with laser intensity as shown in Figure 4.5 (p. 85) and, thus, lower laser intensity will generate less X-ray photons. Another factor that can strongly influence the X-ray emission is the plasma density gradient. In air, the preplasma formed initially by the nanosecond prepulse may not expand as much as it would in vacuum conditions because of the air pressure. As a result, the hot electron distribution may be changed and accordingly the X-ray emission.

Usually, laser produced X-ray studies have been carried out in vacuum defined by a pressure of ~ 10^{-6}-10^{-5} torr, but keV X-ray emission from solid targets can be generated in ambient air background as well [17]. Figure 4.7 indicates that the X-ray conversion efficiency stays constant up to pressures of 50 torr. This is an interesting case because the X-ray source may be simplified considerably if the need for relatively high vacuum is eliminated. For instance, two pumps and two pressure gauges are needed to evacuate the chamber to a pressure of 10^{-6}-10^{-5} torr, while only one pump and one gauge, is necessary to achieve 50 torr. Moreover, while the number of X-ray photons obtained in ambient air background is ten times lower than the one obtained for pressure lower than 50 torr, this might be enough for some applications where only one event can be processed per laser pulse (e.g. pulse height analysis). In this case, the need for a vacuum chamber and vacuum system can be eliminated. Another benefit for working at higher pressure, especially in air, is the inhibition of target debris, as the presence of gas will slow down the material removed from the target.

As discussed in the previous section the K_α X-ray spot size is measured using the penumbral knife-edge technique, where the shadow of a sharp edge is projected onto DEF X-ray film. A diagram of the experimental setup used for this technique is shown in Figure 3.15 (p. 75). To determine the source size of the Cu K_α X-ray emission, a Gaussian spot emission was assumed. Because the penumbra shadow image of the knife-edge on the film contains 1D information on the X-ray source spatial profile, the intensity can be described by the following equation:

$$I(x') = I_0 \exp\left(-\frac{2(x')^2}{(\omega'_{ox})^2} \right) \qquad \textbf{(4. 1)}$$

Using the diagram in Figure 4.8, the recorded signal on the film at point M is given by:

$$S_M = I_0 \int_{x'_N}^{+\infty} \exp\left(-\frac{2(x')^2}{(\omega'_{ox})^2} \right) dx' \qquad \textbf{(4. 2)}$$

where ω'_{ox} is the X-ray beam waist in the x-direction, and $x'_N = \frac{a}{b} x_M$.

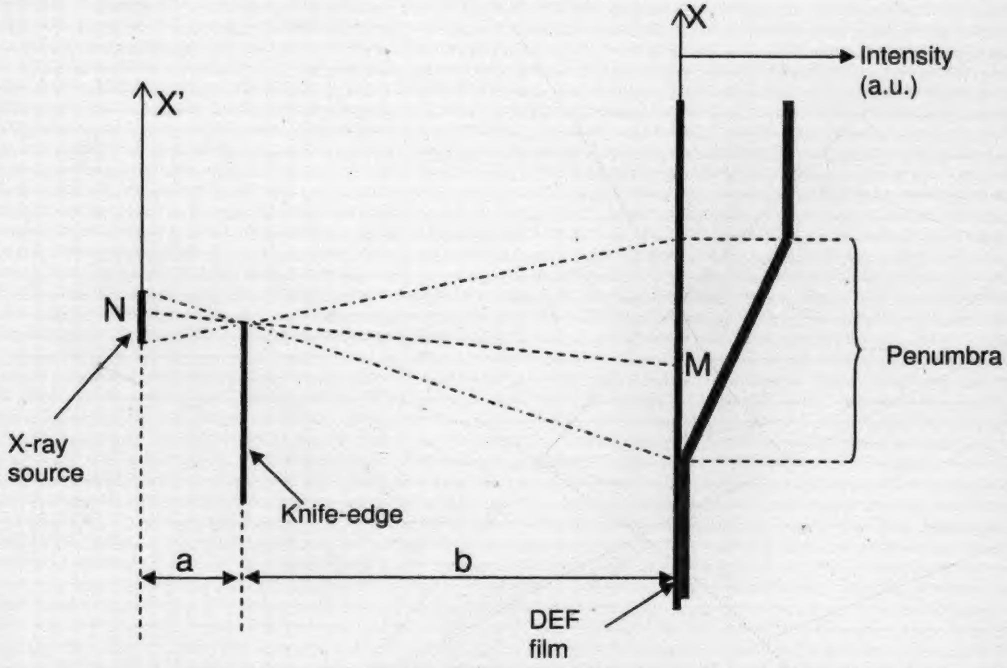
X
Intensity (a.u.)
X'
N
M
Penumbra
X-ray source
Knife-edge
a
b
DEF film

Figure 4.8. A schematic diagram of the knife-edge technique

The complementary error function, denoted by *erfc(x),* is defined in terms of the error function, *erf(x)* :

$$erfc(x) = 1 - erf(x) = \frac{2}{\sqrt{\pi}} \int_x^{+\infty} \exp(-t^2) dt \qquad \textbf{(4. 3)}$$

Using equation (4.3) and magnification ratio, $R = \frac{b}{a}$, the signal recorded on the film is given by:

$$S(x) = A\left[1 - erf\left(\frac{\sqrt{2}}{\omega'_{0x}} x'\right)\right] = A\left[1 - erf\left(\frac{\sqrt{2}}{\omega'_{0x}} \frac{a}{b} x\right)\right] = A\left[1 - erf\left(\frac{\sqrt{2}}{\omega_{0x}} x\right)\right] \qquad \textbf{(4. 4)}$$

where A is a constant ($2A = S_{max}$ represents the maximum signal) and $\omega_{0x} = \omega'_{0x} \frac{b}{a}$.

The results are presented in Figure 4.9. The spot size diameter at full width half maximum is determined from least squares fit of the experimental values with the theoretical model given by equation (4.4) and found to be 8.3±1.3 μm averaged over thousands of shots. The spatial resolution of the penumbral imaging is limited by the inaccuracy of the knife-edge shape. The spatial resolution is estimated to be 2 μm. In the present setup, since the X-ray spot is viewed at an angle of 38° relative to the target normal, the axial wobble of the target positioning system, which was approximately ± 5 μm, also contributes to the measured spot size and the actual emission spot size may be somewhat smaller.

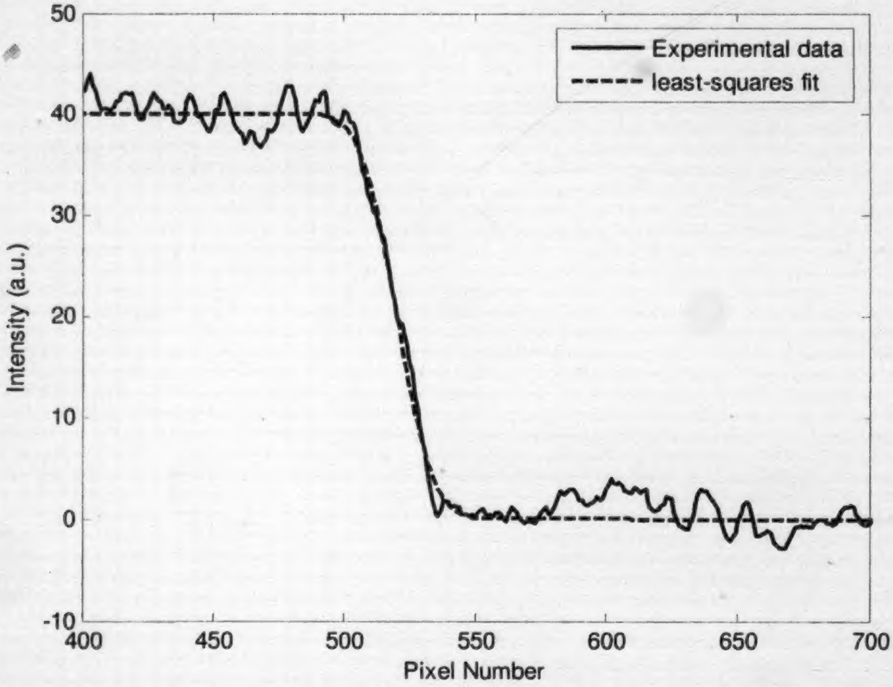

Figure 4.9. The scan of the DEF film at the location of the penumbra. The DEF film is the X-ray detector employed to measure the K_α X-ray source size using the knife-edge technique. The knife-edge is a 25 μm Fe filter located 7 mm from the source. Due to its K-edge absorption edge at 7.11 keV, the filter completely blocks the Cu K_α 8.05 keV radiation. The DEF stripfilm is located 147 mm away from the knife-edge. The scanned region was a strip 300 μm wide on the film.

As seen previously, for 800 nm laser pulses, the laser spot size at FWHM is measured to be 2.24 μm if the Mitutoyo 10X microscope objective is employed to focus the laser pulses as is the case for K_α X-ray spot size measurements. Therefore, the K_α X-ray spot size is a factor of 3.7 times larger than the laser spot size. This result is similar to the one obtained by Eder et al. [14]. They obtained a K_α X-ray spot size a factor of about 4 times larger than the laser spot size for a prepulse contrast ratio of 10^{-4}

(similar to the one in the current measurement) and an incident laser intensity of about 10^{17} W/cm^2. However, their spot sizes were much larger being 10 μm for the laser focal spot and 40 μm for the X-ray source size. Because the preplasma is not very large in their experiments as well, they explain that the large spot size of K_α emission is due to the complex orbits of the hot electrons. In the case of very low or no prepulse, the hot electrons near the center of the laser spot leave the surface and return to it due to electrostatic forces at a significant distance from the laser spot. This is also supported by other measurements performed with longer pulse duration [87]. Kieffer et al [87] measured a long duration of K_α emission, which is explained by longer trajectories of the hot electrons re-entering the surface at significant distances from the laser central spot size. Another contribution to the large K_α emission can be associated with the low-intensity wing surrounding the hot central spot that can produce cooler electrons than the ones from central part of the laser spot, but still able to create K_α emission [14]. However, this mechanism would be most effective if the central peak intensity already is above the optimum intensity for maximum K_α conversion efficiency.

A summary of the measured conversion efficiency for the cases presented up to now is displayed in Figure 4.10. All results are reported in terms of energy conversion efficiency into 2π sr assuming isotropic emission. The measurements made with the 4X microscope objective in air show well over an order of magnitude increase in X-ray yield when a prepulse of 10^{-1} is employed compared to when a prepulse of $5\text{x}10^{-4}$ is employed. The measurements made at around 22° angle of incidence indicate slightly higher X-ray yields than those made at around 42-45° angle of incidence. While such an angular dependence might be indicative of an interaction with the critical density region in the presence of a density gradient scale length of the order of a wavelength, via resonance absorption, further studies are required to clarify this angular dependence. The increase in X-ray yield obtained with 10^{-1} prepulse contrast compared to the 5×10^{-4} contrast indicates that the preplasma plays a role in the optimum generation of the hot electrons. Such an increase in X-ray yield with prepulse energy has already been reported in the past [6] for the generation of aluminum and iron K_α radiation. However, a higher level of preplasma may lead to an increase in the X-ray pulse duration and size [14], which is undesirable for some applications. When comparing cases for X-ray generation at the higher contrast of 5×10^{-4} with ambient background gas at atmospheric pressure, higher X-ray yield was obtained at higher intensities of 5×10^{16} W/cm^2 when using a 10X objective than the 4X objective.

Finally, comparing the X-ray yield when working in vacuum versus ambient pressure nitrogen, a 10 times increase in X-ray conversion efficiency is observed at 5×10^{-4} contrast ratio using the 10X microscope objective.

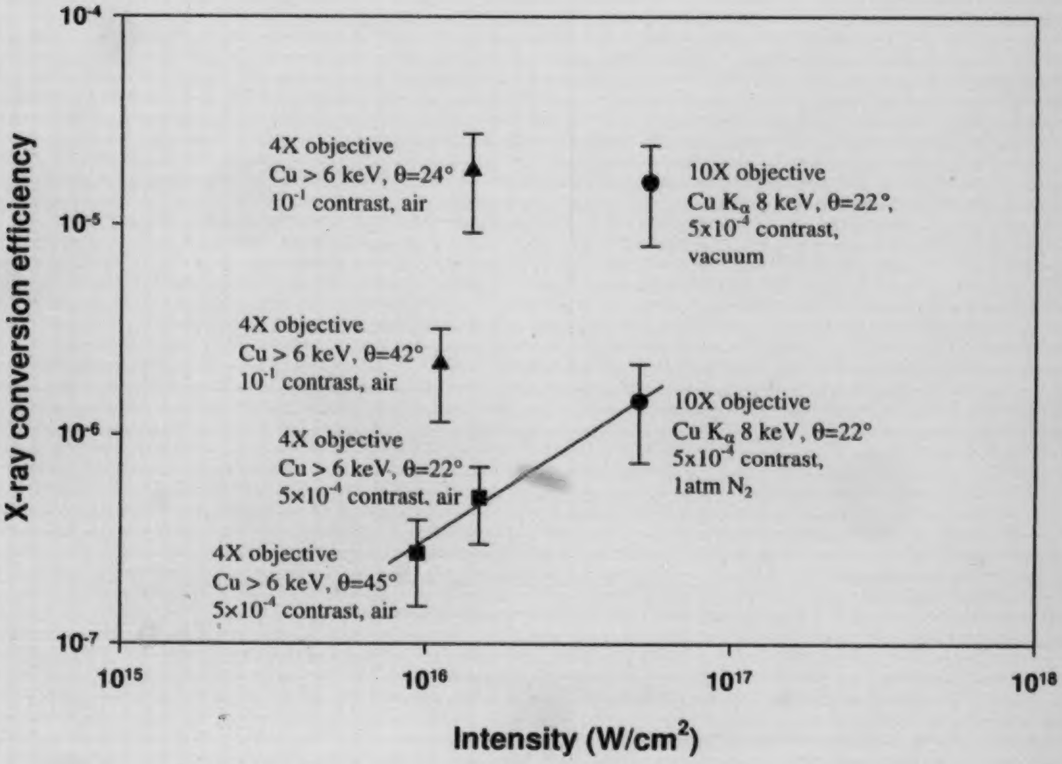

Figure 4.10. Summary of the X-ray experimental results. The solid squares represent the results from 4X objective on copper film and the solid circles for the 10X objective on a bulk target for a contrast of $5x10^{-4}$ and p-polarized incidence. The solid triangles are for the case of the 4X objective on copper film for 10^{-1} contrast and p-polarized incidence. The measurements with the 4X objective were taken with a simple 62.5 μm aluminum filter while those for 10X objective were taken using the Ross filter pair. The solid line is a visual aid to connect the data points corresponding to $5x10^{-4}$ contrast taken at 1 atm pressure.

4.2 K_α X-ray source operated at kilohertz repetition rate

This section describes the experimental results obtained at high laser repetition rates. In preparation for the K_α X-ray source operation at 1 kHz repetition rate the X-ray conversion efficiency versus laser firing frequency has been investigated. In addition, the hot electron temperature has been analyzed based on the continuum X-ray bremsstrahlung spectrum. All the measurements presented here are performed with p-polarized radiation at an angle of incidence of 30° relative to the target normal. The 10X microscope objective (Newport) was used throughout these measurements. The experiments were conducted in vacuum, using a prepulse ratio of 5×10^{-4}.

Samples of X-ray spectra are presented in Figure 4.11 and Figure 4.12. Each spectrum consists of mainly two strong lines corresponding to the K_α (8.05 keV) and K_β (8.91 keV) lines of Cu with a small fraction of bremsstrahlung radiation. The K_α X-ray flux is determined using the counts recorded under the line at 8.05 keV, between 7.51 keV and 8.48 keV on the spectrum as shown by the dotted lines in Figure 4.11 (a) and Figure 4.12 (a). The spectrum displayed in Figure 4.11 was acquired in 63 seconds using laser pulse energies of 275 μJ at 1 kHz repetition rate. The K_α X-ray flux was $5.4\pm1.2\ \times10^9$ photons/s resulting in a conversion efficiency of $2.5\pm0.6\ \times10^{-}5$. This is calculated in 2π sr solid angle assuming an isotropic X-ray emission into 2π sr. The spectrum displayed in Figure 4.12 was acquired in 58 seconds using laser pulse energies of 290 μJ at 1 kHz repetition rate. The K_α X-ray flux was $6.7\pm1.5\times10^9$ photons/s or $1.1\pm0.2\ \times10^9$ photons/sr/s as measured by the Amptek detector resulting in a conversion efficiency of $3.2\pm0.7\times10^{-5}$.

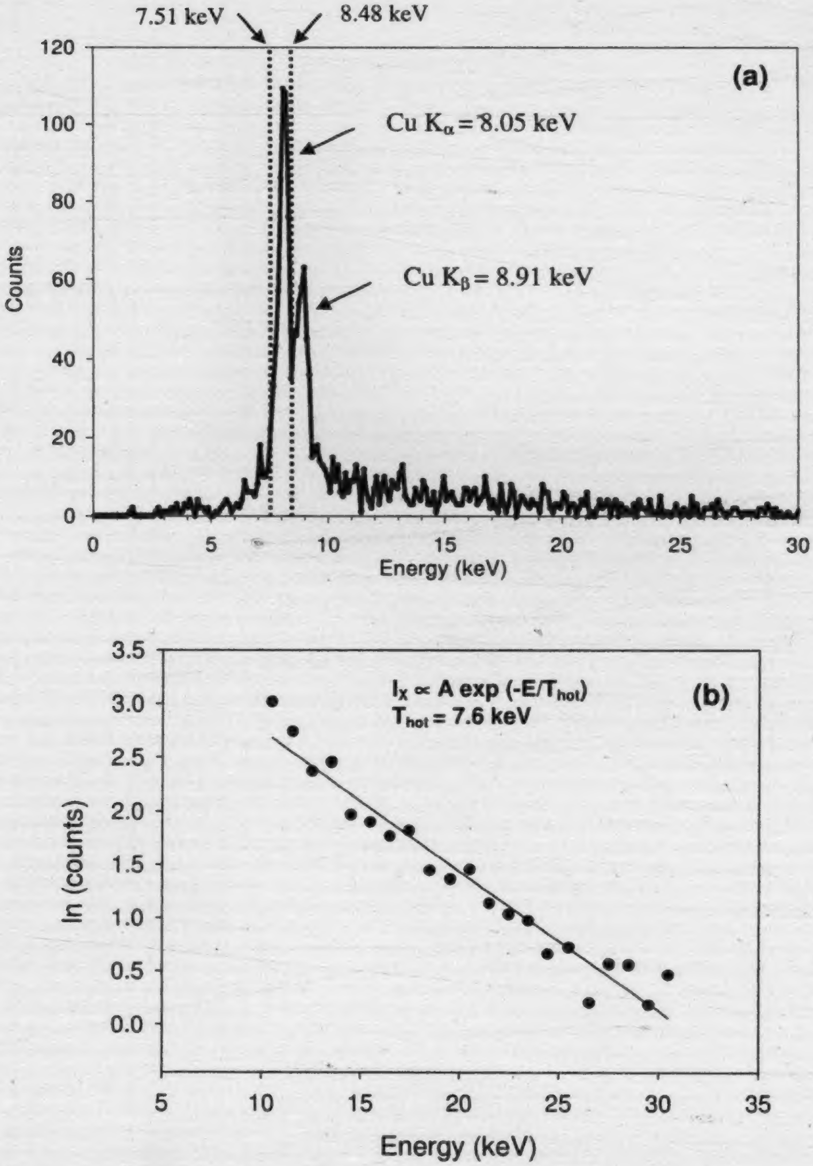

Figure 4.11. (a) Raw Cu X-ray spectrum obtained with CdTe detector from 275 μJ femtosecond laser pulses at 1 kHz repetition rate. The spectrum was recorded in 63 seconds. (b) The signal from the high-energy tail has been fitted by a Maxwellian electron distribution and the hot electron temperature has been found to be $T_h = 7.6 \pm 0.5$ keV. Only the X-ray bremsstrahlung signals with energies in the range of 10.5 keV to 30 keV have been considered for the fit.

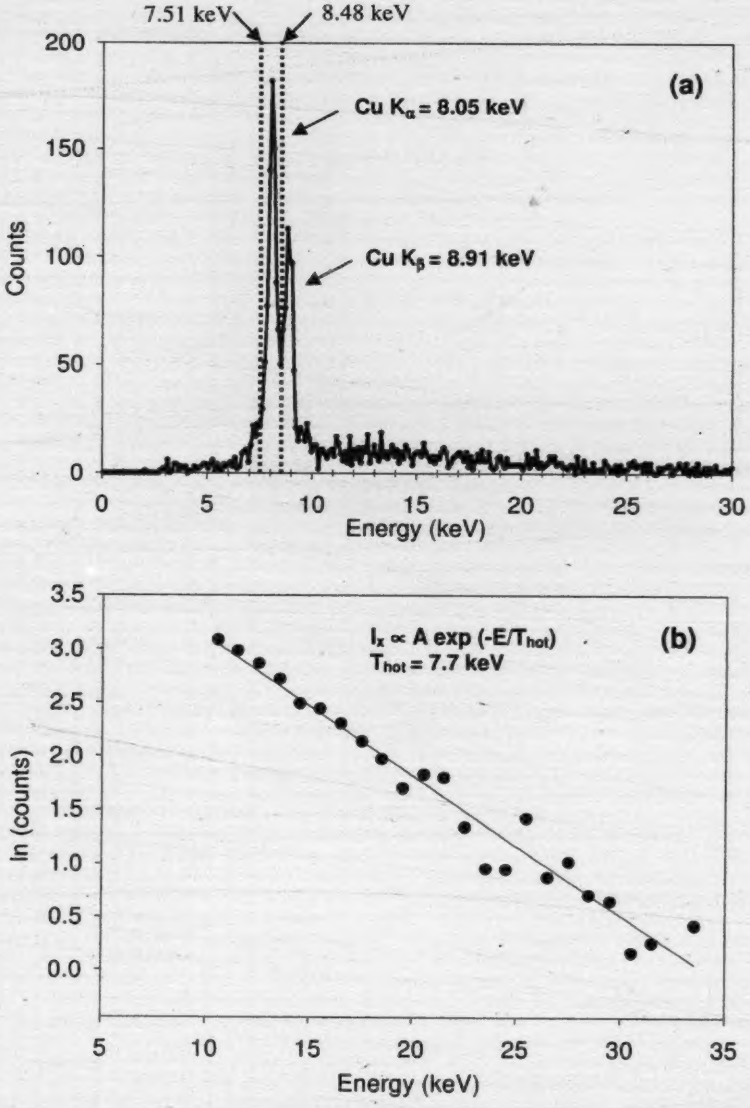

Figure 4.12. (a) Raw Cu X-ray spectrum obtained with CdTe detector from 290 μJ femtosecond laser pulses at 1 kHz repetition rate. The spectrum was recorded in 58 seconds. (b) The signal from the high-energy tail has been fitted by a Maxwellian electron distribution and the hot electron temperature has been found to be $T_h = 7.7 \pm 0.4$ keV. Only the X-ray bremsstrahlung signals with energies in the range of 10.5 keV to 30 keV have been considered for the fit.

The yield of detected K_α X-rays per laser pulse was measured to be almost constant for different laser repetition rates. Starting from single shot mode, which clearly ensures a pristine surface target, the K_α X-ray conversion efficiency per pulse is $4.3 \pm 0.5 \times 10^{-5}$ and decreases to $2.8 \pm 0.5 \times 10^{-5}$ for 1 kHz repetition rate as seen in Figure 4.13. The data for single shot mode was taken with a PIN diode filtered with 15 μm Ni + 9 μm Al and corrected using a calibration factor to convert to the signal levels seen by the Amptek detector. The calibration factor was determined from the high repetition runs taking the ratio of the Amptek K_α signal to the average of the PIN diode signals. The data for repetition rates of 50 Hz and higher was based on the Amptek K_α signal integrated in the region from 7.51 keV to 8.48 keV. The raw X-ray signals measured by the filtered PIN diode were up to factor of 2 times higher than the Amptek K_α signal and thus the calibration factor was used to scale to Amptek equivalent K_α reading for consistency with the higher repetition rate data. This small decrease may be attributed to various factors like the target vibration at the faster rotation speeds leading to partial overlapping of the laser ablation spots, and the contribution from the residual target debris plume from one shot interfering with the subsequent laser pulse at high repetition rates. Further investigation will be required to resolve this issue.

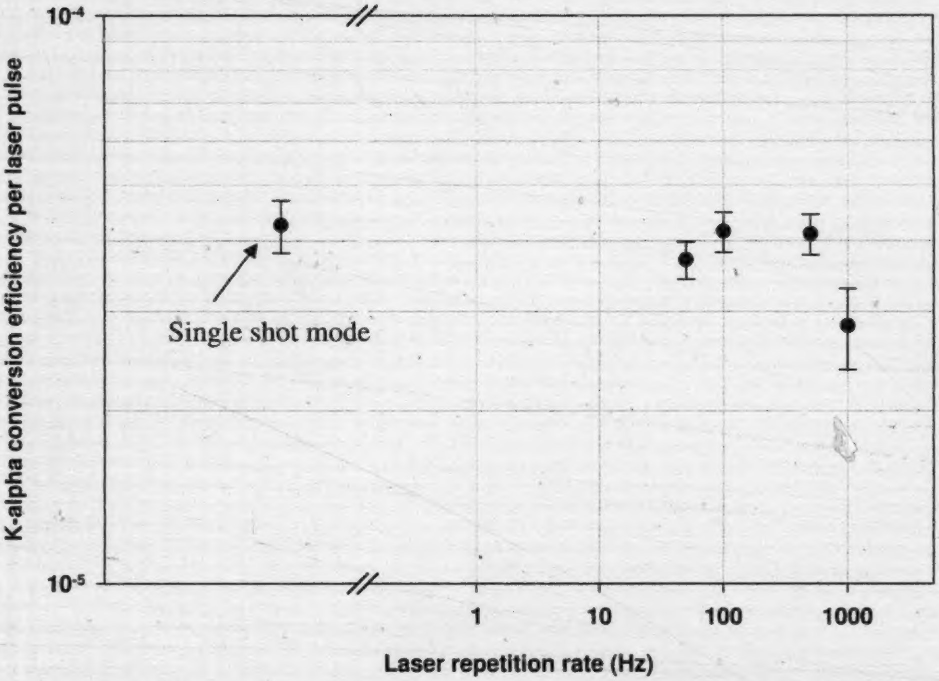

Figure 4.13. Cu K_{α} X-rays conversion efficiency generated for different laser repetition rate. P-polarized laser pulses with energies of 200-300 μJ have been employed and focused with the 10X objective onto the rotating disk copper target at an angle of incidence of 30°.

A higher conversion efficiency of almost four times was measured in single shot mode during these experiments. This may be attributed to the differences in the experimental settings used for the measurements presented in this section compared to the ones presented in the previous section. For instance, it is possible that the fraction of absorbed laser energy is higher for the angle of incidence of 30° than the one used previously at 22° for the same prepulse contrast ratio of 5×10^{-4}. In addition, a different 10X microscope objective (Newport) was employed for these measurements as compared to the previous ones where a 10X microscope objective (Cooke) was used. Although they have similar focal length and numerical aperture, they may focus the laser pulses differently leading to uncertain values for the laser intensity, which is a key parameter in the generation of the K_α X-ray photons. In addition, some damage in the Cooke objective was noticed at the end of the previous measurements, which also could lead to a degraded focal spot and reduced K_α conversion efficiency.

This is the highest K_α X-ray flux reported for kHz sources from sub-millijoule laser pulses. This is more than 500 times higher than the one reported by Hagerdon et al. [18] also from sub-millijoule laser pulses at 1kHz repetition rate for a similar target system and similar laser energy per pulse. The laser intensity used in these experiments is 100 times higher than in reference [18] and it is in the optimum intensity range for Cu targets [71] explaining the higher conversion efficiency in our experiments. It is predicted that the K_α yield from copper bulk targets is optimum for laser intensities in the range of about 10^{16}-10^{17} W/cm^2 for high contrast laser pulses [71]. Other types of laser-produced plasma hard X-ray sources operated at kHz repetition rate have been designed using different kinds of targets such as tape targets [19], thin wire targets [20], and liquid jet targets [21,22]. Jiang et al. [20] reported much lower conversion efficiencies of 10^{-8} into Cu K_α than those measured here using laser intensities of 10^{17} W/cm^2. Perhaps, this could be explained by their higher contrast ratio of 10^{-7} and the fact that they only moved the target a fraction of the focal spot between the shots. Conversion efficiencies of 6×10^{-8} and 9×10^{-6} have been reported for the higher energy 9.2 keV Ga K_α line by Korn et al. [21] and Zhavoronkov et al.[22], respectively. These K_α sources have been obtained using liquid-metal Ga jet as a target for laser plasma. Sources of K_α with a conversion efficiency of 6.3×10^{-6} have also been obtained using ferric audio tape targets [19] using a large prepulse. However, both tape and liquid targets offer a more limited range of materials, which can be used, and thus limited tuning range for a K_α X-ray source.

All the other experimental investigations on K-shell emission from solid metal targets have been performed using much higher laser pulse energies from several to hundreds of millijoules, and at low repetition rate. Comparing to these measurements, we find that our results are in line with those of Rousse et al. [6]. They obtained a conversion efficiency of 3.4×10^{-5} for the 6.4 keV Fe K_α emission at an intensity of 3×10^{16} W/cm^2, with an optimized prepulse (0.7 J/cm^2) of amplified spontaneous emission (ASE) close to damage threshold of the material. Eder et al. [14] reported a much higher conversion efficiency of 4×10^{-4} at much larger energy of 200 mJ per pulse and an intensity of nearly 10^{17} W/cm^2 for 200 fs duration pulses. Intrinsic prepulses and a pulse pedestal on the 10^{-4} level were present in their experiments. The interaction of the main laser pulse with preplasma can change the amount of laser absorption and the hot electron distribution.

It is worth mentioning here that Sjögren et al. [81] have also reported a very high conversion efficiency of 6×10^{-4} from a broadband X-ray source working at kHz repetition rate. However, this is for bremsstrahlung emission integrated over the broadband spectrum. All these previously reported results have various focal spot conditions and varied degrees of preplasma and clearly, the level of preplasma is an important parameter in the efficiency of K_α generation.

Generally, the plasma electrons can be characterized by two electron temperatures; the low-temperature thermal electrons, which create only very low energy XUV radiation and high-temperature electrons with hot electron temperature, T_{hot} that generate keV X-ray radiation. The level of preplasma will influence the hot electron temperature. In some of the previously reported experiments T_{hot} is of the order of tens of keV, while in other cases only a moderately hot electron temperature can be observed of the order of few keV. Hot electron jets of much higher energy, exceeding 250 keV, have been generated by sub-millijoule 120-fs Ti:Sapphire laser pulses using the same experimental setup [26], as will be discussed in more details in the next section. However, due to their high energy, directional emission and very small fraction of energy of only 0.01% of the incident laser energy they will not contribute significantly to the present keV X-ray emission. From the spectra shown in Figure 4.11 (a) and Figure 4.12 (a) (p.97-98), the hot electron temperature is derived from the tail of the high-energy bremsstrahlung emission in the range of 10.5 keV to 30 keV as shown in Figure 4.11 (b) in Figure 4.12 (b). The present results indicate that K_α line emission is produced by a distribution function of hot electrons characterized by a temperature of 7.65 ±0.6 keV. Therefore, a large fraction of the hot electrons would have sufficient energy (> 9 keV) to excite Cu K_α photons for which the energy is 8.05 keV. The small fraction of bremsstrahlung radiation observed for our X-ray spectra can be explained by the fact that the hot electron temperature from these plasmas has a value close to the Cu K-absorption edge, $E_{K,\,\mathrm{abs}}$= 8.98 keV. Thus, most of these fast electrons knock out the K inner shell electrons generating narrow K_α line emission rather than higher energy bremsstrahlung emission.

Using the scaling law of the hot electron temperature T_{hot} derived in early work for nanosecond laser-plasma interactions [31] we can compare to the present observations. The hot electron temperature T_{hot} due to resonance absorption in a self-consistent sharp density gradient is given by equation (2.16) [31]. For a wavelength of 0.8 μm, a hot temperature of 7.7 keV would be predicted for intensities of 10^{16} W/cm^2 and a cold electron temperature of about 100 eV. This is in agreement with other reported results for cold electron temperature [6] where it is expected that plasmas with cold electron temperatures of the order of hundreds of electron volts will be created when femtosecond laser pulses are focused on solid targets.

In practice, the X-ray source can become an almost monochromatic source as filters of Nickel can be used to eliminate the Cu K_β line at 8.91 keV and nearby higher energy bremsstrahlung radiation since the nickel absorption K-edge is at 8.33 keV. A simulated Ni edge absorption spectrum convolved with the one presented in Figure 4.12 is presented in Figure 4.14. The 15 μm thick filter was chosen to filter the raw spectrum. The ratio of the K_α line and the residual radiation 1-7.51 keV plus 8.48 keV-30 keV is 0.69 after filtering, while before filtering, the ratio was 0.45 in terms of photon number. Further improvement could be obtained by using a gold-coated mirror at a grazing incidence angle of 0.5° to cut off radiation above 10 keV, and such a mirror can be also used to refocus the X-rays to a higher intensity probe spot for applications.

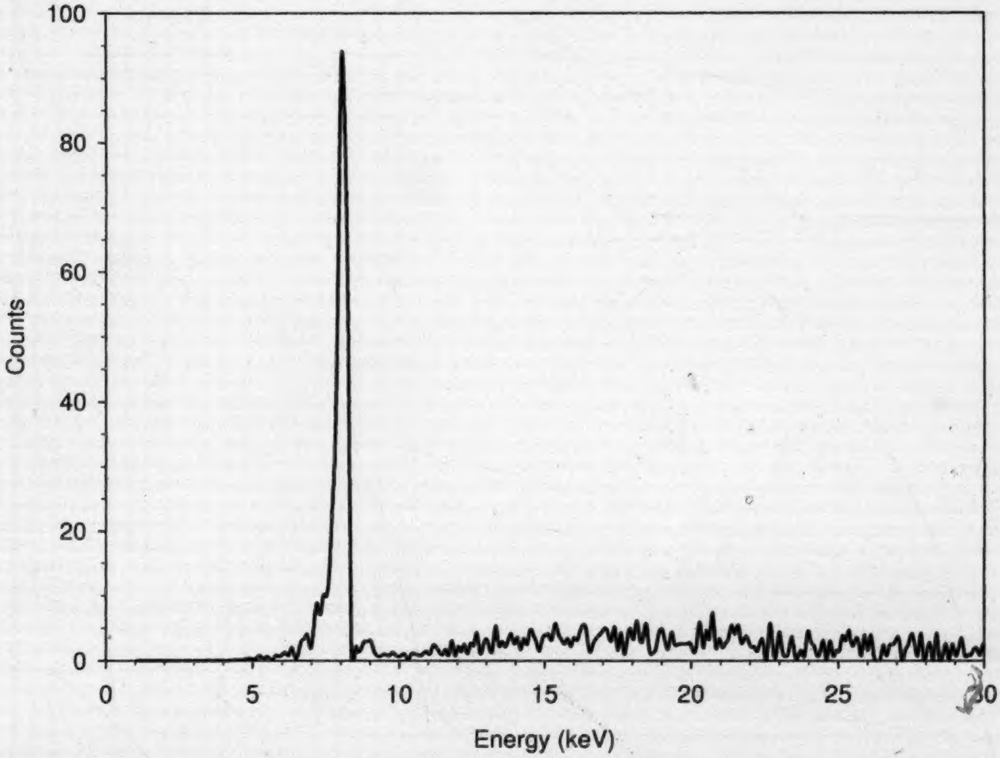

Figure 4.14. A simulated Cu K_α X-ray spectrum obtained after the raw Cu K_α X-ray spectrum from Figure 4.12 is filtered with 15 μm Ni foil. The ratio of the K_α line and the residual radiation 1-7.51 keV plus 8.48 keV-30 keV is 0.69 after filtering.

Chapter 5

HOT ELECTRONS AND ELECTRON JETS FROM SOLID TARGETS[1]

5.1 Electron jets measurements and discussion

Directional emission of very energetic electrons was observed for *p*- and *s*-polarized laser light, which was found to be dependent on the laser polarization and the target geometry. The electron jets were found to be in the plane of electric field polarization for both *p* and *s* polarizations. The results have shown that for the case of *p*-polarized laser pulses only the film placed above the focusing lens detected the hot electron signal while the two lateral film strip measured no signal. Conversely, for the case of *s*-polarized laser pulses, the two lateral film strips detected the hot electron signal while the strip placed above the lens measured no hot electron signal. It was found that the electrons exposed the DEF film on both the front and rear sides of the film allowing measurements of their angular distributions for two different energy ranges. The energy threshold for electrons to reach the first emulsion surface through the 33 μm thick aluminum filter used is approximately 80 keV, while the energy required to reach the backside emulsion through the 212 μm thick film is approximately 250 keV [70, 89]. To determine these threshold energy values, the total stopping power for electrons have been utilized. The total stopping power is the sum of the collision and radiative stopping powers.

---

[1] Parts of this chapter have been published in Ref. [26]

For electrons, the energy loss in matter is due to both Coulomb collisions that result in the ionization and excitation of atoms, and collisions with atoms and atomic electrons in which electromagnetic radiation (Bremsstrahlung quanta) is emitted. The total energy loss is the sum of the two contributions: collisional and radiative. Bethe derived the expressions for the energy loss per unit path length for electrons [90]:

$$\left(\frac{dE}{dx}\right)_{coll}=\left(\frac{e^2}{4\pi\varepsilon_0}\right)^2\frac{2\pi N_0 Z\rho}{mc^2\beta^2 A} \times\left[\ln\frac{T\left(T+mc^2\right)^2\beta^2}{2I^2mc^2}+\left(1-\beta^2\right)-\left(2\sqrt{1-\beta^2}-1+\beta^2\right)\ln 2+\frac{1}{8}\left(1-\sqrt{1-\beta^2}\right)^2\right] \tag{5. 1}$$

$$\left(\frac{dE}{dx}\right)_{rad}=\left(\frac{e^2}{4\pi\varepsilon_0}\right)^2\frac{N_0 Z^2\left(T+mc^2\right)\rho}{137m^2c^4A}\left[4\ln\frac{2\left(T+mc^2\right)}{mc^2}-\frac{4}{3}\right] \tag{5. 2}$$

where $(dE/dx)_{coll}$ is the energy loss per unit path due to collisions, $(dE/dx)_{rad}$ is the energy loss per unit path due to radiation, T is the kinetic energy of the fast electron, Z, A, and ρ are the atomic number, atomic weight, and density of the absorber, m is the electron mass, N_0 is Avogadro's number and $\beta=\frac{v}{c}$ (v is velocity of the particle). The parameter I represents the mean excitation energy and it is regarded as an empirical constant. For instance, for Al, I =166 eV in NIST database ESTAR of Stopping Powers and Ranges for Electrons [70].

Total energy loss per unit path length is:

$$\left(\frac{dE}{dx}\right) = \left(\frac{dE}{dx}\right)_{coll} + \left(\frac{dE}{dx}\right)_{rad} \tag{5. 3}$$

The radiative term is significant only at high energies in heavy materials, as can be seen from the relative contributions of the two terms [84]:

$$\frac{(dE/dx)_{rad}}{(dE/dx)_{coll}} \approx \frac{T + mc^2}{mc^2}\frac{Z}{1600} \tag{5. 4}$$

Calculations of the range of electrons could in principle be done by integrating Equations 5.1 and 5.2 over the path of the electrons, but this is difficult due to the random path of the electrons because the electrons suffer single and multiple scattering in traversing the material. Therefore, the range of electrons represents an average value since any appreciable energy loss by ionization is accompanied by a large number of small-angle scattering processes producing statistical fluctuations of the path length of the electrons in the stopping material. The values for average stopping power for the DEF film and the various Aluminum foil filters employed are taken from Ref. [89] and [70], where, in principal, they are computed as the sum of the collision and radiative stopping powers using the analytical high-energy theory of Bethe that was briefly described above.

To reach the backside emulsion of the DEF film, the electrons must go through a 33 μm-thick aluminum filter, a 1 μm plastic coating, a 13 μm thick front side emulsion and a 185 μm thick plastic substrate [84]. These successive layers block electrons with energies below ~250 keV. The angle of incidence of the electrons on the DEF film was also considered when calculating these energy values. For *p*-polarization case, the angle of incidence of the electrons on the DEF film wa considered to be 30°, while for *s*-polarization case, the angle of incidence of the electrons on the DEF film is about 20°.

The resultant images of the electrons on DEF film show a narrow cone of high-energy electrons with energies greater than 250 keV in the middle of a broader cone of electrons with energies greater than 80 keV. The narrow cone of high-energy electrons was revealed when the emulsion was removed from the front side of the film along a thin line as shown in the Figure 5. 1 and Figure 5. 2. For *p*-polarized laser pulses, the thin line on the film is actually the intersection between the film plane and the incident plane while for *s*-polarized laser pulses the thin line is the intersection between the film plane and the plane defined by the electric field vector and the incident propagation direction vector. Figure 5.1 and Figure 5.2 show that the outgoing hot electrons escaping from the plasma with energies higher than 250 keV are collimated in a well-defined narrow cone angle for both polarizations. For *p*-polarized incidence a single electron jet is observed in the plane of incidence at an angle between the target normal and the specular direction. For *s*-polarized radiation the electron jet is observed in the lateral directions in the plane of the incident k-vector and incident electric field.

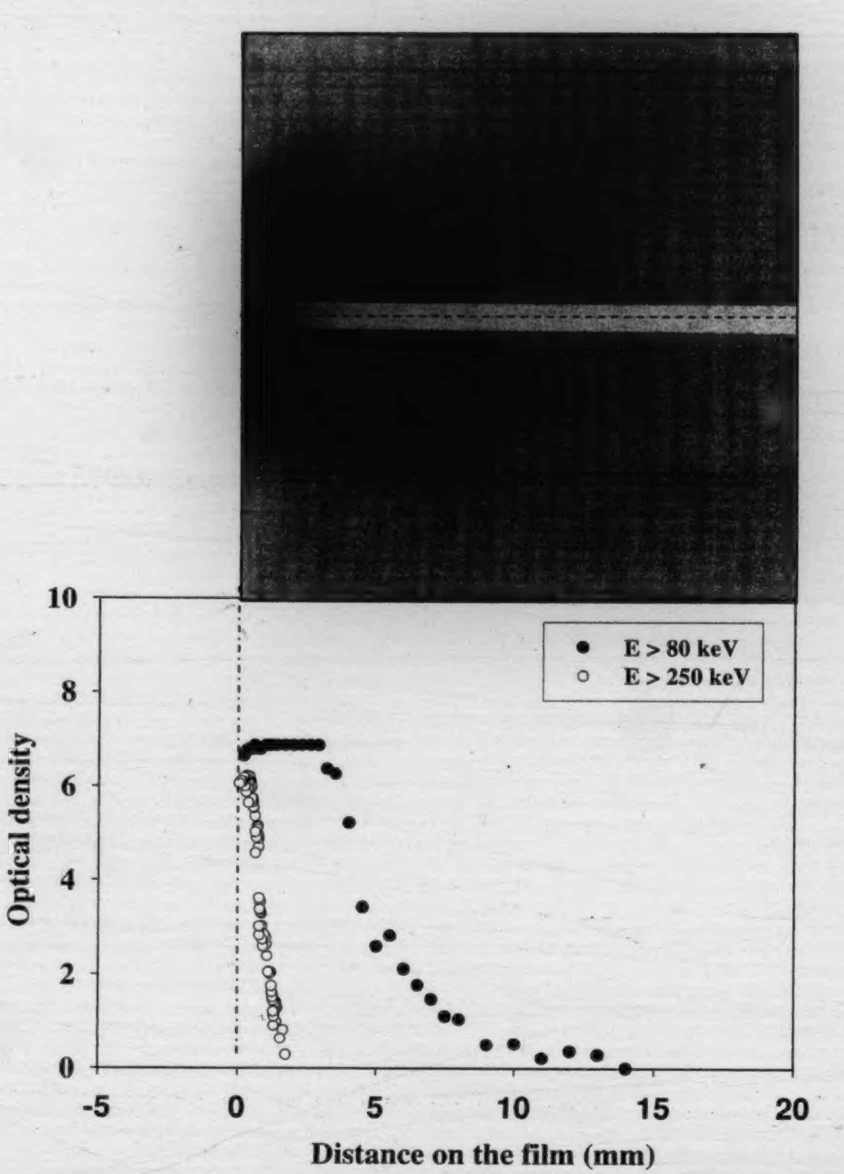

Figure 5. 1. Electron jet images on the front and back sides of DEF film for >80 keV and >250 keV energies ranges respectively for p-polarized 30° incidence (top). The image from the electrons with energies higher than 250 keV, on the back side of the film, can be seen in the central line of the DEF film. The exposure resulted from 7 shots on target. Measured electron distribution of the outgoing hot electrons given by the optical density of both the front and rear sides of DEF film (bottom). The DEF film was placed at 5.5 mm from the target spot.

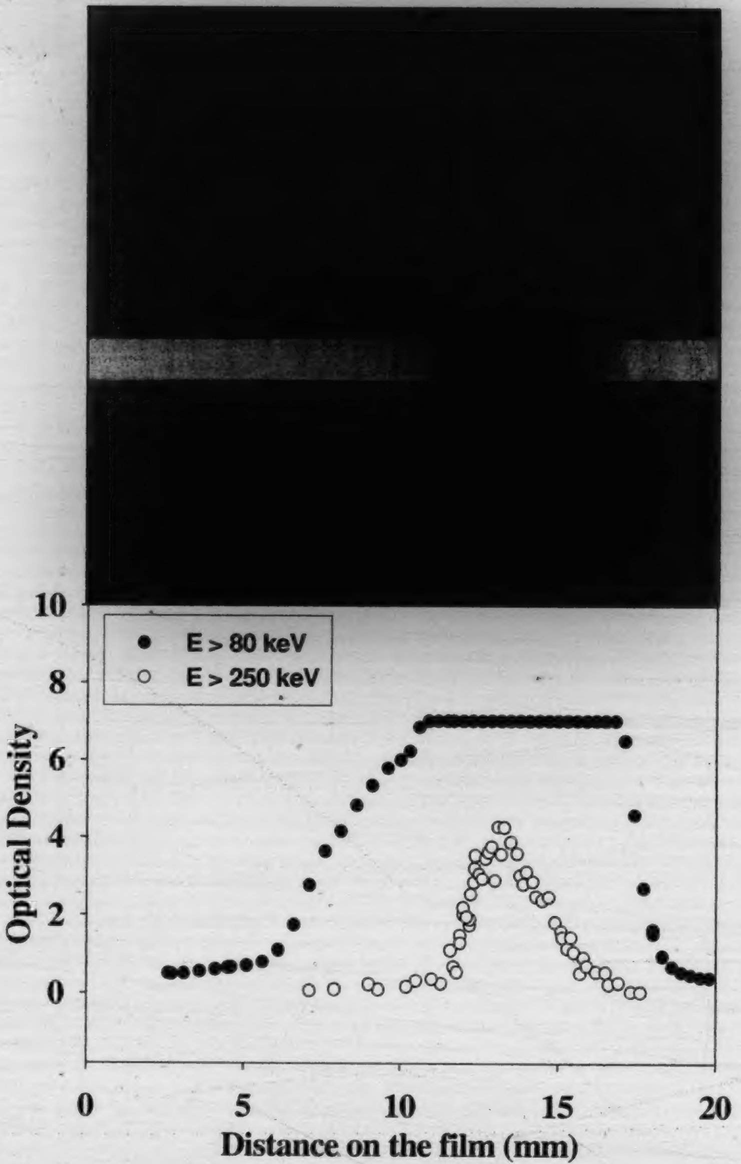

Figure 5. 2. Electron jet images on the front and back sides of DEF film for >80 keV and >250 keV energies ranges respectively for s-polarized 30° incidence (top). The image from the electrons with energies higher than 250 keV, on the back side of the film, can be seen in the central line of the DEF film. The exposure resulted from 7 shots on target. Measured electron distribution of the outgoing hot electrons given by the optical density of the both front and rear sides of DEF film (bottom). The DEF film was located at 16.5 mm from the target spot.

The angular distributions of the hot electrons emitted from the plasmas with energies higher than 80 keV and higher than 250 keV respectively are calculated from the measured signals only on the front and back surfaces of the DEF film . To calculate the electron flux, the film response determined experimentally for the X-ray radiation was utilized. The film response is given by the density-exposure relationship [91], which relates the optical density of the DEF film to the exposure flux (X-ray photons/cm^2). In order to carry out the exposure calculation, it was assumed that the electron energies were 80 keV on the first film emulsion surface and 250 keV on the second emulsion surface of the DEF film. For each film emulsion, for a given optical density, the corresponding energy deposition of an X-ray exposure was related to an equivalent energy deposition of the incident electron beams of 80 keV and 250 keV respectively. Assuming that the same response to energy deposited by the electrons as energy deposited by X-rays to obtain the same optical density on the film, the incident electron flux in terms of the number of electrons per steradian for each DEF film emulsion surface was computed.

The stopping powers for the X-rays and the deposition per unit length for electrons were taken from National Institute of Standards of Technology (NIST) databases [69, 70]. Specifically, the energy deposition required to obtain a given film density was obtained using 4.51/4.93 keV exposure curves from Rockett et al. [91] corrected for the specular measurement geometry used here using the correction factors found in Henke et al. [84]. The 4.51/4.93 keV exposure was used since approximately 95% of the deposition occurs in the first surface of the DEF film and thus this corresponds to the single sided response of the film. The resultant density response curves are plotted in Figure 5.3.

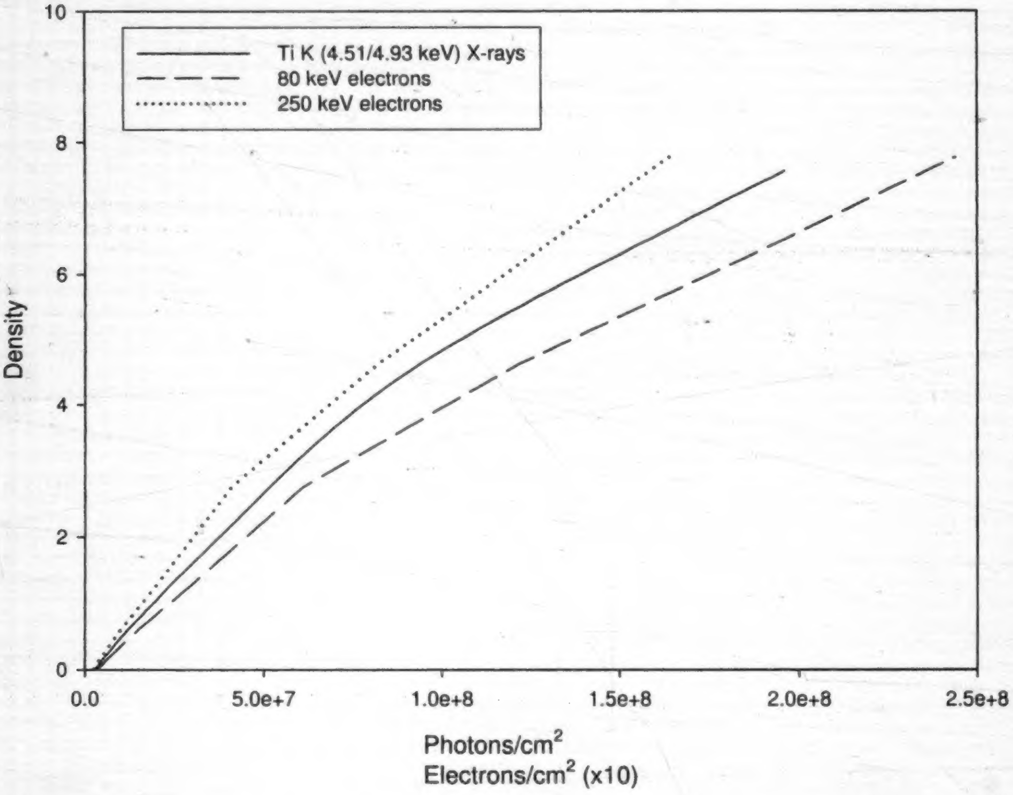

Figure 5.3 The density response curves for X-rays, 80 keV electrons and 250 keV electrons. The exposures are calculated for 80 keV electrons on the first film emulsion surface and for 250 keV electrons on the second emulsion surface of the DEF film. The X-ray exposures are given for X-rays with energies of 4.51 keV and 4.93 keV, which are taken from Rockett at al. [91] from an experimental calibration data of Kodak DEF film.

The angular distributions of the hot electrons emitted from the plasmas with energies higher than 80 keV and higher than 250 keV respectively in Figure 5.4.

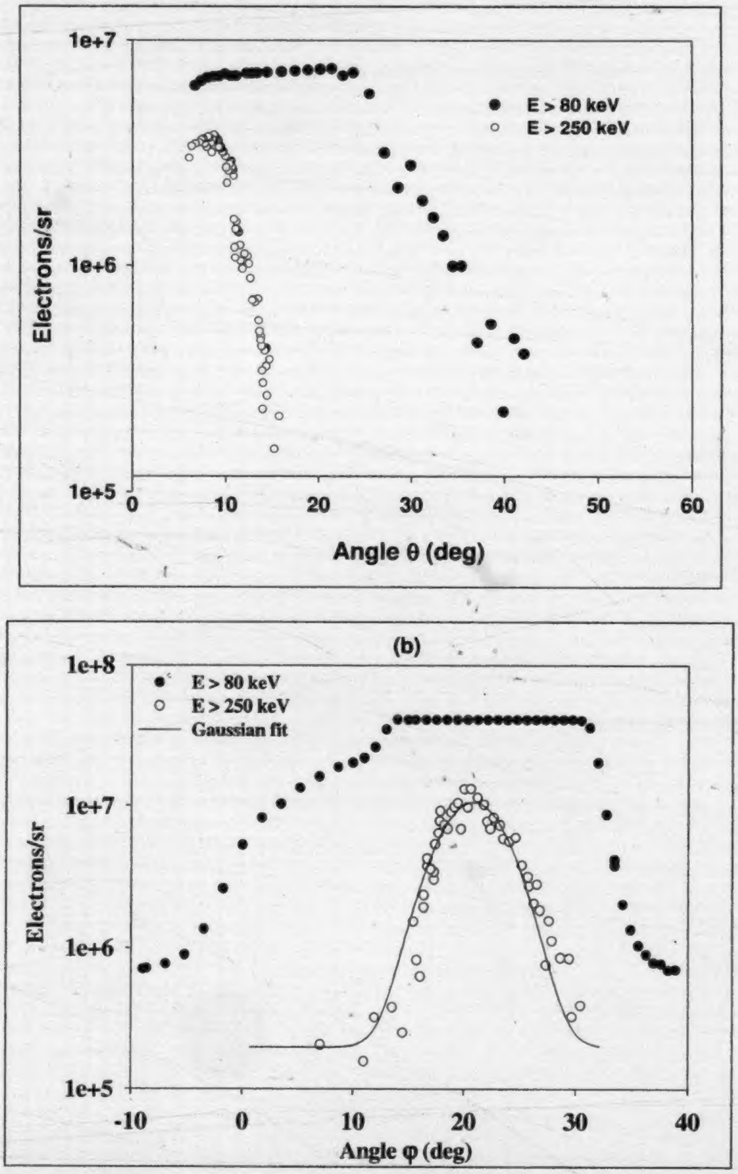

Figure 5.4 The angular distribution of the outgoing hot electrons for > 80 and > 250 keV energies ranges respectively, deduced from the DEF film measurements: (a) p-polarized at 30° incidence and (b) s-polarized at 30° incidence. The DEF films were covered with 33 μm Al filter in both cases. For p-polarization case: θ is measured with respect to the target normal, in the plane of incidence. For s-polarization case: φ is measured with respect to the electric field direction in the plane of laser electric field polarization.

When scanning the DEF film to obtain its optical density, the same optical configuration previously employed for the X-ray film calibrations [84, 92] was utilized as shown in Fig. 5.5. The same matched influx-efflux optics of 0.1 N.A. were used here as well.

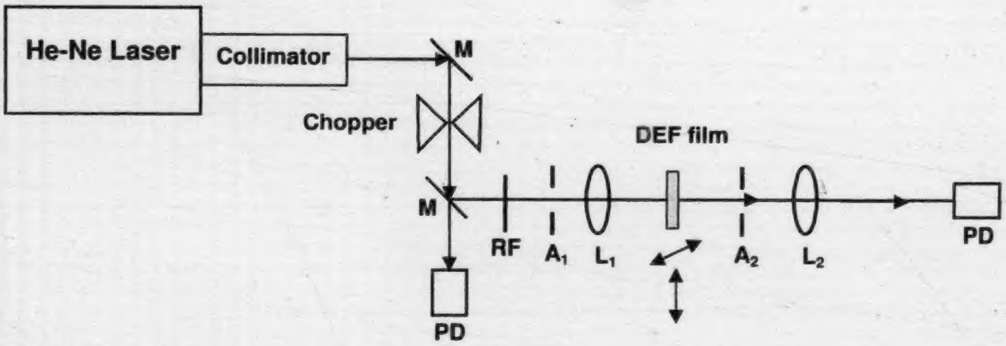

Figure 5.5 The schematic diagram of the setup used to scan the DEF films. M is a mirror, PD is a photodiode, RF is a reflective filter (different filters have been used), A is an aperture, L is a lens (positive). The DEF film was mounted on two-axis stages as to allow movement in both the horizontal and vertical directions. The optical densities are measured using matched influx-efflux optics of 0.1 N.A. The lenses used were L_1=6 cm f.l. and L_2=10 cm f.l.

As mentioned above, the stopping power used to compute the energy deposition of the electron beam represents the average energy loss per unit path length suffered by an electron in traversing the medium due to collision and radiative processes. The electrons incident on an absorber material will be deflected due to scattering in the material and the beam spreads out as a function of depth. Hence, after traversing the aluminum filter and while traversing the film emulsion and the substrate the electron beam experiences an increase in its angular spread. Thus, the real effective path lengths are longer than the straight-line trajectories used to estimate the electron flux.

The reported density-exposure relationship for the DEF film is slightly different for different X-ray photon energies and also varies between different reported experimental calibrations [84, 92]. Due to these differences and because of the angular straggling effect, it is estimated that the accuracy of the computed electron flux is on the order of a factor of two-to-four. However, this is still sufficient to give better than order of magnitude estimates of the electron flux.

Given that the emission direction of the electrons is dependant on the laser electric field polarization, the angular distribution for each polarization case is plotted separately as shown in Figure 5.4 (a) and (b). For *p*-polarized incidence a single electron jet is observed in the plane of incidence, therefore the flux of the electron jet is specified with respect to the angle θ, measured from the target normal in the plane of incidence. For *s*-polarized radiation, the electron jet is observed in the lateral directions in the plane of the incident *k*-vector and incident electric field, therefore the flux of the electron jet is specified as a function of the angle φ, measured with respect to the electric field direction in the plane of laser electric field polarization.

For the *s*-polarized case, the outgoing hot electrons are found to be in a direction approximately 20° from the laser electric field polarization direction as shown in Figure 5.4 (b). The results for *s* polarization show that the emission angle for the fast electrons over 250 keV is of the order of 10° at full width at half maximum, which indicates very directional emission of these electrons. From these results, the energy of the electrons with energies greater than 250 keV is estimated to be about 10^{-4} of the laser energy for both polarizations.

In order to confirm that the exposures on the DEF films were due to the hot electrons, tests by adding permanent magnets were performed. Magnets with magnetic fields of 1500-3000 G were employed in front of the DEF film to deflect the electrons. With magnets, no signal on the DEF film was measured. This is in agreement with the much lower expected X-ray flux on the film measured before as reported in the previous chapter on X-ray measurements [23], which would not be blocked by the magnets. Indeed, for an X-ray conversion efficiency for 8 keV K_α X-rays of $1.7\text{x}10^{-5}$ from the incident laser energy, the expected X-ray exposure on the DEF film for 8 shots on the target would lead to maximum optical density of 0.13. This indicates that the X-rays lead to a negligible contribution to the exposure of the DEF films.

There are many potential mechanisms for the fast electron generation from laser-produced plasmas. Some of these mechanisms have been presented in chapter 2 such as resonance absorption, vacuum heating, and various plasma instabilities like Raman scattering and two-plasmon decay. The ponderomotive force and the $\vec{J} \times \vec{B}$ heating are known to accelerate electrons but for laser intensities higher than 10^{18} W/cm^2, and thus are rather inefficient for intermediate laser intensities of a few times 10^{16} W/cm^2. Different generation mechanisms produce different hot electron distributions, each being characterized by its hot electron temperature T_{hot} and its angular distribution. For instance, the resonance absorption process is expected to produce hot electrons mainly in the direction of the density gradient for *p*-polarized laser light with a distribution described by hot electron temperature T_{hot} of about 10 keV for laser intensities in the range of a few times 10^{16} W/cm^2. The ponderomotive force and the $\vec{J} \times \vec{B}$ heating will produce fast electrons mainly in the direction of the laser propagation. On the other hand, the self-generated fields might be able to affect the low energy electrons more easily, and thus, interfering with the initial emission direction. Recently, the generation of high-energy electrons along the electric field direction via knock-on Coulomb collisions of the oscillating electrons in the incident laser field has been proposed [92] in a process similar to that leading to enhanced inverse Bremsstrahlung absorption for high field intensities [93]. Only a very small number of electrons propagating close to the direction of the electric field [93] will participate in these knock on collisions and the accelerated electrons will be directional along the incident electric field vector. There is experimental evidence of the existence of a hot and super hot component for the electron distribution for laser intensities higher than approximately 2×10^{16} W/cm^2 [94]. Using the X-ray continuum spectra obtained from plasmas created for laser intensities of approximately 5×10^{16} W/cm^2, two hot electron temperatures have been identified, both described by a Maxwellian distribution. For the lower component T_{hot} is 21 keV and for the higher component T_{hot} is 85 keV. The existence of a super hot component for the electron distribution in the current experiments could possibly be given by the observed emission of hot electrons with energies over 250 keV.

In the context of fast ignition, but also from the point of view of other practical applications, it is important to understand the acceleration mechanisms under different plasma conditions. In the recent years, a number of experimental studies have been reported on the dependence of fast electron emission on the laser polarization, laser wavelength, plasma density scale length and laser intensity [58-65]. Particle-in-cell (PIC) simulations have been performed to identify the mechanisms of laser acceleration. Chen et al. [60] found that both s- and p-polarized laser pulses can generate jet emission of fast electrons at moderate intensities of 2×10^{16} W/cm^2. Laser pulses of 5 mJ energy, 800 nm and 150 fs duration emitted at 10 Hz, were incident at 45° on aluminum target with a prepulse contrast ratio better than 10^{-5} (at 1 ps before the main pulse). Some measurements were performed with a prepulse formed by 8% energy of the main pulse, which was sent 50 ps in advance of the main pulse to create a corona preplasma. For s-polarized irradiation without prepulses, the outgoing fast electrons were collimated along the laser polarization direction perpendicular on the plane of incidence at an angle of approximately 7° from the target surface. Our results agree well with Chen's results as we also observed that the jet emission of fast electrons is in the plane of polarization of the laser electric field, perpendicular to the plane of incidence, but at slightly higher angle from the target surface of approximately 20°. For p-polarized irradiation, Chen et al. observed a significant variation in the emission angle of the jet of fast electrons with respect to the prepulse level. When the target was irradiated with p-polarized laser pulses without prepulse, the jet of electrons was observed in the specular direction, while for the observation with a prepulse, the jet was observed between normal and specular direction at an angle that varies with the electron energy. For instance, they observed that the jet of electrons with energies over 50 keV was emitted almost along normal, the jet of electrons with energies over 250 keV was emitted at 16° from normal and the small fraction of electrons with energies over 1MeV was emitted at 30° from the target normal. Our measurements with p-polarized laser pulses shows that fast electrons with energies over 250 keV are emitted between normal and specular at approximately 8° from the target normal for a prepulse contrast ratio of 5×10^{-4}. This suggests that the density profile of the corona preplasma plays an important role in the emission direction of fast electrons. The angular distribution of the electrons is related to the plasma wave propagation directions. Long acceleration lengths and high phase velocity plasma waves are necessary to obtain energetic electrons from laser produced plasmas. Bastiani et al. [51] observed the presence of an electron emission peak in the specular direction during the interaction of high contrast ultrashort laser pulses with steep electron density gradient. The electron energies were approximately 20-30 keV and were generated at moderate intensities of 4×10^{16} W/cm^2 and 45° angle of incidence using laser pulses of 50 mJ energy, 120 fs duration, 800 nm incident on SiO_2 targets with high prepulse contrast ratio. This result is in good agreement with Chen's results for the case without prepulse. When an optimum prepulse was used higher electron energies were detected of about 180 keV with a rather broad emission angle. Sentoku et al. [59] investigated the electron jet emission by simulation with a 2D PIC code for higher laser intensities of $1\text{-}2\times10^{18}$ W/cm^2. In the case of p-polarized laser pulses at a 29° angle of incidence, the outgoing electrons were observed between normal and specular direction, at an angle of about 17° with respect to the normal direction, while the specular reflection angle was at 29° with respect to the target normal. For these high intensities, for s-polarized laser pulses, the electron jets were emitted in the specular direction. The electrons were accelerated through the coronal plasma by the reflected laser light, which was modulated at the reflection point.

5.2 Angular dependence of the hot electrons

In order to improve the understanding the mechanism of generation of the fast electron jets, measurements were also made for different angles of incidence. The hot electrons ejected outwards from the plasma generated by p-polarized laser pulses at various angles of incidence were measured using silicon PIN diodes filtered with 33 and 50-μm aluminum foils. The energy threshold for electrons to reach the PIN diode sensitive layer surface through the 33 μm and the 50 μm thick aluminum foils used was approximately 80 keV and 95 keV, respectively [82, 83]. The experimental geometry is displayed in Figure 3.13 in chapter 3. The angular dependence of the hot electron signal was detected for four angles of incidence, i.e. 30°, 36°, 42° and 65°. The emission was measured in the plane of incidence and the angle of emission, θ, is measured versus the incident laser direction, for which $\theta = 0°$. Initially, the hot electron signal was measured as a function of target position for each set of experiments in order to determine the focal position for maximum hot electron signal. The focal scan measurements for hot electron signal were performed using a similar procedure to the one employed for the X-ray focal scan measurements. In particular, the focusing objective was translated along the incident laser direction to different positions, in front and behind the best focus position. This position was defined as the location for the maximum hot electron signal. The rest of the measurements were carried out at this best focus position. A focal scan of the hot electron signal measured by the PIN diode detector is shown in Figure 5.6 where the PIN diode was located at a distance of 4.9 cm at θ =35° with respect to the incident laser direction of propagation for p-polarized laser pulses incident at θ_{inc}=30°.

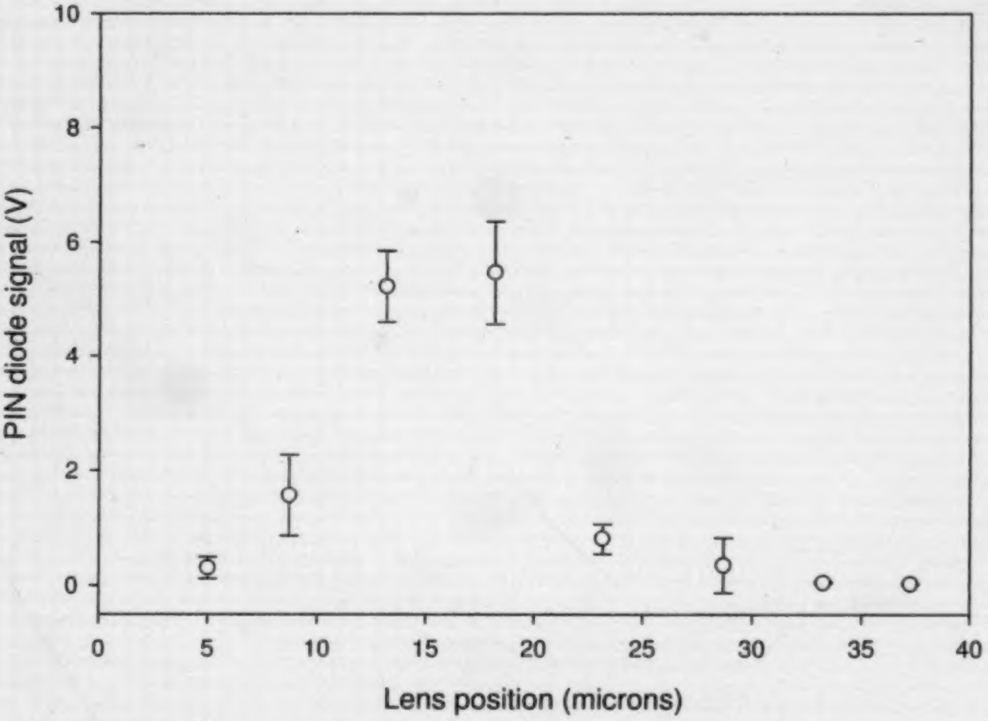

Figure 5.6 A hot electron focal scan performed to determine the location for maximum hot electron signal using PIN diode detector. Each point represents the average of a minimum of three laser shots. The error bars represents the standard deviation. The PIN diode was located at a distance of 4.9 cm at $\theta = 35°$ for p-polarized laser pulses incident at $\theta_{inc} = 30°$.

Two plots of the angular dependence of hot electrons obtained for 30° angle of incidence are shown in Figures 5.7, and 5.8. In Figure 5.7, the PIN diode was located at a distance of 4.9 cm away from the plasma, while in Figure 5.8, the PIN diode was located at a distance of 6.1 cm. The laser pulse energies were 260 μJ and 275 μJ (± 5%), respectively. The 10X microscope objective blocks the hot electrons emitted between -26° and 26°. However, when the PIN diode is positioned closer to the plasma, i.e. at 4.9 cm versus 6.1 cm, the outer case of the PIN diode also blocks the emission up to 32°.

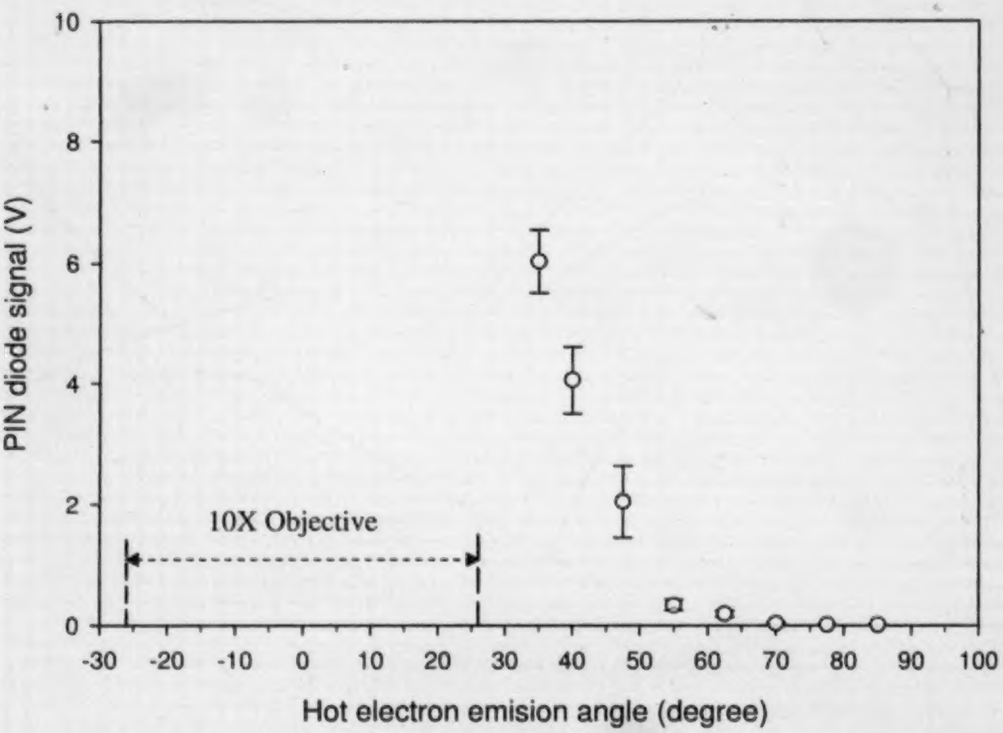

Figure 5.7 A hot electron angular plot obtained by means of PIN diode detector filtered with 50 μm Al foil for p-polarized laser pulses with energies of *E* =260 μJ (± 5%) incident at θ_{inc}=30°. Each point represents the average of five laser shots. The error bars represents the standard error. The PIN diode was located at a distance of 4.9 cm. The angle interval from -26° to 26° was blocked by the 10X microscope objective. The emission angle is given with respect to the direction of the incidence of the laser. Normal and specular directions are represented by the angle θ=30° and 60°, respectively.

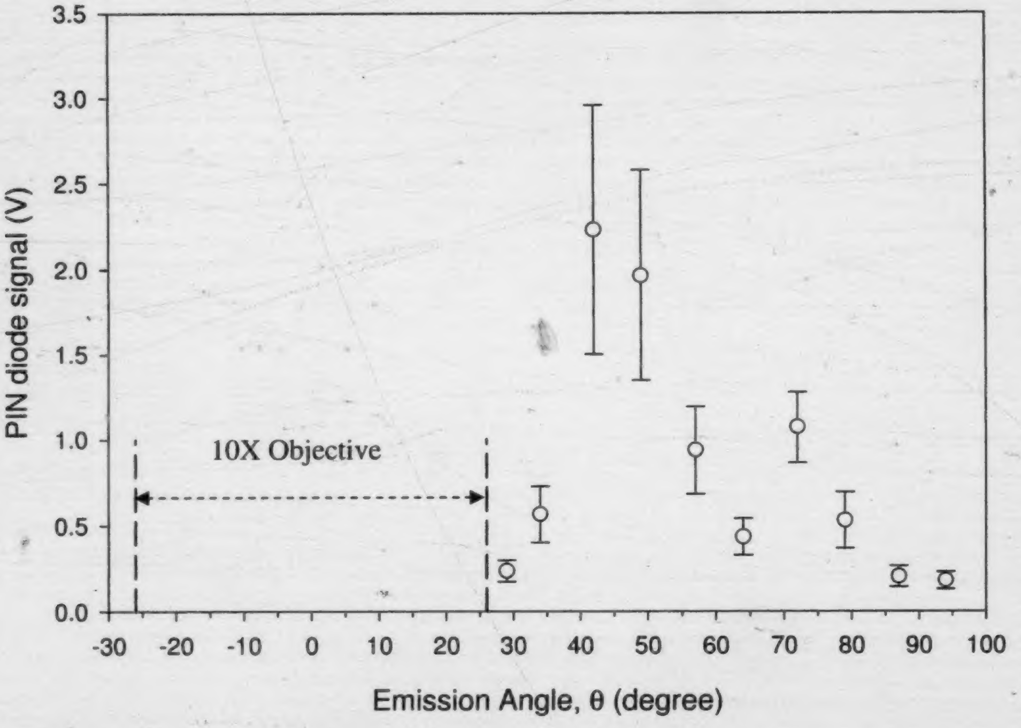

Figure 5.8 A hot electron angular plot obtained by means of PIN diode detector filtered with 50 μm Al foil for p-polarized laser pulses with energies of *E* =275 μJ (± 5%) incident at θ_{inc}=30°. Each point represents the average of a minimum of three laser shots. The error bars represents the standard error. The PIN diode was located at a distance of 6.1 cm. The angle interval from -26° to 26° was blocked by the 10X microscope objective. The emission angle is given with respect to the direction of laser propagation. Normal and specular directions are represented by the angle θ=30° and 60°, respectively.

When slightly lower laser pulse energies *E* =235 μJ (± 5%) were used, the hot electron signal decreased almost an order of magnitude as shown in Figure 5.9.

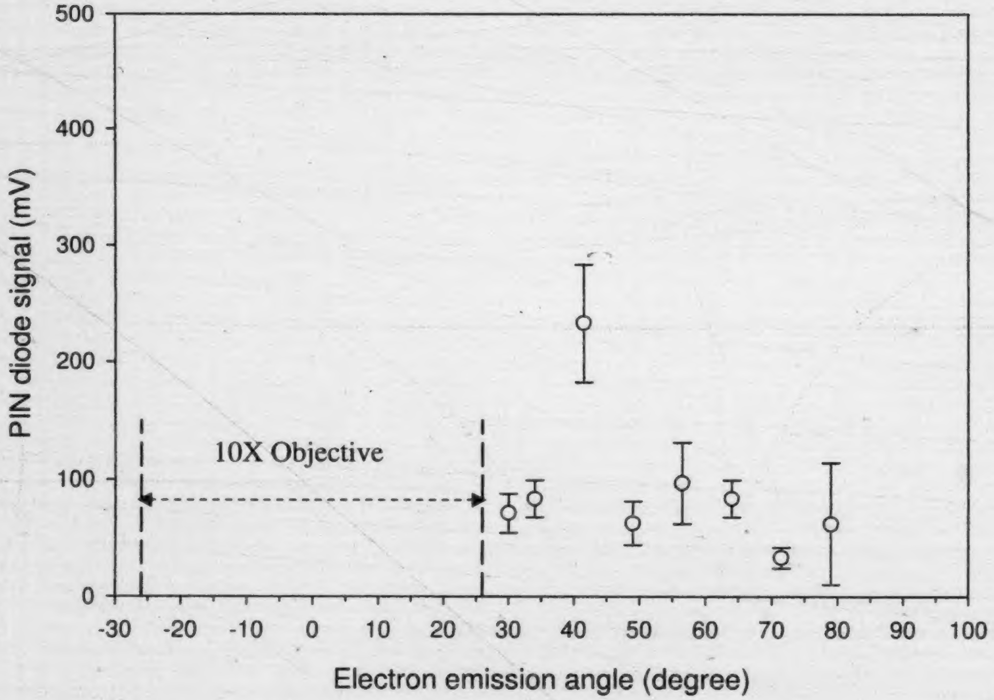

Figure 5.9 A hot electron angular plot obtained by means of PIN diode detector filtered with 50 μm Al foil for p-polarized laser pulses with energies of *E* =235 μJ (± 5%) incident at θ_{inc}=30°. Each point represents the average of a minimum of three laser shots. The error bars represents the standard error. The PIN diode was located at a distance of 6.1 cm. The angle interval from -26° to 26° was blocked by the 10X microscope objective. The emission angle is given with respect to the direction of laser propagation. Normal and specular directions are represented by the angle θ=30° and 60°, respectively.

For 30° angle of incidence, the hot electrons are emitted into angles between approximately 35° to 42°, with an average value of 40°.

Plots of the angular dependence of hot electrons obtained for 36°, 42° and 65° angles of incidence are presented in Figures 5.10, 5.11 and 5.12.

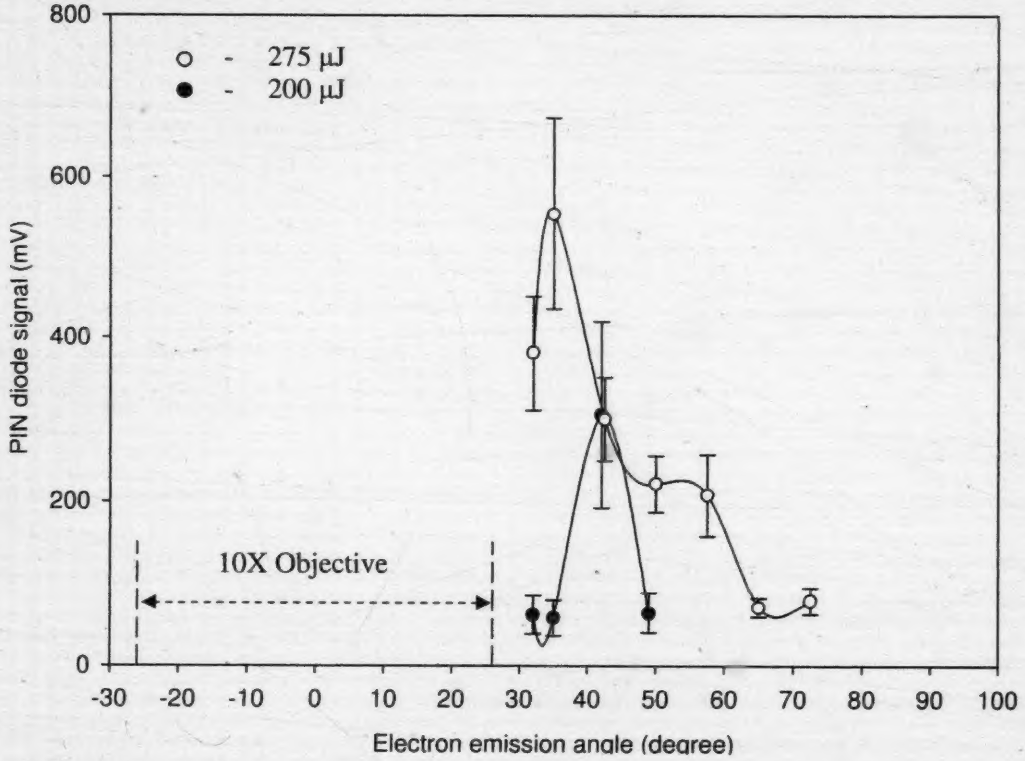

Figure 5.10 Hot electron angular plot obtained by means of PIN diode detector filtered with 50 μm Al foil for p-polarized laser pulses with energies of E =200 μJ (full circles) and E =275 μJ (open circles) incident at θ_{inc}=36°. The PIN diode was located at a distance of 5.4 cm. The angle interval from -26° to 26° was blocked by the 10X microscope objective. The emission angle is given with respect to the direction of laser propagation. Normal and specular directions are represented by the angle θ=36° and 72°, respectively.

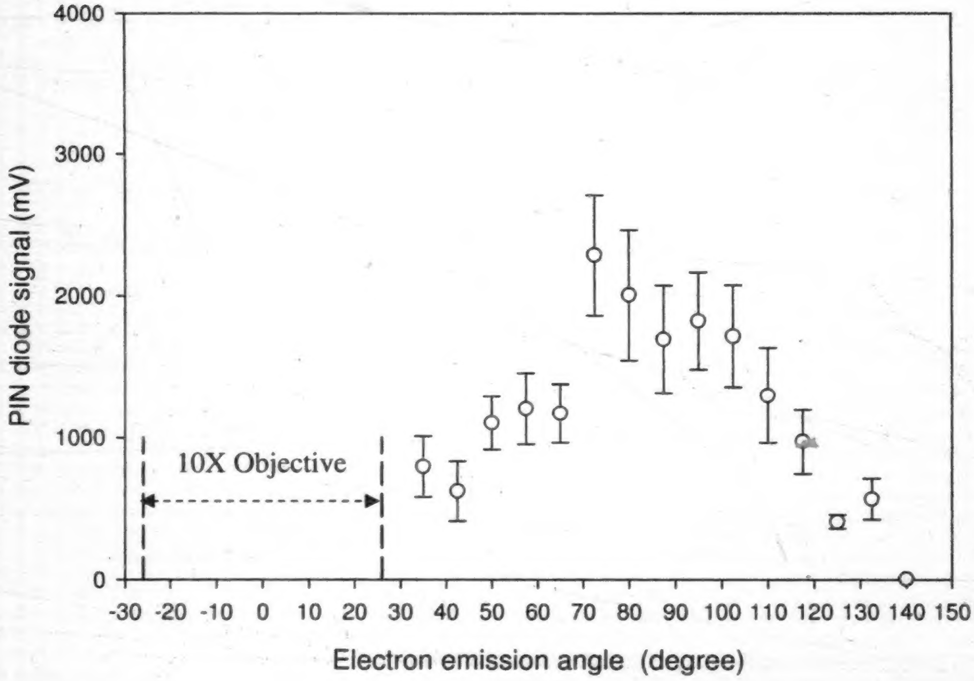

Figure 5.11 A hot electron angular plot obtained by means of PIN diode detector filtered with 33 µm Al foil for p-polarized laser pulses with energies of *E* =250 µJ (± 5%) incident at θ_{inc} =42°. Each point represents the average of eleven laser shots. The error bars represents the standard error. The PIN diode was located at a distance of 5.5 cm. The angle interval from -26° to 26° was blocked by the 10X microscope objective. The emission angle is given with respect to the direction of laser propagation. Normal and specular directions are represented by the angle θ=42° and 84°, respectively.

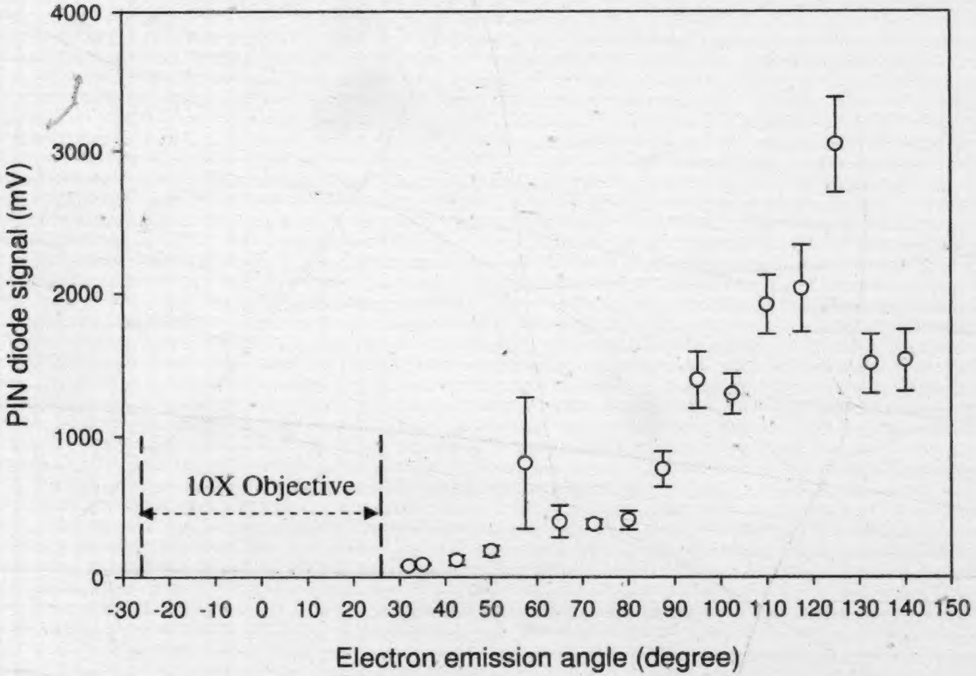

Figure 5.12 A hot electron angular plot obtained by means of PIN diode detector filtered with 33 μm Al foil for p-polarized laser pulses with energies of E =290 μJ (± 5%) incident at θ_{inc} =65°. Each point represents the average of seven laser shots. The error bars represents the standard error. The PIN diode was located at a distance of 5.6 cm. The angle interval from -26° to 26° was blocked by the 10X microscope objective. The emission angle is given with respect to the direction of laser propagation. Normal and specular directions are represented by the angle θ=65° and 130°, respectively.

The experimental results obtained for angles of incidence of 30°, 36°, 42° and 65° are summarized in Figure 5.13.

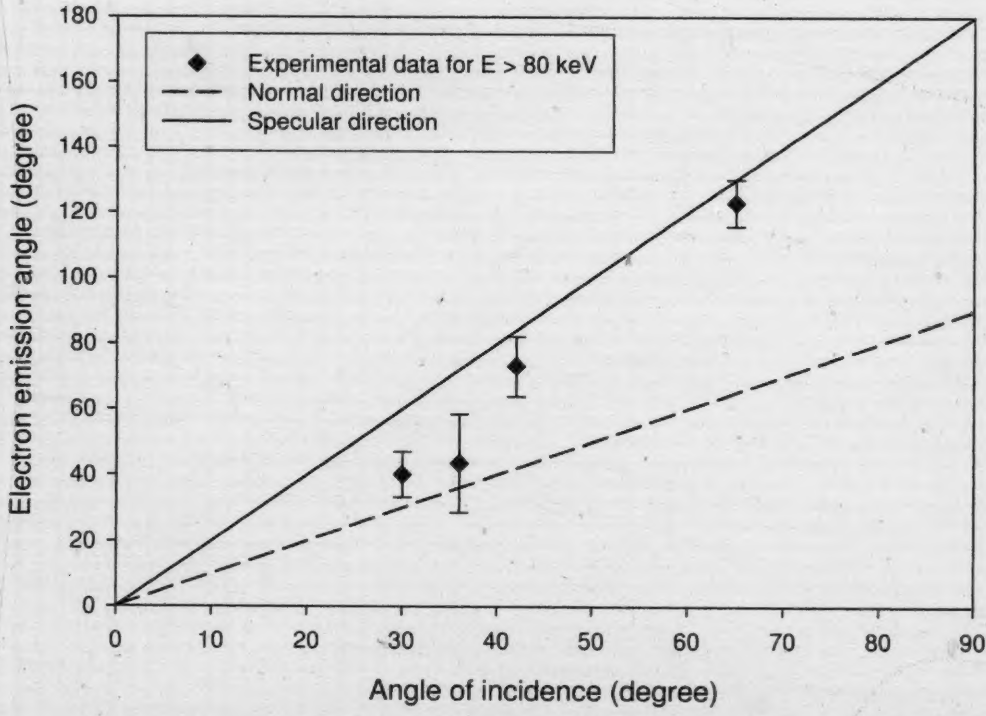

Figure 5.13 Angular dependence of laser angle of incidence obtained by means of PIN diode detector filtered with 50 μm Al foil for p-polarized laser pulses with energies with energies of *E* =200-300 μJ. The emission angle is given with respect to the direction of laser propagation.

Experimentally, variations were observed in the emission angles and sometimes in the width of the emission angle or strength of the signal for the same angle of incidence. The variation in the emission angle or the width of the emission angle can probably be attributed to the competition between the various interaction processes that occur in the plasma to generate such hot electrons. However, it appears that the hot electrons with energies higher than 80 keV are emitted between normal and specular direction. 2D PIC simulations were carried out for similar angles of incidence. The results are provided in chapter 6 as well as the comparison between the experimental and simulation results.

5.3 Electron radiography using hot electron jets

In order to demonstrate their usefulness for applications, the hot electron jets were used in initial radiography imaging experiments. Two test objects, a metal grid and an insect (bee) were located in contact with a DEF film, which was covered with 33 μm Al filter. The geometric layout for obtaining the images is given in Figure 5.14. The metal grid and the bee were positioned at 17.1 mm from the focal point and at 14.7 mm respectively. The projection images are shown in Figure 5.15. The images have been obtained using the outgoing hot electron jets with energies higher than 250 keV when the laser pulses were *s*-polarized. The metal grid was placed in between two DEF filmstrips. Thus, the jet of the high-energy electrons traversed the first DEF film and then the metal grid, and the image of the metal grid was recorded on the first emulsion of the second DEF film. The exposure was taken using 17 laser shots on target. The bee was placed in front of a DEF film; hence, the image of the bee is obtained from the rear side of the film after removing its first emulsion. The exposure was taken using 23 laser shots on target. It can be seen from the lower part of second image that where the first emulsion layer was not removed the film is completely black (saturated). The marks observed on the film of the metal grid are due to adhesive tape used to keep the grid against the film. Only two legs of the bee can be actually seen in the picture.

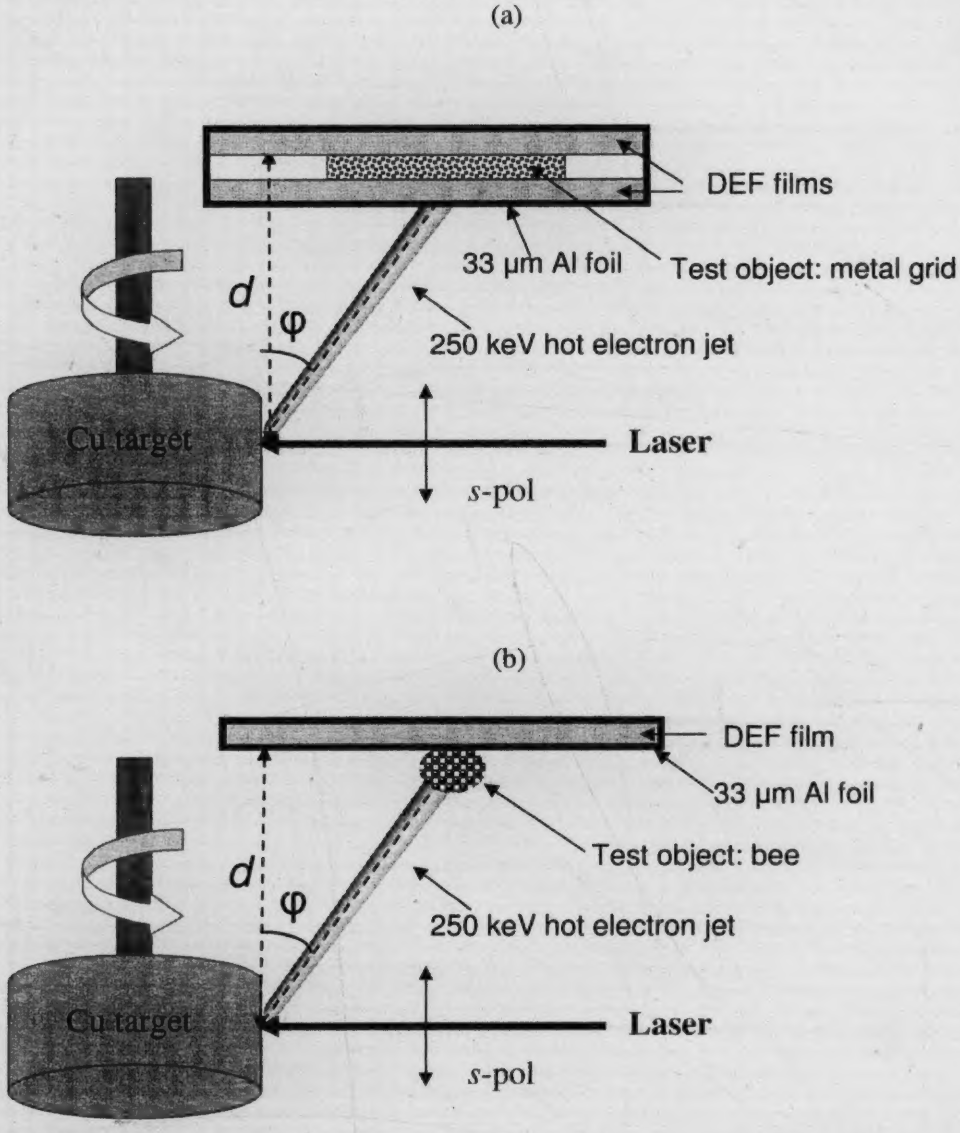
(a)
DEF films
33 μm Al foil
Test object: metal grid
d
φ
250 keV hot electron jet
Cu target
Laser
s-pol
(b)
DEF film
33 μm Al foil
Test object: bee
d
φ
250 keV hot electron jet
Cu target
Laser
s-pol

Figure 5.14. Geometric layout for obtaining the radiographic images for two test objects, a metal grid and a bee. The images were obtained using hot electrons with energies higher than 250 keV generated by *s*-polarized laser pulses: (a) a metal grid was located between two film strips at a distance of 17.1 mm from the focal point. (b) A bee was positioned at a distance of 14.7 mm from the focal point. Both objects were located against the DEF film covered in 33 μm aluminum, which is shown as black bands in the pictures.

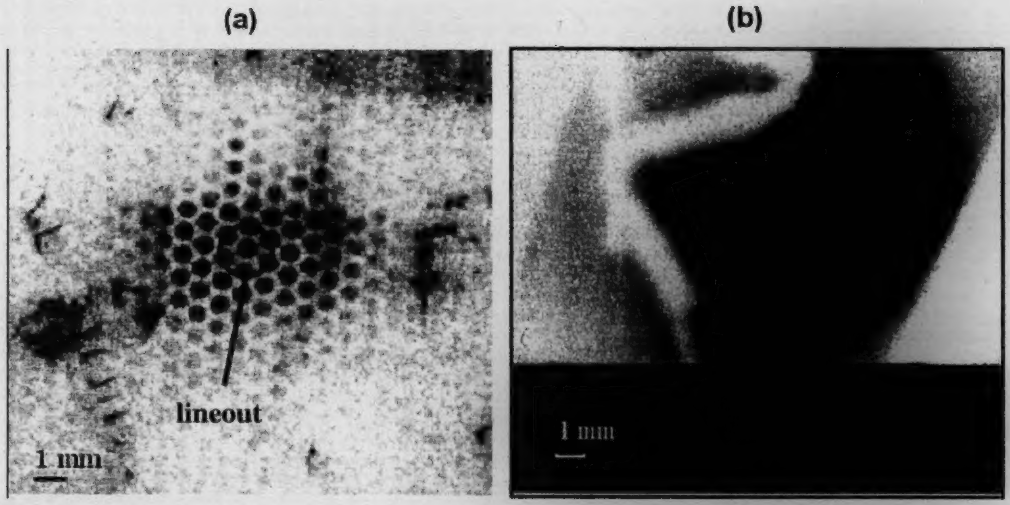

Figure 5. 15. Radiographic images obtained with the hot electrons with energies higher than 250 keV when the laser pulses were s-polarized. (a) The test object was a nickel grid placed between two DEF filmstrips. The exposure was taken using 17 laser shots on target. (b) The test object was the leg of a bee placed in front of a DEF filmstrip, which was initially covered in aluminum foil of 33 μm. The exposure was taken using 23 laser shots on target.

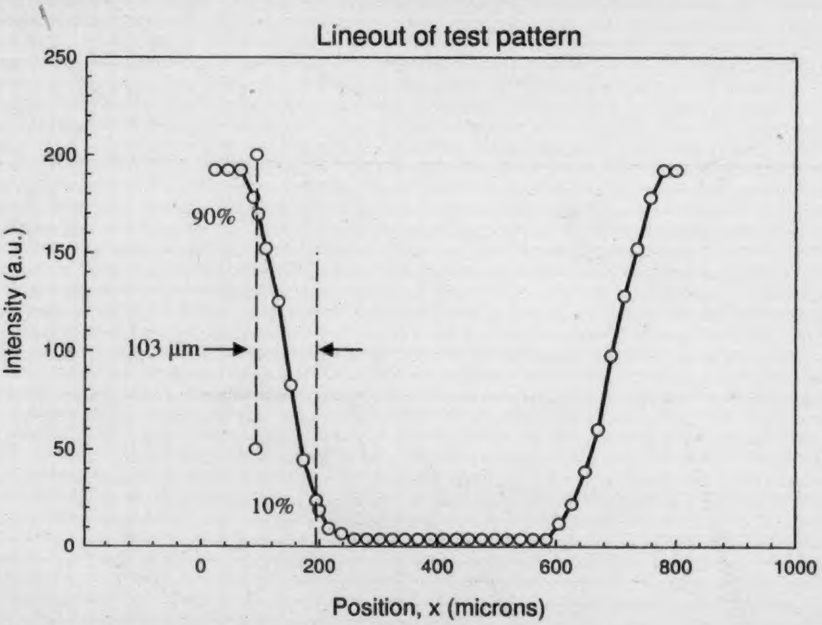

Figure 5. 16. Lineout of the test pattern shown in Figure 5.15 (a). The experimental data indicates a 10% to 90% resolution of 103 μm.

The intensity profile of a test pattern is shown in Figure 5.16. The 10% to 90% intensity variation indicates a spatial resolution of 103 μm. The spatial resolution of these images is mostly affected by the scattering of electrons in the aluminum filter and the DEF film substrate. For a better spatial resolution one could select the electron energy by means of an electrostatic or magnetic analyzer to avoid scattering of lower energy electrons in the filter materials. In this way, a much thinner filter can be used in front of the DEF film and the image can be obtained from the first emulsion layer of the film, avoiding scattering in both the filter and the film substrate.

Being generated by femtosecond laser pulses, these electron pulses are expected initially to have very short time durations on the order of the laser pulse duration, ~130 femtoseconds. Therefore, they can be applied in time-resolved pump-probe diffraction experiments. Thus, these electron pulses can be used to study rapid dynamics of structural changes with high temporal resolution based on time resolved electron diffraction. Initial electron diffraction from a thin aluminum sample using hot electrons produced by femtosecond laser plasma has been recently demonstrated [96].

It is important to note that while these pulses are very short initially they will spread out temporally when traveling from the source to the target due to their broad energy distribution. To use these electrons for time resolved experiments a monochromatic bunch can be selected as has been previously demonstrated by means of an electrostatic filter [13]. With improved spatial resolution the electron pulses may also be exploited in time-resolved microscopy by directly observing dynamics with simultaneous high temporal and spatial resolution. Moreover, these short electron pulses are useful for measuring time dependant electric and magnetic fields. Using time resolved-electron imaging, a charge-separated electric field induced in a femtosecond-laser ablation process has been initially investigated [97]. It is interesting to note that femtosecond laser pulses incident on solid targets can produce both short electron and X-ray pulses simultaneously. The electron pulses have higher intensity (because they are directly generated in the laser plasma interaction process and emitted in a narrow cone angle) and the interaction of electrons with matter is much stronger (several orders of magnitude) than that of X-rays. However, they suffer multiple scattering and thus the structure determination is sometimes more difficult from thicker samples. It may thus be advantageous in some experiments to employ both time-resolved electron diffraction and X-ray diffraction simultaneously for direct observation of structural dynamics with high temporal resolution. The current results indicate that sub-millijoule femtosecond laser plasmas may offer an interesting source of such synchronized electron and X-ray bursts.

Chapter 6

PIC SIMULATION

6.1 General description of the particle in cell (PIC) code

There are three basic approaches to describe and analyze the laser plasma coupling: the hydrodynamic, kinetic and the particle approaches. In the hydrodynamic model, the plasma is treated as two charged fluids (the electrons as one fluid and the ions as the other) and conservation laws of mass, momentum and energy are coupled to Maxwell equations. For a fluid description, a local thermodynamic equilibrium is assumed and the knowledge of the equation of state is necessary to close the system of equations. In kinetic theory, the evolution of the electron and ion distribution functions are calculated as a function of time.

In the particle approach, the plasma behaviour is analyzed using the equations of motion for the individual plasma particles that are introduced in particle simulation codes, known as particle-in-cell (PIC) codes [29, 43]. Thus, using PIC codes, the plasma is modeled as a collection of charged particles, electrons and ions, which are moving in their self-consistent, electric and magnetic fields, both that they themselves produce as well as any external applied field. Initially, a distribution of charged particle positions and velocities $f(\vec{r},\vec{v};t)$ is selected. Using the positions and the velocities of the particles, the electric charge and current densities are calculated on a spatial grid, sufficiently fine to resolve collective motions, using the following equations:

$$\rho = \sum_i q_i \int f_i\left(\vec{r},\vec{v};t\right) d\vec{v} \tag{6. 1}$$

$$\vec{J} = \sum_i q_i \int f_i\left(\vec{r},\vec{v};t\right) \vec{v}\, d\vec{v} \tag{6. 2}$$

where i is a quasi-particle, $f_i(\vec{r},\vec{v};t)$ is the particle distribution function, q_i, m_i, $\vec{r}$ and $\vec{v}$ are respectively the charge, mass, position and velocity of a particle denoted by index i, ρ is the electric charge density, and $\vec{J}$ is the current density.

The electric charge and current densities are then used to compute the electric and magnetic fields on a fixed spatial grid using Maxwell's equations:

$$\vec{\nabla} \cdot \vec{E} = \frac{\rho}{\varepsilon_0} \tag{6. 3}$$

$$\vec{\nabla} \cdot \vec{B} = 0 \tag{6. 4}$$

$$\vec{\nabla} \times \vec{E} = -\frac{\partial \vec{B}}{\partial t} \tag{6. 5}$$

$$\vec{\nabla} \times \vec{B} = \mu_o \vec{J} + \mu_o \varepsilon_0 \frac{\partial \vec{E}}{\partial t} \tag{6. 6}$$

where $\vec{E}$ is the electric field, $\vec{B}$ is the magnetic field, μ_0 is the permeability in free space, and ε_0 is the permittivity of free space. These fields are used in the equations of motion to determine the new positions and velocities of the particles. Knowing the new positions and velocities of the particles the whole cycle is repeated with a time step sufficiently small to resolve the phenomena of interest. Typically, the time step is determined by the highest frequency in the problem, which is often the electron plasma frequency [29]:

$$\Delta t \approx \frac{2\pi}{\omega_p} = \left(\frac{2\pi\varepsilon_0 m_e}{e^2 n}\right)^{1/2} \tag{6.7}$$

where e and m_e are the charge and the mass of the electron accordingly and n is the particle density.

As mentioned before, the spatial grid must be sufficiently small to resolve collective motions, which occur on a space scale greater or comparable to the electron Debye length rather than smaller scale length determined by direct particle collisions. The process is shown schematically in Figure 6.1:

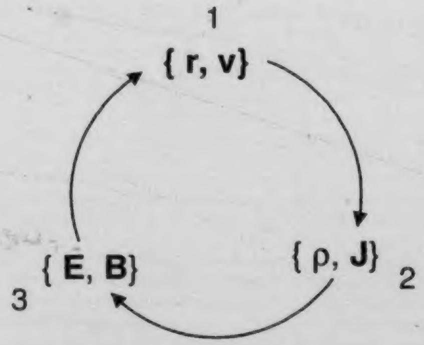

Figure 6.1 The basic cycle of a particle in cell simulation cycle. (Following Kruer [29])

Thus, PIC simulations codes are particularly useful to study particle kinetics and wave-growth in non-linear laser plasma interaction. In this thesis, 2D PIC simulations have been performed to investigate the laser-pulse interaction with plasma and the resulting generation of the highly accelerated electrons. A relativistic, parallel Particle-In-Cell (PIC) code MANDOR 2 [95] was utilized to perform these simulations.

Due to computer limitations, the number of particles included in the current computer simulation is limited to 10^6-10^7 particles. Therefore, typically, in PIC simulations the plasma consists of as a large number of quasi-particles, with each quasi-particle representing the action of a large number of physical particles. Each quasi-particle is described by its mass *m*, charge *q*, coordinates *x* and *y*, and responds to the values of the electrical and magnetic fields, $\vec{E}$ and $\vec{B}$ at the point of the quasiparticle. In the simulation, it is necessary to keep the mass-to-charge ratio of the electron quasi-particle equal to e/m_e.

A rectangular grid divides the simulation domain into cells where the electric and magnetic fields, current density and charge density are converted into discrete variables. The values of electrical and magnetic fields are calculated in any point inside the cell by interpolation. Therefore, the greater number of cells, the more precise is the representation of electrical and magnetic fields.

All physical variables depend on two spatial coordinates, *x* and *y*. The ions are treated as a fixed charge neutralizing background. The layout employed for the simulations is shown in Figure 6.2. Usually, a 1250×1250 grid is used with approximately 5×10^6 particles. The boundary conditions for the electromagnetic fields are periodic in the *y* direction (transverse direction) and absorbing in the *x*-direction

(direction of propagation). Typically, the electron foil is positioned in the middle of the simulation domain and a density profile is employed on the side of the foil facing the laser beam (front side) to simulate the preplasma conditions in the experiment. The laser pulse enters the domain from the left with polarization in the *y*-direction (p-polarized). The laser pulse parameters, i.e. intensity, wavelength, pulse duration, polarization, beam waist, and location of the focus, are defined in the first input file. The laser pulse characteristics are recorded on an interface, which is used as the boundary conditions for the main simulation domain. The metal foil (electron foil) is located in a second simulation domain, known as the main domain where the actual simulation of the laser-plasma interaction takes place. The characteristics of the main domain, i.e. size, number of cells, boundary conditions, interface, are chosen based on the specifics of the simulation. A second input file is run to create this environment. The laser beam is activated inside of the main domain using its recorded data at the entrance interface.

The Mandor 2 PIC code [95] was prepared and tested to run on either a single cpu mode or on the WestGrid' parallel computer facility [98]. Several diagnostics are available for users such as particle diagnostics, total energy averaged over the domain and spatial distributions of $\vec{E}$, $\vec{B}$, ρ, and $\vec{J}$. The visualization tool is Tecplot, which is installed on one of the computers with IP address glacier.westgrid.ca.

Schematic diagrams of the PIC run setup are shown in Figure 6.2 and Figure 6.3. The laser beam propagates along the *x* direction. The laser beam is incident on a metal foil, at an angle of 45°. In Figure 6.2, $\vec{N}_1$ and $\vec{N}_2$ are the normal directions of the frontside and backside of the metal foil, respectively. Each normal is represented by the angle with respect to the x direction, φ_z. In the case of 45° angle of incidence $\overrightarrow{N}_1$ is described by the angle $\varphi_z = 135°$, $\overrightarrow{N}_2$ is represented by the angle $\varphi_z = -45°$, and the specular direction, $\overrightarrow{S}$ is describe by the angle $\varphi_z = 90°$.

To replicate the experimental conditions, a density profile for the foil is employed such that the electron density profile is exponential from 0.03 n_c to 5 n_c for a 5 μm thick metal foil, as shown in the Figure 6.3. The main domain is a square of 50 μm ×50 μm, with a mesh size of 1250 along both x and y directions. The first simulations have been performed with a domain of 40 μm ×40 μm [3] [99].

---

[3] The first simulations were performed by D. Romanov and all subsequent simulations were performed by the author.

The laser beam is introduced into the main domain at the left boundary and it propagates along the *x* direction. Initially, it travels through a region of vacuum before reaching the underdense plasma created in front of the metal foil.

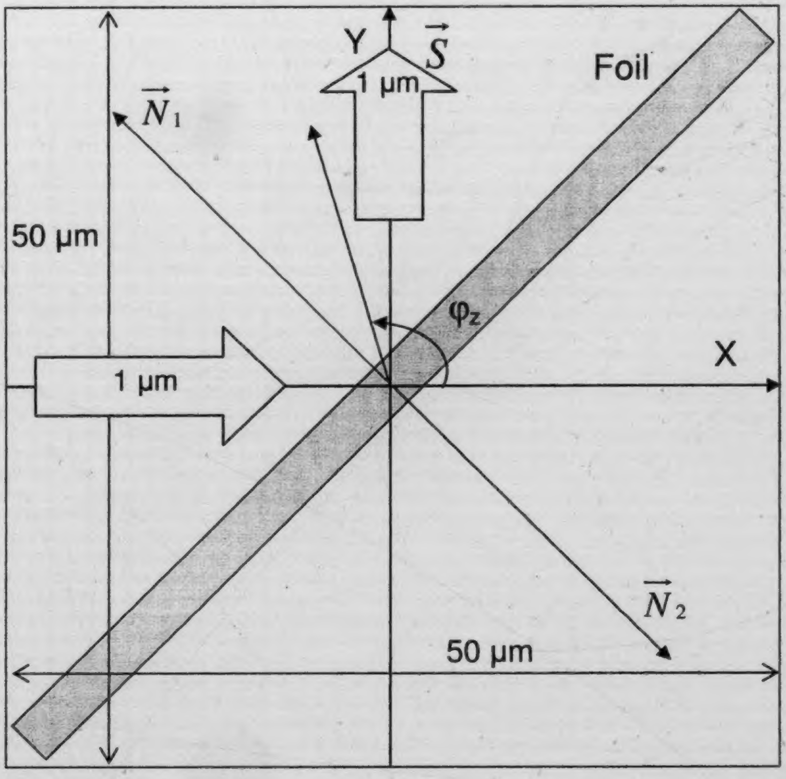

Figure 6.2 Schematic diagram of the PIC run setting. The laser beam propagates along the *x* direction. The laser beam is incident on a metal foil at 45°. $\vec{N}_1$ is the direction of the front side foil normal ($\varphi_z = 135°$). $\vec{N}_2$ is the direction of the back side foil normal ($\varphi_z = -45°$). $\vec{S}$ is the specular direction ($\varphi_z = 90°$).

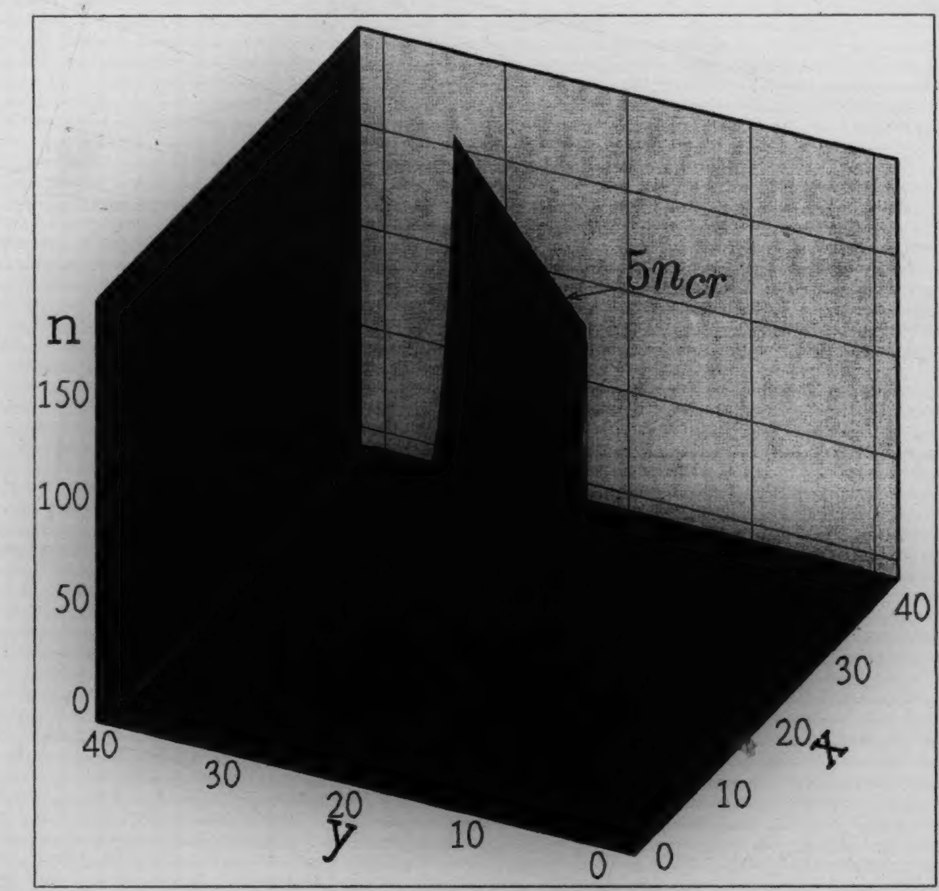

Figure 6.3 Schematic diagram of the PIC run setting. The laser beam is propagating along the *x* direction. The laser beam is incident on a metal foil at 45°. The initial electron density profile of the foil is set to be exponential from 0.03 n_c to 5 n_c[4].

---

[4] This figure was prepared by D. Romanov.

6.2 Simulation results

The figures 6.4 to 6.17 correspond to the same simulation. The laser beam has a Gaussian intensity profile with a beam diameter (FWHM) of 5 μm, a pulse duration (FWHM) of 130 fs and a peak intensity of 5.7×10^{16} W/cm^2 ($a_0 = 0.2049$). A Gaussian pulse truncated at ± 156 fs from the peak of the pulse at intensities of 0.018 I_{pk} is used in the simulations. Initially, the electron density profile of the foil is set to be exponential from 0.03 n_c to 5 n_c with a scale length of $L_n = \lambda_0$, where the wavelength used in the simulation is $\lambda_0 = 1\mu m$. The ions are fixed for this run. The domain size is 50 μm ×50 μm. The total time of the simulation run is 405 fs, the time the laser pulse takes to propagate through vacuum to the foil, interact with it and leave the domain. The number of particles used in this simulation is 5.3×10^6. To better resolve the main interaction between the laser pulse and metal foil a fine time resolution was used for the main part of the interaction. Three different time steps are used for this simulation. A time resolution of 20 fs is set for the initial 220 fs, a 1 fs time resolution for the next 55 fs, in which the main interaction takes place and for the last 130 fs, the time resolution is 10 fs. Due to the computer requirements, this simulation was performed on the WestGrid parallel computer facility using four cpu's [98]. Figure 6.4 (a) displays the laser pulse that enters the domain from left and propagates along the x-direction in vacuum before interacting with the foil at time t = 80 fs. The profile of $\left|\vec{E}_L\right|^2$ is extracted along the foil normal direction and is presented in Figure 6.4 (b) as a function of x-coordinate. Figure 6.5 (a) presents the electron density profile at the same time t =

80 fs, and because at this time there is little interaction yet the density profile is the initial density profile. The profile of n_e is extracted along the foil normal direction and presented in Figures 6.5 (b) as a function of x-coordinate. The output plots for electron density use a negative scale to indicate the negative charge of the electrons.

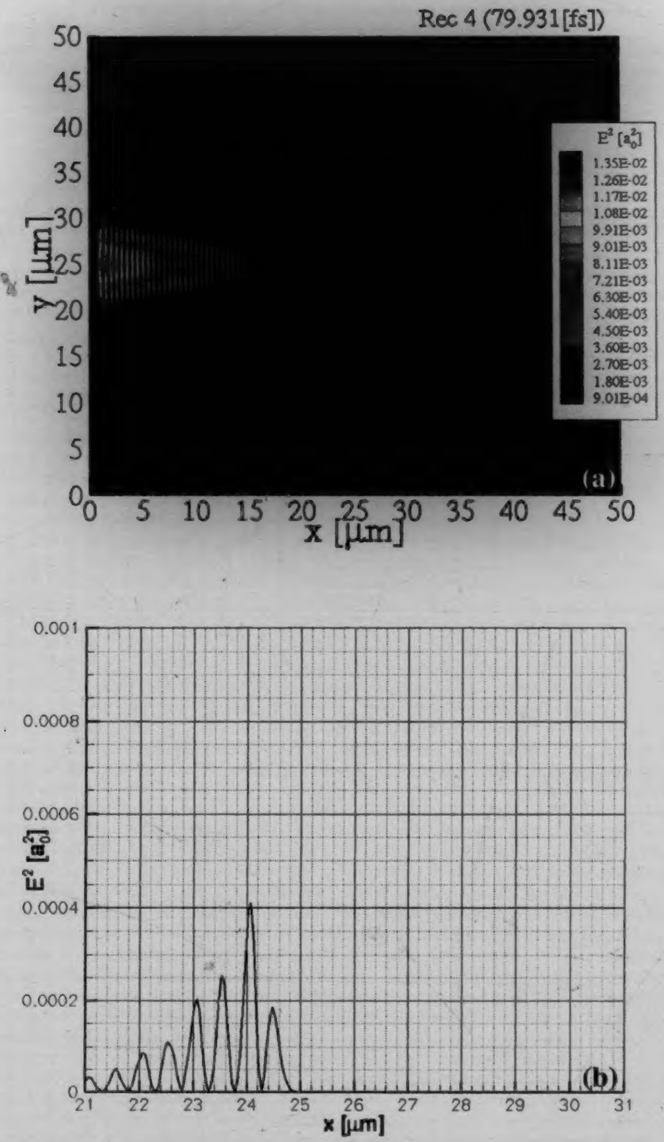

Figure 6.4 The laser electric field squared $\left|\vec{E}_L\right|^2$ at t = 80 fs. (a) The laser electric field squared $\left|\vec{E}_L\right|^2$ ($\left|\vec{E}_L\right|^2 \propto I_L$) propagating in the domain, and (b) $\left|\vec{E}_L\right|^2$ extracted along the foil normal direction as a function of x-coordinate. The beam enters the simulation domain from left and propagates along the x direction into the vacuum until it interacts with a 5-μm thick metal foil located in the central part of the domain at an angle of 45° with respect to the laser propagation direction.

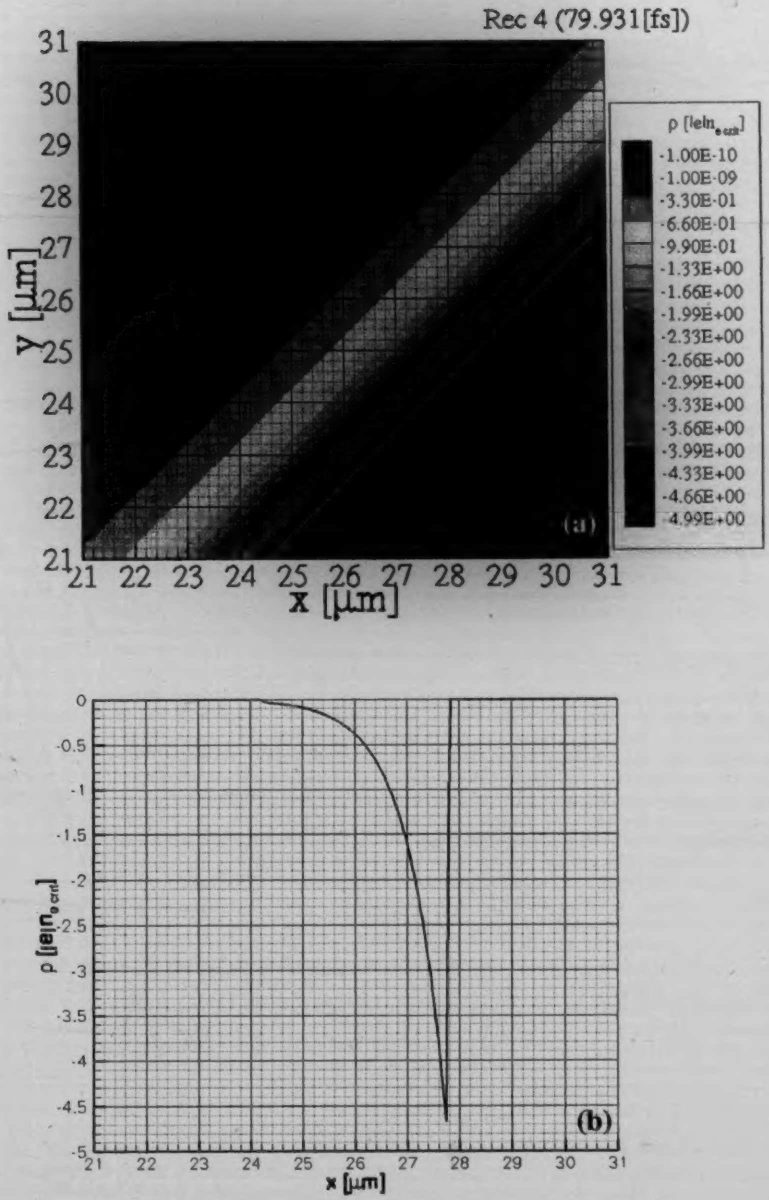

Figure 6.5 The electron charge density (n_e) at t = 80 fs. (a) The magnified central part of the electron density (n_e) profile, and (b) n_e extracted along the foil normal direction as a function of x-coordinate. The beam enters the simulation domain from left and propagates along the x direction into the vacuum until it interacts with a 5-μm thick metal foil located in the central part of the domain at an angle of 45° with respect to the laser propagation direction.

The peak of the laser pulse hits the foil target at the time t =244 fs. However, the first modifications of the foil density profile are observed at early times of the interaction between the laser pulse and the electron foil. For instance, the simulation results at t = 140 fs are presented in Figure 6.6 and Figure 6.7. The laser electric field squared $\left|\vec{E}_L\right|^2$ and its profile extracted along the normal foil direction as a function of x-coordinate at t = 140 fs are presented in Figure 6.6 (a) and (b), respectively. The electron density (n_e) and its profile extracted along the foil normal direction from (x=31μm, y=21 μm) to (x=21μm, y=31 μm) are provided in Figure 6.7 (a) and (b) , respectively, as a function of x-coordinate. At this time (t =140fs), the foil interacts with the foot of the laser pulse. At the reflection point, interference is observed between the incident and the reflected beams leading to an increase in the laser light intensity locally. Plasmas waves at critical density are created from the interaction between the laser pulse and the initial preplasma. One can notice from Figure 6.7 (b) an electron density perturbation at critical density.

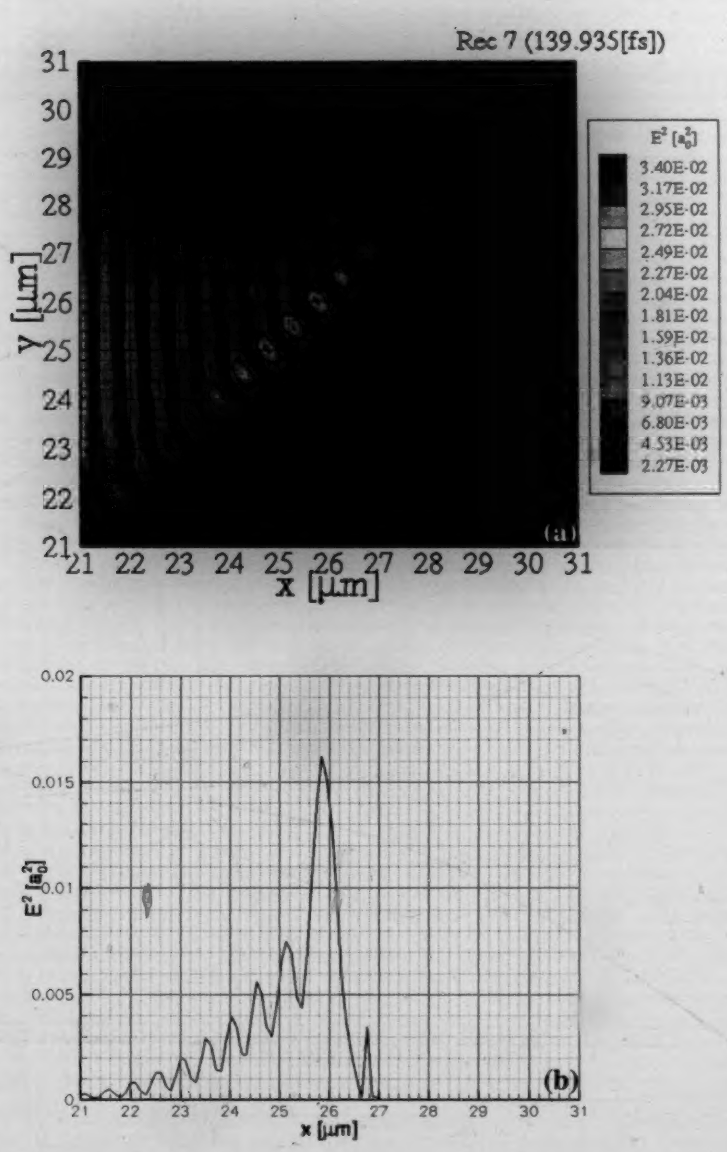

Figure 6.6 The laser electric field squared $\left|\vec{E}_L\right|^2$ at t = 140 fs. (a) The laser electric field squared $\left|\vec{E}_L\right|^2$ ($\left|\vec{E}_L\right|^2 \propto I_L$) propagating in the domain for y=25 µm, and (b) $\left|\vec{E}_L\right|^2$ extracted along the foil normal direction as a function of x-coordinate. The beam enters the simulation domain from left and propagates along the x direction into the vacuum until it interacts with a 5-µm thick metal foil located in the central part of the domain at an angle of 45° with respect to the laser propagation direction.

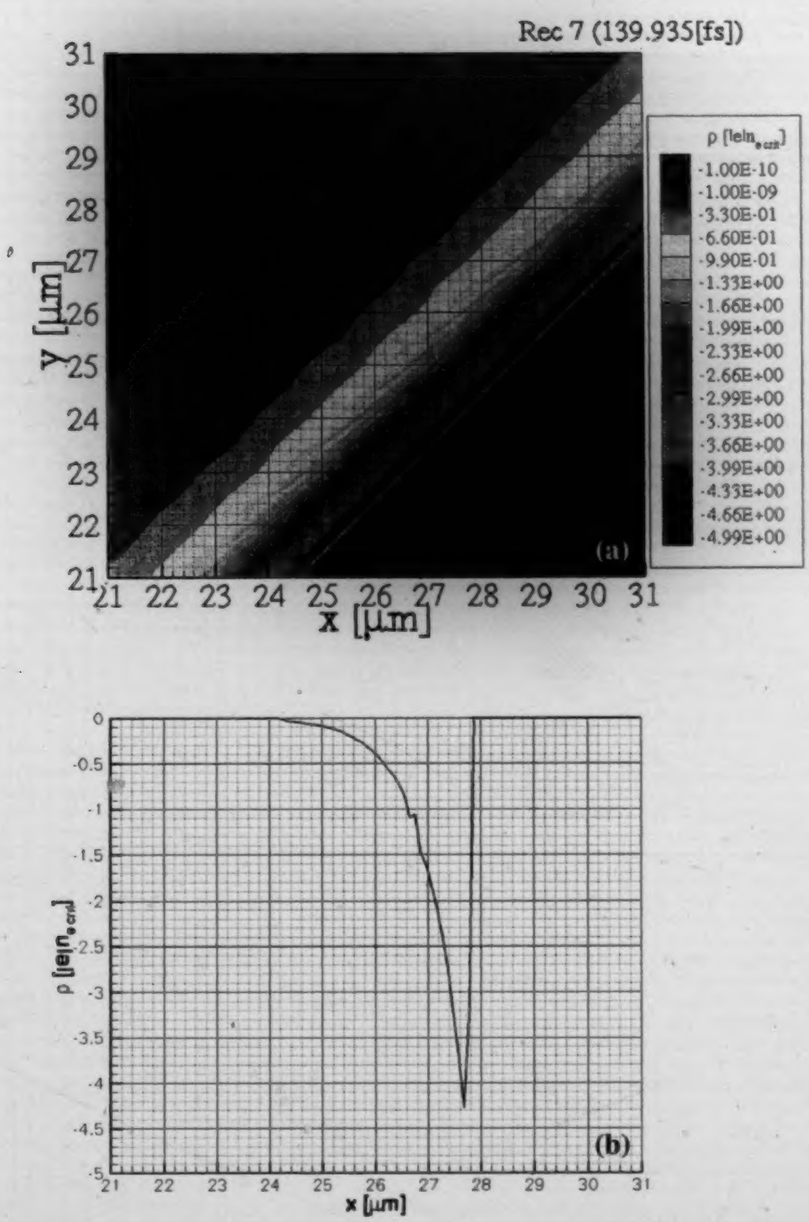

Figure 6.7 Electron density at t = 140 fs. (a) The magnified central part of the electron density (n_e) profile, and (b) n_e extracted along the foil normal direction from (x=31μm, y=21 μm) to (x=21μm, y=31 μm). The beam enters the simulation domain from left and propagates along the x direction into the vacuum until it interacts with a 5-μm thick metal foil located in the central part of the domain at an angle of 45° with respect to the laser propagation direction.

Figures numbered from 6.8 to 6.15 correspond to the same time interaction, t = 244 fs. At this time, the laser pulse reached the peak intensity of 5.7×10^{16} W/cm^2. Figure 6.8 and Figure 6.9 display the laser electric field squared $\left|\vec{E}_L\right|^2$ and the electron density n_e at this time, t = 244 fs. The laser pulse propagates into the underdense plasma up to the electron density $n_c cos^2\theta_{inc}$ (where θ_{inc} is the laser angle of incidence) before it is specularly reflected. At the reflection point, interference is observed between the incident and the reflected beams leading to a strong increase in the laser light intensity locally, i.e. $a_0^2 = 0.145$ at $x \approx 26\mu m$ versus a maximum $a_0^2 \doteq 0.042$ in vacuum. The electron density for this position is close to ½ n_c, which is consistent with the density at $n_c cos^2\theta_{inc}$ for $\theta_{inc} = 45°$. The laser electric field will tunnel through to the critical density at $x \approx 26.6\mu m$ but will decay exponentially in a distance determined by the penetration depth, which is $l = c/\omega_{pe}$ in the nonrelativistic case, where ω_{pe} is the plasma frequency. Accelerated electrons are leaving the foil from both the front and rear sides of the foil as can be observed from the magnified view of the foil density in Figure 6.9 (b). Waves in plasma can be seen at different electron densities in Figure 6.6 (b) as well. Close to the critical density n_c, these plasma waves appear to be quite strong as it is revealed by the electron density profile in Figure 6.10 (b). Figure 6.10 (a) and Figure 6.10 (b) represent the profile of laser electric field squared $\left|\vec{E}_L\right|^2$ and the electron density n_e, which are extracted along the foil normal direction from one corner to the other of the domain for the data presented in the Figure 6.8 and Figure 6.9.

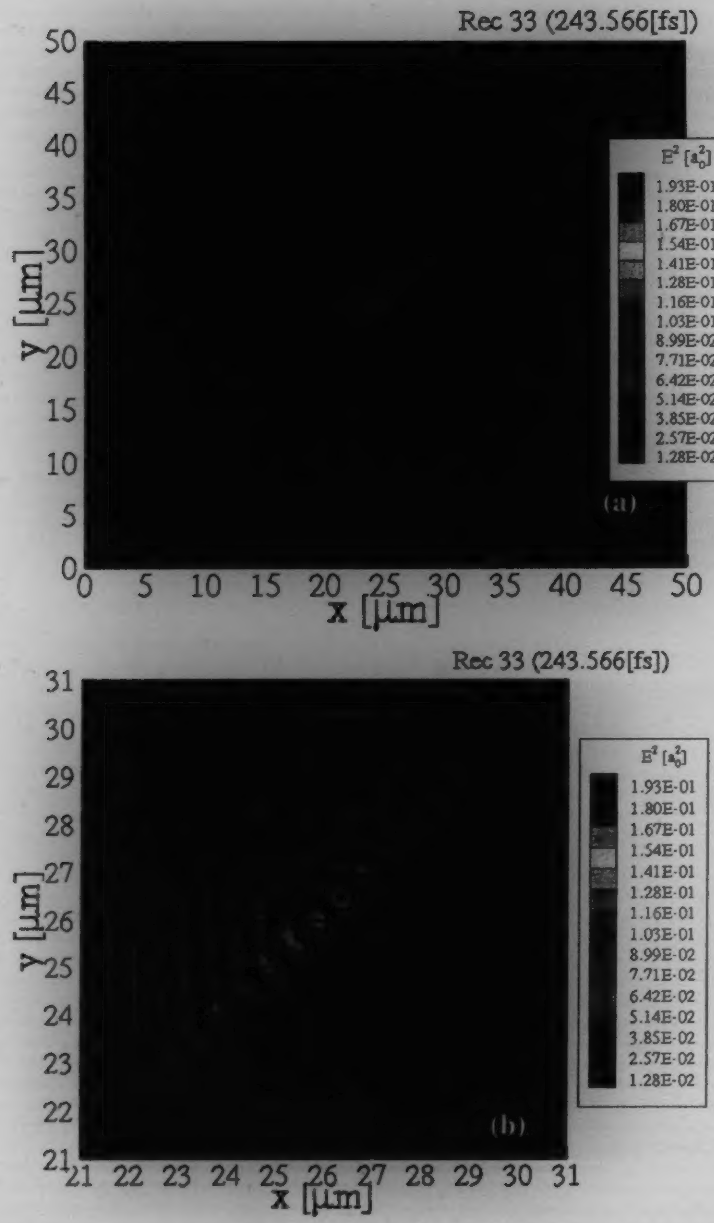

Figure 6.8 The laser electric field squared, $\left|\vec{E}_L\right|^2$ ($\left|\vec{E}_L\right|^2 \propto I_L$) at the peak of the laser pulse (t = 244 fs): (a) in the whole domain and (b) a magnified image of the interaction area. The laser beam is reflected by 5-μm thick metal foil located in the central part of the domain at an angle of 45° with respect to the initial laser propagation direction. The laser pulse has a peak intensity of 5.7×10^{16} W/cm^2, pulse duration (FWHM) of 130 fs and a beam diameter (FWHM) of 5 μm. The initial electron density profile of the foil is set to be exponential from 0.03 n_c to 5 n_c.

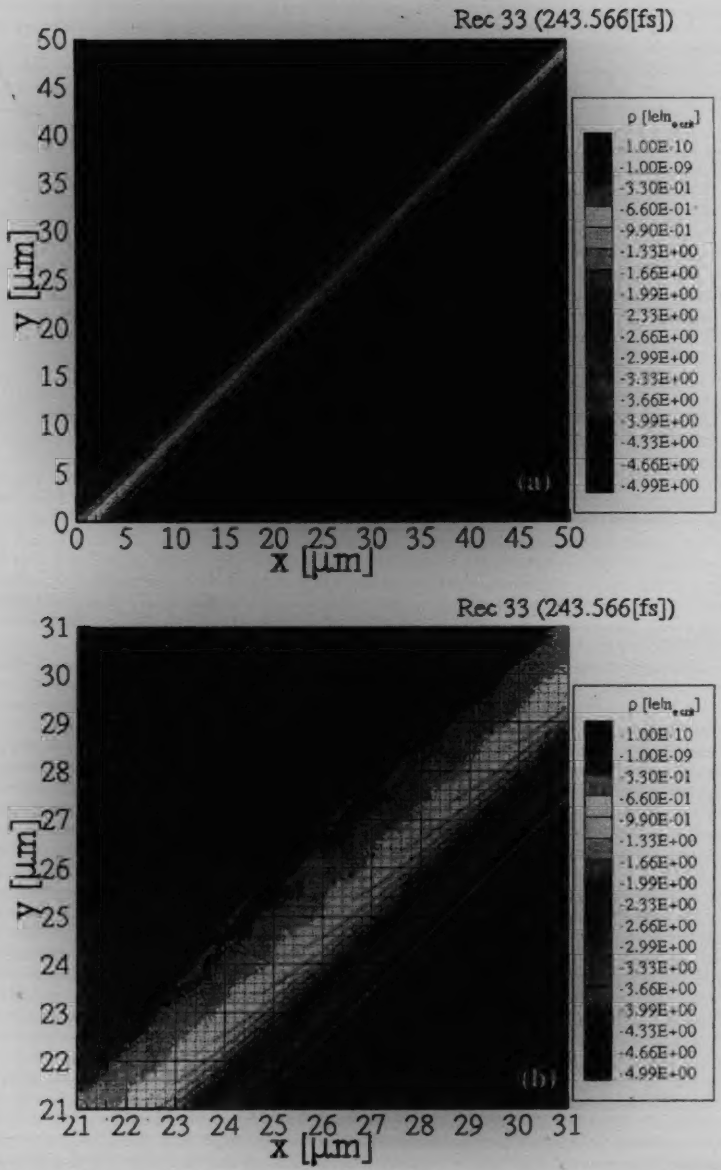

Figure 6.9 The electron density (n_e) at time t=244 fs when the peak of the laser pulse interacts with the 5-µm thick foil positioned at 45° with respect to the initial laser propagation direction: (a) in the whole domain and (b) a magnified image of the interaction area. The laser pulse has a peak intensity of 5.7×10^{16} W/cm^2, pulse duration (FWHM) of 130 fs and a beam diameter (FWHM) of 5 µm. The initial electron density profile of the foil is set to be exponential from 0.03 n_c to 5 n_c. Accelerated electrons are leaving the foil from both front and rear sides. Waves in plasma can be observed at different electron densities.

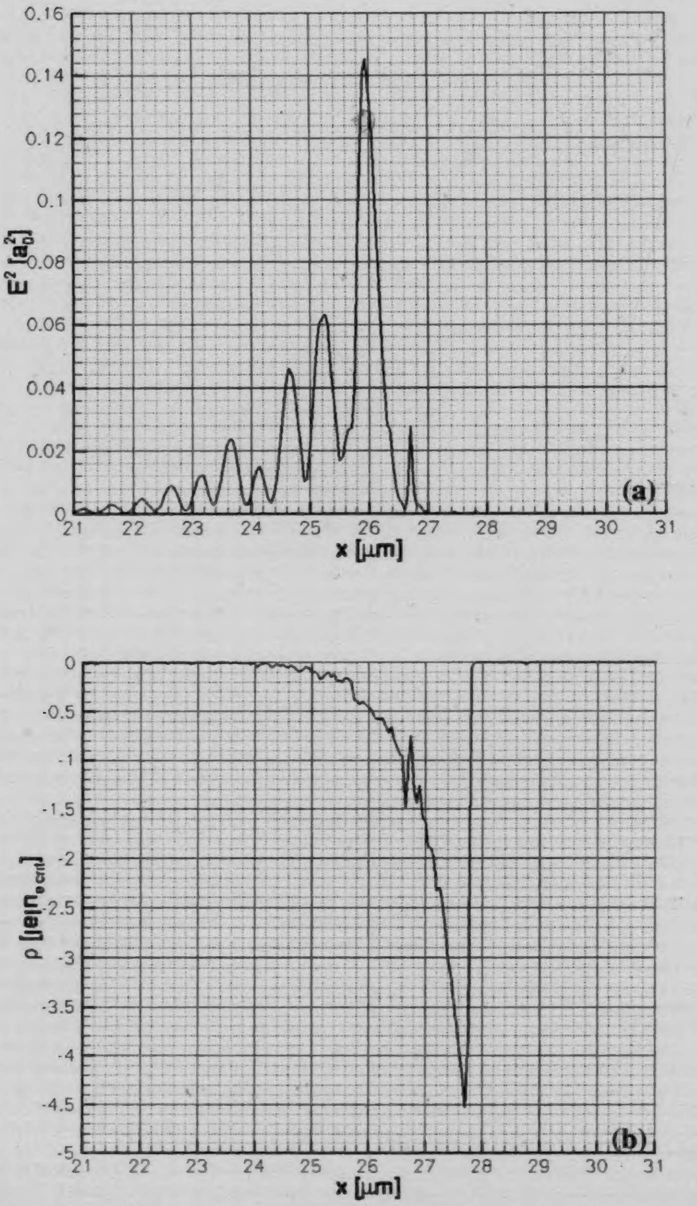

Figure 6.10 Profiles of (a) the laser electric field squared $\left|\vec{E}_L\right|^2$ at y=25 μm and (b) the electron density n_e extracted along the foil normal direction at t=244 fs. The normal direction used to extract n_e is defined by the two points, A(x= 21 μm, y=31 μm) and B (x= 31 μm, y=21 μm).

The density profile perturbation at critical density shown in Figure 6.10 (b) can be attributed to the resonance absorption process, as this involves the excitation of the electron plasma wave by the *p*-polarized laser light at the critical surface [29]. The electron density pattern is maintained for density profiles taken along the normal foil direction for different points in the foil as shown in Figure 6.11. An electron density scan along the foil, close to the critical density confirms that the electron plasma has a period of oscillation along the foil surface consistent with the incident laser wavelength of $\lambda_0 = 1\mu m$. This is illustrated in Figure 6.12. It is interesting to note that the electron density profiles along the *x* direction at different *y* positions display electron density perturbations in the underdense plasma close to the quarter critical density ($\frac{1}{4}n_c$) as seen in Figure 6.13, but also at few times the critical density as can be seen in Figure 6.14.

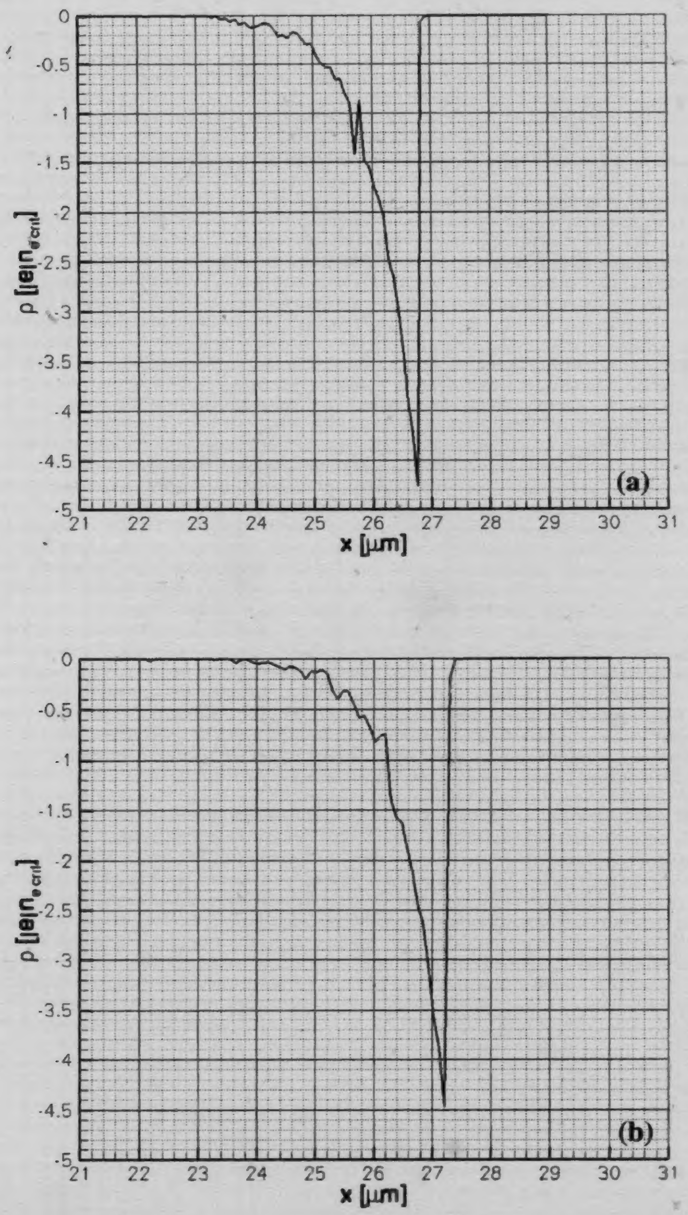

Figure 6.11 Profiles of the electron density n_e extracted along the foil normal direction at t=244 fs. (a) The foil normal direction is defined by the two points A(x=21 μm, y =29μm) and B(x=29 μm, y = 21μm) (b) The foil normal direction is defined by the two points A(x=21μm, y = 30μm) and B(x=30 μm, y = 21μm).

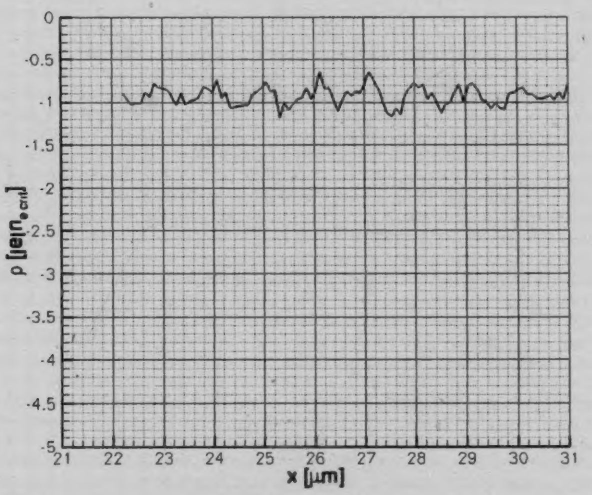

Figure 6.12 Electron density n_e extracted parallel to the foil surface close to the original critical density contour at t=244 fs. It can be observed that the electron wave has a period of 1 μm when plotted as a function of x-coordinate as done here, which is, as expected, the same as the laser period.

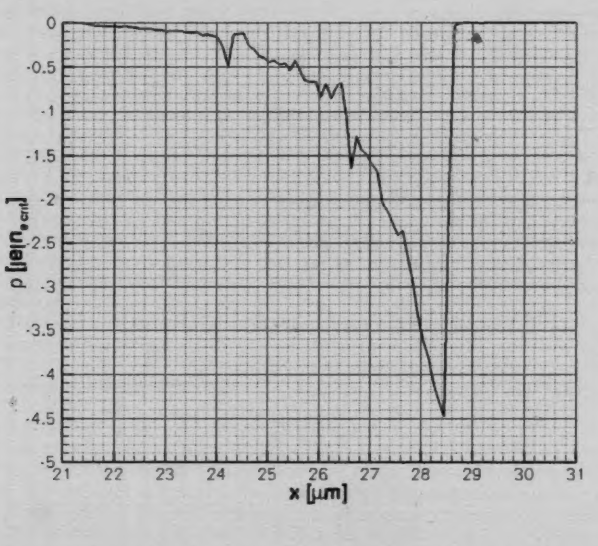

Figure 6.13 Electron density n_e extracted along the x-direction at y = 25 μm t=244 fs. Besides the electron density perturbation observed at critical density, another electron density perturbation can be seen in the underdense plasma close to the quarter critical density (¼ n_c).

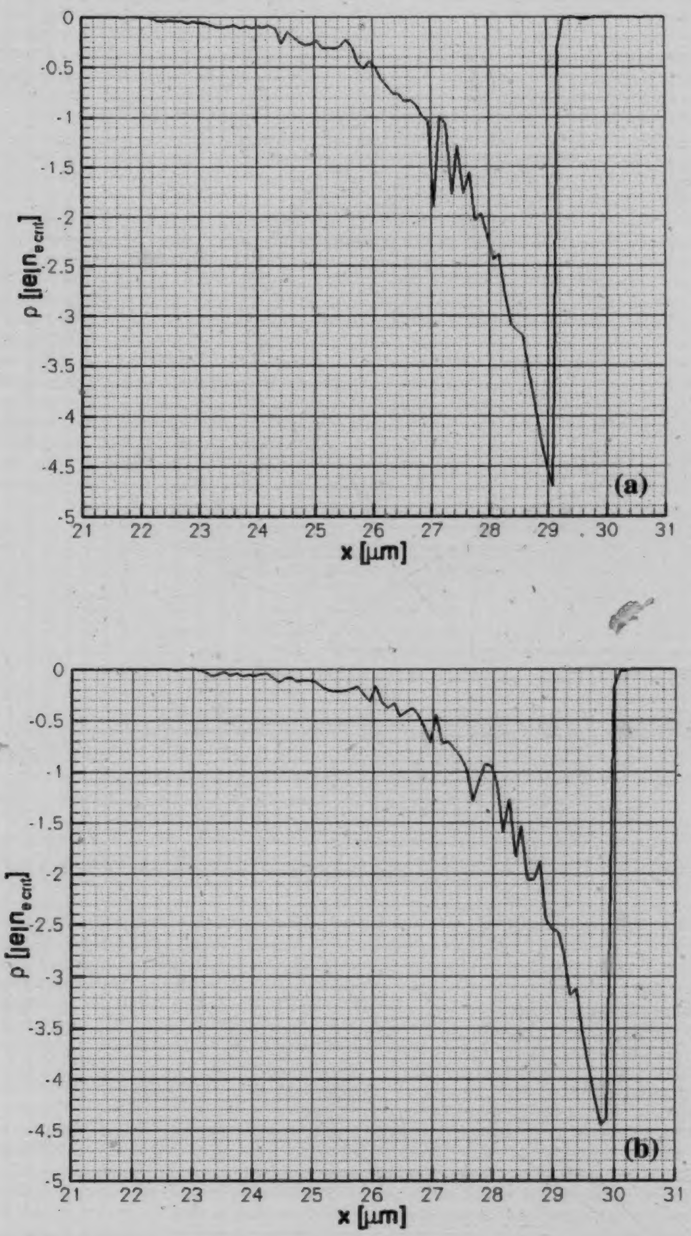

Figure 6.14 Profiles of the electron density n_e extracted along x-direction (a) at $y = 25.6$ μm and (b) at $y = 26.4$ μm at t=244 fs. These indicate that the laser light is also causing perturbations at several times the critical density.

The electron energy distribution versus angle φ_z at the peak of laser pulse is provided on Figure 6.15. Two electron jets with energies over 200 keV are observed to be emitted from the foil, one from the front side and the other from the rear side of the foil. The electron jet emitted from the front side is peaked at an angle $\varphi_z = 120°$, while the jet from rear side of the thin foil is found to be emitted at an angle $\varphi_z=-35°$. From PIC simulation setting provided in Figure 6.2 one observes that the direction of the foil normal is given by $\varphi_z = 135°$, while the specular direction is defined by $\varphi_z = 90°$. Therefore, the outgoing electrons are emitted between the specular and normal directions. The jet emitted from the rear side of the foil was not observed experimentally because a solid target was employed.

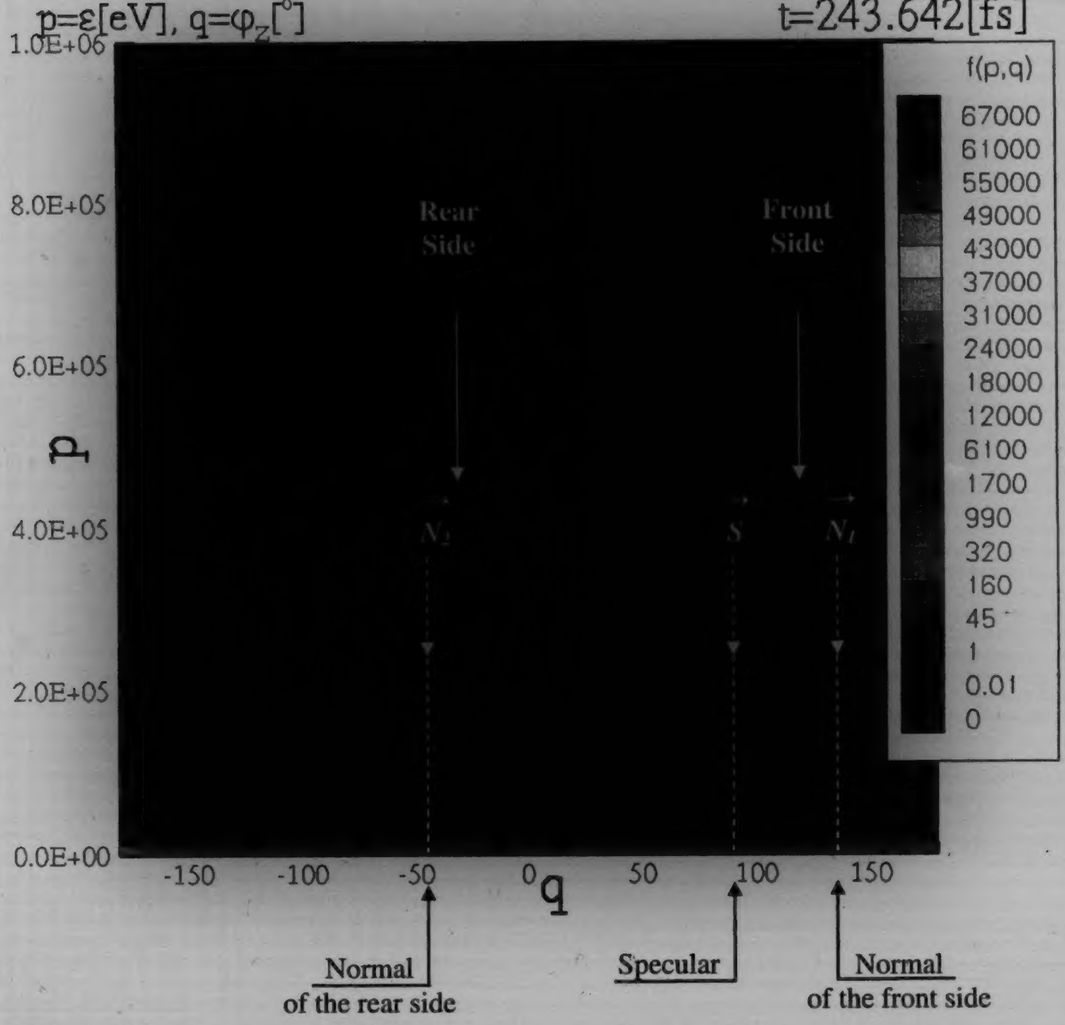

Figure 6.15 Electron energy distribution versus angle φ_z at the peak of laser pulse (t=244 fs). Two electron jets with energies over 200 keV are observed. The electron jet emitted from the front side is found to be between the specular and normal directions (angle $\varphi_z = 120°$). The jet from rear side of the thin foil is also observed in the simulations (angle $\varphi_z=-35°$), which is not measured in the experiments since a solid target was employed. The metal foil has 5-μm thickness and an initial exponential density profile from 0.05 n_c to 5 n_c. The laser pulse has a peak intensity of 5.7×10^{16} W/cm^2, pulse duration (FWHM) of 130 fs and a beam diameter (FWHM) of 5 μm. The normal direction of the front side, $\overrightarrow{N}_1$ is described by the angle $\varphi_z = 135°$. The normal direction of the rear side, $\overrightarrow{N}_2$ is represented by the angle $\varphi_z = -45°$, and the specular direction, $\overrightarrow{S}$ is describe by the angle $\varphi_z = 90°$.

These 2D PIC simulation results are found to be in good agreement with the experimental results for *p*-polarized laser pulses. In both cases, electron jets are observed with similar electron energies and angles of emission. For instance, electron jets with energies above 250 keV were detected experimentally as shown in Figure 5.1 and Figure 5.3 for laser angle of incidence of 30°. Although, only part of hot electron jet showed up on the film, assuming a symmetric spatial distribution, the jet appears to be emitted at an angle of about 8° from the target normal. From simulations, electrons with energies above 200 keV were observed as shown in Figure 6.15. The emission angle is 15° from the target normal. However, at this moment, it is still unclear what the exact origin of these accelerated high energy electrons is in both the experiments and PIC simulations. As discussed in Chapter 2, a number of collisionless processes can couple the laser energy into the plasma at these laser intensities, in the range of 10^{16} W/cm^2. The resonance absorption process is believed to be the principal candidate responsible to accelerate electrons in the plasma at critical density. This is confirmed by the electron density profile shown in Figure 6.10 and 6.11, and by the hot electron temperature T_{hot} determined from X-ray bremsstrahlung spectrum in Figure 4.11 and 4.12 as described in Chapter 4. From the electron density profiles displayed in Figure 6.11, 6.13 and 6.14, one can observe that the density profile is locally steepened near the critical density. As explained in Chapter 2, at critical density the electromagnetic wave can drive the plasma wave at resonance where $\omega_p=\omega_0$. The electrostatic field will grow in time and it will become more and more localized to the critical surface. The electrons entering in this strong localized field can be efficiently accelerated. The ponderomotive force of the intense electrostatic field will expel plasma, modifying the density profile [29]. However, these electrons are much too cold (in the range of 10 keV) to correspond to the super hot electrons forming the jets. In addition, there is disagreement in the angular dependence because resonance absorption will accelerate electrons along the normal direction, while in both the experiments and simulations, the electrons are found to be emitted between the normal and specular directions.

The electron distribution function F_e (E) at t=244 fs of all electrons in the simulation box is fitted with a sum of three electron Maxwellian distributions using a least-squares fit. The starting temperature in the PIC simulation is T_e=0. The hot electrons with energies in the energy range 15 keV to 60 keV were used to determine T_{1hot} with a resultant temperature of T_{1hot} = 15 keV. The hot electrons in the energy range 70 keV to 250 keV were used to determine T_{2hot} with a resultant temperature of T_{2hot} = 42 keV. T_{cold} = 2.6 keV describes the temperature of the bulk of the electrons with energies from zero to 15 keV. Similar values for the two hot electron temperatures were found when only the outgoing electrons from the front side of the foil were analyzed instead of the all electrons in the simulation box. This new electron distribution F'_e (E) at t=244 fs is shown in Figure 6.17. The outgoing (backwards) electrons were collected using a box described by the following coordinates x = [21, 27] and y = [25.5, 33.6]. The hot electrons with energies in the energy range 5 keV to 55 keV were used to determine T'_{1hot} with a resultant temperature T'_{1hot} = 15 keV. The hot electrons in the energy range 70 keV to 205 keV were used to determine T'_{2hot} with a resultant temperature T'_{2hot} = 41 keV.

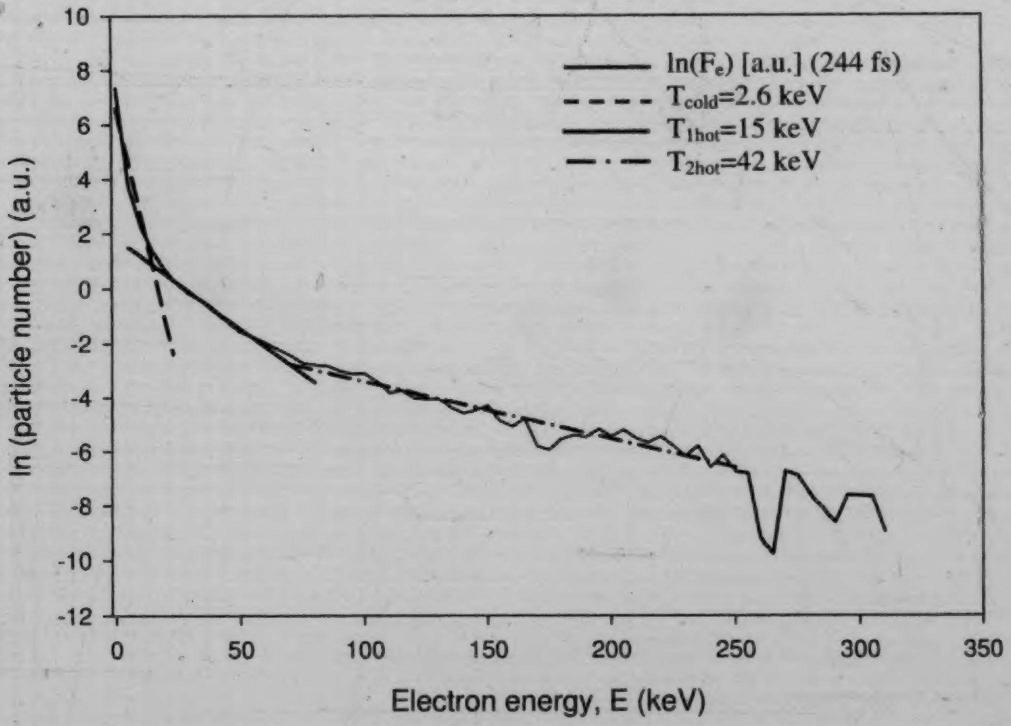

Figure 6.16 The electron distribution function of all electrons in the simulation box is fitted with three electron Maxwellian distributions using the least-square fit. T_{cold}=2.6 keV describes the temperature of the bulk of the electrons. The hot electron component is described by two electron temperatures: T_{1hot}=15 keV and T_{2hot}=41 keV.

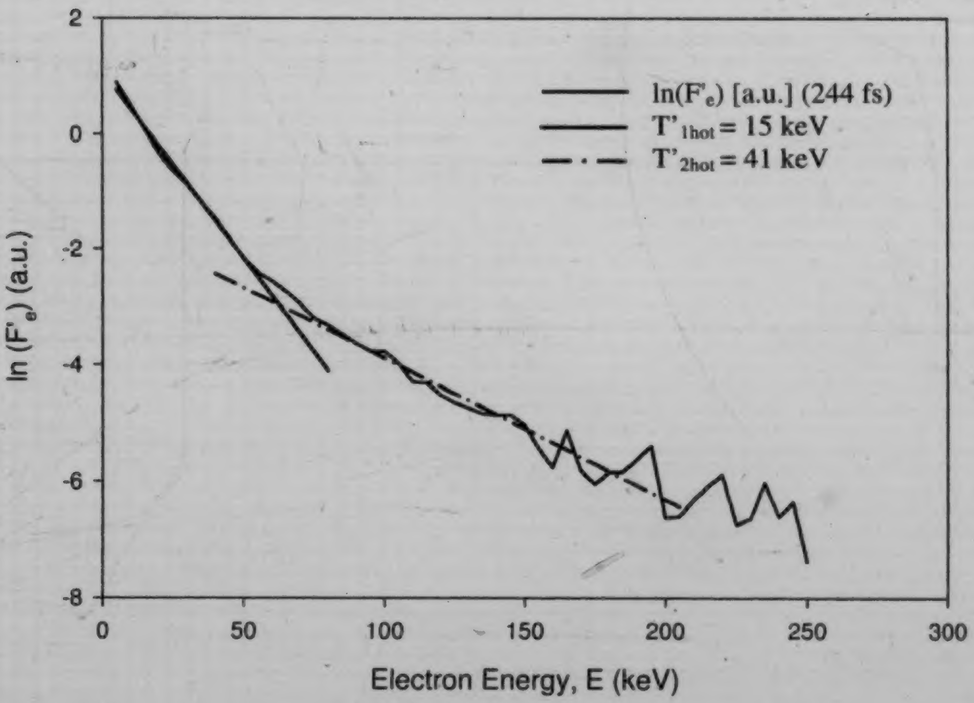

Figure 6.17 The hot electron component is described by two electron temperatures: T'$_{1hot}$=15 keV and T'$_{2hot}$=41 keV. Only the outgoing electrons have been considered in this case, which are located in the box described by the coordinates, x = [21, 27] and y=[25.5 33.6] at *t*=244 fs.

It was pointed out previously that in the case of simulations, electron density perturbations are found at quarter critical density (¼ n_c) as well. In the underdense plasma, electron plasma waves may be generated at quarter critical density due to so-called two-plasmon ($2\omega_{pe}$) instability. The hot electron temperatures of 30-60 keV have been reported with observable tails of up to 250 keV energy [49, 50]. However, again there is disagreement in the angular dependence because the high-energy electrons were typically found to be at an angle of 45 degrees to the incident *k*-vector in the plane of polarization.

The generation of very energetic electrons can also occur from the forward Raman scattering process [100], which occurs at densities of ¼ n_c or less. This would tend to generate electrons in the forward specular direction from the outgoing reflected radiation.

6.3 Simulations of angular hot electron distribution

In this section, a study of the hot electron angular dependence on the laser angle of incidence is presented. Simulations were performed for three angles of incidence: 30°, 45° and 60° and the angular distribution of the outgoing hot electrons have been analyzed for each case. Besides the angle of incidence, all the other parameters are kept the same, and they are very similar with the ones used in the simulation presented in the previous section. The time interval between output plots is about 38 fs, larger compared to the one used in the previous simulation. A better time resolution for all these simulations would give rise to excessive storage requirements that were too large for the computer facility that was available at the time this research was carried out.

The laser beam has a Gaussian intensity profile with a beam diameter (FWHM) of 5 μm, a pulse duration (FWHM) of 167 fs, a peak intensity $I_{pk} = 5.7\times10^{16}$ W/cm^2 and a wavelength $\lambda_0 = 1$ μm. The Gaussian pulse was truncated at ± 200 fs from the peak of the pulse at intensities of 0.019 I_{pk}. Initially, the electron density profile of the foil is set to be exponential from 0.03 n_c to 5 n_c, where n_c is the critical density, over a length of 5 μm for a scale length of L_n = 1 μm. For each angle of incidence, the angular distributions of the electrons with energies higher than 80 keV is determined at different times. There are two peaks of hot electrons that are observed in each simulation run. One peak appears at positive angles, which is formed by the hot electrons emitted from plasma in the backward direction, and the other peak is situated usually at negative angles and represents the electrons emitted from the rear side of the thin metal foil.

The angular distribution for 30° is shown in Figure 6.18. The peak of the laser pulse hits the foil at t =285 fs. However, the electrons begin to be emitted from the plasma at t=165 fs and by the time the peak of the laser pulse hits the foil, the particles have already reached the walls of the simulation box. Because of this, the data is not presented for times longer than 264 fs. The angle of the outgoing electron emission is fitted with a Gaussian function for the portion of the peak for the various output times. For t =264 fs, the peak angle is then obtained to be 114°. The normal direction of the front side of the foil is described by the angle $\varphi_z = 150°$ and the specular direction is described by the angle $\varphi_z = 120°$. The emission width of the outgoing electrons with energies over 80 keV is 88° (FWHM) at t=264 fs.

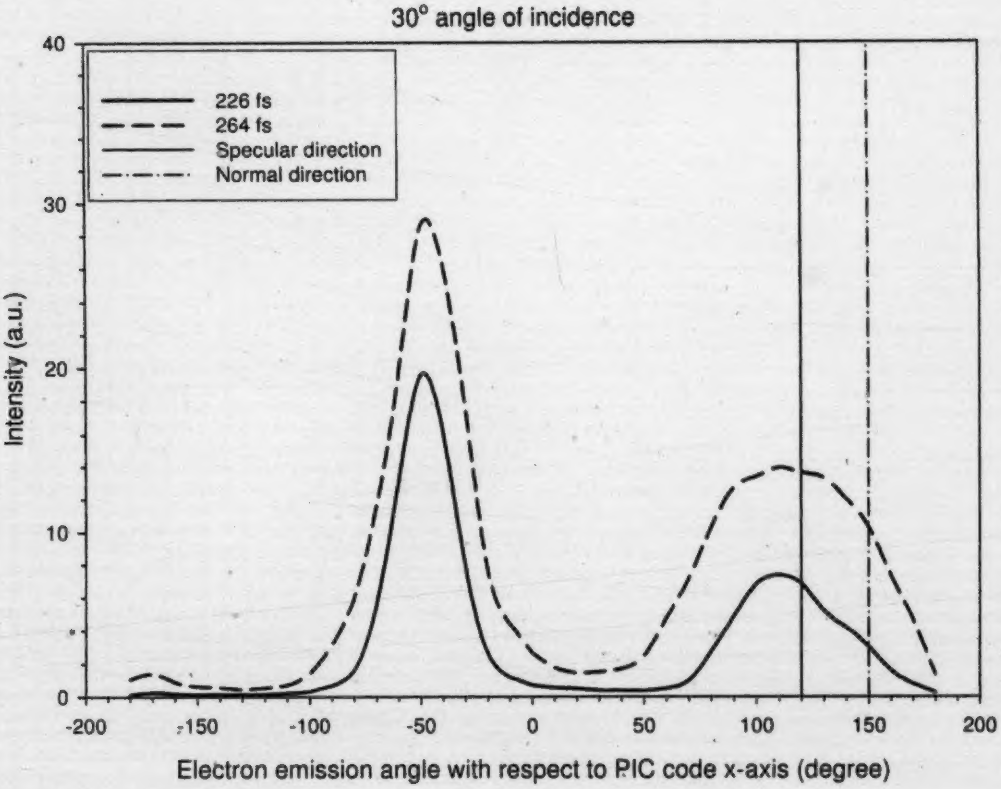

Figure 6.18 Angular distributions of the plasma electrons for two different times. The laser beam is incident on a 5.0 μm thick metal foil, at 30° angle of incidence in a p-polarized beam. The foil initial density profile was exponential starting from 0.03 n_c to 5.0 n_c corresponding to a density scale length $L_n = 1$ μm.

When the laser is incident at 45°, the emission angle is observed to be between normal and specular direction. The angular distribution for this angle of incidence is shown in Figure 6.19 for three different times. The electrons begin to be emitted from the plasma later (t =226 fs) compared to the previous case. The peak of the laser pulse hits the target surface at t=285 fs. The data is not presented for times longer than 377 fs because about this time the particles reach the walls of the simulation box and start to bounce back in the domain. The angular distribution of the outgoing electron emission is fitted with a Gaussian function for each of the three times. From the fits, the peak angles are obtained and they are presented in Table 6.1. The normal direction of the front side of the foil is described by the angle $\varphi_z = 135°$ and the specular direction is given by the angle $\varphi_z = 90°$.

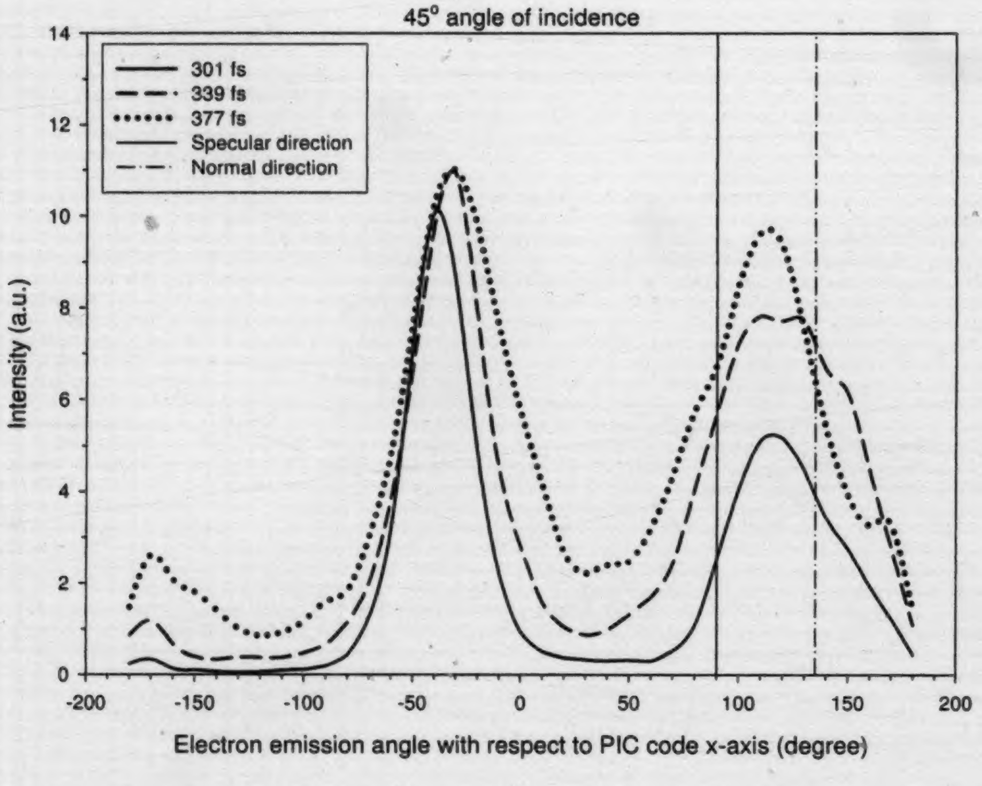

Figure 6.19 Angular distributions of the plasma electrons for three different times. The p-polarized laser beam is incident on a 5.0 μm thick metal foil, at 45° angle of incidence. The foil initial density profile was exponential starting from 0.03 n_c to 5.0 n_c corresponding to a density scale length $L_n = 1$ μm.

Table 6.1 The peak of the outgoing electrons with energies over 80 keV obtained at three different times, at 301 fs, 339 fs and 377 fs when laser beam is incident on a 5.0 μm thick metal foil, at 45° angle of incidence. The peak laser pulse hits the 5 μm thick foil target at the time t = 285 fs. The initial foil density profile is exponential starting from 0.03 n_c to 5 n_c, corresponding to a density scale length of 1 μm. The angles are measured from the PIC code x-axis.

Absolute emission time [fs]	301	339	377
Emission time after the peak laser intensity [fs]	16	54	92
Electron emission angle from PIC code x-axis [degree]	120	120	111

When the laser is incident at 60° the emission angle is observed to be close to the specular direction. The angular distribution for this angle of incidence is shown in Figure 6.20 for three different times. The electrons begin to be emitted from the plasma at later times (t =301 fs) compared to the previous case. The peak of the laser pulse arrives at the target surface at t=285 fs. The data is not presented for times longer than 415 fs because about this time the particles reach the walls of the simulation box and start to bounce back in the domain. The angular distribution of the outgoing electron emission at t = 415 fs is fitted with a Gaussian function and the peak angle is φ_z = 73°. The normal direction of the front side of the foil is described by the angle φ_z = 120° and the specular direction is describe by the angle φ_z = 60°.

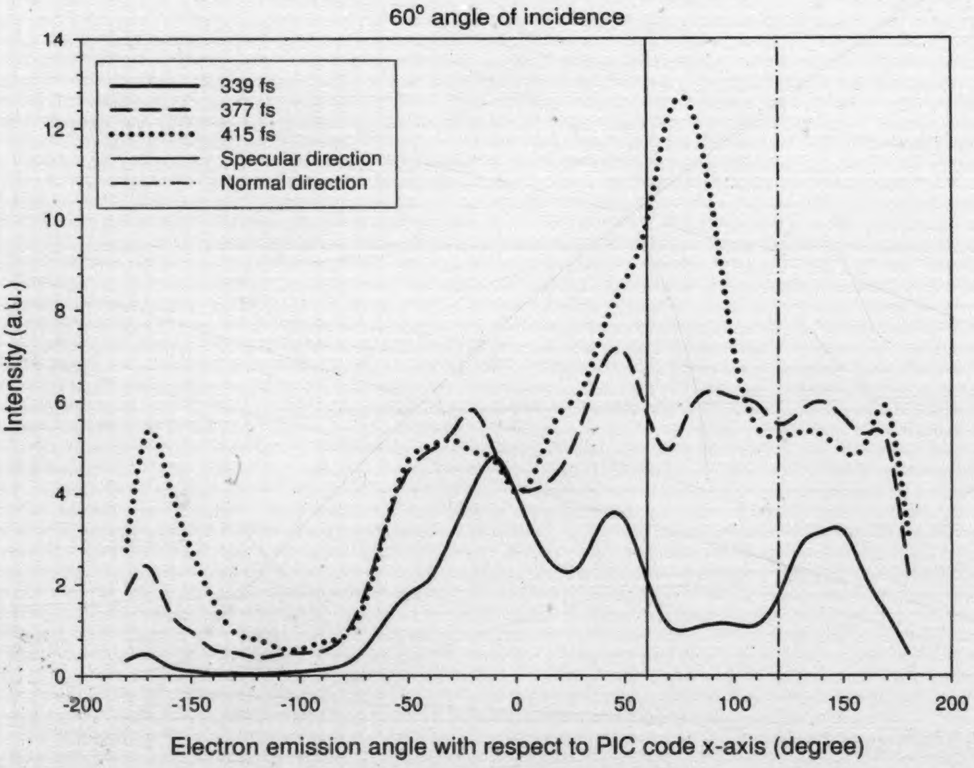

Figure 6.20 Angular distributions of the plasma electrons for three different times. The laser beam is incident on a 5.0 μm thick metal foil, at 60° angle of incidence. The foil initial density profile was exponential starting from 0.03 n_c to 5.0 n_c corresponding to a density scale length $L_n = 1$ μm.

A summary of the simulation results is provided in Figure 6.20 along with the experimental results obtained for angles of incidence of 30°, 36°, 42°, and 65°. The angular dependence of the emission of the outgoing hot electrons with energies over 80 keV is presented in chapter 5. The simulation results obtained for the angles of incidence of 45° and 60° agree reasonably well with the measurements. However, for smaller angle of incidence, i.e. 30°, the emission angle obtained from simulation is much higher than the one obtained experimentally. However, in the simulation at 30°, the electrons hit the edge of simulation box before the peak of the laser pulse and the emission angle may change at later times.

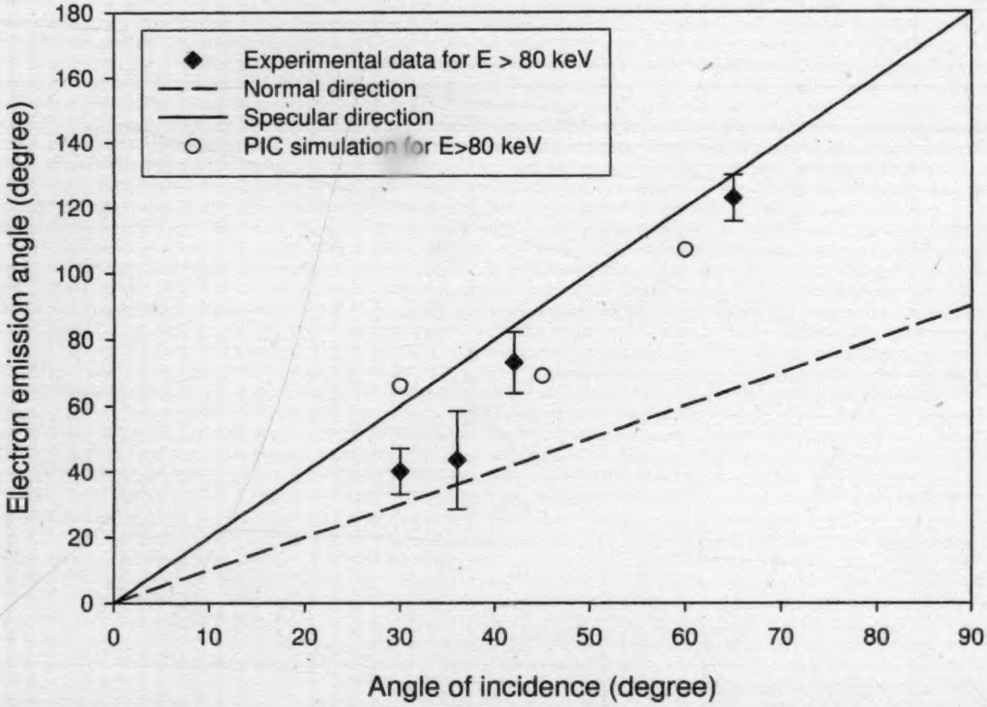

Figure 6.21 The angular distribution of the hot electrons with energy higher than 80 keV. The filled diamond points represent the experimental data while the open circles represent the simulation results. The angles obtained from the simulations are considered for the latest time for each simulation run, but before the particles reach the walls of the simulation box as they bounce back in the domain and alter the results. For θ_{inc}=30° this occurred before the peak of the laser pulse.

Both the experiments and the simulations were performed with p-polarized laser pulses. Experimentally, the emission angles of these hot electrons are between normal and specular directions and it appears that, with the increasing in the angle of incidence, the direction of the hot electron emission tends to move from target normal direction to the specular direction. It thus appears at higher angles of incidence it becomes more likely that the reflected light or the plasma surface wave may deflect the initial emission angle towards the specular direction. The 2D PIC simulation results agree well with the experimental measurements for 45° and 65°. However, the simulations did not reproduce the peak of the emission angle obtained for 30° angle of incidence.

6.4 Plasma density scale length effect on the hot electron emission

In order to understand the generation mechanisms better, further scaling studies have been carried out using PIC simulations. In this section, the hot electron emission is studied under different plasma scale length conditions using the 2D PIC simulation. The plasma density scale length is an important parameter in the physics of laser interaction with the plasma. For laser intensities above 10^{15} W/cm^2, the laser energy can be coupled to the plasma through numerous collisionless mechanisms depending on the characteristics of the density profile. Typically, most of the laser energy is absorbed close to the critical density n_c via resonance absorption. Nevertheless, the short laser pulse duration will create a small coronal region in front of the target. Many plasma instabilities are inhibited without a substantial region of coronal plasma. Due to the much steeper density profile laser energy can be absorbed at much higher density (several times critical density) in the femtosecond laser plasma interaction. This is applicable only for high contrast femtosecond laser systems because the physics of laser absorption will be significantly changed in the presence of a prepulse. If the prepulse is large enough, a large preplasma is created in front of the target and the laser interacts mainly with coronal plasma where many plasma instabilities usually occur. The different absorption mechanisms described in chapter 2 produce different hot electron distributions with different characteristics.

The laser beam used in the simulation has as a Gaussian intensity profile with a beam diameter (FWHM) of 5 μm, a pulse duration (FWHM) of 167 fs and a peak intensity of 5.7×10^{16} W/cm^2. The domain size is 50μm ×50μm. A mesh of 1250×1250 is used in each case. The laser pulse enters the domain from left and propagates along the x direction in vacuum before interacting with the foil. An electron foil represents the metal foil and the ions are treated as a fixed charge neutralizing background. An initial electron density profile is chosen for the electron foil to simulate an initial preplasma in front of the target. All the simulations have been performed at 45° angle of incidence. The incident radiation wavelength was $\lambda_0 = 1$ μm. The laser light has vertical polarization (along y direction) and thus it is p-polarized on the metal foil. Figure 6.1 and Figure 6.2 provide the simulation geometry employed for these PIC simulations. The time interval between output plots is 38 fs. The peak of the laser pulse hits the foil target at the time t = 285 fs. The density scale length is changed by changing the metal thickness and/or modifying the initial density profile. The following cases are considered:

1. 5-μm thick electron foil with an initial exponential density profile from 0.03 n_c to 5 n_c corresponding to $L_n = 1$ μm.
2. 2.5-μm thick electron foil with an initial exponential density profile from 0.03 n_c to 5 n_c corresponding to $L_n = 0.5$ μm.
3. 2.5-μm thick electron foil with an initial exponential density profile from 0.03 n_c to 7.5 n_c corresponding to $L_n = 0.45$ μm.
4. 5-μm thick electron foil with an initial exponential density profile from 4.9 n_c to 5 n_c. corresponding to $L_n = 0$ μm.

The results for the first case are presented in the previous section for the angle of incidence of 45° in Figure 6.19 and Table 6.1. The angular distributions of the outgoing hot electrons with energies higher than 80 keV for the other three cases are presented in Figure 6.22, Figure 6.23, and Figure 6.24. Again, there are two peaks of hot electrons that can be observed in all simulation runs. One peak appears at angles between the normal and specular directions, which is formed by the hot electrons emitted from plasma in the backward direction, and the other peak is situated at negative angles, usually at $\varphi_z \approx -30°$, which represents the electron emitted from the rear side of the thin metal foil. For each case, the angular distribution of the hot electron emission is plotted for three different times after the interaction between the laser peak intensity and the metal foil. The peak emission angle of the outgoing electron emission is fitted with a Gaussian function for each record time. The emission angles are summarized in Table 6.1 (p. 169), Table 6.2, and Table 6.3.

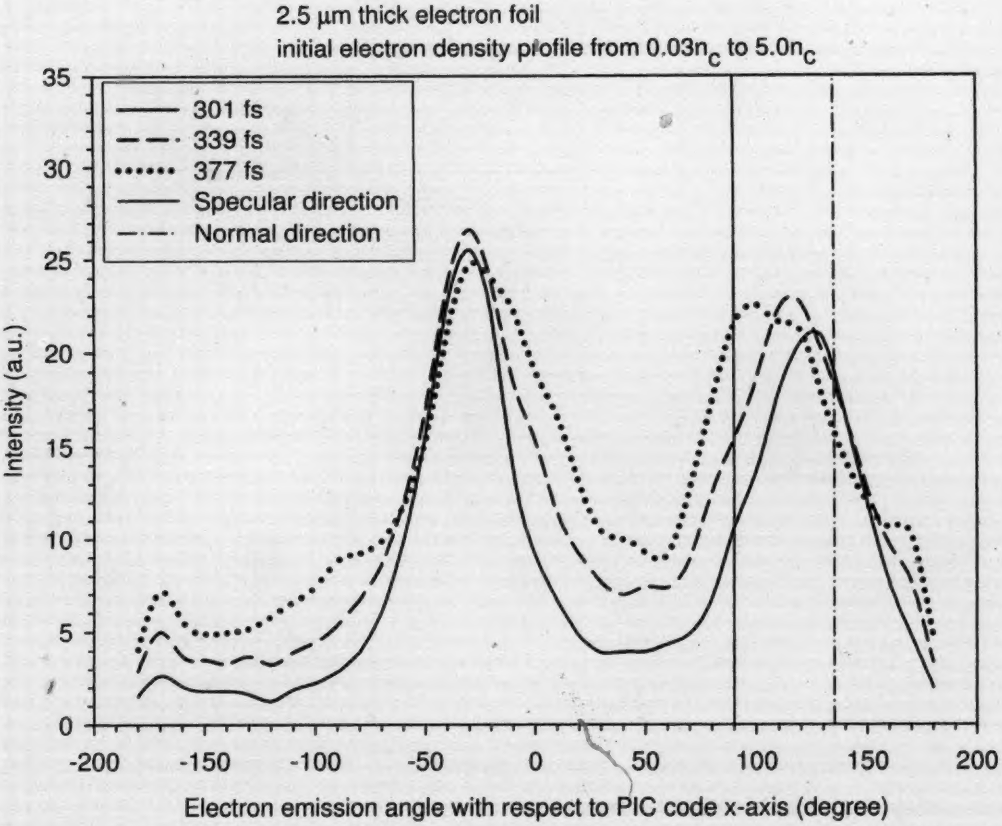

Figure 6.22 Angular distributions of the hot electrons with energies over 80 keV for three different times. The laser beam is incident on a 2.5 μm thick metal foil, at 45° angle of incidence. The foil initial density profile was exponential starting from 0.03 n_c to 5.0 n_c corresponding to a density scale length $L_n = 0.5$ μm..

Table 6.2 The peak of the outgoing electrons with energies over 80 keV obtained at three different times, at 301 fs, 339 fs and 377 fs. The peak laser pulse hits the 2.5 μm thick foil target at the time t = 285 fs. The initial foil density profile is exponential starting from 0.03 n_c to 5 n_c, corresponding to a density scale length of 0.5 μm. The angles are measured from the PIC code *x*-axis.

Absolute emission time [fs]	301	339	377
Emission time after the peak laser intensity [fs]	16	54	92
Electron emission angle from PIC code *x*-axis [degree]	123	116	106

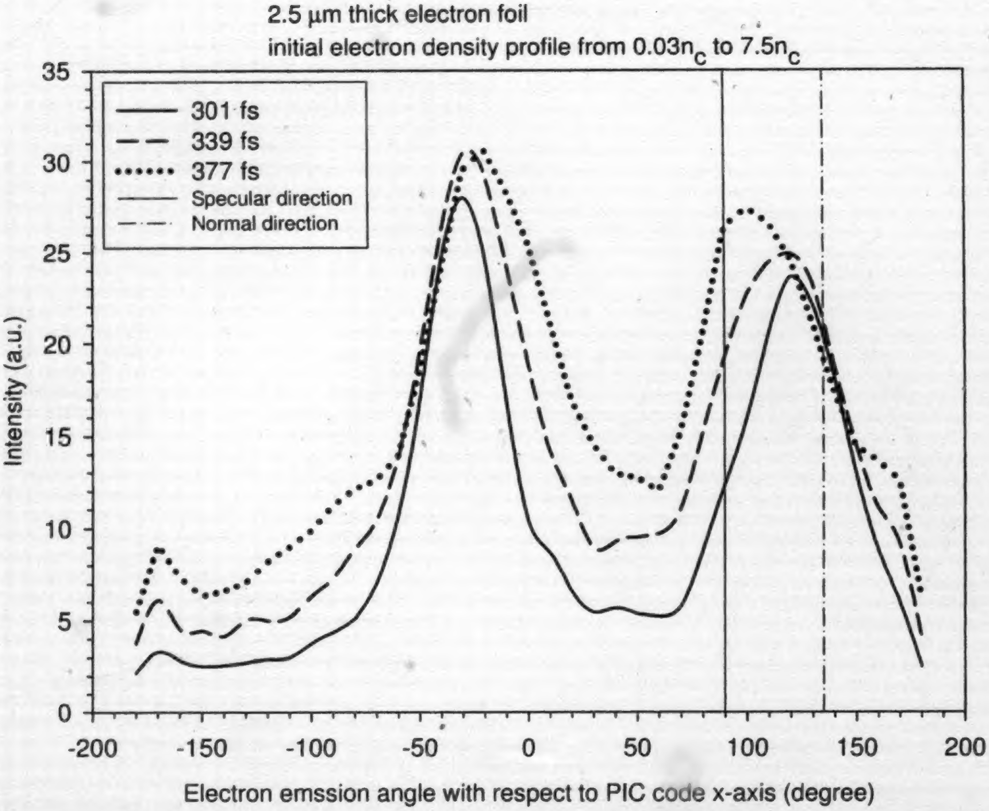

Figure 6.23 Angular distributions of the hot electrons with energies over 80 keV for three different times. The laser beam is incident on a 2.5 μm thick metal foil, at 45° angle of incidence. The foil initial density profile was exponential starting from 0.03 n_c to 7.5 n_c corresponding to a density scale length $L_n = 0.45$ μm.

Table 6.3 The peak of the outgoing electrons with energies over 80 keV obtained at three different times, at 301 fs, 339 fs and 377 fs. The peak laser pulse hits the 5 μm thick foil target at the time $t = 285$ fs. The initial foil density profile is exponential starting from 0.03 n_c to 7.5 n_c, corresponding to a density scale length of 0.45 μm. The angles are measured from the PIC code *x*-axis.

Absolute emission time [fs]	301	339	377
Emission time after the peak laser intensity [fs]	16	54	92
Electron emission angle from PIC code *x*-axis [degree]	120	115	106

When the laser pulse is incident on steeper density gradients as it is the case for the simulations performed with 2.5-μm thick foil for which the density scale length is L_n= 0.5 μm and L_n= 0.45 μm, the electrons are emitted initially in the direction very close to the target normal. The original emission direction changes in time from the target normal to the specular direction. In about 90 fs, the emitted direction changes by approximately 17° and 15° as presented in Figure 6.20, and 6.21, respectively. A smaller change of 9° in the emission angle is observed in the case of 5-μm thick foil as shown in Figure 6.19. This suggests a change in the relative importance of different mechanisms of hot electron generation as the scale length becomes steeper. The data is not analyzed for times longer than 377 fs since about this time, the particles start to reach the walls of the simulation box.

When the laser pulse is incident on step like density profile, i.e. in the case of 5-μm thick electron foil with an initial exponential density profile from 4.9 n_c to 5 n_c, the number of electrons accelerated is very small with most of hot electrons having energies of 50 keV. There are very few electrons with energies higher than 100 keV and no electrons are observed with energies above 150 keV. The emission angle of the outgoing hot electrons peaks at φ_z=119° (16° from the normal direction and 31° from the specular direction). This is directed more towards the normal direction than in the cases with preplasma considered above. There are no experimental results from our measurements for the case of no preplama to compare with the simulation results presented here. However, results reported by Chen et al. [60] have indicated that the emission of the hot electrons was observed in the specular direction when the target was irradiated by the p-polarized laser pulses without prepulses, contrary to the above trend.

Chen et al. [60] also noted that their simulations are contrary to the experimental results for the no prepulse case. In the future, the preplama can be suppressed in our experiment by introducing another Pockels cell into the laser beam path prior to the grating compressor. This would allow a better comparison with the 2D PIC simulation results.

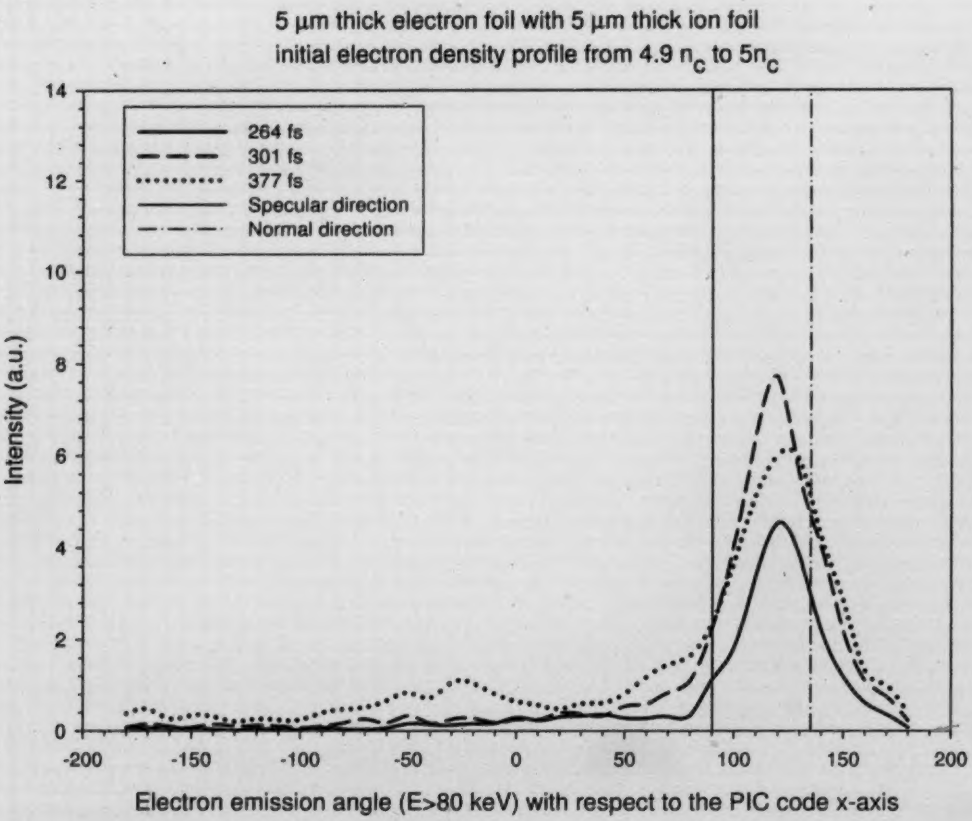

Figure 6.24 Angular distributions of the hot electrons with energies over 80 keV for three different times. The laser beam is incident on a 5.0 μm thick electron foil. The initial density profile was set to be exponential starting from 4.9 n_c to 5.0 n_c corresponding to a density scale length $L_n = 0$ μm.

The influence of the ion motion on the hot electron emission is tested by adding, besides the 5-μm thick electron foil with an initial exponential density profile from 0.03

n_c to 5 n_c, another foil of ions with the same thickness and density profile. The ions have charge q=+1 and mass m=1840 m_e (where m_e is the electron mass). The results are presented in Figure 6.25 and Table 6.4. The simulations are carried out for an exponential density scale length of L_n = 1 µm.

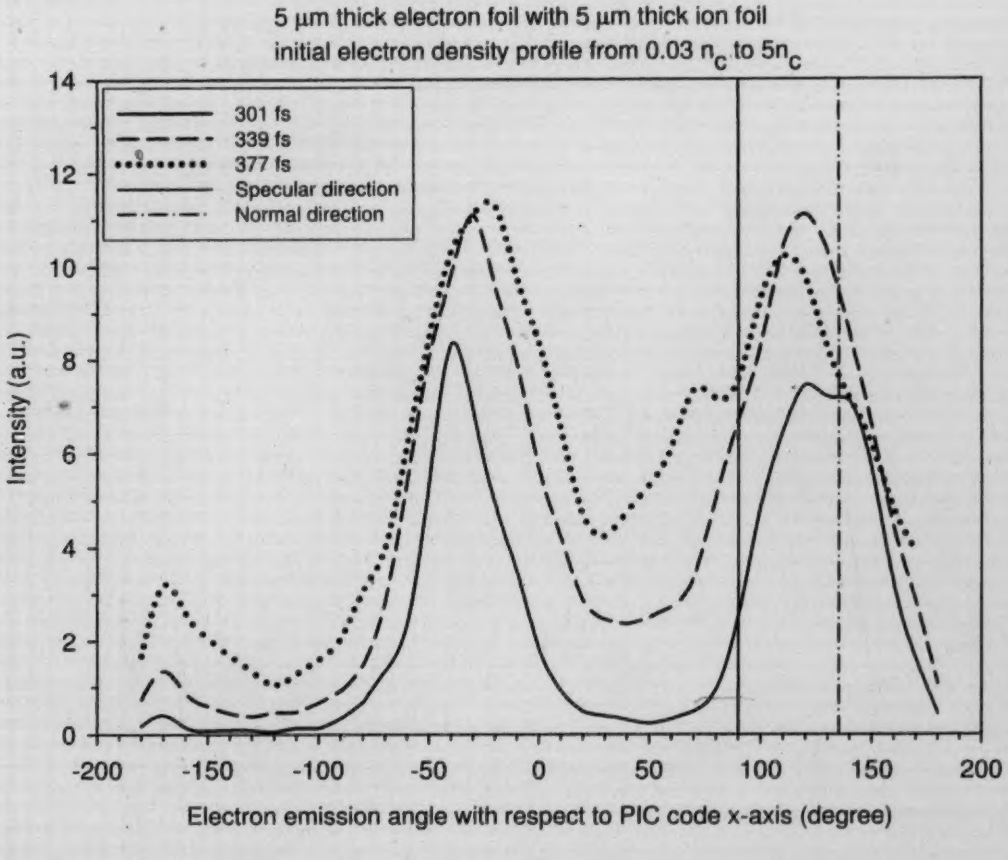

Figure 6.25 Angular distributions of the hot electrons with energies over 80 keV for three different times. The laser beam is incident on a 5.0 µm thick electron foil accompanied by a 5.0 µm thick ion foil at 45° angle of incidence. The initial density profile for both foils was set to be exponential starting from 0.03 n_c to 5.0 n_c corresponding to a density scale length L_n = 1 µm. The ions have charge q=+1 and mass m=1840 m_e (where m_e is the electron mass).

Table 6.4 The peak of the outgoing electrons with energies over 80 keV obtained at three times at 301 fs, 339 fs and 377 fs. The peak laser pulse hits the 5 μm thick foil target at the time $t = 285$ fs. The initial foil density profile is exponential starting from 0.03 n_c to 7.5 n_c, corresponding to a density scale length of 0.45 μm. The ions are free to move and have a mass of 1840 m_e and charge of $q = +1$. The angles are measured from the PIC code *x*-axis.

Absolute emission time [fs]	301	339	377
Emission time after the peak laser intensity [fs]	16	54	92
Electron emission angle from PIC code *x*-axis [degree]	127	119	112

At early times of interaction, very close to the interaction between the laser peak intensity and the foil, the emission is almost along the normal direction. The direction of these hot electrons changes by 15° towards the specular direction in 92 fs. At this time, the laser beam is almost all reflected.

In conclusion, the electron jets consisting of high energies of 80 keV to over 200 keV can be generated by the tail of the hot electron distribution from plasma instabilities, two-plasmon instability or forward Raman scattering. It appears less likely that the electrons are generated directly by Resonance Absorption since these electrons would be much colder. It is possible that in the present case electric and magnetic fields generated by the laser plasma interaction may also contribute to give some deflection of these electrons from their initial direction. It is also possible that the surface waves that have been observed propagating along the critical and quarter critical surface in the simulation may steer the hot electrons towards the specular direction, but it is not immediately clear how effective these surface waves are in the present case.

In the future, measurements of the $3\omega_0/2$ emission can be carried out in order to determine if two-plasmon instability is present in the experiment as well. The $3\omega_0/2$ emission occurs from the interaction between the incident and reflected laser radiation with a plasma wave close to the quarter critical density [29]. Therefore, $3\omega_0/2$ emission can be a useful signature of the two-plasmon decay instability in the underdense plasma. This diagnostic was used in different laser-plasma experiments [101, 102] in the past. Another diagnostic that may be used for future experiments is the measurement of the very hard X-ray bremsstrahlung spectrum in order to determine the hot electron temperature of the very energetic electrons. An electron energy spectrometer could also be used to measure the high-energy electron distribution function directly.

Chapter 7

CONCLUSION

The emission of keV X-rays from laser-produced plasmas using a tabletop femtosecond laser system was studied in order to develop a compact and efficient K_α X-ray source to be operated at kilohertz repetition rate. The development of such sources is of considerable interest for application of time-resolved X-ray diffraction and X-ray microscopy.

These studies were carried out using pulses from a 120fs, 800nm, 0.75mJ Ti:sapphire laser system, focused on solid copper targets to intensities in the range of 10^{16} -10^{17} W/cm^2. K_α X-ray conversion efficiency from copper targets was measured for various angles of incidence and laser pulse energies. In order to try to improve the K_α X-ray conversion efficiency some measurements were performed using two different prepulse regimes with prepulse contrast ratios of 10^{-1} and 5×10^{-4}. The increase in the keV X-ray production obtained with 10^{-1} prepulse contrast ratio compared to 5×10^{-4} indicates that the interactions in the underdense plasma may also contribute to hot electron and keV X-ray generation. Using the knife-edge technique, the size of the K_α X-ray emission was measured to be approximately 8 μm. The K_α X-ray emission was characterized in both vacuum and air. The X-ray conversion efficiency into Cu K_α had a constant value of over 10^{-5} for a large range of pressure values, from vacuum to approximately 50 Torr and it dropped almost one order of magnitude when using ambient background pressure. This demonstrates that the K_α X-ray source can be simplified considerably since the need for relatively high vacuum can be eliminated.

A K_α X-ray point source was constructed to operate at 1 kHz repetition rate. Emission rates of 6.7×10^9 photons/s into 2π sr at 1 kHz repetition rate were demonstrated resulting in peak observed X-ray conversion efficiency into Cu K_α line emission of 3.2×10^{-5}. This is the highest K_α X-ray flux reported for kHz sources from sub-millijoule laser pulses. This work demonstrates that K_α X-ray energy conversion efficiencies higher than 10^{-5} reported for high-energy laser systems can be obtained at low pulse energies as well. In addition, current results indicate that commercial tabletop laser systems with low energy pulses but with high (kilohertz) repetition rate can make an effective source of narrow linewidth K_α radiation. High repetition laser systems can speed up applications where only one event can be processed per laser pulse (e.g. pulse height analysis) and they are advantageous in high-resolution applications, which require micro X-ray sources with very small source size with limited energy. The acquisition time could be decrease 10 times using the new commercial laser systems with repetition rates of 10 kHz, which are currently available.

The emission of hot electrons from laser-produced plasmas in the same intermediate intensity range from 10^{16} to 10^{17} W/cm^2 was studied as well using sub-millijoule 120 fs Ti: Sapphire laser pulses focused to spots of a few microns in diameter. Strong emission of hot electrons with energies from 80 keV to above 250 keV from microplasmas created with both *p*- and *s*-polarized 250 μJ laser pulses were observed experimentally. Electron jets with energies exceeding 250 keV were observed to be highly directional. The electron jets are found to be in the plane of electric field polarization for both p and s polarizations in a narrow emission cone angle of around 10° (FWHM). The hot electrons emitted from these femtosecond laser plasmas were also used for radiographic imaging. It is expected that the short initial duration of these electron pulses would make them useful for time resolved applications.

The angular dependence of the hot electrons with energies over 80 keV ejected outwards from the plasma was studied for four angle of incidence, 30°, 36°, 42°, and 65°, in order to better understand the mechanisms of generation of the fast electron jets. It found that these electrons are emitted between normal and specular direction changing from normal towards specular direction with increasing the angle of incidence.

A 2D particle-in-cell (PIC) code has been utilized to study the hot electron emission from femtosecond laser-produced plasmas in the intensity regime of 10^{16} to 10^{17} W/cm^2 using near infrared laser pulses. Modeling of the interaction process is potentially useful to understand the generation mechanisms and explain the features observed in the experiments. In the case of *p* polarization, hot electrons with energies over 200 keV were observed numerically as well. In case of *s* polarization, it is expected that full 3D simulation is necessary in order to properly resolve all the field components. In both cases further theoretical work is required in order to identify the exact combination of mechanisms leading to collimation and directionality of the observed electron emission. Simulations were performed to study the emission of the hot electrons and the electrons jet formation in case of *p*-polarized beams at different angles of incidence. The simulation results obtained for the angles of incidence of 45° and 60° agree reasonably well with the measurements. However, for 30°angle of incidence, the emission angle obtained from simulation is much higher than the one obtained experimentally. Hot electron emission was studied using 2D PIC code under different plasmas scale length conditions for 45° angle of incidence. The emission angle is observed to be between normal and specular direction for different scale lengths. When the laser is incident on steeper preformed density gradients, the emission direction changes in time from target normal to specular direction. In the absence of the preplasma altogether the angle of emission of high energy electrons remained closer to the normal direction.

The generation mechanism for the bulk of the hot electron emission leading to K_α radiation in the case of p-polarized laser pulses is attributed to resonance absorption. However, resonance absorption will not explain the production of the hot electron jets with energies over 250 keV. The tentative mechanisms responsible for the generation of such energetic and directional beam of electrons are attributed to either two-plasmon decay or stimulated Raman scattering, or both. However, further investigations are necessary to clarify this and to elucidate whether other mechanisms are involved.

There are a number of technical improvements that could be implemented in the future to advance the development of the tabletop X-ray source for ultrafast structural measurements. For instance, implementing an automatic system to correct continuously the target position would be desirable. It has been pointed out that one of the key parameters is the laser focusing when high numerical aperture lenses with limited depth of field are used to achieve the required intensities. A stable target positioning system would ensure constant laser intensity over one rotation and thus a steady X-ray flux from one laser shot to another.

The solid target used in the current experiments lasts for 366 revolutions with laser operating at 1 kHz, after which it must be repolished. The target lifetime can be extended by using another type of solid target. For instance, a wire target would provide longer acquisition times for the same X-ray fluxes.

In terms of the laser system, an additional Pockels cell inserted in the laser system would permit studies of X-ray generation for the case of no prepulse. While it has been shown that the keV X-ray flux is higher for the case of 10^{-1} prepulse contrast ratio compared to 5×10^{-4}, it is desirable to measure and optimize the K_α X-ray conversion efficiency for the case of no prepulse. This is because a large prepulse will produce a long preplasma, where very energetic hot electrons can be generated, which are not desirable because they undergo larger trajectories away from the initial focal spot, resulting in an elongated X-ray pulse duration and spatial size. The no prepulse case may also help to elucidate the generation mechanism of the hot electron jets from femtosecond laser-produced plasmas.

Finally, it was pointed out that one of the key parameter in the production of K_α radiation is the laser intensity because of a possible existence of an optimum intensity for each material. In order to demonstrate if this is the case, studies are required at various intensities and accurate measurements of the exact laser intensities at the focus of high power laser pulses are necessary. One possible technique to measure the peak intensity is to use the intense field ionization of various low-pressure gas targets. The peak laser intensity can be determined from the dependence of the threshold laser intensity on the ionization potential and the charge state of the species generated at focus.

Efficient high repetition rate sources of narrow linewidth K_α X-ray radiation and of 80-250 keV electrons have been demonstrated in this thesis. These results open the way for exploration of many application areas including femtosecond time resolved studies of molecular and solid state processes.

BIBLIOGRAPHY

[1] J. Hares, J. D. Kilkenny, M. M. Key and J. G. Lunney
"Measurement of Fast-Electron Energy Spectra and Preheating in Laser-Irradiated Targets"
Phys. Rev. Lett. **42**, 1216 - 1219 (1979)

[2] N. H. Burnett, G. D. Enright, A. Avery, A. Loen, and J. C. Kieffer
"Time-resolved Kα spectra in high-intensity laser-target interaction"
Phys. Rev. A **29**, 2294 - 2297 (1984)

[3] E. M. Campbell,
"The physics of megajoule, large-scale, and ultrafast short-scale laser plasmas"
Phys. Fluids B **4**, 3781-3799 (1992)

[4] M. M. Murnane, H. C. Kapteyn, and R. W. Falcone
"High-Density Plasmas Produced by Ultrafast Laser Pulses"
Phys. Rev. Lett. **62**, 155 - 158 (1989)

[5] U. Teubner, C. Wülker and W. Theobald, E. Förster
"X-ray spectra from high-intensity subpicosecond laser produced plasmas"
Phys. Plasmas **2**, 972-981 (1995)

[6] A. Rousse, P. Audebert, J. P. Geindre, F. Fallies, J. C. Gauthier, A. Mysyrowicz, G. Grillon, and A. Antonetti
"Efficient K_α x-ray source from femtosecond laser-produced plasmas"
Phys. Rev. E **50,** 2200-2207 (1994)

[7] H. Chen, B. Soom, B. Yaakobi, S. Uchida, and D. D. Meyerhofer
"Hot-electron characterization from Kα measurements in high-contrast, p-polarized, picosecond laser-plasma interactions"
Phys. Rev. Lett. **70**, 3431 - 3434 (1993)

[8] M. Schnürer, M. P. Kalashnikov, P. V. Nickles, Th. Schlegel, and W. Sandner, N. Demchenko, R. Nolte and P. Ambrosi
"Hard x-ray emission from intense short pulse laser plasmas"
Phys. Plasmas **2**, 3106-3110 (1995)

[9] J. D. Kmetec, C. L. Gordon, III, J. J. Macklin, B. E. Lemoff, G. S. Brown, and S. E. Harris
"MeV x-ray generation with a femtosecond laser"
Phys. Rev. Lett. **68**, 1527 - 1530 (1992)

[10] Christoph Rose-Petruck et al.
"Picosecond–milliångström lattice dynamics measured by ultrafast X-ray Diffraction"
Nature **398**, 310-312 (1999)

[11] A. Rousse et al.
"Time-resolved femtosecond X-ray diffraction by an ultra-short pulse produced by a laser"
Meas. Sci. Technol. **12**, 1841-1846 (2001)

[12] R. Toth, J. C. Kieffer, S. Fourmaux, T. Ozaki and A. Krol
"In-line phase-contrast imaging with a laser-based hard x-ray source"
Rev. Sci. Instrum. **76**, 083701 (2005)

[13] R. Tommasini, E. E. Fill, R. Bruch, G. Pretzler
"Generation of monoenergetic ultrashort electron pulses from a fs laser plasma"
Appl. Phys. B **79**, 923-926 (2004)

[14] D. C. Eder , G. Pretzler, E. Fill, K. Eidmann, A. Saemann
"Spatial characteristic of K_α radiation from weakly relativistic laser plasmas"
Applied Physics B **70**, 211-217 (2000)

[15] L. M. Chen, P. Forget, S. Fourmaux, J. C. Kieffer, A. Krol, C. C. Chamberlain, B. X. Hou, J. Nees, and G. Mourou
"Study of hard x-ray emission from intense femtosecond Ti:sapphire laser-solid target interactions"
Phys. Plasmas **11**, 4439 (2004)

[16] H.-S. Park, N. Izumi, M. H. Key, J. A. Koch, O. L. Landen, P. K. Patel. T. W. Phillips, and B. B. Zhang
"Characteristics of high energy K_α and Bremsstrahlung sources generated by short pulse petawatt lasers"
Rev. Sci. Instrum. **75**, 4048 (2004)

[17] J. Thogersen , A. Borowiec, H. K. Haugen, F. E. McNeill, I. M. Stronach
"X-ray emission from femtosecond laser micromachining"
Applied Physics A. **73** (3), 361-363 (2001)

[18] Hagerdon, J. Kutzner, G. Tsilimis, H. Zacharias
"High-repetition-rate hard X-ray generation with sub-millijoule femtosecond laser pulses"
Appl. Phys. B **77**, 49-57 (2003)

[19] J. Kutzner, M. Silies, T. Witting, G. Tsilimis, H. Zacharias
"Efficient high-repetition-rate fs-laser based X-ray source"
Appl. Phys. B **78**, 949 (2004)

[20] Y. Jiang, T. Lee, W. Li, G. Ketwaroo, and C. G. Rose-Petruck
"High-average-power 2-kHz laser for generation of ultrashort x-ray pulses"
Optics Letters, **27** (11), 963-965 (2002)

[21] G. Korn, A. Thoss, H. Stiel, U. Vogt, M. Richardson, and T. Elsaesser
"Ultrashort 1-kHz laser plasma hard x-ray source"
Optics Letters, **27**, 866-868 (2002)

[22] N. Zhavoronkov, Y. Gritsai, G. Korn, T. Elsaesser
"Ultra-short efficient laser-driven hard X-ray source operated at a kHz repetition rate"
Appl.Phys. **79**, 663 (2004)

[23] C. G. Serbanescu, J. Santiago and R. Fedosejevs
"Micro X-ray Sources from Femtosecond Laser Plasmas"
SPIE **5196,** 344-351 (2003)

[24] C. Serbanescu, J.A. Juzer and R. Fedosejevs
"Efficient K_α X-ray source from sub-millijoule femtosecond laser pulses operated at kHz repetition rate"
Submitted to Rev. Sci. Instrum.

[25] R. Fedosejevs, C. Serbanescu, F. Dorchies, C. Fourment, C. Bonté, F. Blasco, J. Santos, S. Petit, D. Romanov, W. Rozmus, V.Yu Bychenkov, C.E. Capjack and V. Tikhonchuk
"Hot electron jets from femtosecond heated plasmas at intensities of 10^{16}-10^{17} W/cm^2"
J. Phys. IV **133**, 271-275 (2006)

[26] C.G. Serbanescu and R. Fedosejevs
"Electron radiography using hot electron jets from sub-millijoule femtosecond laser pulses"
Appl. Phys. B, 83, 521-525 (2006)

[27] F. F. Chen
Introduction to Plasma Physics and Controlled Fusion, Vol. 1: Plasma Physics
Plenum Press, New York (1984)

[28] D. Attwood
Soft X-rays and extreme ultraviolet radiation
Cambridge University Press, Cambridge (1999)

[29] W. L. Kruer
The Physics of Laser Plasma Interaction
Westview Press, Oxford (2003)

[30] D. W. Forslund, J. M. Kindel, Kenneth Lee, E. L. Lindman, and R. L. Morse
"Theory and simulation of resonant absorption in a hot plasma"
Phys. Rev. A **11**, 679 - 683 (1975)

[31] D. W. Forslund, J. M. Kindel, and K. Lee
"Theory of Hot-Electron Spectra at High Laser Intensity"
Phys. Rev. Lett. **39**, 284-288 (1977)

[32] K. G. Estabrook, E. J. Valeo, and W. L. Kruer
"Two-dimensional relativistic simulations of resonance absorption"
Phys. Fluids **18**, 1151-1159 (1975)

[33] K. Estabrook and W. L. Kruer
"Properties of Resonantly Heated Electron Distributions"
Phys. Rev. Lett. **40**, 42 - 45 (1978)

[34] R. Fedosejevs, R. Ottmann, R. Sigel, G. Kühnle, S. Szatmari, F.P. Schäfer
"Absorption of Femtosecond Laser Pulses in High-Density Plasmas"
Phys. Rev. Lett. **64**, 1250-1253 (1990)

[35] D. F. Price, R. M. More, R. S. Walling, G. Guethlein, R. L. Shepherd at al.
"Absorption of Ultrashort Laser Pulses by Solid Targets Heated Rapidly to Temperatures 1-1000 eV"
Phys. Rev. Lett. **75**, 252-255 (1995)

[36] P. Gibbon and E. Förster
"Short-pulse laser-plasma interactions"
Plasma Phys. Control. Fusion **38**, 769-793 (1996)

[37] K. Eidmann, J. Meyer-ter-Vehn, T. Schlegel, S. Hüller
"Hydrodynamic simulation of subpicosecond laser interaction with solid-density matter"
Phys. Rev. E **62**, 1202-1214 (2000)

[38] F. Brunel
"Not-So-Resonant, Resonant Absorption"
Phys. Rev. Lett. **59** (1), 52-55 (1987)

[39] G. Pretzler, Th. Schlegel, and E. Fill, D. Eder
"Hot-electron generation in copper and photopumping of cobalt"
Phys. Rev. E **62**, 5618 - 5623 (2000)

[40] V. M. Gordienko, I. M. Lachko, P. M. Mikheev, A. B. Savel'ev, D. S. Uryupina and R. V. Volkov
"Experimental characterization of hot electron production under femtosecond laser plasma interaction at moderate intensities'

Plasma Phys. Control. Fusion **44,** 2555–2568 (2002)

[41] T. W. Johnston and J. M. Dawson
"Correct values for high-frequency power absorption by inverse bremsstrahlung in plasmas"
Phys. Fluids **16**, 722 (1973)

[42] S. Eliezer
The Interaction of High-Power Lasers with Plasmas
Institute of Physics Pub., Bristol (2002)

[43] P. Gibbon
Short Pulse Laser Interactions with Matter-An Introduction
Imperial College Press, London (2005)

[44] K. R. Manes, V. C. Rupert, J. M. Auerbach, P. Lee, and J. E. Swain
"Polarization and Angular Dependence of 1.06-μm Laser-Light Absorption by Planar Plasmas"
Phys. Rev. Lett. **39**, 281 (1977)

[45] A. G. M. Maaswinkel, K. Eidmann, and R. Sigel,
"Comparative Reflectance Measurements on Laser-Produced Plasmas at 1.06 and 0.53 μm"
Phys. Rev. Lett. **42**, 1625 (1979).

[46] J. C. Kieffer, P. Audebert, M. Chaker, J. P. Matte, H. Pépin, and T. W. Johnston
P. Maine, D. Meyerhofer, J. Delettrez, D. Strickland, P. Bado, and G. Mourou
"Short-Pulse Laser Absorption in Very Steep Plasma Density Gradients"
Phys. Rev. Lett. **62**, 760 - 763 (1989)

[47] U. Teubner, J. Bergmann, B. van Wonterghem, and F. P. Schäfer, R. Sauerbrey
"Angle-dependent x-ray emission and resonance absorption in a laser-produced plasma generated by a high intensity ultrashort pulse"
Phys. Rev. Lett. **70**, 794 - 797 (1993)

[48] D. D. Meyerhofer, H. Chen, J. A. Delettrez, B. Soom, S. Uchida, and B. Yaakobi
"Resonance absorption in high-intensity contrast, picosecond laser–plasma interactions"
Phys. Fluids B **5**, 2584-2588 (1993)

[49] H. Figueroa, C. Joshi, H. Azechi, N. A. Ebrahim, and Kent Estabrook
"Stimulated Raman scattering, two-plasmon decay, and hot electron generation from underdense plasmas at 0.35 μm"
Phys. Fluids **27**, 1887-1896 (1984)

[50] N. A. Ebrahim , H. A. Baldis, C. Joshi , and R. Benesch
"Hot Electron Generation by the Two-Plasmon Decay Instability in the Laser-Plasma Interaction at 10.6 μm"
Phys. Rev. Lett. **45**, 1179-1182 (1980)

[51] S. Bastiani, A. Rousse, J. P. Geindre, P. Audebert, C. Quoix, G. Hamoniaux, A. Antonetti, and J. -C. Gauthier
"Experimental study of the interaction of subpicosecond laser pulses with solid targets of varying initial scale lengths"
Phys. Rev. E **56**, 7179 - 7185 (1997)

[52] M Schnürer, R Nolte, T Schlegel, M P Kalachnikov, P V Nickles, P Ambrosi and W Sandner
"On the distribution of hot electrons produced in short-pulse laser - plasma interaction"
J. Phys. B **30**, 4653-4661 (1997)

[53] J. Yu, Z. Jiang, and J. C. Kieffer, A. Krol
"Hard x-ray emission in high intensity femtosecond laser–target interaction"
Phys. Plasmas **6**, 1318-1322 (1999)

[54] U. Teubner, I. Uschmann, P. Gibbon, D. Altenbernd, and E. Förster, T. Feurer, W. Theobald, and R. Sauerbrey, G. Hirst, M. H. Key, J. Lister, and D. Neely
"Absorption and hot electron production by high intensity femtosecond uv-laser pulses in solid targets"
Phys. Rev. E **54**, 4167 - 4177 (1996)

[55] M. Schnürer, R. Nolte, A. Rousse, G. Grillon, G. Cheriaux, M. P. Kalachnikov, P. V. Nickles, and W. Sandner
"Dosimetric measurements of electron and photon yields from solid targets irradiated with 30 fs pulses from a 14 TW laser"
Phys. Rev. E **61**, 4394 - 4401 (2000)

[56] P. Gibbon and A. R. Bell
"Collisionless Absorption in Sharp-Edged Plasmas"
Phys. Rev. Lett. **68**, 1535- 1539 (1992)

[57] S. C. Wilks, W. L. Kruer, M. Tabak, and A. B. Langdon
"Absorption of Ultra-Intense Laser Pulses"
Phys. Rev. Lett. **69**, 1383- 1386 (1992)

[58] Shridhar Aithal, Pierre Lavigne, Henri Pépin, and Tudor Wyatt Johnston, Kent Estabrook
"Superthermal electron production from hot underdense plasmas"
Phys. Fluids **30**, 3825-3831 (1987)

[59] Y. Sentoku, H. Ruhl, K. Mima, R. Kodama, K. A. Tanaka, and Y. Kishimoto
"Plasma jet formation and magnetic-field generation in the intense laser plasma under oblique incidence"
Phys. Plasmas **6**, 2855-2861 (1999)

[60] L. M. Chen, J. Zhang, Y. T. Li, H. Teng, T. J. Liang, Z. M. Sheng, Q. L. Dong, L. Z. Zhao, Z. Y. Wei, and X. W. Tang
"Effects of Laser Polarization on Jet Emission of Fast Electrons in Femtosecond-Laser Plasmas"
Phys. Rev. Lett. **87**, 225001 (2001)

[61] Z. -M. Sheng, Y. Sentoku, K. Mima, J. Zhang, W. Yu, and J. Meyer-ter-Vehn
"Angular Distributions of Fast Electrons, Ions, and Bremsstrahlung x/ γ-Rays in Intense Laser Interaction with Solid Targets"
Phys. Rev. Lett. **85**, 5340 - 5343 (2000)

[62] M. I. K. Santala, M. Zepf, I. Watts, F. N. Beg, E. Clark, M. Tatarakis, K. Krushelnick, A. E. Dangor, T. McCanny, I. Spencer, R. P. Singhal, K. W. D. Ledingham, S. C. Wilks, A. C. Machacek, J. S. Wark, R. Allott, R. J. Clarke, and P. A. Norreys
"Effect of the Plasma Density Scale Length on the Direction of Fast Electrons in Relativistic Laser-Solid Interactions"
Phys. Rev. Lett. **84**, 1459 - 1462 (2000)

[63] C. Rousseaux, F. Amiranoff, C. Labaune, and G. Matthieussent
"Suprathermal and relativistic electrons produced in laser–plasma interaction at 0.26, 0.53, and 1.05 μm laser wavelength"
Phys. Fluids B **4**, 2589-2595 (1992)

[64] Jun Zhang, J. Zhang, Z. M. Sheng, Y. T. Li, Y. Qiu, Z. Jin, and H. Teng
"Emission direction of fast electrons in laser-solid interactions at intensities from the nonrelativistic to the relativistic'
Phys. Rev. E **69**, 046408 (2004)

[65] Y.T. Li, J. Zhang, L.M. Chen, Y. F. Mu, T. J. Liang, Z.Y. Wei, Q.L. Dong, Z. L. Chen, H. Teng, S.T. Chun-Yu, W. M. Jiang, Z.J. Zheng, and X. W. Tang,
"Hot electrons in the interaction of femtosecond laser pulses with foil targets at a moderate laser intensity"
Phys. Rev. E **64**, 046407 (2001)

[66] Ferenc Ráksi, Kent R. Wilson, Zhiming Jiang, Abdelaziz Ikhlef, Christian Y. Côté, and Jean-Claude Kieffer
"Ultrafast x-ray absorption probing of a chemical reaction"
J. Chem. Phys. **104**, 6066-6069 (1996)

[67] C. Hombourger
"An empirical expression for K-shell ionization cross section by electron impact"
J. Phys. B: At. Mol. Opt. Phys. **31**, 3693-3702 (1998)

[68] M. O. Krause
"Atomic Radiative and Radiationless Yields for *K* and *L* Shells"
J. Phys. Chem. Ref. Data **8**, 307-327 (1979)

[69] NIST database: Tables of X-Ray Mass Attenuation Coefficients and Mass Energy-Absorption Coefficients
http://physics.nist.gov/PhysRefData/XrayMassCoef/cover.html

[70] NIST database: ESTAR: Stopping Powers and Ranges for Electrons
http://www.physics.nist.gov/PhysRefData/Star/Text/ESTAR.html

[71] Ch. Reich, P. Gibbon, I. Uschmann and E. Forster
"Yield Optimization and Time Structure of Femtosecond Laser Plasma Kα Sources"
Phys. Rev. Lett. **84**, 4846 (2000)

[72] Margaret M. Murnane; Henry C. Kapteyn; Mordecai D. Rosen; Roger W. Falcone
"Ultrafast X-Ray Pulses from Laser-Produced Plasmas"
Science **251**, 531-536 (1991)

[73] C. W. Siders, A. Cavalleri, K. Sokolowski-Tinten, Cs. Tóth, T. Guo, M. Kammler, M. Horn von Hoegen, K. R. Wilson, D. von der Linde, C. P. J. Barty
"Detection of Nonthermal Melting by Ultrafast X-ray Diffraction"
Science **286**, 1340 – 1342 (1999)

[74] A. Rousse, C. Rischel, S. Fourmaux, I. Uschmann, S. Sebban, G. Grillon, Ph. Balcou, E. FÃ¶rster, J.P. Geindre, P. Audebert, J.C. Gauthier, D. Hulin
"Non-thermal melting in semiconductors measured at femtosecond resolution"
Nature **410**, 65 - 68 (2001)

[75] A. Cavalleri, Cs. Tóth, C. W. Siders, J. A. Squier, F. Ráksi, P. Forget and J. C. Kieffer
"Femtosecond Structural Dynamics in VO2 during an Ultrafast Solid-Solid Phase Transition"
Phys. Rev. Lett. **87**, 237401 (2001)

[76] Adeline Bonvalet, Adeline Darmon, Jean-Christophe Lambry, Jean-Louis Martin, and Patrick Audebert
"1 kHz tabletop ultrashort hard x-ray source for time-resolved x-ray protein crystallography"
Opt. Lett. **31**, 2753-2755 (2006)

[77] P. P. Pronko, S. K. Dutta, and D. Du, R. K. Singh
"Thermophysical effects in laser processing of materials with picosecond and femtosecond pulses"
J. Appl. Phys. **78,** 6233-6240 (1995)

[78] Kirkwood S. E., Van Popta A. C. , Tsui Y. Y. , Fedosejevs R.
"Single and multiple shot near-infrared femtosecond laser pulse ablation thresholds of copper"
Appl. Phys. A **81**, 729-735 (2005).

[79] C. Momma, S. Nolte, B. N. Chichkov, F. V. Alvensleben, and A. Tünnermann
"Precise laser ablation with ultrashort pulses"
Appl. Surf. Sci. **109/110**, 15-19 (1997)

[80] A. E. Siegman
Lasers
University Science Books, Mill Valley, California, 1986

[81] J. W. Robinson
Handbook of Spectroscopy, vol. I
CRC Press, Inc., Florida (1974)

[82] A. H. Compton and S.K. Allison
X-Rays in Theory and Experiments
D. Van Nostrand, New York, Second Edition (1935)

[83] Yoichiro Hironaka, Kazutaka G. Nakamura, and Ken-ichi Kondo
"Angular distribution of x-ray emission from a copper target irradiated with a femtosecond laser"
Appl. Phys. Lett. **77**, 4110 (2000)

[84] B. L. Henke, J. Y. Uejio, G. F. Stone, C. H. Dittmore, F. G. Fujiwara
"High-energy x-ray response of photographic films: models and measurement"
J. Opt. Soc. Am. B **3**, 1540-1550 (1986)

[85] Y. M. Li, J. N. Broughton, R. Fedosejevs and T. Tomie
"Formation of plasma columns in atmospheric pressure gases by picosecond KrF laser pulses"
Optics Comm. **93**, 366-377 (1992)

[86] T. Auguste, P. Monot, L. -A. Lompré, G. Mainfray and C. Manus
"Defocusing effects of a picosecond terawatt laser pulse in an underdense plasma"
Optics Comm. **89**, 145-148 (1992)

[87] J. C. Kieffer, Z. Jiang, A. Ikhlef, C. Y. Cote, and O. Peyrusse
"Picosecond dynamics of a hot solid-density plasma"
J. Opt. Soc. Am. B 13, 132-137 (1996)

[88] A. Sjögren, M. Harbst, C.-G. Wahlström, S. Svanberg, C. Olsson
"High-repetition-rate, hard x-ray radiation from a laser-produced plasma: Photon yield and application considerations"
Rev. Sci. Instrum. **74**, 2300-2311 (2003)

[89] D.E. Gray
American Institute of Physics Handbook
McGraw Hill, New York, 1973

[90] K. S. Krane
Introductory Nuclear Physics
Wiley, New York, 1987

[91] P. D. Rockett, C. R. Bird, C. J. Hailey, D. Sullivan, D. B. Brown, and P. G. Burkhalter
"X-ray calibration of Kodak Direct Exposure film"
Appl. Opt. **24**, 2536-2542 (1985)

[92] H.J. Kull and V.T. Tikhonchuk
"Fast electrons from electron-ion collisions in strong laser fields"
Phys. of Plasmas **12**, 063301 (2005)

[93] A. Brantov, W. Rozmus, R. Sydora, C. E. Capjack, V. Yu. Bychenkov, V. T. Tikhonchuk
"Enhanced inverse bremsstrahlung heating rates in a strong laser field"
Phys. of Plasmas **10**, 3385-3396 (2003)

[94] M. M. Aleonard, F. Gobet, G. Claverie, M. Gerbaux, F. Hannachi, G. Malka, J. N. Scheurer, M. Tarisien, F. Dorchies, D. Descamps, C. Fourment, S. Petit, R. Fedosejevs, V. Meot and P. Morel
"Energetic electrons produced in the interaction of a kilohertz femtosecond laser with tantalum targets"
Submitted to Journal of Modern Optics.

[95] D. V. Romanov, V. Yu. Bychenkov, W. Rozmus, C. E. Capjack, and R. Fedosejevs
"Self-Organization of a Plasma due to 3D Evolution of the Weibel Instability"
Phys. Rev. Lett. **93**, 215004 (2004)

[96] E. E. Fill, R. Trushin, G. Bruch, and R. Tommasini
"Diffraction of laser-plasma-generated electron pulses"
Appl. Phys. B **81**, 155-157 (2005)

[97] Y. Okano, Y. Hironaka, K. Kondo, and K. G. Nakamura
"Electron imaging of charge-separated field on a copper film induced by femtosecond laser irradiation"
Appl. Phys. Lett. **86**, 141501 (2005)

[98] http://www.westgrid.ca/home.html

[99] Cristina Serbanescu, Rahim Janmohamed, Babak Shokri, Ying Tsui, Dmitri Romanov, Clarence Capjack, Wojciech Rozmus and Robert Fedosejevs,
"Hot electrons, keV X-rays and Fast Ions from Femtosecond Laser Produced Micro Plasma"
Oral presentation at the 31st IEEE International Conference on Plasma Science June28-July1, Baltimore (2004)

[100]C. Joshi, T. Tajima, J. M. Dawson, H. A. Baldis and N. A. Ebrahim
"Forward Raman Instability and Electron Acceleration"
Phys. Fluids **27**, 511-515 (1984)

[101]R. E. Turner, D. W. Phillion, B. F. Lasinski, and E. M. Campbell
"Half- and three-halves harmonic measurements from laser-produced plasmas"
Phys. Rev. Lett. **47**, 1285-1288 (1981)

[102]P. D. Carter, S. M. L. Sim, H. C. Barr, and R. G. Evans
"Time-Resolved Observations of the Three-Halves Harmonic Spectrum from Laser-Produced Plasmas"
Phys. Rev. Lett. **44**, 1407-1410 (1980)

Appendix A

ENERGY LEVEL DIAGRAM FOR COPPER

Figure A.1 [28] displays the energy level diagram for the copper atom ($Z = 29$). The figure includes several major transitions, values of the quantum numbers n, l, and j for each subshell accompanied by the subshell designation and spectroscopic notations. The figure uses the X-ray notation where the state defined by the principal quantum number $n = 1$ is referred to as the *K*- shell, the state specified by $n = 2$ is referred to as the L-shell, the state defined by $n = 3$ is referred to as the *M*- shell, etc. The emission lines K_α, K_β, etc are related to the transitions terminating in the ground state ($n = 1$). The *K*-absorption edge $E_{K,\ abs}$ represents the energy required to lift a *K*-shell electron to a free state of zero binding energy. The notations for emission lines and absorption edges are similar for L-shell, M-shell, etc.

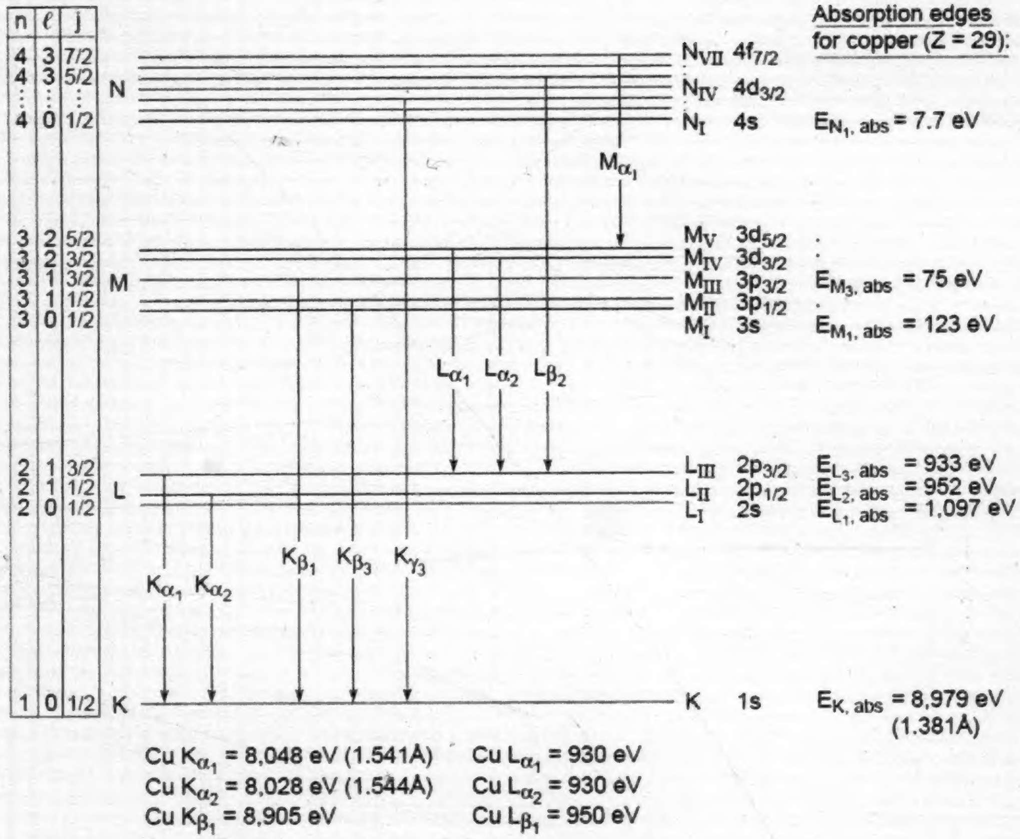
n ℓ j
N
M
L
K
Absorption edges for copper (Z = 29):
N_{VII} $4f_{7/2}$
N_{IV} $4d_{3/2}$
N_{I} 4s
$E_{N_1, abs}$ = 7.7 eV
M_{α_1}
M_{V} $3d_{5/2}$
M_{IV} $3d_{3/2}$
M_{III} $3p_{3/2}$
M_{II} $3p_{1/2}$
M_{I} 3s
$E_{M_3, abs}$ = 75 eV
$E_{M_1, abs}$ = 123 eV
L_{α_1} L_{α_2} L_{β_2}
L_{III} $2p_{3/2}$
L_{II} $2p_{1/2}$
L_{I} 2s
$E_{L_3, abs}$ = 933 eV
$E_{L_2, abs}$ = 952 eV
$E_{L_1, abs}$ = 1,097 eV
K_{α_1} K_{α_2}
K_{β_1} K_{β_3} K_{γ_3}
K 1s
$E_{K, abs}$ = 8,979 eV (1.381Å)
Cu K_{α_1} = 8,048 eV (1.541Å)
Cu K_{α_2} = 8,028 eV (1.544Å)
Cu K_{β_1} = 8,905 eV
Cu L_{α_1} = 930 eV
Cu L_{α_2} = 930 eV
Cu L_{β_1} = 950 eV

Figure A.1 Energy level diagram for copper ($Z = 29$) [202]. The transitions allowed by the selection rules are also included. In the X-ray nomenclature, the *K*-shell corresponds to $n = 1$, *L*-shell corresponds to $n = 2$, *M*-shell corresponds to $n = 3$, etc. (Following Attwood [28]).

Appendix B

PIC FILES

The input files used to perform the PIC simulation are included in this section. As mentioned before MANDOR 2 PIC code requires two input data files, one for the preprocessing run to generate the incident EM filed to provide the desired focal conditions and the second being the main interaction run.

2D_LaserFoil.rec.input

```
[units]
@ 1.0          Positive => works as wavelengh in microns [10^-4 cm].
               Negative => works as critical electrons' density [cm^-3].

[mesh]
@ 1500         imax: mesh size along X axis
@ 750          jmax: mesh size along Y axis
@ 0            kmax: mesh size along Z axis
@ 60.0e0       Lx:   domain size along X axis
@ 30.0e0       Ly:   domain size along Y axis
@ 40.0e0       Lz:   domain size along Z axis
@ -0.8         tau:  time step (if negative that means [t] = 1/sqrt (1/h1^2 + .. + 1/h3^2))

[boundaryConditions]
@ 2            xMin
@ 2            xMax
@ 0            yMin
@ 0            yMax
@ 0            zMin
@ 0            zMax
```

```
 Type of boundary condition is:
  0 - periodic;
  1 - mirror;
  2 - Mur's first order absorbing boundary condition.

[gaussSpot]
@ 5.7425e+16positive => peak intensity [W/cm^2] / negative => eE/mc\omega.
@ 1.0          Cyclic frequency [omega_0]. Must be 1 (or you understand what do you
do).
@ 55.0         Focus X coordinate [micron].
@ 15.0         Focus Y coordinate [micron].
@ 20.0         Focus Z coordinate [micron].
@ 5.0          Gauss-spot width (FMHW for laser intensity) [micron].
@ 130.00       Pulse duration (FMHW for laser intensity) [fs].
@ 156.00       Pulse leading front offset [fs].
@ 1            EY != 0
@ 0            EZ != 0
> 28.0         TF/SF emitter face position [micron].

[TFSF]
@ 700          TF/SF interface position (X).
@ 1400         TF/SF interface position (X).
@ 30           TF/SF interface position (Y).
@ 720          TF/SF interface position (Y).
@ 0            TF/SF interface position (Z).
@ 0            TF/SF interface position (Z).
@ record       TF/SF interface regime (record, playForward, playBackward).
```

2D_LaserFoil.play.input

```
[units]
@ 1.0           Positive => works as wavelengh in microns [10^-4 cm].
                Negative => works as critical electrons' density [cm^-3].

[mesh]
@ 1250          imax: mesh size along X axis
@ 1250          jmax: mesh size along Y axis
@ 0             kmax: mesh size along Z axis
@ 50.0e0        Lx:  domain size along X axis
@ 50.0e0        Ly:  domain size along Y axis
@ 40.0e0        Lz:  domain size along Z axis
@ -0.8 tau:  time step (if negative that means [t] = 1/sqrt (1/h1^2 + .. + 1/h3^2))

[boundaryConditions]
@ 2             xMin
@ 2             xMax
@ 2             yMin
@ 2             yMax
@ 0             zMin
@ 0             zMax

 Type of boundary condition is:
  0 - periodic;
  1 - mirror;
  2 - Mur's first order absorbing boundary condition.

[TFSF]
@ 20                 TF/SF interface position (X).
@ 720                TF/SF interface position (X).
@ 280                TF/SF interface position (Y).
@ 970                TF/SF interface position (Y).
@ 0                  TF/SF interface position (Z).
@ 0                  TF/SF interface position (Z).
@ playBackward       TF/SF interface regime (record, playForward, playBackward).

[TFSF: open faces]
> xMax               Removes xMax face.
> yMin               Removes yMin face.
> yMax               Removes yMax face.

 Helps to remove one or more faces without doing some cut-plane manipulations.

===============================================================
```

Composite target with preplasma (middle part is better resolved)

Cuts off plasma outside the box [<domain left-bottom-rear corner> / (10, 10, 10)].

```
[aligned foil]
@ 22.5         X coordinate of the center [micron].
@ 22.5         Y coordinate of the center [micron].
@ 0.0          Z coordinate of the center [micron].
@ -1.0         x component of the foil normal.
@ 1.0          y component of the foil normal.
@ 0.0          z component of the foil normal.
@ 5.0          Width of the foil [micron].
@ exponential Type of the profile (linear or exponential)
@ -3.0e-2      Start concentration (positive => [cm^-3];  negative => [n_cr for
electrons]).
@ -5.0e+0      End   concentration (positive => [cm^-3];  negative => [n_cr for
electrons]).
@ -1.0         Charge of particle [e].
@ +1.0         Mass of particle [m].
@ 5            Nx: number of particles per cell along X.
@ 5            Ny: number of particles per cell along Y.
@ 1            Nz: number of particles per cell along Z.
```

Cold preplasma/foil.